UNIVERSITY OF SOUTHAMPTON

FACULTY OF ENGINEERING AND THE ENVIRONMENT

Bioengineering Science Research Group

Development of A Novel Acetabular Cup Component for Large Bearing Total Hip Arthroplasty

by

Faye Catherine Gillard

A thesis submitted in partial fulfilment of the requirements for the degree of Engineering Doctorate

February 2014

UNIVERSITY OF SOUTHAMPTON

ABSTRACT

FACULTY OF ENGINEERING & THE ENVIRONMENT

Engineering Doctorate

DEVELOPMENT OF A NOVEL ACETABULAR CUP COMPONENT FOR LARGE BEARING TOTAL HIP ARTHROPLASTY

by Faye Catherine Gillard

Total hip replacement (THR) is a successful procedure that demonstrates excellent long term survival rates in the elderly patient population. Resurfacing and large diameter bearing total hip components were introduced to improve survivorship in younger patients but problems associated with high levels of wear and component loosening has limited their acceptance in regular clinical practice. Aurora Medical Ltd (Southampton, UK) identified a need for a large diameter bearing hip replacement which offered high postoperative quality of life in the younger patient cohort through the development of a more biomechanically compliant acetabular component. Carbon fibre reinforced polyetheretherketone (CFRPEEK) has been identified as a potential bearing material for orthopaedic applications due to its proven mechanical and chemical properties, and its biocompatibility. This thesis outlines a preliminary design evaluation of a large diameter bearing CFRPEEK acetabular component, and focusses on four areas:

First, a novel cup design was investigated; the intention of the design was to provide more natural load transfer across the joint. The anatomic geometry of the acetabular load bearing surface was characterised, and incorporated into the design of a varying thickness acetabular cup.

Second, the relationship between the manufacturing processing parameters and the internal structure of CFRPEEK was investigated, assessing fibre orientation, distribution and defect population. It was found that the material injection location influenced fibre orientation and although a homogeneous fibre distribution was identified, the presence of porosity suggested that the injection holding pressure and/or the holding time were not adequate for successful moulding.

Third, implant fixation was considered; a primary fixation method was developed which involved creating a unique arrowhead structure onto the cup's backing surface through two-stage moulding. The initial fixation provided by the moulded arrowheads was successfully verified through implantation and extraction investigations. However, further research needs to be conducted on the moulding procedure to ensure a consistent arrowhead shaped structure free from defects is formed. Two osseointegrative coating options to enhance secondary fixation of the cup were assessed. A hydroxyapatite on titanium coating exhibited the highest adhesion strength and did not compromise fatigue or tensile properties of the material.

Finally, studies were conducted to evaluate the feasibility of the digital volume correlation (DVC) technique to assess the change in the peri-prosthetic bone strain distribution as a result of implantation. It was found that bone was an ideal material candidate for DVC when imaged alone; however, the introduction of an acetabular component generated artefacts which compromised image quality and restricted the outcomes. A set of alterations to the image acquisition process were recommended to reduce these artefacts enabling the feasibility of the technique in calculating strains in the peri-prosthetic bone to be realised.

Contents

List of tables

List of figures

DECLARATION OF AUTHORSHIP

I, Faye Catherine Gillard

declare that the thesis entitled

Development of A Novel Acetabular Cup Component for Large Bearing Total Hip Arthroplasty

and the work presented in the thesis are both my own, and have been generated by me as the result of my own original research. I confirm that:

- this work was done wholly or mainly while in candidature for a research degree at this University;
- where any part of this thesis has previously been submitted for a degree or any other qualification at this University or any other institution, this has been clearly stated;
- where I have consulted the published work of others, this is always clearly attributed;
- where I have quoted from the work of others, the source is always given. With the exception of such quotations, this thesis is entirely my own work;
- I have acknowledged all main sources of help;
- where the thesis is based on work done by myself jointly with others, I have made clear exactly what was done by others and what I have contributed myself;
- parts of this work have been published as:

    - Gillard, F.C., Dickinson, A.S., Schneider, U., Taylor, A.C., Browne. M. *Multi-pelvis characterisation of articular cartilage geometry.* Proceedings of the Institution of Mechanical Engineers, Pt H: Journal of Engineering in Medicine, 2013. 227(12):1255-64.

    - Gillard, F.C Boardman, R., Mavrogordato, M., Hollis, D., Sinclair, I., Pierron, F., Browne. M. *The application of digital volume correlation (DVC) to study the microstructural behaviour of trabecular bone during compression.* Journal of the Mechanical Behavior of Biomedical Materials, 2014. 29:480-499.

Signed: ……..

Date:…….

Acknowledgements

The challenges that I have faced over the last 4 years sometimes made me think that I would never get to this stage, but now that I am here the EngD process has been one of the most challenging but rewarding experiences of my life. I feel very proud and slightly relieved to get to this point, but I would not be in this position without the help of brilliant colleagues, friends and family who all need to be thanked.

I can't go any further without thanking my supervisors Professor Martin Browne, Dr Andy Taylor and Dr Alex Dickinson. Martin's enthusiasm and guidance has been invaluable for my development as a researcher and his extremely high tolerance to my constant nagging for corrections and expenses amongst other things deserves an award. I couldn't have asked for a better 'Boss'!

Dr Andy Taylor talked me into the PhD route when I was on placement and his expertise and eagerness has been infectious. I would like to thank Andy for the opportunities that I have been able to experience and the responsibilities given to me from working with you and everyone at Aurora Medical Ltd.

Dr Alex Dickinson, thank you for always remaining positive when the project didn't quite go to plan, always having a spare few minutes to help me (usually with the Instron!) and providing essential guidance throughout this project.

The diversity of the work conducted in my thesis has allowed me to collaborate with many exceptional individuals at the University of Southampton and further afield. Firstly, I would like to thank everyone in the Bioengineeirng group who have all been supportive throughout this experience. μ-Vis fellows especially Mav and Rich, thank you for all the help with the CT work and allowing me to scan my smelly animal specimens. I also need to thank Professor Fabrice Pierron who provided vital expertise and guidance on the DVC work and Professor Urs Schneider whose links with Dr von Hagens allowed me to visit the amazing but slightly bizarre plastinarium in Germany. Rich, Danny, Dan, Nick and Liam, thank you for being a bunch of great guys who listen to my 'occasional' rants and for suggesting the pub when it was truly needed. I am afraid that I can't mention everyone and there are lots of people that I have missed so to everyone in Engineering Sciences…. thank you for such a great time!

But the most important people to thank is my family and my partner Anthony, I truly could not have got through this without your continual support; escaping back to the Somerset countryside was the best way to get away and recharge when the EngD got a little too much.

Definitions and Abbreviations

ADEPT	Hip resurfacing component (MatOrtho, Leatherhead, UK)
ALVAL	Aseptic lymphocytic vasculitis associated lesions
AP	Anterior-posterior
ASR	Articular Resurfacing Component (DePuy, Warsaw, Indiana)
ASTM	American Society for Testing and Materials (standard organisation)
AVN	Avascular Necrosis, cellular death of bone due to reduction in blood supply
BHR	Birmingham Hip Resurfacing (Resurfacing component, Smith and Nephew)
BlueHill	Instron processing programme
BSI	British Standard Institution (standard organisation)
BMI	Body Mass Index
CC	Cross Correlation
CE mark	European Conformity mark (mandatory conformance mark)
CFRPEEK	Carbon fibre Polyetheretherketone (bearing material)
CFR-PBT	Carbon fibre reinforced polybutyleneterephthalate
CoC	Ceramic-on-ceramic (bearing combination)
CoCrMo	Cobalt chromium (bearing material)
CTE	Coefficient of thermal expansion
CT	Computer tomography
DaVis	Digital Volume Correlation processing programme
DeltaMotion	Hip Resurfacing Component (DePuy, Warsaw, Indiana)
DEXA	Dual-energy x-ray absorptiometry
DIC	Digital Image Correlation
DVC	Digital Volume Correlation
EngD	Engineering Doctorate
FFT	Fast Fourier Transform
FEA	Finite Element Analysis
HA	Hydroxyapatite (coating)
HXLPE	Highly cross linked polyethylene
ISO	International Organisation for Standardization (standard organisation)
LaVision	Provider of computational programme for DVC
MATLAB	Computational programme
MITCH PCR	CFRPEEK Resurfacing Component (Stryker Ltd)
MOTIS	CFRPEEK grade produced by Invibio Biomedical Solutions (Thornton Cleveleys, UK)

μCT	Micro Computer Tomography
MoM	Metal-on-metal (bearing combination)
MoP	Metal-on-polyethylene (bearing combination)
OA	Osteoarthritis
PDP	Product Development Process
PE	Polyethylene (bearing material)
PEEK	Polyetheretherketone (orthopaedic material)
PTFE	Polytetrafluoroethylene (bearing material)
RHR	Resurfacing hip replacement
RSA	Roentgen Stereophotogrammetric Analysis (imaging technique)
SEM	Scanning electron microscopy
TC	Texture correlation
T_g	Glass Transition Temperature (polymer)
THA	Total hip arthroplasty
THR	Total hip replacement
Ti	Titanium (coating)
Ti-6Al-4V	Titanium alloy (hip implant material)
T_m	Melt Temperature (polymer)
UHMWPE	Ultra high molecular weight polyethylene
VFM	Virtual Fields Method

1 Introduction

1.1 Motivation & Objectives

Until recently metal-on-metal hip resurfacing was accepted as an effective procedure showing good clinical results, in particular for young, active male patients. However, the patient demographic is restricted and the procedure is not suitable for elderly, female patients for a number of reasons. These include the requirement for good bone stock to support the femoral prosthesis and increased sensitivity to wear debris (1). In addition to the restricted patient demographic, problems associated with a specific resurfacing design in 2009 prompted a sharp decline in the number of resurfacing procedures and a deterioration in confidence in the procedure (2). This was reflected in the number of operations reported in the Australian hip registry in 2011 which showed a 39.7 % reduction between 2008 and 2009 and a 68.5 % reduction compared to the peak in 2005 (3). From a national perspective hip resurfacing procedures declined by over 50 % between 2008 and 2011 (4). This decline has encouraged product developers to either develop new ways of improving resurfacing prosthesis survival to regain surgeon and patient confidence in the procedure or to develop large diameter bearing total hip arthroplasty components which are intended to be more suitable for the younger patient demographic.

Metal-on-metal (MoM) and ceramic-on ceramic (CoC) articulations are used in large diameter bearing combinations; whilst MoM combinations only currently exist for hip resurfacing. However, component failures due to stress shielding (5, 6) and the body's immune response to metallic ions (7) mean non-metallic biomaterials could be employed to address these limitations. Clinical evidence has suggested that there is scope for improvement in the choice of material used and the design of large diameter bearing acetabular components (8).

Aurora Medical Ltd (Southampton, UK) consists of the research and development team from Finsbury Orthopaedics Ltd (acquired by DePuy International in 2009) who identified a need for a large diameter bearing hip system that was biocompatible, reduced incidences of stress shielding, loosening, wear and metal ion sensitivity all with the intention of extending the product's life. Aurora Medical Ltd identified a ceramic-on-polymeric bearing combination using carbon fibre reinforced polyetheretherketone (CFRPEEK) as a possible replacement biomaterial for the acetabular component. PEEK is a semi-crystalline polyaromatic linear chain polymer which has been extensively used in fusion cages in spinal surgery (9) and more recently investigated as a possible substitute for metallic implant materials because of its biocompatibility and low modulus. The addition of carbon fibres (CFRPEEK) improves the material's mechanical properties and makes it suitable for load bearing applications (9).

Developing a new prosthesis requires the medical device company to complete an extensive product development process (PDP). This process involves a series of preclinical analyses with the objective of scientifically proving a new design is superior to existing products.

This thesis outlines the preliminary design stage work carried out for a large diameter bearing acetabular component. It is the largest part of the PDP and extends the design concept into a feasible project, defining the scope and basic deliverables to produce a CE marked product. Unless specified, in this document the term large diameter bearing refers to a resurfacing and a total hip acetabular component.
In particular, the preliminary design work focusses on three areas: component design, component manufacture and component fixation.

- Design of cup – The geometry of the component is based on the ADEPT (MatOrtho Ltd, Leatherhead, UK) device. However, alterations are investigated to develop a more biomechanically compliant component.
- Manufacturability – Aurora Medical Ltd has proposed CFRPEEK as a potential large diameter bearing acetabular component material substitute as it is currently used for spinal implants and has excellent mechanical and biocompatible properties. This thesis focuses on the injection moulding manufacturing technique as a large diameter bearing acetabular component is a complex shape and the processing conditions must be optimised to ensure a component is moulded which exhibits the tensile and fatigue mechanical properties required.
- Acetabular Cup fixation – The outer surface of the prosthesis, which is primarily responsible for bone integration was investigated to address the fixation limitations experienced by current designs. A new approach to primary fixation outlined in Section 3.4 aims to overcome the problems associated with current cementless methods. As this approach has not been previously explored, a series of investigations were undertaken to explore the feasibility of the new fixation concept.

The preliminary design generated from these investigations was studied in the final section of this thesis. With any orthopaedic device, it is essential that preclinical testing is conducted to ensure it is resistant to the predominant cause of failure, aseptic loosening. This is particularly true of the novel device under investigation in this thesis, which is more compliant and was expected to elicit a different response in the bone compared to traditional metallic and ceramic devices. Therefore, the final phase of the work describes the implementation of a novel full-field 3D strain measurement technique to compare the response of bone to implantation of the CFRPEEK cup and a traditional ceramic bearing cup. Figure 1 is a flowchart showing the approach taken in this research; this chart is referred to at the start of each section to help put the study into context. The methodology employed in each study is contained within the relevant section.

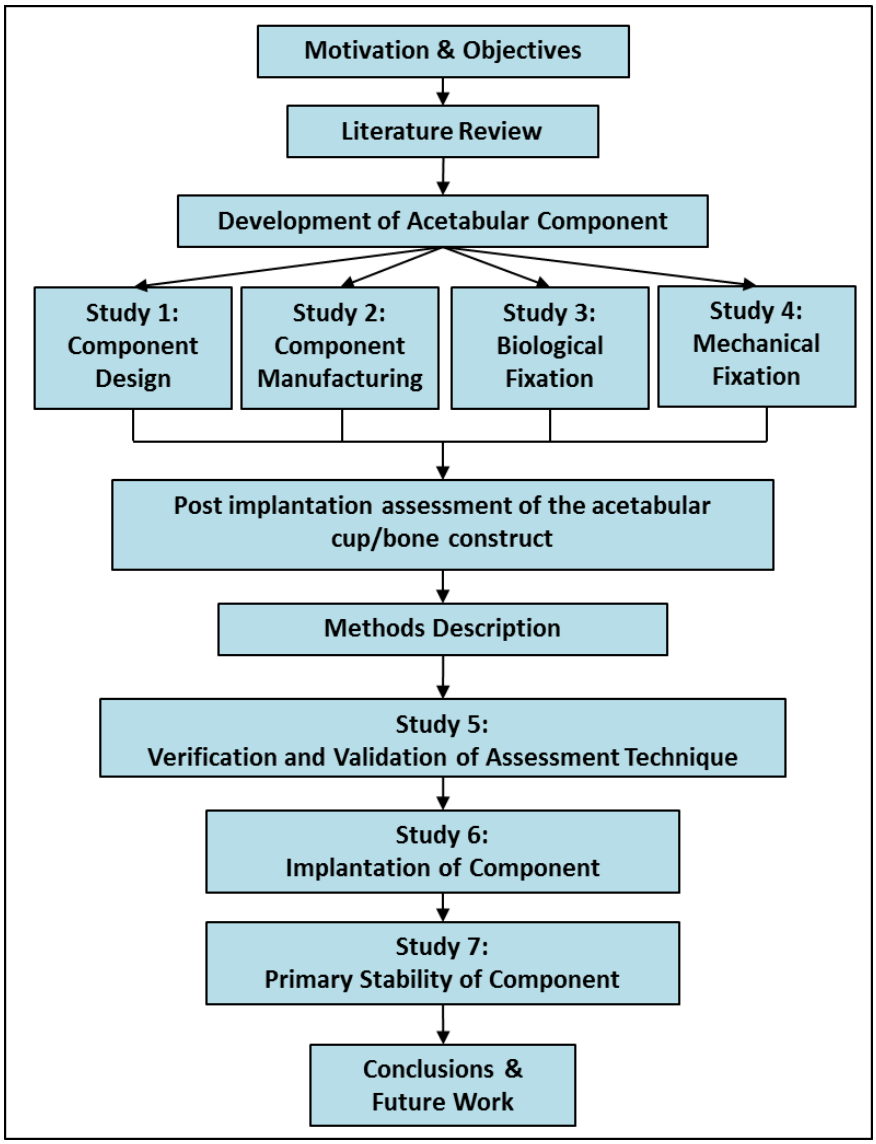

Figure 1: Project Roadmap illustrating the structure of the planned research

2 Literature Review

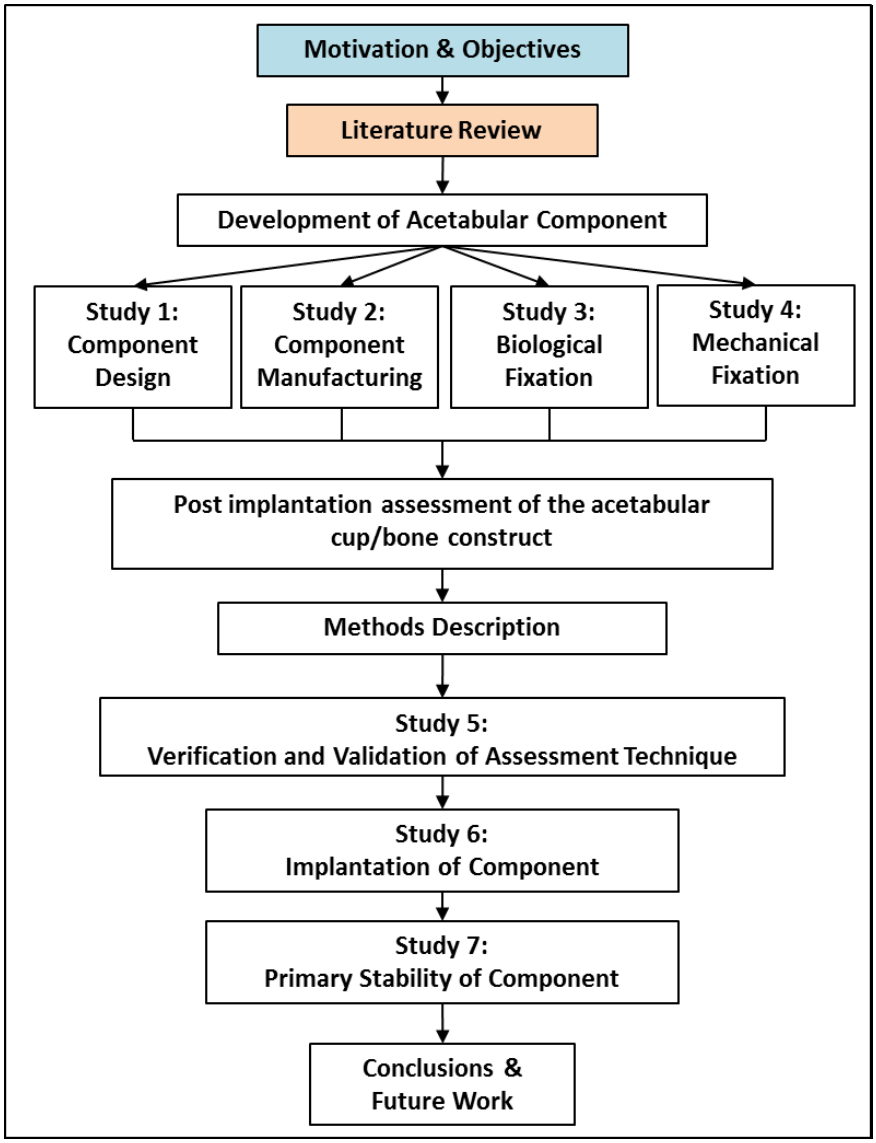

2.1 The Hip Joint, Degeneration and Treatments

2.1.1 Joint Anatomy and Degeneration

The hip joint (Figure 2) is a congruous joint consisting of a ball and socket. Both the concave and the convex parts are symmetrical, and the joint space is equal at all points with slight deviation to permit adequate lubrication (10). The ball is called the femoral head and is located at the proximal end of the femur. This articulates against the acetabulum which is located in the pelvis.

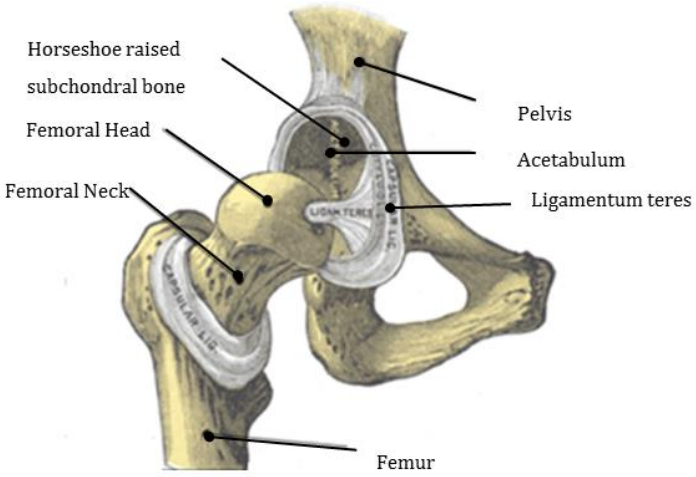

Figure 2: Hip Joint laid open (11).

It is a synovial joint that features hyaline cartilage covering both articulating surfaces. The cartilage is thicker at the centre of the head of the femur than at the circumference, covering the entire surface with the exception of a depression just below its centre for the attachment of the ligementum teres (11). The acetabular cup exhibits a horseshoe raised subchondral bone and articular cartilage layer that extends around the posterolateral rim. The principal function of the articular cartilage is to provide a smooth, lubricating bearing surface with low friction and minimal wear (12).

The hip joint is exposed to very large loads ranging from 250 % body weight during walking up to eight times body weight on occasion when stumbling (13). This demanding environment that the hip must operate in can lead to degeneration of the cartilage which can have a severe effect on quality of life. A number of conditions can accelerate this degradation and these are described below:

Osteoarthritis (OA)

OA refers to the acute degradation of articular cartilage when the wear rate exceeds the rate of repair. The lack of cartilage leads to painful bone-on-bone articulation, inflammation and joint swelling. National joint registries outline OA to be the single largest indication for hip replacement surgery, accounting for approximately 75 % of all primary operations (4, 14).

Rheumatoid Arthritis (RA)

A chronic, usually progressive, systemic inflammatory condition of unknown cause. It is a condition in which the body's immune system attacks its own healthy tissue in an autoimmune response (15). Like OA it can cause painful joints, stiffness, disability but also deformity and the formation of cysts and nodules.

Femoral Neck Fracture and Avascular Necrosis (AVN)

This can occur in the elderly following minor hip trauma (e.g. a fall) as conditions such as osteoporosis leads to a loss in bone mineral density increasing the risk of femoral neck fracture. In younger patients, it usually follows major trauma (e.g. car accident). Trauma can

result in a reduction in blood supply to the femoral head and is the cause of avascular necrosis (16). This results in femoral head collapse and fracture. In order to restore the function of the hip joint, hip arthroplasty is required.

Other Conditions

Abnormalities in the joint can lead to joint degeneration; examples include benign and malignant bone tumours and Paget's disease. Tumours can alter the shape and composition of the joint whilst also affecting the blood supply. This can lead to the onset of vascular necrosis and collapse of the joint. Paget's disease causes a malfunction in the normal process of bone remodelling. The destroyed bone is replaced by weak and brittle bone more prone to fracture.

2.1.2 Treatment of Joint Degeneration

A number of treatments can be used to treat joint degeneration depending on the condition of the underlying bone structure. If arthritic disease is restricted to the bearing surfaces and not considered sufficient for surgical intervention, treatment can take the form of physical therapy, walking aids, anti-inflammatory medications, cortisone injections, and joint supplements such as glucosamine sulphate which may slow down the rate of cartilage damage (17). In advanced cases where the cartilage degeneration is severe and the support bone has deteriorated, surgical intervention in the form of arthroplasty is necessary.

Total Hip Arthroplasty

Total hip arthroplasty involves the replacement of both bearing surfaces of the joint (Figure 3). A typical implant features a ball and socket couple consisting of the femoral and acetabular components. The femoral component features a ball mounted on a metal stem that is implanted with or without the use of cement into the femoral canal. The acetabular component consists of a cup that is implanted into the prepared acetabulum. There have been many varieties of hip replacements that have all stemmed from the first successful examples by Charnley and McKee & Watson-Farrar (Figure 4). The predominant distinguishing features between components are material choice, bearing diameter and fixation type. Figure 4 shows an example of a small bearing metal-on-polyethylene (MoP) component and a large diameter bearing metal-on-metal (MoM) bearing prosthesis. Section 2.2 outlines the different materials which can be selected for a large bearing total hip component.

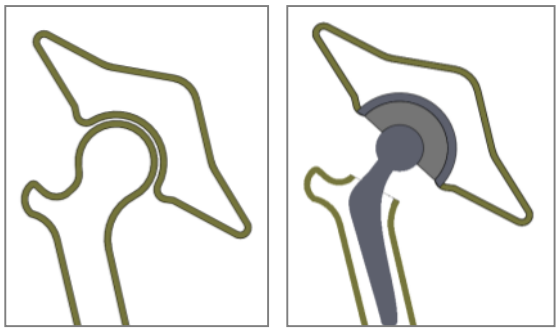

Figure 3: Schematic of Total hip arthroplasty.

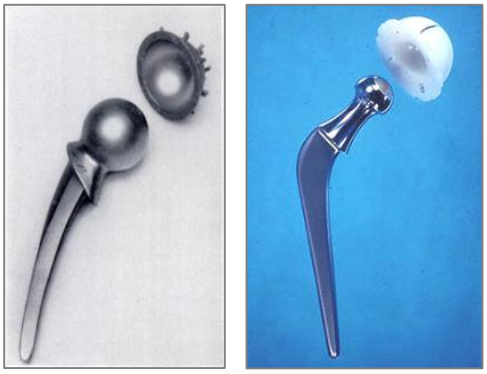

Figure 4: Examples of the first successful THA prostheses: Large diameter bearing McKee & Watson Farrar (Left) (Reproduced with permission and copyright © of the British Editorial Society of Bone and Joint Surgery (18)) and small bearing Charnley (Right) (19).

The most common condition for which a total hip arthroplasty is performed is severe osteoarthritis which has damaged the underlying bone. Other conditions for which THA is particularly appropriate include developmental dysplasia of the hip, Paget's disease, AVN and patients with femoral head fracture as the regions of affected bone are replaced completely. Until recently THA was generally performed in patients older than 60 years because at this age, the physical demands on the prosthesis are fewer, bone quality is poor and the life expectancy of the patient is less than the prosthesis. Additionally, THA surgery is an established procedure, with low risk to the patient. In the last decade, a drop in the success of resurfacing procedures and the development of more appropriate THA devices for younger patients has seen an increase in the number of procedures performed in patients younger than 60 years (3).

Resurfacing Hip Arthroplasty

If degeneration of the hip joint is restricted to the bearing surfaces, a resurfacing component can be implanted. This procedure retains the femoral neck by replacing the contact surfaces only. As with THR surgery, the implant features a ball and socket (Figure 5). However, the femoral component has a thin (3 to 4 mm) hollow ball surface and small stem which is implanted into the femoral neck. Cement is applied to the inside surface of the head component which is then seated onto the prepared femur. The Birmingham hip resurfacing

(BHR) arthroplasty (Figure 6) is the pioneering device and was introduced in July 1997. To date most of the major hip resurfacing systems use a MoM articulation with the BHR considered the gold standard product in the resurfacing market with it dominating the market share in many registries (2, 3, 20). In England and Wales the BHR was used in over 50 % of all resurfacing procedures during 2011 (4). The implications of using a MoM articulation are discussed in more detail in Sections 2.2 and 2.3.

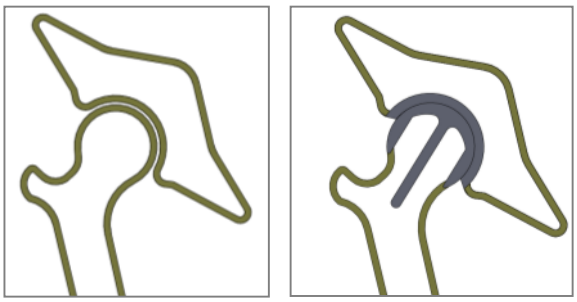

Figure 5: Schematic of resurfacing arthroplasty.

Figure 6: The Birmingham Hip Resurfacing (BHR) implant an example of the first successful prosthesis (1).

As discussed earlier, primary osteoarthritis only affects the bearing surface of the joint. It is expected that in a younger patient the underlying bone stock in the femoral head and neck is of good quality, making excessive bone resection unnecessary and the implantation of a resurfacing component favourable. Generally, patients between the ages of 40-65 years are considered to have good bone stock. In the case of metal designs, females are not the preferred cohort as the recorded levels of metal ions tends to be higher than in males (21). There have been several suggested reasons for this finding, including differences in gait patterns (22) and the tendency to have smaller acetabular components implanted (23). The consequences of high levels of metallic ions are explained further in Section 2.3.3.

Resurfacing treatment brings many benefits in addition to bone conservation. A summary of these includes:

- Lower rate of dislocation (1)
- Earlier return to high performance activities
- Preservation of proximal bone stock
- Reduced risk of leg lengthening
- Revision to THA technically less demanding
- Closer to normal loading on femur reduces proximal stress shielding (6)

2.2 Evolution of Hip Arthroplasty Components

Hip arthroplasty is not a modern concept; with many material combinations being investigated. The earliest form was introduced by Smith-Petersen in Boston. The original design was a ball-shaped hollow hemisphere of glass which could fit over the ball of the hip joint. The objective was to stimulate cartilage regeneration on both sides of the glass joint. Smith-Petersen intended to remove the glass after the cartilage had been restored. In 1923 the design was implanted, while proving biocompatibility; the glass could not withstand the loads during gait and failed. Over the following years many other biomaterials were tried and tested including Viscaloid (a celluloid derivative), pyrex glass, Bakelite and Vitallium cobalt-chromium alloy. Although these implants failed as a result of unsatisfactory material selection and poor manufacturing techniques, improvements in metal manufacturing led to the introduction of the next generation of metal hip components. The next section outlines the evolution in materials used for hip arthroplasty.

2.2.1 Metal on Polymer (MoP) Bearings

The first total hip resurfacing prosthesis was introduced by Sir John Charnley in the early 1950's. The implant comprised of a polytetrafluoroethylene (PTFE/PTFE) bearing combination as this produced the lowest friction amongst existing engineering materials at that time (Figure 7). However, its poor wear resistance combined with the increased sliding distance due to the larger bearing diameter meant the device had a high early failure rate (1). Failures were put down to the technical resurfacing surgical procedure and osteolysis a result of excessive PTFE wear. It was realised that a large diameter resurfacing hard-on-soft bearing using PTFE would also give rise to excessive wear, prompting Charnley to focus on developing a metal-on-polymer (ultra-high-molecular-weight-polyethylene, (UHMWPE)) THA device that could incorporate a small head diameter and a less technical surgical procedure. The MoP bearing combination is a popular choice for total hip replacement and many other small diameter bearing implants have been introduced since Charnley's low-friction arthroplasty device (Figure 4).

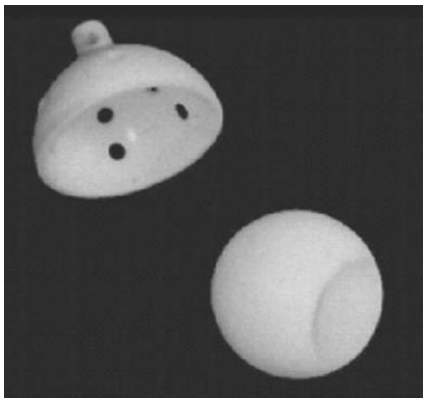

Figure 7: The Charnley Press Fit PTEE/PTFE hip resurfacing component (24).

Other large bearing MoP devices were investigated and although the results seemed promising in the early post-operative years, the medium and long term results were poor and the procedure was abandoned in the mid 1980's. At the time the assumed reasons for failure included stress shielding (25), femoral head osteonecrosis (25), poor surgical technique, high frictional torque forces and cement disease (26). It is now known that many of the failures were a result of excessive wear causing an inflammatory response and osteolysis (1, 27). Wear can be improved by using other hard-on-polymer bearing combinations including Ceramic-on-polymer (CoP) which possess a lower wear rate due to the ceramics ability to be polished to a smoother surface. Nevertheless polyethylene remains an inappropriate material for a large diameter bearing acetabular component.

2.2.2 Metal on Metal (MoM) Bearings

In THA, metal on metal articulations were originally used when the procedure was in early development. However, these were later abandoned and replaced by the small diameter MoP bearings owing to Charnley proposing that MoM bearings would for a number of reasons lead to early failure rates. He suggested the bearings would seize up or give rise to high frictional torque. Although some of the components did have early failure rates, some were successful for a significant number of years (28). These include the McKee Farrar (28), Ring (29) and Stanmore THR prostheses (29). These first prostheses were relatively crude in design and quality meaning high wear, osteolysis and loosening were common problems. New research performed into the reasons for failure in early large diameter bearing MoM designs and improvements in manufacturing, prompted re-investigations into this bearing combination.

In 1991, Derek McMinn also began using a new metal-on-metal large bearing hip resurfacing component. The BHR component was developed alongside Corin (Cirencester, UK) and used cast cobalt chromium alloy. It was implanted using a hybrid system with a cementless HA-coated acetabular cup and cemented femoral head component (Figure 6). The main advantage of using a MoM combination over MoP and other hard-on-soft bearings (CoP) is that thin-walled large diameter bearing components can be made without compromising the structural integrity of the component. Thinner components reduce the amount of bone removal from the acetabulum and allow large diameter bearing heads to be used. Increasing bearing diameter reduces the risk of dislocation as there is an increase in the distance required for the femoral head to translate inferiorly below the lower edge of the acetabular liner before dislocation can occur (30).

The large femoral head surface area produces an increased contact area compared to a small femoral head to which load is transferred, reducing the contact pressure and lowering the amount of wear (31). It has also been suggested that the larger diameter generates a protective lubrication film between the bearing surfaces further lowering wear, whilst smaller diameter MoM bearings of size 16 and 22.225 mm promotes a boundary lubrication regime (32). Wear is also influenced by heat treatments applied to the CoCrMo alloy which

alters the microstructure of the material (33, 34). The reader is directed to McMinn and Daniel (2006) (1) and Helsen and Breme (35) for an in-depth overview of metal-on-metal components. The release of cobalt and chromium wear ions raises concerns over the likelihood of carcinogenic affects *in-vivo* especially in the early post-operative stages. Evidence of toxicity of metallic ions following MoM joint replacements are described in Section 2.3.2.

2.2.3 **Ceramic-on-Ceramic (CoC) Bearings**

Ceramic-on-ceramic is another hard-on-hard bearing option which exhibits excellent wear rates especially in young, high demand patients with end-stage arthritis (36). The ceramics used are zirconia and alumina which both have excellent mechanical properties including high strength, high hardness, good wear resistance and biocompatibility.

Early CoC devices suffered set-backs due to fracture problems and flaws in the design (9) but improvements in the quality of ceramic and manufacturing techniques brought the risk of fracture down with the incidence reported as 1 in 25,000 (37).

Studies have documented that large diameter bearing CoC total hip pairings have wear rates approximately 100-fold lower than the MoM pairings (38), with the wear debris being smaller in size (39). The combination of small size and low volume of debris makes it an attractive material alternative to MoM bearings.

CoC components require correct positioning in order to obtain optimum performance. Excessive cup inclination can produce high edge wear indicated in retrieved components as a 'stripe' on the bearing surfaces (40, 41). A worst case situation can result in the prosthesis fracturing which requires revision surgery to correct.

Due to the brittle nature of ceramics, a metal backing or shell is required to support the ceramic liner and help prevent fracture. In addition, the liner can aid osseointegration through the inclusion of screws, porous in-growth features and osseointegrative coatings in the design. These fixation methods are discussed in Section 2.5.

The main downfall of a CoC bearing is the requirement of the metal shell as it increases the amount of bone that is removed from the pelvis in comparison to a MoM component. In addition, the stiff ceramic liner and metal shell introduces stress shielding (outlined in Section 2.3.3). These factors reduce the appeal of this material option for a large bearing acetabular component. The next section reviews the performance of total hip and resurfacing arthroplasty components which have been described in this section.

2.3 Review of Total Hip and Resurfacing Hip Arthroplasty and Associated Complications

The choice of surgical treatment depends on the patient's initial condition and demographic. Each type of arthroplasty is suited to a certain patient cohort and the following sections will outline the performance of THA and RHR components. The component considered in this thesis is proposed to be adopted for a large diameter bearing total or resurfacing hip acetabular component. Therefore, it is important to understand the complications associated with both type of arthroplasty.

2.3.1 Total Hip Arthroplasty: Survivorship

THA procedures are more commonly performed than resurfacing procedures with figures showing that over 90 % of hip procedures are for a primary hip replacement (2, 3). At the time of writing the Australian Orthopaedic Association National Joint Replacement Registry contained the most comprehensive total hip replacement data, indicating a yearly percentage cumulative revision rate of 7.4 % at 11 years which is lower than the resurfacing revision rate (3, 4). Figure 8 shows the cumulative percentage revision for primary THA procedures over an 11 year period indicating a higher revision rate in the first post-operative year.

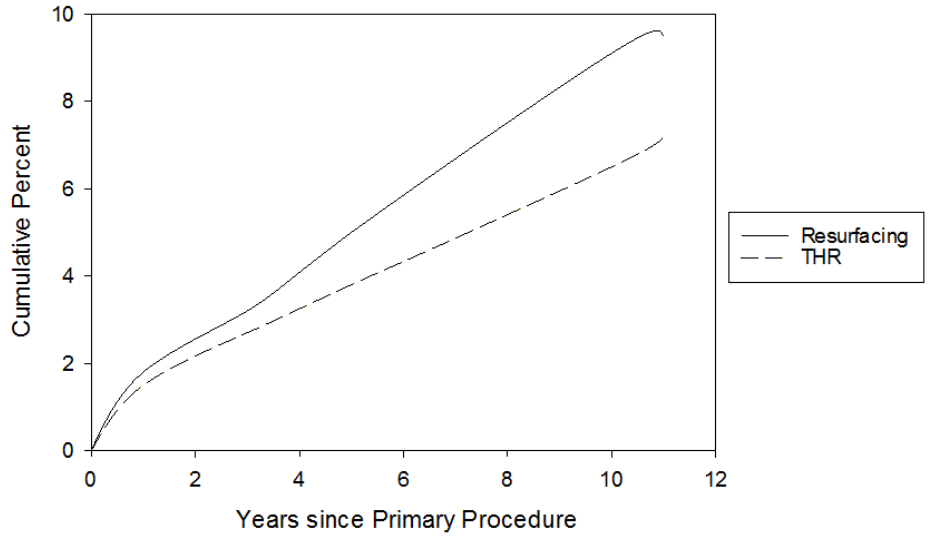

Figure 8: Cumulative percent revision of primary total conventional hip and resurfacing replacement implants. Adapted from the Australian Orthopaedic Association National Joint Registry, 2012 (3).

Long term THA survival outcomes have shown results of 80 % at 17 years (14, 20) and 73 % at 25 years (20). Various refinements in surgical technique and implant design has contributed to improvements in pain, function and the overall survival of the implant (42) with figures rising to 95 % at 10 years (2, 14),

THA was originally intended for elderly, low-demand patients which is reflected by the excellent history of long term performance in this patient cohort; 5.4 % revision rate exhibited for patients over 75 at 11 years (3). Trends have shown that the number of THA procedures

performed in younger patients is increasing. The 2012 Australian hip registry has documented a rise in patients under 55 undergoing a THA procedure from 11.7 % in 2003 to 12.9 % in 2011 (3). The rate of revision for younger patients is 9.2 % at 11 years (2, 3, 14) and given the high revision rate, improvements in implant design and surgical technique are necessary to ensure the implant will outlast these younger more active patients.

The leading cause of THA failure is aseptic loosening followed by prosthesis dislocation (Figure 9). Surgeons and engineers have tried to address these problems by investigating alternative bearing surfaces that have lower wear and allow for larger head sizes. The use of alternative bearings has been discussed in Section 2.2 and more novel alternatives are discussed in Section 2.4. Section 2.2.2 discussed the reasons for the lower dislocation risk when large diameter bearing combinations are used. Registry data has shown that the material combination of the large diameter bearing also affects the revision rate. Larger head MoM THA components (> 40 mm diameter) exhibit higher revision rates in the medium term (43) which is primarily attributed to excessive wear (44, 45). By contrast larger head CoC articulations sizes (> 32 mm) exhibit better implant survival compared to smaller bearings (< 28 mm) (3, 4). These more recent findings have resulted in a decline in the use of large diameter bearing MoM devices in some countries (3, 4) and an increase in the use of CoC bearing combinations.

Aside from bearing combination, age, and head size, many other factors affect the survival of a THA component. Registries have identified significant differences in revision rates with respect to gender and component fixation type. Males tend to exhibit a slightly higher rate of revision than females (7.8 % compared to 6.7 % at 11 years (3)). Fixation methods are discussed in more detail in Section 2.5 but registries have shown that hybrid fixation has the lowest cumulative percent revision compared to cemented and cementless options. Cementless has a higher rate of revision compared to cemented in the early post-operative stages but in the long term the rate of revision associated with cemented devices has been shown to be significantly higher (3).

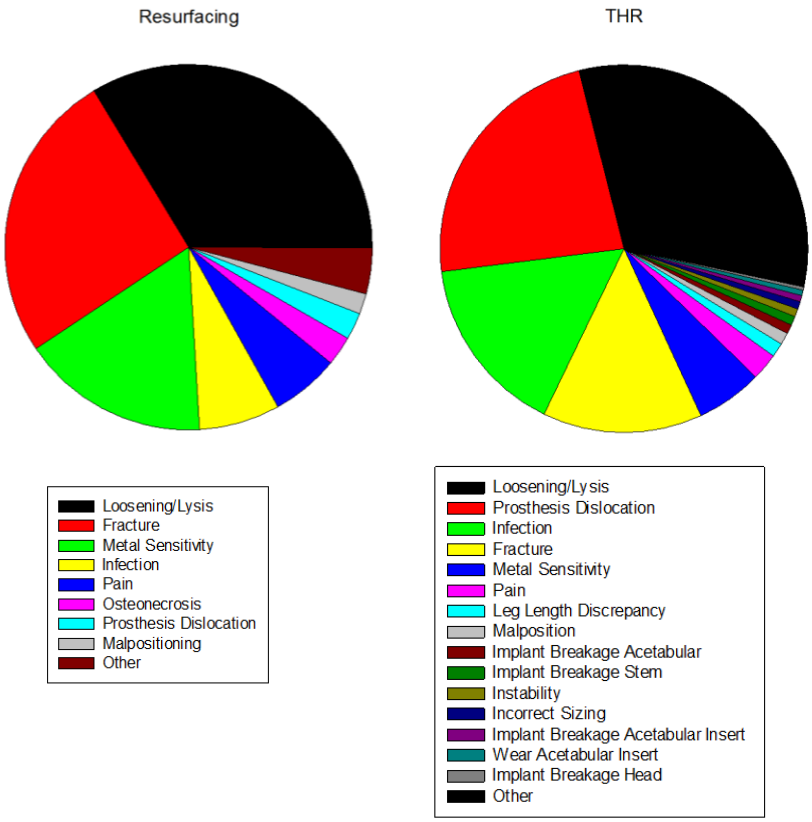

Figure 9: Reasons for failure in all types of resurfacing components (left) and Total hip replacements (right), According to the 2012 Australian Joint Registry (3).

Although modern designs are increasingly being tailored for the intended patient demographic, revision data still highlights that there are important problems that should be addressed. To reduce the high level of loosening and dislocation shown by current components careful selection of bearing material and size as well as the correct choice in patient demographic are critical for the survival of the component.

2.3.2 Resurfacing Hip Arthroplasty: Survivorship

RHR accounted for 8 % of all primary hip replacements and 40 % of those were performed in patients aged between 55 and 64 years in England and Wales in 2008 (4). At the time of writing the Australian Orthopaedic Association National Joint Replacement Registry (3) contained the most comprehensive hip resurfacing data, indicating a yearly percentage cumulative revision rate of 9.5 % at 11 years.

There was a higher risk of revision for patients who were 65 years or older and female. Females exhibited nearly three times the risk of revision compared to males (10 year cumulative percent revision of 16.9 % and 6.1 % respectively (3)).

Registry data shows that resurfacing procedures are in decline. The number of operations reported in the Australian hip registry in 2011 had reduced by 39.7 % compared to the previous year and was 68.5 % less compared to the peak in 2005 (3). From a national perspective hip resurfacing procedures declined by over 50 % between 2008 and 2011 (4) amid on-going concerns which are discussed below. Figure 10 illustrates the declining use

of resurfacing components in England and Wales between 2003 and 2009. The decline could be attributed to a number of reasons. Firstly, it is possible there had been a loss in confidence in resurfacing procedures and the implants themselves due to poor short and midterm survival rates. Secondly, the operation is technically demanding accompanied with a substantial learning curve for surgeons. This is evidenced by improved survival rates for the BHR in specialist centres (46, 47). Thirdly, short and midterm studies indicate that the procedure is only suitable for young males, placing a limitation on the eligible number of patients and subsequent surgeries being performed. Therefore surgeons favour the use of conventional THA components with which they are familiar.

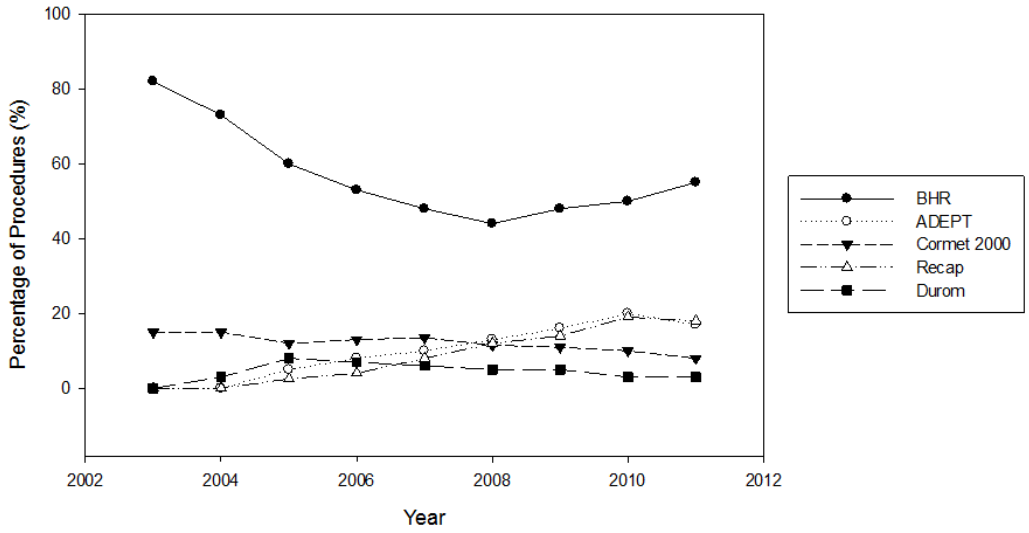

Figure 10: Top five resurfacing head brands, usage 2002 to 2011. Adapted from the National Joint Registry for England and Wales (2012) (4).

The Articular Surface Replacement (ASR) designed and manufactured by DePuy (Warsaw, Indiana) contained a number of specific modifications that aimed to increase ease of implantation, function and survival. The ASR had a low diametrical clearance to reduce metal wear, a sub-hemispherical design of the acetabular component to preserve bone stock and an internal geometrical taper of the femoral head of 3.0 ° to improve seating. After its launch in 2003, the percentage of resurfacing procedures using the ASR rapidly increased but short term data from registries reported early revision rates for the ASR to be higher than anticipated. Data published by the England and Wales registry (48) showed a 5 year revision rate of approximately 9.63 %, over two times greater than other leading devices (BHR 3.44 %, ADEPT 4.42 % at 5 years). Many patients experienced severe groin pain, prompting early revision surgery. During ASR revision procedures gross swelling of the newly formed capsule around the hip joint, black staining and destruction of the periprosthetic tissue and a large volume of fluid bathing the implant were frequently observed (21, 49). In addition, levels of metal ions in the blood were elevated which was associated with high articular wear experienced by the component when it was incorrectly implanted. It was concluded that the swelling observed was due to an adverse reaction to large quantities of metal debris, which

initiated aseptic lymphocytic vasculitis associated lesions (ALVAL), hypersensitivity and pseudotumours (49, 50). The term ALVAL has been created to describe the lymphocyte-dominated inflamed lesions in bone that can be found around implants. Due to the extent of tissue damage a THA component was implanted during most revisions.

2.3.3 Failure Modes associated with total and resurfacing components

These extremely poor results prompted the manufacturer to recall the ASR in August 2010 and the acceptance and confidence in the procedure declined dramatically. Figure 9 illustrates a breakdown of the failure modes associated with total and resurfacing components. Modern designs have almost eliminated failure due to implant fracture and excessive wear with the use of more appropriate materials and choice of patient. Nonetheless, the main areas of failure appear to be in the supporting bone (15 % fracture in total and 36 % in resurfacing) and at the bone/implant interface (loosening/lysis). The main failure modes are explained in the next section.

Femoral Neck Fracture

The technically demanding resurfacing procedure can result in incorrect alignment of the femoral component or notching of the femoral neck, leading to mechanical weakening and subsequent fracture. A secondary factor which is less documented is notching that may also damage vessels that carry the blood supply to the remaining femoral neck (51). Damaging these vessels impairs the blood supply to the head resulting in osteonecrosis. Osteonecrosis is a disease where there is cellular death of bone tissue due to a reduction in blood supply (25).

Femoral component impaction has also been speculated to introduce micro-fractures in the femoral neck which may also weaken the underlying bone (52) and promote loosening. Improved surgical technique and instrumentation may solve these problems, by reducing the impaction loads and ensuring correct alignment. Aside from surgical technique, the risk of femoral neck fracture is multifactorial. Patient characteristics including body mass index (BMI), gender and host bone quality are all possible indicators. More than one group has identified older, overweight female patients to possess a higher risk of neck fracture (21), making patient selection a critical factor in implant success.

Aseptic Loosening

Aseptic acetabular loosening is the mechanical failure of prosthesis fixation due to repeated dynamic loading. It is a common failure mode associated with RHR and THA implants and was associated with 29 % of THA revisions in Australia in 2011 (3), this value is considerably higher for early metal-on-polyethylene (MoP) total hip components including the Charnley device. It has been described that beyond 8 years acetabular component loosening is more common than failure of the femoral component. It was originally thought that loosening in cemented components was due to ‘cement disease’ due to a foreign body reaction to the cement. However, the introduction of cementless components failed to eliminate the

problem and it was subsequently identified that the wear of the bearing couple and the release of particulate debris was the main cause of acetabular loosening in MoP components (53, 54).

The body's immune response to polyethylene wear debris causes bone death which is known as osteolysis. In response to the debris, the body produces osteolytic mediators (e.g. macrophages and osteoclasts) which encapsulate the debris releasing enzymes in an attempt to destroy them. However, these enzymes damage the surrounding implant tissue leading to the formation of osteolytic lesions. Osteolytic lesions are areas around the implant where bone cell death occurs compromising the implant-bone interface, leading to loosening and permanent migration of the cup. This causes inflammation, pain and can affect the overall performance of the component.

Since it was hypothesised that the generation of sub-micron sized polyethylene particles were a key factor in limiting the long-term fixation of a total hip replacements, polyethylene was removed from resurfacing and large bearing THA acetabular cups and MoM and CoC couples were explored (31, 55).

Metal ion Release

Systemic release of metal ions and the likelihood of carcinogenesis has been a major concern with metal-on-metal bearings. Continual research is being conducted to understand the effects of metal ions *in-vivo*, particularly in the early post-operative stages when the running-in wear rate and release of metallic ions is at its highest (7).

The circulating levels of cobalt (Co) and chromium (Cr) ions following a MoM arthroplasty are elevated compared to the normal population after a MoP or CoC arthroplasty (7). Although the metal ions give rise to restricted inflammatory osteolysis, a biological response is present. The contact of metallic ions and body fluids results in the ions forming complexes with proteins (7). These complexes are potentially allergenic and may in some individuals initiate an inflammatory response in the periprosthetic tissues known as hypersensitivity. This can lead to aseptic lymphocytic vasculitis associated lesions (ALVAL) as seen with the ASR component. Unexplained pain in patients with MoM replacements is usually a consequence of ALVAL. If hypersensitivity is expected when revision is undertaken a reduced exposure to cobalt and chromium ions could be achieved by the use of CoC or MoP bearing combinations.

Stress Shielding

The insertion of a metal prosthesis into bone results in the load being shared between the prosthesis and the bone, which had previously been carried by the bone itself. The stiffer implant bears most of the internal load, altering the normal mechanical stimulus for bone maintenance. This phenomenon is known as stress shielding and follows Wolff law, that states bone is an adaptive tissue that reacts to unloading through resorptive remodelling (56).

Stress shielding induced bone loss can contribute to implant loosening, increasing the chances of revision.

The severity of stress shielding is dependent on mechanical factors including the geometry and material properties of the implant components, the quality of bone before implantation and the loading of the bone and implant by musculoskeletal forces.

Femoral stems made of a high modulus material that also possess a large proximal cross-sectional area are more likely to cause stress shielding over other hip replacement designs.

There have been attempts to reduce femoral stress shielding by replacing the metal stem with a material such as carbon fibre reinforced plastic (CFRP) (57, 58). The material has a lower modulus and aims to more equally share the load with the surrounding bone. Changes to the stem and coating geometry have also been investigated as a means of reducing stress shielding. A shorter femoral stem and a small area of coating on a long stem can help to reduce proximal bone resorption by transferring the load proximally.

Acetabular Cup Loosening

Acetabular component loosening has been suggested to be one of the main limiting factors of THA and RHR (59, 60). According to the Swedish hip register, 65 % of THA re-operations are to revise the acetabular component (14). Aseptic loosening is a key complication in THA and can be caused by wear debris and poor load transfer caused by stress shielding (61).

Studies examining bone resorption around acetabular components have reported a 20 % to 34 % (62, 63) decrease in the bone density above the dome of a press-fit acetabular component 1 year after implantation. It is believed that when the stiffer acetabular component is inserted, the elasticity mismatch focuses contact stress at the peripheral zones of the host-implant interface (64, 65); meaning a greater portion of the weight-bearing load is transmitted to the peripheral cortex of the ilium. Consequently, the cancellous bone of the central part of the ilium (e.g. around the pole of the component) is subjected to less force than in normal loading circumstances (63) and the adaptive nature of bone reacts to this unloading by being resorbed. Previous predictions have shown that stiffer components increase the rim stress and the peripheral cortex loading (64, 65) more so than a lower stiffness polymeric cup which experiences a more even transfer of load (8, 64, 66).

Press-fit fixation which is described in more detail in Section 2.5 is used in many modern large diameter bearing acetabular components. Oversizing the component generates compression at the peripheral interface of the acetabulum after implantation which forms the basis of the fixation technique. When the component is incorrectly implanted into the acetabulum, dome gaps can form between the implant and reamed acetabulum. The poor seating further increases rim stress as contact between the implant and acetabulum occurs around the rim of the cup only. This intensifies the load into the peripheral cortex of the ilium than a correctly positioned component promoting stress shielding (62, 63).

It is suggested that bone stock in the central part of the ilium could be preserved by tailoring the acetabular component so it more effectively transmits forces to the central part of the

ilium rather than to the acetabular rim (63). This could be achieved by altering the material, design and fixation method of the component. Recent studies have begun to investigate advanced polymer based composite materials (66-68) as well as alterations to the acetabular design (64, 68) with varying degrees of success. This aspect is discussed in more detail in Section 2.4.2.4.

2.3.4 Summary of Failure Modes and scope for improvement

This section has shown the choice of procedure depends on the severity of the patient's condition and their demographic as the type of arthroplasty is suitable to particular patient groups. The clinical data and review of the failure modes showed improvements are required for large diameter bearing procedures in order for it to become more successful in a wider patient cohort.

2.4 Use of Novel Materials for Large Diameter Bearing Arthroplasty

The previous sections have explained the history and performance of the materials used in large diameter bearing THA prostheses, from early metal-on-polyethylene designs to metal-on-metal and more recently ceramic-on-ceramic. Each material combination has exhibited advantages and disadvantages and it is concluded that there is scope for improvement in terms of material selection and design.

Wear and the *in-vivo* response to wear debris have been highlighted as issues relating to both soft and hard bearings. Additional issues relating to acetabular components include stress shielding and primary fixation. An appropriate material for the acetabular component would be able to withstand the forces that are experienced in the hip under tension, compression and cyclic loading whilst possessing high wear resistance and eliminating the release of deleterious wear debris. The material must exhibit adequate mechanical properties in order to eliminate the need for a metal shell for support but its modulus should be similar to bone to address the problem of stress shielding.

Recently there has been a move towards polymer based materials, in particular, reinforced polymer materials in biomedical applications, with growing interest for their use in bearing applications (9).

2.4.1 Highly Cross-Linked Polyethylene

During the late 1990's, it was realised that irradiation above the typical sterilisation dose range of 25 – 40 kGy could substantially improve the wear performance of polyethylene (69) by increasing the number of cross-links between the polymer chains. It has been suggested that cross-linking the polymer enhances the resistance to plastic flow and lamellae alignment at the articulating surface resulting in better resistance to wear. On this basis highly cross-linked polyethylene was introduced as a total hip bearing surface with the potential for use in resurfacings. Nevertheless, cross-linking alters the polymer structure and the mechanical properties of UHMWPE. Studies have shown that cross-linking UHMWPE can result in a reduction in strength, ductility, fracture toughness and crack propagation resistance (69).

Although the long-term clinical implications for such changes are unknown, there have been incidences of rim cracking in HXLPE acetabular liners *in-vivo* (70, 71).

As seen with UHMWPE, HXLPE liners require a metal backing for support which introduces the problem of stress shielding. In addition, the minimum required thickness is between 6-8 mm (72) which would increase the outer diameter of the acetabular component, compromising bone conserving properties. Based on these findings, it has proposed that HXLPE was not an appropriate material for large diameter bearing acetabular components.

2.4.2 Carbon Fibre Reinforced Polyetheretherketone (CFRPEEK)

Aurora Medical Ltd identified CFRPEEK as a potential material for future cup applications and the reasons for this choice are discussed below.

Polyetheretherketone (PEEK) is a thermoplastic polymer that has been approved as a medical grade material since the late 1990's. It has more recently been studied and used as a substitute for metallic implant materials because of its inertness and relatively low elastic modulus (3-4 GPa) (9). Although the modulus is low, the addition of carbon fibres (CFRPEEK) improves the materials strength and creep resistance and alters the stiffness to be closer to bone (~15 GPa). This reduces the extent of stress shielding often observed in metallic implants and alongside the advantages previously mentioned makes CFRPEEK an attractive material for load-bearing applications. In addition, PEEK's proven biocompatibility indicates long term use without an adverse reaction *in-vivo* due to the material's excellent chemical stability (9) which is a particular problem associated with the wear debris produced by UHMWPE and metal cups. The material possesses a stable chemical structure which makes it extremely unreactive and inherently resistant to chemical and post irradiation degradation (9).

The thermal stability of the polymer has been investigated because of its high temperature industrial applications. Studies have shown degradation occurs between the glass transition (T_g ~143 °C) and melt temperatures (T_m ~343 °C) but a temperature exceeding the processing temperature of PEEK (above 420 °C) are needed to produce volatile degradation products. It is clear that thermal degradation is not a concern during clinical use of PEEK biomaterials which operate in conditions around 37 °C. This stability makes it an ideal material candidate for implants as it can be repeatedly sterilised using gamma irradiation in air without post-irradiation aging or degradation in mechanical properties (9).

The addition of carbon fibres into PEEK increases its strength and stiffness. The similarity in modulus to bone together with its high strength means there is the potential that an acetabular component could be designed that does not require a metal backing for support, reducing the likelihood of stress shielding. This section provides an introduction into composites and CFRPEEK in order to explain the advantages and disadvantages of its use for a large bearing acetabular cup. The material's form, function as well as the processing considerations for device manufacture is reviewed to further assess Aurora Medical Ltd choice of material.

2.4.2.1 *Composite Structure and Mechanical Properties*

A composite is a multiphase material in which dissimilar constituents are combined at a microscopic level to macroscopically give superior physical properties to those of either of the constituent parts. A harder and stronger discontinuous phase is usually embedded into a continuous phase and is called the reinforcement or reinforcing material. The continuous phase is the matrix which typically has a lower tensile strength and stiffness compared to the reinforcement material. For CFRPEEK, polyetheretherketone is the polymer and short PITCH carbon fibres are the reinforcement material.

A composite's properties are not only influenced by the nature of the polymeric matrix material but also by the properties of the reinforcing material, reinforcement distribution, orientation and the interaction amongst them and the matrix.

The main role of the matrix is to hold the fibres in position relative to each other and transfer load to the fibres. The matrix binds to the fibres to create a unified material so the two constituents can function together to withstand the applied load. A further role of the matrix is to protect the fibres from chemical attack, mechanical damage and provide a toughening mechanism for the whole system. The matrix aims to blunt, deflect or redirect cracks along the fibre/matrix interface and absorb increasing amounts of energy (73). PEEK is an ideal polymer matrix as in its melted form it coats the carbon fibres and on solidification produces an inherently strong interface between the two constituents.

To provide reinforcement, fibres must be stronger and stiffer than the matrix and be of suitable geometry to enable efficient load transfer (73). CFRPEEK uses 6 μm diameter PITCH carbon fibres which are made from coal tar pitch and milled to a length of 150 μm. The consequences of these parameters are discussed below. The fibres can exhibit a very high stiffness (620-900 GPa (74)) but comparatively low strength (3400-3600 MPa (74)) which makes handling them difficult if they are in continuous form.

Load Transfer

The interface between the two constituents is the site of load transfer but as the fibres in CFRPEEK are discontinuous they exist mostly as discrete entities completely surrounded by the matrix. Therefore to transfer external loads individual fibres must use a mechanism which transfers loads from the matrix through fibres ends and also through the cylindrical surface of the fibres near the ends (75).

Figure 11 shows that under tensile loading the regions near the fibre ends are exposed to less strain than in the matrix. As a result, stresses are generated around the fibres in the direction of the fibre axis and the fibre is stressed in tension. When the fibres length is much greater than the length over which the transfer takes place, the end effects can be neglected and the fibre is considered infinite and the stress on the fibre can be assumed constant over its entire length i.e. a continuous fibre (76). However, with discontinuous fibres these end effects cannot be neglected.

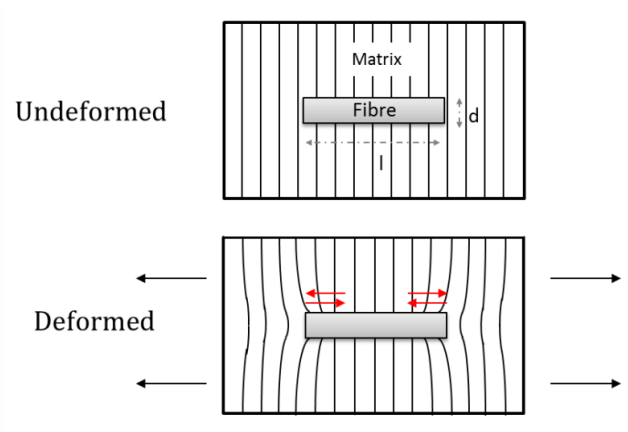

Figure 11: Effect of deformation on strain around a short fibre. Adapted from Campbell (2010) (77).

The stress distribution along a fibre can be analysed by assessing the equilibrium of a small element of fibre shown in Figure 12. By analysing the force equilibrium of the fibre a relationship between the fibre stress σ_f, shear stress on the cylindrical fibre-matrix τ_f and the fibre radius *r* can be achieved (75). If the fibre is well bonded to the matrix, the stress applied to the matrix will be transferred to the fibre across the interface. As a result of the strain difference due to the moduli difference between the two constituents, shear stresses are induced around the fibres. This relationship is shown in equation [1].

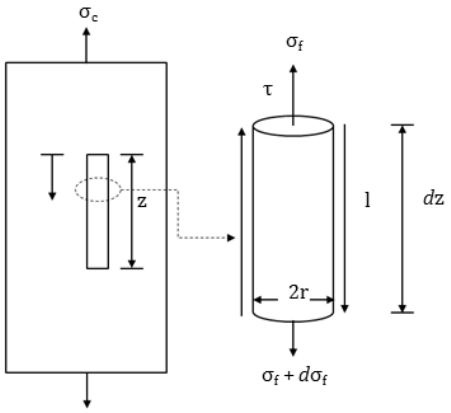

Figure 12: Equilibrium of infinitesimal length of fibre discontinuous fibre aligned in parallel to applied load. Adapted from Agarwal (2006) (75).

$$(\pi r^2)\sigma_f + (2\pi r dz)\tau = (\pi r^2)(\sigma_f + d\sigma_f)$$

$$\frac{d\sigma_f}{dz} = \frac{2\tau}{r} \qquad [1]$$

Critical Fibre Length

For short fibres the maximum fibre stress occurs at the mid-fibre length and a critical fibre length l_c exists which allows for maximum allowable load transfer to be achieved (75).

Figure 13 illustrates the tensile stress experienced along the length of a discontinous fibre embedded in a matrix loaded in tension. Load on the composite must be transferred into the

fibre by shear at the interface with no transfer occurring at the extremities of the fibre. Therefore the tensile stress will build from zero at the ends to the maximum halfway along the fibre's length (76). In addition the interface shear stress will be high at the fibre ends and will fall to zero when the full extent of load transfer has been achieved.

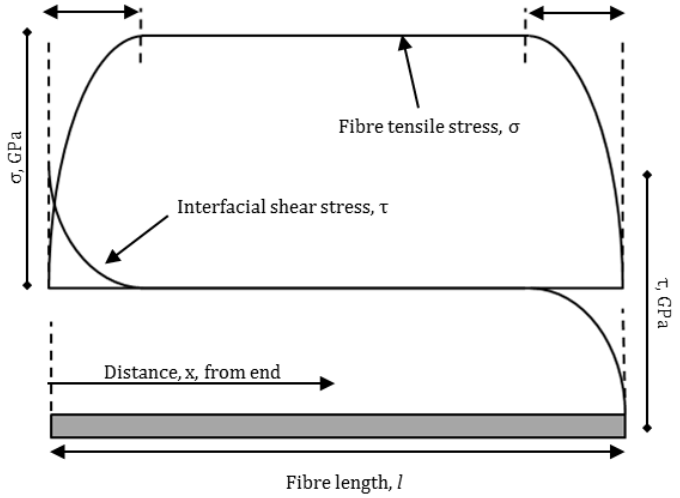

Figure 13: Variation of tensile stress, σ, in the fibre and shear stress, τ at the interface along the length of a short fibre embedded in a matrix. Adapted from Harris (1999) (76).

The two end sections display a noticeable reduction in fibre reinforcement efficiency as they constitute a theoretical 'ineffective' length (Figure 13). Figure 14 illustrates three fibre lengths and the fibre tensile stress experienced when the fibres in the composite are aligned parallel to the applied load.

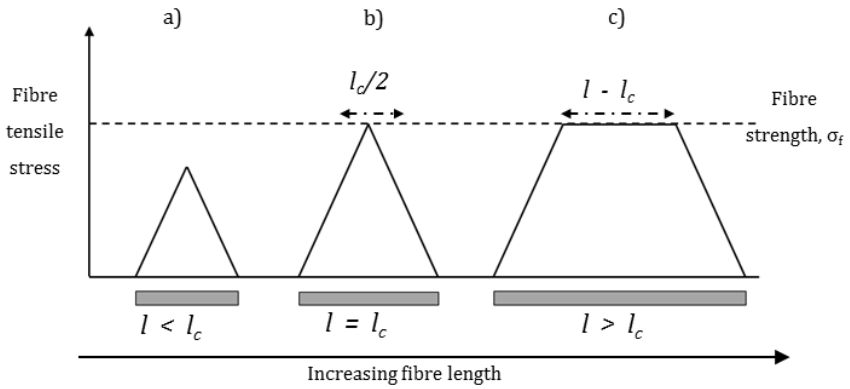

Figure 14: Illustration of the variation of tensile stress in a short fibre as a function of fibre length where σ_f is the fibre breaking stress and l_c is the fibre critical length. Adapted from Harris (1999) (76).

In the case of $l = l_c$ (Figure 14b) the tensile breaking stress has been reached at a point in the middle of the fibre and therefore fibre breakage can occur. However, the load bearing ability of the whole composite will be less than that of a continuous fibre as the average stress in each fibre of length l_c is $0.5\sigma_f$. Figure 14c shows that a fibre with a length greater than l_c has two inefficiently loaded end sections where the average stress is $0.5\sigma_f$ and a middle section

equal to l-l_c where the stress is equal to σ_f. This shows that the ends of finite length fibres are stressed to less than the maximum fibre stress which lowers the elastic modulus and strength of short fibre composite. The reduction in mechanical properties is further decreased when the fibre length is below the critical fibre length as the fibre tensile stress is never reached (Figure 14c).

The next section describes manufacturability of a short fibre composite and the influence of fibre orientation on the mechanical properties of the composite.

2.4.2.2 *Manufacturability*

Injection moulding is the common technique employed to manufacture CFRPEEK as complex shapes can be produced quickly. Although the initial cost outlay is high as mould tools are expensive to design and manufacture, the subsequent price for individual components on a mass produced scale is low. This offers many benefits over other implant materials which require expensive and labour intensive manufacturing techniques.

The injection moulding process begins with the fibre/matrix mixture being fed into a hopper and transferred into a heated barrel. Once the material is inside the heated barrel, it softens. To further aid material heating, a screw rotates within the barrel. The molten material is collected in front of the screw as it rotates and is then injected with a high pressure into the mould cavity through the injector nozzle which consists of a sprue, runner and gate. With the molten material contained within the mould, it is then cooled to below the solidification temperature of the material to produce the moulded component. Figure 15 provides a schematic diagram of an injection moulding machine.

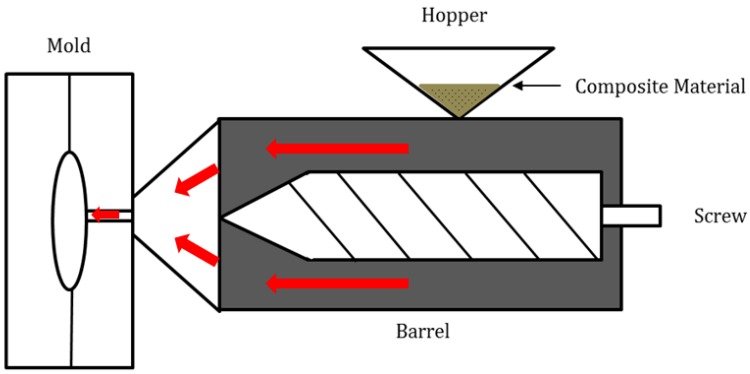

Figure 15: Schematic diagram of an injection moulding machine with flow direction of material shown with the red arrows. Adapted from online source (78).

The material suppliers processing guide (Invibio Biomedical Solutions, Thornton Cleveleys, UK) (79) outlines the key conditions for successful moulding of CFRPEEK. The PEEK polymer is supplied in granules for injection moulding which are packed in a clean environment in order for medical grade components to be manufactured. Prior to moulding the granules are dried to remove moisture which may have been absorbed before use. The material is processed using conventional thermoplastic processing equipment with high temperature capability as shown in Figure 15. It is recommended that the equipment is made

from martensitic chromium tool steel (D2 Tool Steel) to reduce machine wear and the mould surfaces are highly polished to reduce the likelihood of the material adhering to the surface after moulding. It is essential that the CFRPEEK composite is moulded in a completely clean environment to ensure a medical grade material can be manufactured. Therefore, the equipment must be purged with CFRPEEK prior to moulding to flush out any impurities that may be present in the system. This should ensure that there are no foreign bodies or inclusions in the final injection moulded component.

The hopper is kept at a temperature of 70 – 100 °C to ensure correct feeding into the barrel and it is recommended that the barrel temperature is kept between 365 °C at the rear of the barrel and 390 °C at the front of the barrel which is higher than the melting temperature of the material (343 °C). To promote heat transfer from the barrel into the material, the screw is rotated at a speed between 50 and 100 rpm which is a compromise between cycle time and reducing the amount of localised heating in the molten material.

When the molten PEEK is injected from the barrel into the mould through the nozzle, the materials temperature can significantly reduce causing freeze-off. Freeze-off is where the material cools and solidifies onto the walls of the mould network, blocking the flow. In some cases this blocks the channels entirely but in others it can cause the solidified material in the gate or the nozzle to be transported into the mould causing marking or 'cold slugs' in the moulded part. These aspects can be avoided by choosing the correct conditions for the nozzle, sprue, runner and gate. It is recommended that the nozzle temperature is slightly higher than the barrel at 395 °C and the sprue is designed to be as short as possible and not be smaller than 4 mm in diameter whilst possessing a minimum taper angle of 2 °. According to the material supplier, these characteristics are ideal as a large diameter short tapered sprue aids filling in complex moulds, preventing the material from solidifying in the channels and allowing for successful de-moulding of the material. The injection pressures of the material into the moulds should be between 7-14 MPa with holding pressures of 4 – 10 MPa to ensure enough material is injected into the mould and voids are absent.

Although these conditions have been set by the material supplier to ensure the key physical and chemical parameters of CFRPEEK are achieved, they are guidelines and complex mould designs, changes to the barrel geometry (gate, sprue, and nozzle) and changes to the processing conditions can lead to specific problems. Problems such as freeze-off and cold slug formation have already been highlighted but other problems such as shrinkage, streaking, burn marks and warping can be rectified with alterations to the injection moulding process. Even so, there are some problems which are not so easily solved by changing the processing temperature, time over which the moulding occurs or pressure that the molten material is held under during forming. In short fibre composites these factors include fibre damage, fibre distribution, fibre orientation and void formation.

Void formation is an important defect to discuss as their presence undermines the property and performance benefits of fibre reinforced composites (80, 81); their formation is sought to

be avoided during injection moulding. Porosity can be caused by incorrect cure parameters such as duration, temperature and pressure (82). In addition, the shape of the component can affect void formation with large changes in part thickness promoting void formation (83). This aspect is important to consider when using CFRPEEK for an acetabular component as the mould tool will be more complex than a simple dog-bone specimen. The internal morphology of the designed CFRPEEK component was investigated in Section 6.2 to determine whether the injection moulding settings and the mould tool design were appropriate for forming a defect free component.

Due to the extensive mixing with high-shear and passage through narrow delivery channels, extensive fibre damage can occur. CFRPEEK is made from PITCH fibres with a length of 150 μm which is critical for the mechanical properties of the component. The size reduction is affected by the shape and dimensions of the gate as well as the processing conditions (e.g. speed of screw rotation). Invibio Biomedical Solutions outline that the diameter of the channels between the barrel and the mould should be no less than 4 mm with the screw speed (50 to 100 rpm) chosen to reduce the extent of fibre breakage. In some instances, companies ensure the length of the fibres prior to mixing with the polymer is greater than the critical length to ensure that any damage experienced by the fibres during processing does not reduce their length below the critical length (84).

In order to obtain satisfactory performance from moulded short-fibre composite parts, the fibres should be uniformly distributed in the polymer matrix (85). Therefore it is necessary to form a homogeneous mixture of fibres within the melted polymer before the molten material flows into the mould. This is accomplished by the screw located in the barrel, but the flow of the melt through the channels from the barrel to the mould may result in the fibres migrating and clumping together producing resin rich areas and clusters of fibres. The resin rich areas are weak and more compliant than the composite part whilst the clusters of fibres are susceptible to micro-cracking (85) which means both these occurrences affect the overall performance of the composite part. Inhomogeneity is due to the combination of the initial distribution of fibres in the suspension and the flow of the melt during moulding. Previous studies (86, 87) have shown that including the reinforcing material in the granules prior to reforming produces a more evenly dispersed starting mixture meaning the clustering effect is only due to flow configuration. CFRPEEK is moulded from granules with the carbon fibres already dispersed into the PEEK matrix meaning inhomogeneity in the moulded part is suggested to be mostly due to the flow of the melt in the mould. The distribution of fibres in CFRPEEK has been assessed in Section 3.2.

The dependence of fibre length and volume fraction on the mechanical properties of a composite are well understood (85). CFRPEEK MOTIS contains 30 % by weight of milled PITCH carbon fibres and this percentage has been determined to be the optimum volume fraction in terms of mechanical performance and wear (9). This parameter is tightly

controlled in the granule processing step prior to injection moulding and therefore will not be investigated in this thesis.

In contrast, the influence of fibre orientation is not as well understood and it can vary strongly amongst injection moulded composite parts due to the imposed processing parameters. Fibre orientation is known to affect the mechanical properties of a composite part with fibres orientated parallel to the load direction offering higher tensile strength and stiffness (88, 89) (Figure 16). The load transfer for a parallel fibre occurs via shear stresses acting on the cylindrical interface between the matrix and the fibre (Figure 11). This cylindrical interface is not easily accessible when fibres are orientated perpendicularly to the load direction.

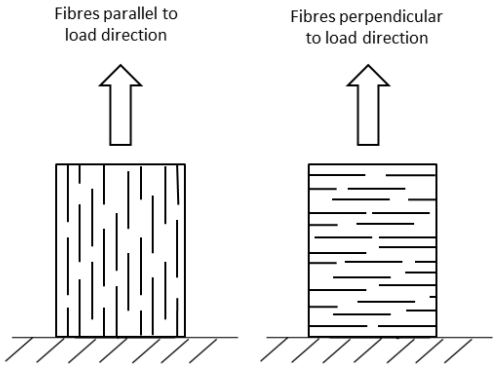

Figure 16: Orientation of fibres parallel and perpendicular to load application. Adapted from Rasheva et al. (2010) (89).

In addition to strength and stiffness, the orientation of fibres has been shown to affect the wear properties of a material (89, 90). Fibre orientation is difficult to control during the injection moulding process, particularly for complex shapes. It is governed by the dynamics of melt polymer filling the mould cavity and behaving like a viscous fluid (76).

Consequently fibre orientation results from complex interactions of two effects:

a) Shear flow, which aligns the fibres with fluid velocity vectors. These are most evident in close proximity to the mould walls.
b) Extensional flow, which arranges the fibres more randomly to the melt polymer flow.

These interactions lead to the formation of a layered structure where fibres tend to align with the injection direction at the outer layer or 'skin' and lie perpendicular to it at the core. Previous studies (88, 89) have shown standard specimen shapes such as dog-bone bars to exhibit this layered structure. Figure 17 shows a transverse section of a dog-bone of PEEK reinforced with PTFE powder, graphite flakes and short carbon fibres taken from the study by Rasheva et al. (2010) (89). The outer layer shows strict alignment of the fibres in the shell zone. This alignment is a consequence of the friction generated between the mould surface and the flow accompanied by accelerated cooling (89). The middle zone experiences fibres with a more random orientation which is a result of the extensional flow and the slow cooling down process of the central section compared to the shell structure which has already solidified.

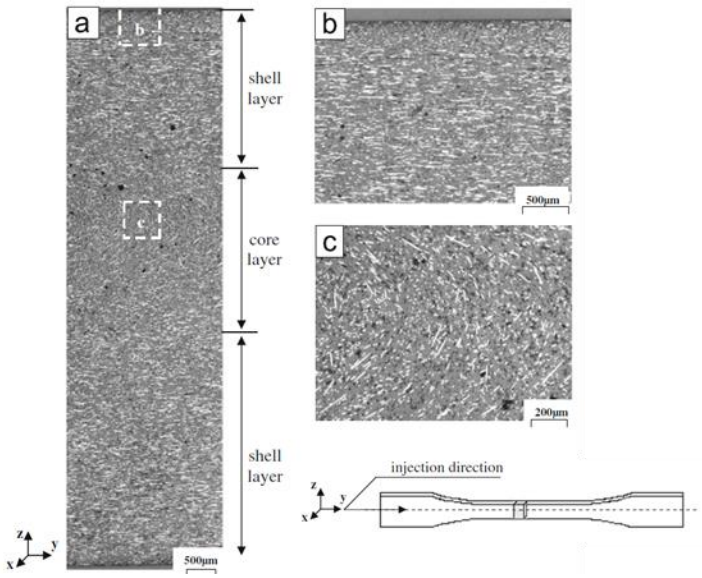

Figure 17: Morphology of a PTFE/graphite/short fibre reinforced PEEK composition. (a) cross section of a dog bone specimen along the injection moulding direction; (b) frame layer of a specimen; and (c) core later of a specimen (89).

As mechanical properties can depend on flow induced fibre orientation, there is considerable interest in establishing relationships between flow and orientation. This is especially true for the use of CFRPEEK in a large diameter bearing acetabular component as wear has been identified as factor contributing to failure of current prostheses (44, 45). It is therefore important to understand the influence of fibre orientation on the tribological behaviour of reinforced polymer composites and this is explored in the following section. Further still, establishing a relationship between certain factors (fibre orientation, strength, stiffness and wear resistance) could inform material suppliers of ways to update the moulding process to control these relationships (85). Although, the specific injection moulding settings are not explored in this thesis, a method of extracting the fibre orientation from injection moulded CFRPEEK components was explored in Section 3.2. The study also investigated fibre distribution and the presence of voids and defects.

2.4.2.3 *Wear Characteristics*

Wear and the clinical problem of wear debris induced osteolysis are critical failure modes associated with hip components. The inclusion of carbon fibres in PEEK has been shown to enhance the wear properties of the material by an order of magnitude when at least 10 % of short carbon fibres are added. In addition, they help to increase the creep resistance of the polymer matrix (89). Wang et al. (1999) (91) carried out an investigation into the influence of carbon fibre content and wear resistance. The study concluded that PEEK resin blended with 30 w/w % of PITCH carbon fibre i.e. CFRPEEK MOTIS gives the optimal wear resistance, five times lower than 10 % reinforcement and three times lower if 50 % reinforcement was used.

Pin on plate studies (92, 93) (Figure 18) have shown a combination of CFRPEEK and ceramic exhibits a five times reduction in wear factor compared to UHMWPE and CoCrMo combinations. Unlike hip simulators, pin on plate experiments do not replicate the conditions *in-vivo*. Instead the test is useful as a material screening technique to compare new potential materials.

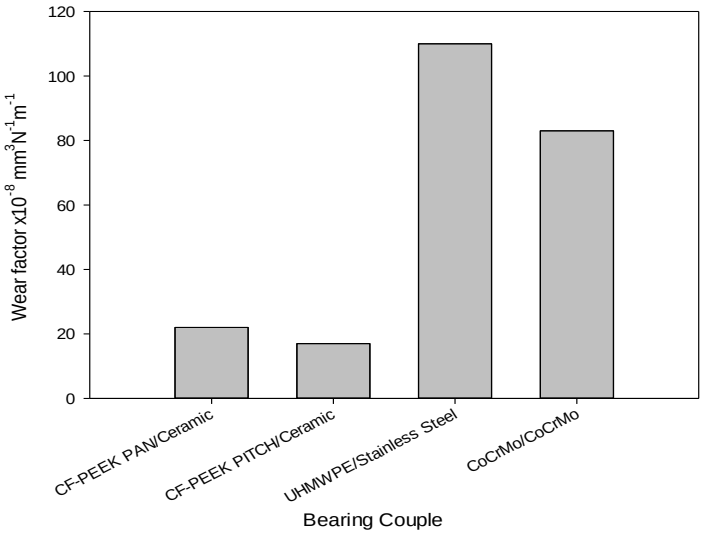

Figure 18: Total wear factors from pin-on-plate analysis using a series of material combinations. Adapted from Scholes et al. (2007) (93).

To gain a greater understanding of PEEK wear rates in a set up that more closely simulates the hip motion and loads through the components, hip simulator studies have been performed (94, 95). The first hip simulator results were reported by researchers from Howmedica (96) who performed an investigation on CFRPEEK MOTIS acetabular cups articulating against zirconia heads. The CFRPEEK combination exhibited two orders of magnitude less wear than the ceramic-UHMWPE combination after 10 million cycles. The type of fibre has been shown to play a role in the tribological behaviour of CFRPEEK with PITCH fibres yielding lower wear rates than PAN fibres (91) as the latter are stiffer and more abrasive.

Wear studies have shown that in general fibre-reinforced polymers exhibit the greatest wear resistance when fibre alignment is normal to the plane of contact (Figure 19a); the poorest resistance is shown when the fibres are aligned perpendicularly to the sliding direction (Figure 19b).

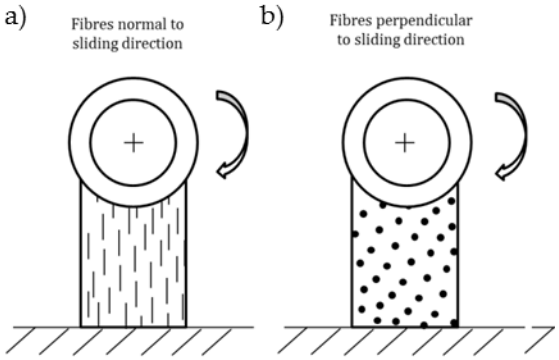

Figure 19: Fibres orientated normal/parallel to the sliding direction (a) tend to exhibit better wear resistance than fibres oriented perpendicular to the sliding direction (b). Adapted from Rasheva et al. (2010) (89)

Although the wear results of ceramic-on-CFRPEEK joints have been promising, two other findings have been observed. Firstly, studies have shown fluid absorption takes place during testing of CFRPEEK components even though they have been pre-soaked for least 50 days before testing and reached apparent fluid saturation (95, 97). Although the reasons for this finding are still under investigation, potential explanations include the accumulation of protein deposition on the bearing surface (95, 97) and fluid being driven into the material due to loading applied to the component in the hip simulator (95, 97). The second finding has been observed by a number of studies (94, 95, 97, 98) which have shown the friction factor at the ceramic/CFRPEEK bearing surface to be significantly higher than conventional bearing types. A high value has also been suggested to be detrimental to component fixation, increasing the likelihood of component loosening (99).

2.4.2.4 *Clinical Applications*

Due to the success of high performance thermoplastics in the aerospace industry, orthopaedic researchers began to explore their application in orthopaedics. Early clinical literature (9) mainly refers to spinal applications in which PEEK has been widely accepted as the material of choice, mainly due to it being x-ray translucent allowing visualisation of the healing process to be identified using normal radiographic techniques. In recent years CFRPEEK has been explored as a bearing and hip stem material. For this literature review, the use of CFRPEEK for total hip and resurfacing components will be investigated.

Total Hip Replacement

During the 1990's CFRPEEK was evaluated as a candidate material for hip replacement and compared with UHMWPE. The first clinical study was initiated in April 2001 using the ABG II total hip system (Stryker SA, Montreux, Switzerland). The component consisted of a polyethylene femoral head and a 30 % CFRPEEK liner held in a metal shell. The CFRPEEK liners were injection moulded and the bearing surface machined to the required tolerance. Initially the component was implanted into 30 patients; this expanded to 121 patients in 2003. After 3 years, there were no cases of liner revision due to aseptic loosening (100). Five

revisions occurred due to infection, loosening and periprosthetic fracture and wear retrieval analysis on one of these revisions showed a 0.13 mm head penetration after 28 months (101). Although these results are promising the mid-term results are not available for analysis.

Hip Resurfacing

A novel horseshoe shaped acetabular component was developed by Field and Rushton at the University of Cambridge in 2008 which contained a 3.0 mm UHMWPE insert with a 1.5 mm thick 30 % carbon fibre reinforced polybutyleneterephthalate (CFR-PBT) backing. It was known as the Cambridge cup and the rationale for its horseshoe shape was to use the principle of load transmission through the hyaline articular cartilage region that covers a horseshoe shaped portion of the acetabulum (67), to reduce incidences of stress shielding which can compromise fixation and facilitate wear debris migration into the periprosthetic bone (9). A clinical study performed in 50 elderly patients aimed to evaluate the fixation and stress shielding effects of the implant. 24 of the 50 implants were coated with HA and the remaining 26 were left uncoated. The application of HA improved fixation and none of these implants exhibited significant wear or migration. However, the uncoated implants migrated and in three cases revision surgery was required at 2 years (102). In a separate DEXA study (67) researchers did not find a significant reduction in periprosthetic bone mineral density compared to the controls concluding a reduction in stress shielding.

As a result of the encouraging clinical results seen by the Cambridge cup and the increased awareness of CFRPEEK as a bearing material candidate, a new flexible horseshoe shaped CFRPEEK cup was developed for hip resurfacing applications. The MITCH cup (MITCH, Stryker) is entirely manufactured from injection moulded CFRPEEK eliminating the UHMWPE liner in the Cambridge cup (68). To accommodate large diameter ceramic femoral heads, the wall thickness was decreased to approximately 3 mm reducing the chances of dislocation and improving bone conservation. Primary fixation was achieved by two fins located on the cup's backing surface. A dual layer coating consisting of a titanium base layer and layer of HA aims to promote long term stability, which is already successful in traditional acetabular components (103). Figure 20 illustrates the differences between the Cambridge and MITCH cups.

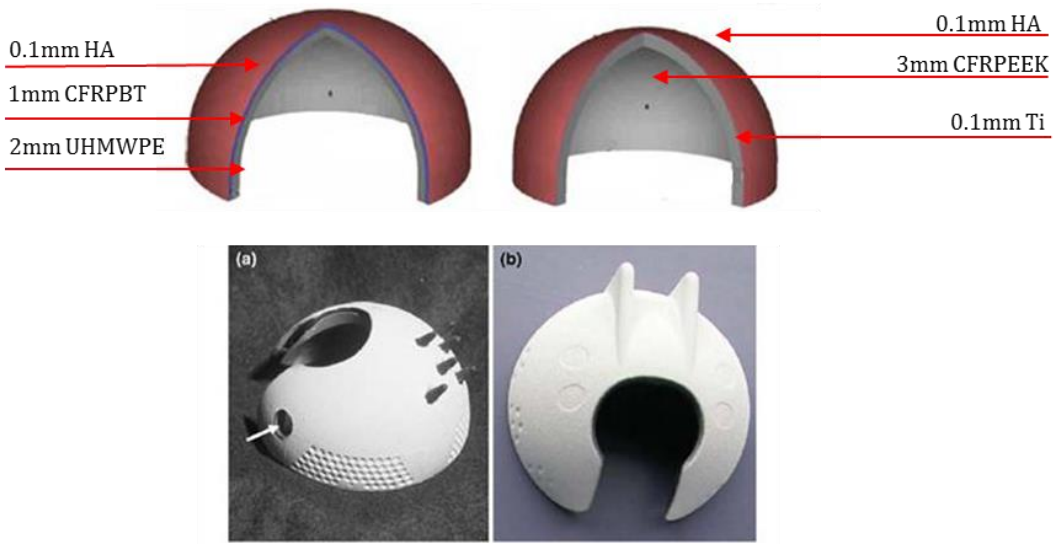

Figure 20: Comparison between the Cambridge Cup (Left) and MITCH PCR Cup (Right) (68).

There is only limited clinical data for the MITCH PCR cup, Field et al. (2012) (104) reported the three-year result of 25 implanted MITCH cups implanted by three surgeons. There were improvements in the mean Oxford and Harris hip scores and one revision undertaken at 21 months due to squeaking. The cause was investigated and the geometry of the horseshoe cut out was altered which was found to resolve the problem during *in-vitro* testing. Radiological analysis showed good early osseointegration, although at 3 years, there were five cases of component migration of which 3 were revised. At the time of writing the cause of the osteolysis was unknown.

The small collection of studies performed on the Cambridge and MITCH cup have indicated promising results. Nevertheless, they do not provide long term clinical data or generate firm conclusions to justify whether the horseshoe shape is beneficial, why it resulted in component squeaking or how the shape was determined and updated. Overall the horseshoe design could produce advantageous qualities; however the design is heavily protected by patents which would add a range of restrictions if a similar cup was developed in this project. It is also possible that diverging away from a conventional hemispherical design could result in a lack of widespread acceptance with surgeons continuing to implant long standing prosthesis designs.

Therefore, the present project focused on a full cup design with features to address the limitations highlighted in the literature review. The following sections of the literature review will employ a full hemispherical design when considering the design of a large diameter bearing PEEK based acetabular cup.

2.4.3 Summary of Material Considerations for Resurfacing Acetabular Component

The literature review on highly crossed linked polyethylene illustrated that the material was not suitable for a large diameter bearing acetabular component and no further investigation into HXLPE will occur. Aurora Medical Ltd proposed developing a non-metallic large

diameter bearing THA combination consisting of a ceramic femoral head and CFRPEEK acetabular component. The preliminary design stage for the ceramic large diameter bearing femoral head has been completed in a separate Aurora Medical Ltd research project. This section has described CFRPEEK properties and found it is suitable for an acetabular cup in terms of mechanical properties, wear characteristics, chemical stability and biocompatibility. Nevertheless, with regards to manufacturing, the relationship between the runner's location in the mould tool and the resulting fibre orientation and distribution is not well understood and forms the basis of the investigation outlined in Section 3.2.

2.5 Fixation Options for a Large Diameter Bearing Acetabular Component

Three types of implant fixation exist: cemented, cementless and hybrid which is a combination of cemented and non-cemented components. Cemented fixation involves the use of a grouting agent such as poly (methyl methacrylate) (PMMA) to fix the prosthesis in place. As the cement acts as a grout instead of an adhesive, there is no strong chemical bond between the two surfaces. Therefore the best fixation is achieved between the cement and cancellous bone which has a porous structure. To achieve an adequate interlock, the surgeon must clean the cancellous bone to expose the pores which are normally occupied by fat and marrow. Secondly pressurisation of the cement is required to overcome the resistance to flow of the cement into the bone and also prevent the displacement of the cement once it is in place by bleeding. Long term follow up studies show significantly higher loosening rates for cemented acetabular components compared to the stem despite attempts to improve the cementing technique (105, 106). Inadequate cement penetration into the bone and the unfavourable geometry of the acetabulum contribute to the reasons for acetabular loosening (107).

Cementless techniques have been explored over the past two decades as an alternative fixation method. There are three main categories (a) *Augmented fixation*, where designs achieve mechanical anchoring into the pelvis by the use of large pegs or screws, (b) *press-fit fixation* in which primary stability is achieved by inserting an 'oversized' cup into an 'under reamed' acetabulum to generate sufficient compression on the prosthesis by the surrounding bone to fix the prosthesis in place, and (c) *micro-interlock fixation* where designs are intended to achieve biologic fixation via bone ingrowth into a modified backing surface on the implant. Although each of these methods can occur individually, many prostheses combine these methods to ensure adequate fixation. In addition each of these methods can be supplemented by a secondary mechanism; an osseoconductive coating that is applied to the backing surface. Clinical studies on these components have yielded mixed results as failure is multifactorial and may include contributing factors such as wear, osteolysis, aseptic loosening and patient characteristics.

The large diameter bearing acetabular component developed in this thesis will be cementless as it is aimed to be implanted into younger patients. Younger patients place an increased demand on the components (108) and it has been suggested that the microinterlock obtained

by bone ingrowth into porous coated acetabular components appears to provide fixation superior to that with cemented sockets (109).

An investigation into current acetabular cementless techniques is performed in the section below, which has compared each method and identified the downfalls associated with each type.

- **Augmented Fixation**

Primary stability of the acetabular component is improved by the use of screws (110). Figure 21 illustrates an example of an acetabular component that uses screw fixation. The presence of multiple holes allows the surgeon to choose the number and placement of these screws depending on patient characteristics. This method can theoretically close any gap created by non-congruous reaming especially in patients with poor bone quality and reduced bone coverage in the acetabulum. However, incorrect placement of long screws increases the risk of injury and it is important that screws or pegs are placed in areas of the acetabulum that provide the best bone stock while minimising the risk of damage to vital intrapelvic structures (111).

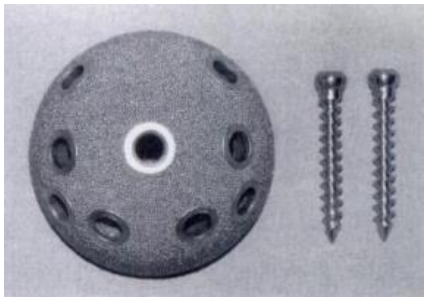

Figure 21: Acetabular shell with holes for fixation (Reproduced with permission and copyright © of the British Editorial Society of Bone and Joint Surgery (112)).

The anatomical structures in the acetabulum that are at a higher risk are the external iliac, obturator, superior and inferior gluteal, internal pudendal arteries and veins and the obturator and sciatic nerves (111). Figure 22 illustrates the location of each structure highlighting the large cumulative area covered by them which must be approached with care. Vascular injury by screw insertion can lead to complications during surgery.

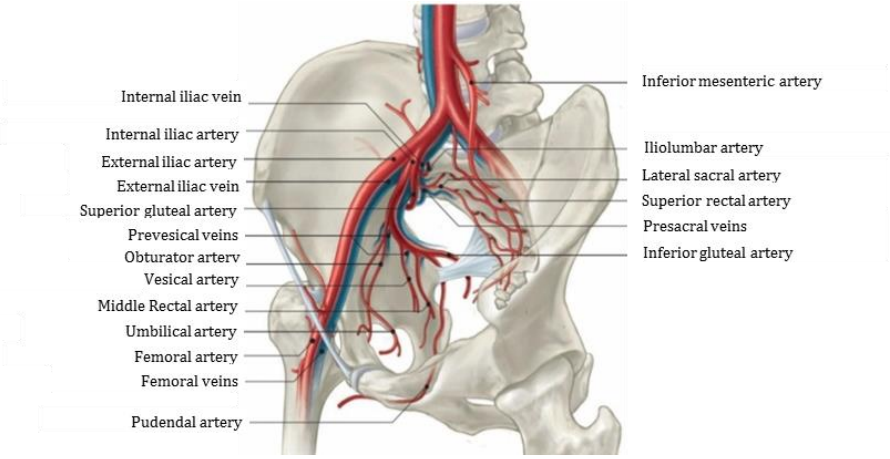

Figure 22: Illustration of the main veins and arteries in the pelvis (113).

There have been studies into the optimal placement of screws in the acetabulum using a quadrant system (111, 114). Figure 23 illustrates the quadrant system and enables a 'safe zone' for screw fixation to be defined based on the bone stock in the acetabulum. The anterior and inferior quadrants and the centre of the acetabulum endanger the external iliac vein and artery as well as the obturator pedicle meaning any protruding fixation features should not be present in these areas.

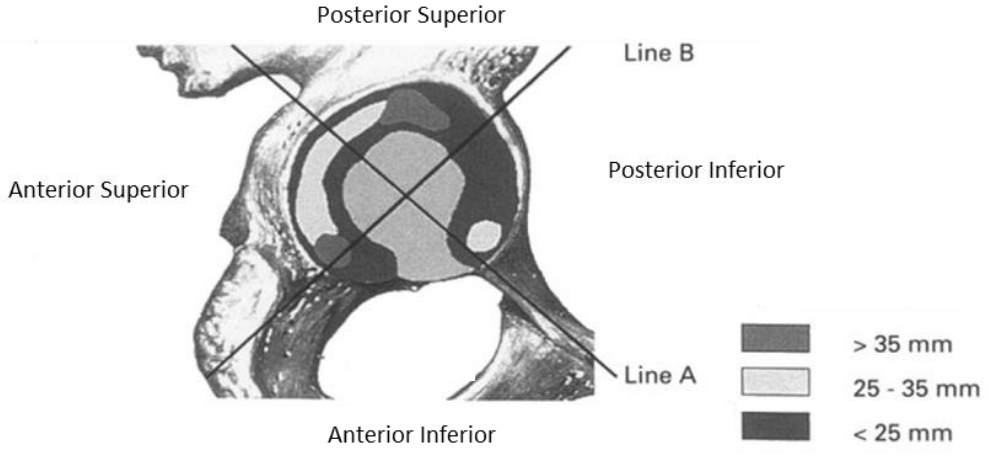

Figure 23: Tomography map of bone stock in the acetabulum (114).

As well as vascular injury, complications may arise from the screw location holes as they can be a source of fretting. Fretting refers to small cyclic motions, typically less than 100 μm of one surface relative to another, in this case between the metallic shell and screw. Over time wear debris is generated between the shell/screw interface and this can migrate into two main areas a) between the bearing surfaces and b) to the shell/bone interface through areas of minor resistance e.g. unused screw holes. The first occurrence causes third body wear, increasing the bearing surface roughness and accelerating abrasive wear especially evident in polyethylene surfaces due to the difference in hardness between the polymer and metal debris. The presence of polyethylene particles in surrounding tissue can result in osteolysis (53) due to an immune response to the foreign particles, compromising component fixation and leading to early loosening (115). Metal debris may also lead to an immune response and bone resorption (7, 45).

Screw fixation has yielded mixed results. Clohisy and Harris (1999) (116) investigated 213 patients with screw fixed Harris-Galante components. Although the study suggested excellent fixation, radiographs showed 5 % had osteolytic regions and 4 % were revised after an average of 10 years. Similar studies performed on the same prosthesis have shown comparable results; Parvizi et al. (2004) (117) observed 95.7 % survival at 15 years and Curry et al. (2008) (118) Kaplan-Meier study observed 73 % survival rate at 10 years a figure distinctively poorer than the other studies.

- **Press-fit Fixation**

Press-fit fixation relies entirely on the geometry of the component and the acetabulum. Primary stability is achieved by inserting an 'oversized' cup into an 'under reamed'

acetabulum (119, 120) with recommended differences of diameter between the reamer and cup of 1-3 mm (119, 121). Press fitting an oversized cup into a reamed cavity causes pre-compression at the peripheral interface of the acetabulum and minimises gaps at the dome of the cup upon implantation (122). Press fit systems can function without screws meaning any complications relating to vascular injury, screw breakage and fretting wear at the screw/hole interface are eliminated.

Nonetheless, this technique does have complications; recovery time for the patient is prolonged as bone needs to form around the implant before weight-bearing activities can occur. The acetabular bone stock must be sufficient for stable acetabular press fit and prepared correctly to ensure complete component seating. Failure to achieve these aspects will lead to incorrect positioning and micromotion. When this elastic movement ranges between >150 μm (123) bone growth exists however, motions in excess of this value result in no bone growth and instead the accumulation of fibrous encapsulation of the implant (123). Fibrous tissue has poor mechanical properties, deforming significantly in compression and inefficiently transmitting tensile and shear loads often associated with early implant loosening.

- **Micro-interlock Fixation**

In an effort to improve long term fixation of cementless acetabular components, biological fixation via bone ingrowth was introduced. As-cast sintered beaded or titanium fibred porous features on the external surface of the shell provide a surface onto which bone can grow (Figure 24). Threaded cups that initially used a purely augmented method for fixation noted early fixation failure as there was no surface to allow bony ingrowth into the implant (60) (Figure 24). Pupparo and Engh (1991) (124) demonstrated that by adding a porous surface to the threaded cup they created repeated ongrowth onto the surface of the implant. Manley et al. (1998) (125) showed similar findings when comparing three acetabular cups with different fixation methods. Sockets with a porous coating showed a significantly lower failure rate (6 %) than those with a simple coated press fit design (22 %).

Figure 24: An example of a threaded porous cup (Reproduced with permission and copyright © of the British Editorial Society of Bone and Joint Surgery (126)).

Experience with porous surfaces have shown that dense subchondral bone is preserved and the roughened surface engages with a mechanical press-fit meaning little need for additional fixation with screws, pegs or fins (112, 127). The other important requirements include that the implant materials are biocompatible; the component surface possesses the optimal pore

size and roughness which is in contact with the host bone and restricts micromotion to within a safe range.

The *in-vivo* reaction to porous coated implants resembles fracture healing with stable osteosynthesis (109) and bone formation within the pores established by the beads or fibres on the surface (Figure 25). It has been shown that titanium and tantalum provide a favourable ionic environment which encourages bone abutment to the metal. Titanium fibermesh fixation has the longest published follow-up of all the porous surfaces and numerous studies from throughout the world have produced a mechanical failure rate of 1 % at 10 to 15 years (128, 129). Tantalum metal foam is a form of porous material, consisting of 80 % interconnected pores. Its properties can be tailored to mimic the stiffness of trabecular bone with the additional benefit of a high friction coefficient. These qualities make it well suited for revision cases of bone deficiency and therefore its use has been popular in the orthopaedic field.

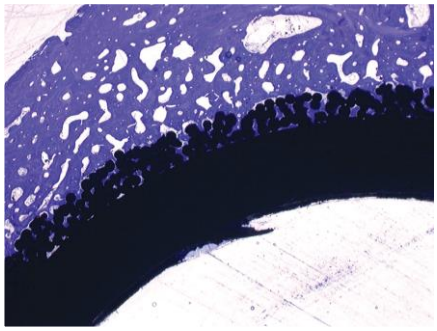

Figure 25: Porous titanium acetabular cup. The material exhibits excellent biocompatibility with bone growth (Purple Medium) into the pores (130).

The main theoretical advantages of porous prostheses are the direct biological bond which promotes long term stability, their hemispherical shape which gives ease of insertion and the high coefficient of friction between the underlying bone and implant which aids fixation. Although porous surfaces offer increased stability the fabrication of the porous surface can be expensive and time consuming. The bond of the porous material to the underlying substrate must be secure enough to prevent bead detachment and delamination.

- **Osseointegrative Coatings**

Secondary fixation is biological and achieved with osseointegration at the implant-bone interface by means of bone growth onto or into the substrate. Clinical studies have shown a coating alone is not adequate for successful primary fixation without a mechanical interlock (125). However, in conjunction with the methods previously discussed a coating can aid fixation. The most common coatings used are Hydroxyapatite (HA), titanium (Ti) or a combined TiHA. HA has the longest clinical history with use in dentistry since the mid-1980s (131) and has shown good clinical results (103, 132). HA consists of calcium phosphate which has the same mineral as the inorganic phase of bone resulting in an osseoconductive response *in-vivo*.

A large group of clinical trials with HA coatings have shown continued fixation for long periods (2-10 years) but doubts are present due to the durability of the coating. A concern relates to the degradation of the HA, in which parts of the coating detach from the components surfaces and travel to the bearing surface, producing third body wear and component loosening. Studies have shown resorption of HA coating with complete loss of a 60 μm thick HA coating after 4 years (133).

Another concern relates to the application process of the coating onto the substrate. It is common for HA coatings to be applied by plasma spraying which can have adverse effects on the mechanical properties of the substrate due to the high processing temperatures required. The initial stage of coating involves blasting the specimen with grit to give a roughened surface finish, which will promote interlocking with the coating. HA in the form of powder is injected into a high temperature plasma flame and accelerated to a high velocity. A spray gun is used to direct the high temperature spray onto the prepared material surface. The molten particles strike the surface of the component where they undergo rapid deformation and solidification to form disk-like splats which make up the coating. It is important that any reduction in strength or fatigue life is investigated especially in this incidence when a novel thermoplastic material with complex mechanical properties is used. Section 3.3 describes the investigations completed to verify whether the coating application process was acceptable.

2.5.1 **Discussion of Fixation Methods**

The top four cementless acetabular cups (Pinnacle, Trident, Trilogy and CSF) implanted in England and Wales in 2012 (2) all have a porous backing. Screws can be used in both the Trilogy and CSF component if additional primary stability is required.

All methods of cementless fixation in general have several consistent features that should be incorporated into a new fixation method. The subchondral bone of the acetabular interface must be maintained, particularly in the dense areas of the anterosuperior ilium and the ischium (134). The shape of the acetabulum should be replicated with hemispherical cup geometry to allow normal loading through a round structure similar to the femoral head. Thirdly as early biomechanical studies demonstrate that the pelvis and the cartilage interface is flexible during loading (134), the fixation surface should allow loading on the periphery which would be the primary contact area of the implanted acetabulum (110, 119). These aspects will be considered in the design of the new primary fixation method described in Section 3.4. In addition, this section has highlighted the ability for osseointegrative coatings to have a detrimental effect on the substrates mechanical properties due to the plasma spray process. Section 3.3 investigates the influence of the plasma spray process on CFRPEEK mechanical properties and the adhesion of two coatings to select the most appropriate for the novel large diameter bearing acetabular component developed in this thesis.

2.6 Design Considerations for a Large Diameter Bearing Acetabular Component

The bearing size and choice of material are the main differences between the early small bearing and large diameter bearing THA acetabular components. Large bearings generally consist of a hard-on-hard articulation (e.g. MoM) and although the overall designs can look similar subtle design variations exist which can limit the success of the component.

2.6.1 Cup Geometry

The material bearing choice and metallurgy have been previously discussed and were shown to alter the wear characteristics of the component. More subtle differences exist including: clearance, entrainment angle, surface finish, roundness, centre edge angle and these can influence the component's performance especially wear.

The entrainment angle relies on the clearance which is the gap between the femoral head and the acetabular cup. For MoM components, this gap must be effective in producing a fluid film which will aid lubrication of the metal bearing protecting it from wear. The lubrication regime also requires a high surface finish and accurate roundness of the bearing surfaces. The centre edge angle is the angle between the superior edge of the bearing surface and the vertical (γ in Figure 26) and is a critical parameter influencing the wear characteristics of a component. This value can range between 39 ° and 45 ° for conventional hip replacements inclined at 45 °. As a result of the less than hemisphere bearing surface on resurfacing and large diameter bearing components which offset the edge of the articulating surface from the cup face, the angle is reduced to between 29 ° and 38 ° depending on the design.

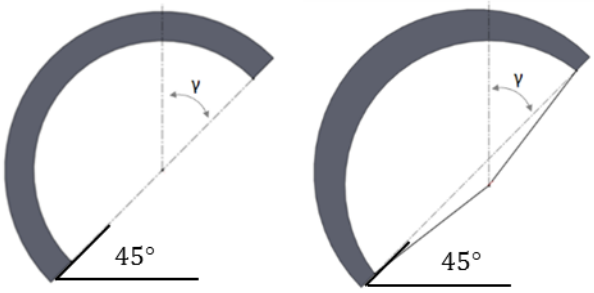

Figure 26: Diagram illustrating the Centre edge angle (γ) of a total hip replacement (Left) and large diameter bearing acetabular cup (Right) implanted at a 45 ° abduction angle. Adapted from Jeffers et al. (2009) (135).

This angle is important as it means MoM components are less forgiving to mal-positioning than a soft bearing component such as polyethylene (135). Normally in a correctly orientated MoM device, point contact exists and high 'running-in' wear occurs immediately after surgery. Once the wear patch reaches a sufficient size to support fluid film lubrication, low wear is exhibited by the device. However, a steep implantation angle changes the tribological conditions at the bearing surface. As a result, fluid film lubrication is no longer achieved and the wear patch grows rapidly. The wear patch can reach the edge of the cup due to the high inclination angle. In this instance no pressure can be generated and the fluid film lubrication

regime is lost initiating 'runaway' edge wear. (135). 'Runaway' wear can be prevented by maximising the centre edge angle and by considering component positioning. Aurora Medical Ltd have chosen to use the proven geometry from an existing large bearing component (ADEPT) for the CFRPEEK component which possesses a centre edge angle of 35 °; one of the highest angles for a less than hemisphere design (135). CFRPEEK/ceramic joints have been shown to operate within the boundary lubrication regime (94, 97, 98) and the extent to which the centre edge angle affects wear performance of this component is unknown. Although, this aspect is not investigated in this thesis it is known that a larger clearance will be required compared to a MoM device due to the joint operating within the boundary lubrication regime and possessing a higher friction at the interface (94, 97, 98).

2.6.2 **Anatomical Cup**

Although the acetabular cartilage is resected during total hip arthroplasty, knowledge of its shape is useful in the development of more biomechanically compliant acetabular cup components. Large diameter acetabular cups aim to restore the hip's natural anatomy and kinematics while reducing the incidence of dislocation. The shape of the artificial cup is conventionally spherical, although research suggests that the acetabulum shape is ellipsoid (12, 136). This shape allows an optimal contact stress distribution in the hip joint.

A large number of studies (137-139) have informed on the geometry of the femur providing an understanding of the variation in femur shape and size for implant designers, thus enabling more biomechanically appropriate implant designs to be developed. Similar studies have been performed on the acetabulum using a range of methods including laser scanning (12, 140), plaster casting (141, 142) and the use of MRI or CT images to generate surface models (143, 144). However there have been a reduced number of iterations in the design of the acetabular component historically (24, 145).

Loosening is a common indication for revision of acetabular components (3, 4). Aside from incorrect positioning and wear induced osteolysis, a critical factor for loosening is the change in strain distribution through the pelvis after the replacement compared to the intact case, known as stress shielding (56). Non-physiological periacetabular bone strain near the pole of press-fit cups has been shown to lead to bone deterioration (63, 64). It has been suggested that this deterioration may promote earlier component loosening, and preservation of the bone-implant interface should be a main objective for implant designers (63, 64).

Recent studies have investigated advanced polymer based composite materials as a possible acetabular cup material in an attempt to reduce stress shielding as they possess a stiffness closer to bone tissue than currently used metals (66, 67, 102). It has been hypothesised that load transmission in the implanted pelvis could be improved by altering the acetabular design to more closely match the natural geometry (64, 68). Mechanical loading influences cartilage formation (146, 147) and the shape of the cartilage gives an indication of the contact stress across the joint, so the specific horseshoe shape of the acetabulum articular cartilage indicates that only part of the acetabulum is loaded (148). This reasoning has been applied

in the design of cartilage shaped implants employing polymer composite materials (67, 68, 102). On this basis, an anatomic survey is performed in this thesis (Section 3.1) to investigate and characterise the articular cartilage geometry to obtain a relationship that can be used to design the internal geometry of the bearing surface of the acetabular component.

2.6.3 Summary of Design Considerations

This section has illustrated the subtle differences between large diameter bearing components which can have a dramatic effect on the performance and success of a component. Key parameters such as centre edge angle, clearance, surface finish can affect the wear performance of conventional MoM components. In the proposed CFRPEEK/ceramic device the internal geometry of the bearing surface, clearance, surface finish and centre edge angle are particularly relevant to the performance.

As Aurora Medical Ltd have chosen to use the proven geometry from an existing component (ADEPT) further investigation into the clearance, surface finish and centre edge angle will not be carried out in this thesis. It has been identified that a more anatomical cup which incorporates the articular cartilage geometry on the bearing surface could improve load transfer into the pelvis. Section 3.1 investigates the acetabular cartilage geometry with the intention of characterising the shape and applying it to the bearing surface of the acetabular component developed in this thesis.

2.7 Implantation and Initial Post-Operative Conditions of the Acetabular Component

Section 2.5 discussed the fixation options for a non-cemented cup highlighting press fit as an option for achieving primary cup stability after implantation. Press fitting is achieved by inserting an 'oversized' cup into an 'under reamed' acetabulum. Sections 2.1 and 2.2 have described the geometrical differences between resurfacing and traditional total hip components and one of the main differences is bearing diameter although large diameter bearing THA components do exist. To preserve bone stock, large diameter bearing THA components are thinner and the suggestion of substituting the acetabular component's material for a polymer composite which possesses a lower modulus than current designs coupled with a thinner wall raises concerns about its behaviour during insertion and the resulting effect on the surrounding bone (149, 150). To understand the implantation process, the surgical approach for implanting an acetabular component will be described in the following section.

The surgical approach for implanting an acetabular component with a press-fit method firstly involves the surgeon reaming a cavity in the acetabulum. This cavity is usually 1-3 mm smaller than the outer diameter of the acetabular component (119, 121). Once the acetabulum is prepared the surgeon assesses the expected component fit with a cup trial. The trial has the same outer diameter as the component and is inserted into the acetabulum. If full bone contact is observed around the trial edge a correct fit has been achieved. With the cavity correctly sized the cup is mounted onto an introducer which assists accurate component

positioning. The cup (attached to the introducer) is placed into the prepared cavity and impacted with several firm hammer strikes until it is fully seated.

Impacting an oversized cup into a reamed cavity causes pre-compression at the peripheral interface of the acetabulum (151) which is essential for primary stability. This pre-compression increases frictional resistance to micromotion which is known to restrict the bone in-growth process (123). In addition, the application of a rough osseointegrative coating to the outer surface of the component increases resistance. Although this technique has been proven successful in promoting long term fixation (152, 153), concerns exist, especially in the development of a new prosthesis.

The first area of concern relates to acetabular fracture, as an oversized component is being forced into a smaller acetabulum. Acetabular fracture is when the socket is broken and this has been demonstrated with cadaveric specimens implanted with press-fitted components oversized by 2 to 4 mm (154); but also in patients with surgically implanted components oversized by 1 and 3 mm (155). The incidence of acetabular fracture is more prominent with stiff acetabular components including ceramic and polyethylene cups supported with a metal backing as they do not easily deform within the acetabulum cavity and therefore this incidence may not be a concern for a polymeric component. However thinner and lower modulus large diameter bearing THA and resurfacing components may still cause bone failure at a discrete level i.e. individual trabeculae (156).

Another concern is that the component may deform more than the surrounding bone meaning inadequate pre-compression for primary fixation may be established. In addition, this excessive deformation could be accompanied by an additional problem relating to increased wear due to induced changes in component sphericity, degradation of fluid-film lubrication, or induced equatorial contact (157, 158).

The influence of cup deformation on wear has been investigated experimentally and computationally using hip simulators, digital image correlation (DIC) and finite element analysis (FEA) (157-159). However, the investigation of the implantation process and the effect on component and pelvis response is not well understood due to the complexity of the process. Computational methods have attempted to investigate (160, 161) the biomechanical response of the pelvis after component implantation. However the results are restricted as static conditions were applied and contact conditions at the bone/implant interface varied between studies (162). Although computational methods are progressing towards more realistic impaction simulations e.g. dynamic conditions (162), both these and experimental methods are limited due to difficulties in simulating the applied impact load and the physiological boundary conditions (163).

Experimental studies (163-166) have primarily focused on investigating the force experienced by the component during impaction whilst component deformation has been assessed using DIC (167) and coordinate-measuring machines (162). However, it has been

noted that these methods are primarily limited by the boundary conditions which may not be physiologically correct (163).

The pelvic response to implantation has only been experimentally investigated in a limited number of studies but the importance of this type of study is critical for implant survival. The amount of pre-compression in the periacetabular bone has already been described as a critical factor in the survival of an acetabular component due to its relation to primary stability. However, the stress state in the surrounding bone after implantation is also important for the implant's long term survival, in particular maintenance of the supporting bone quality. Section 2.3 outlined stress shielding; a detrimental factor to implant survival which occurs due to an alteration in the natural stress distribution through the pelvis and proximal femur which is caused by the mismatch of stiffness between the implant and host bone. Stress shielding is commonly seen in the proximal bone and the medial aspect of the neck in THA femoral components and modifications in the strain and stress patterns induced by the femoral prosthesis have been studied extensively (5, 6). As a result, relations between the roentgenographic changes around the implanted femur and the design and material properties including stiffness and fixation of femoral prostheses have been established.

Although, remodelling and stress shielding of the proximal femur in response to implants have been characterised, the response to cementless total and resurfacing acetabular components has not been as extensively studied. Dual energy x-ray absorptiometry (DEXA) studies (63, 168) have shown unphysiologic periacetabular bone strain near the pole of press-fit cups which has led to bone deterioration. In addition it has shown stiffer metal cups load the superior acetabular rim cortex preferentially compared to polymeric cups. Nevertheless, this data is obtained from long term studies, years after implantation and it cannot be used to predict the bone strain around new components. Numerical analyses have predicted concentration of strain at the component periphery into the cortical bone which produces shielding of the proximal and medial trabecular bone (160, 161). Thompson et al. (2002) (65) assessed pelvis strain distribution when implanted with a series of acetabular component and confirmed that differences are seen with varying implant designs and materials. Numerical studies are restricted by the boundary conditions put upon them and validation must be provided experimentally. Experimental studies examining the pelvis strain have been conducted using DIC (66, 169) and the attachment of strain gauges (163, 170) to the pelvis's surface. Although these studies coincide with finite element findings, they are significantly limited due to the ability to only assess surface strains. Therefore, an understanding of the strain distribution surrounding the full implant cannot be realised. Section 4.2 introduces an emerging measurement tool called Digital Volume Correlation (DVC); a novel experimental technique which can be used to assess internal strains of test subjects. Section 4.4 shows how this technique can be implemented to assess the strains generated around the complete surface of an implant.

3 Experimental Development of a Novel Acetabular Component

3.1 Study 1: Component Design

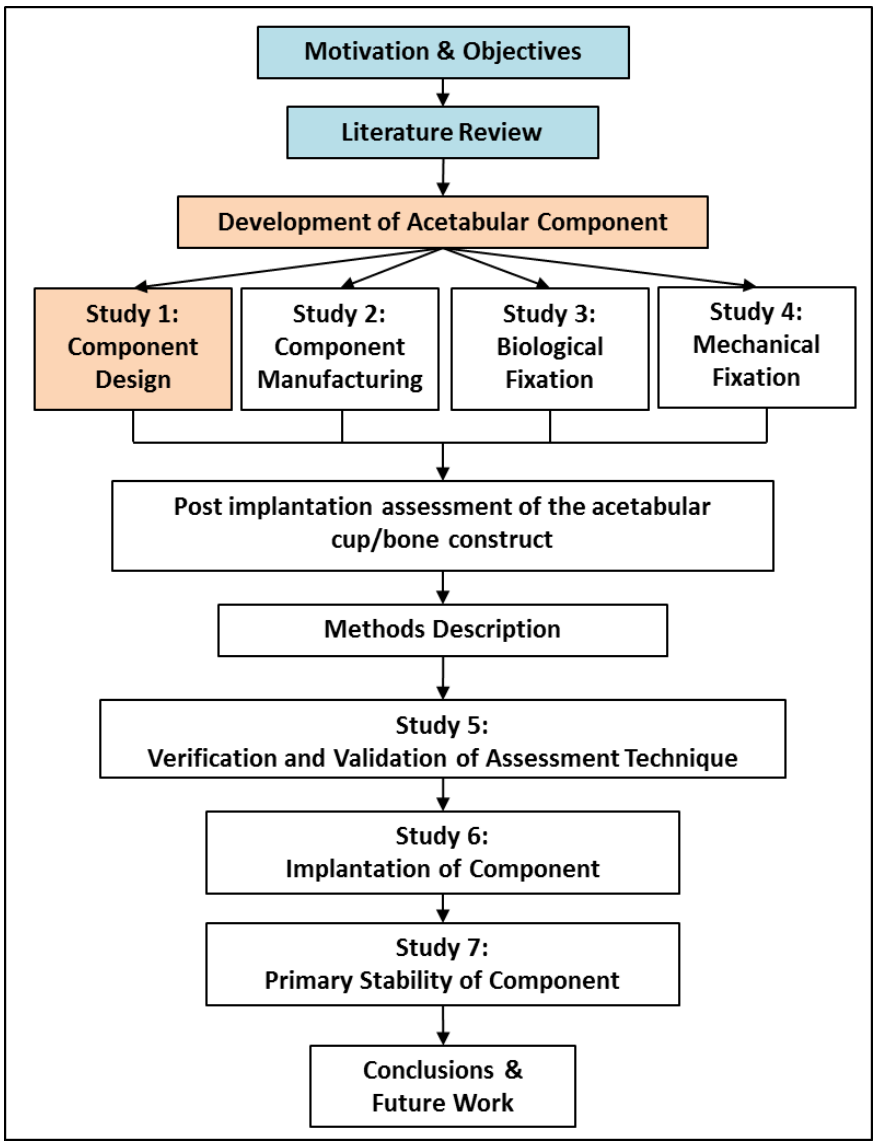

This part of the study has been published as a journal article:
Gillard, F.C., Dickinson, A.S., Schneider, U., Taylor, A.C., Browne. M. *Multi-pelvis characterisation of articular cartilage geometry*. Proceedings of the Institution of Mechanical Engineers, Pt H: Journal of Engineering in Medicine, 2013. 227(12):1255-64.

3.1.1 Characterisation of Acetabulum Articular Cartilage Geometry

The 3D shape of the acetabulum has been a subject of investigation for some time and investigators have used a range of methods including laser scanning (12, 140), plaster casting (141, 142) and the use of MRI or CT images to generate surface models (143, 144). From these 3D shapes, the human acetabulum has been commonly represented as a sphere with studies examining its morphology by fitting best-fit spheres to the models in order to understand how it varies amongst patients. Although informative, these studies have shown that the

acetabulum rarely fits a perfect sphere and have suggested the bony articular surface of the acetabulum may more closely fit an ellipsoid. This could have implications on the design of hip components where historically the spherical-nature of the femoral head and the hemi-spherical nature of the acetabular cup have been used as a justification for modelling from a kinematic perspective, as a pure ball-and-socket joint (171). It is essential to test the limits and validity of this best-fitting approach and the hypothesis that the acetabular shape more closely fits an ellipsoid, as this could have implications on the stress distribution and kinematics of a prosthesis whose design is not based upon authentic natural geometry. Therefore in the present investigation the degree to which the natural surface is out of sphericity was assessed by comparing the efficiency of fitting a sphere and an ellipsoid to the acetabulum surface.

To promote acceptance amongst surgeons, Aurora Medical Ltd decided to base the design of the acetabular component developed in this thesis on a current successful large diameter bearing acetabular cup (ADEPT) meaning certain design factors (centre edge angle, entrainment angle) were fixed and did not require further investigation in this thesis. Most modern larger bearing acetabular components that use solid cobalt/chromium are between 3 and 5 mm in thickness (172). Using this range as a basis, a 3 mm component thickness was selected by Aurora Medical Ltd for the CFRPEEK component to maximise bone conservation and with consideration that injection moulding of thin parts (< 1.5 mm) is difficult to achieve according to the material supplier (79). It is known that the CFRPEEK component will deform more than a traditional metal component (167) and it has been suggested that an even thinner CFRPEEK component (< 3 mm) may deform excessively promoting concerns relating to excessive deformation that have been discussed in Section 2.7.

A key design objective outlined by Aurora Medical Ltd was to establish a more biomechanically compliant component which optimised the contact stress distribution in the replaced hip. Although the cartilage on the acetabular articular surface is resected during total and resurfacing hip arthroplasty, knowledge of its shape and how it varies from patient to patient would be useful when applying it to the design of CFRPEEK component's bearing geometry outlined in this thesis. The cartilage and articular surface outline is particularly important as mechanical loading influences cartilage formation (146, 147) with the shape of the cartilage being shown to indicate the natural contact stresses across the joint. The acetabulum articular surface is horseshoe shaped, surrounding the central non-articular depression called the acetabular fossa or notch. The horseshoe region is the weight bearing section and it is suggested that its specific shape optimises the contact stress distribution in the hip joint, decreasing the peak contact stress and rendering the stress distribution more uniform (148, 173). Total and resurfacing hip arthroplasty components aim to restore the natural biomechanics and loading of the natural joint, however, the insertion of current hemispherical acetabular components have been shown to result in pole contact which is not present in the natural hip even under high loads (174). Therefore, novel acetabular

components like the Cambridge and MITCH PCR components (Figure 23) are being investigated as they mimic the horseshoe weight bearing shape (the natural geometry), (68, 102) and intend to more efficiently restore the natural load transfer in the hip after a joint replacement. Section 2.4.2.4 outlined the clinical and pre-clinical data available at the time of writing on these two components. One of the main differences between these two components and current devices is that they are not full hemispheres as they have a cut-out region in the centre. This has raised concerns over the potential for excessive deformation after implantation and it is advised that care is taken to ensure reaming of the bone is correct to avoid this occurring (175). On this basis Aurora Medical Ltd decided that the CFRPEEK component would have a full hemi-spherical cup design to provide additional support and have a horseshoe shaped raised section that mimics the natural articular geometry; in this way a more natural stress distribution should result across the replaced joint.

This investigation aims to provide original data on the outline and quantification of the acetabular notch geometry which could inform Aurora Medical Ltd on the outline of the horseshoe shape which was required on the bearing surface of the component. The original design provided by Aurora Medical Ltd prior to this investigation is shown in Figure 27 and has a circular region with a thin parallel section near the rim. This design was loosely based upon the MITCH component. There is no literature relating to the rationale of the MITCH outline and this study aimed to provide details of the horseshoe shape which could be used to update the original CFRPEEK design.

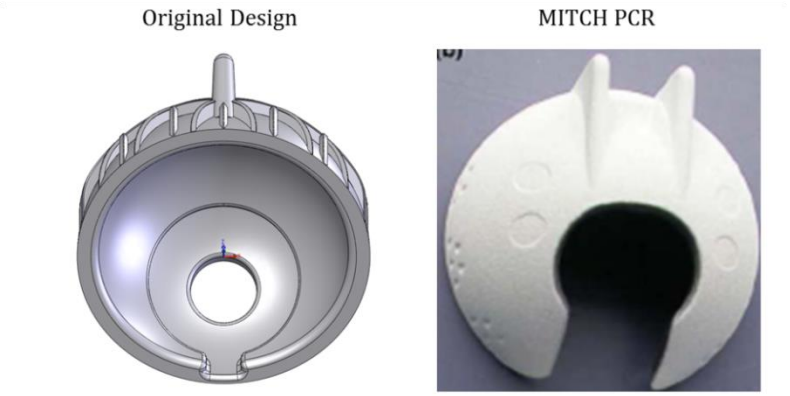

Figure 27: Outline of horseshoe notch on original Aurora Medical Ltd design (left) which is based on the internal outline of the MITCH PCR component (right) (68).

Materials & Methods

24 left acetabulae were analysed, from anonymised human dry bone full- and hemi-pelvis specimens donated with prior informed consent, at Gubener Plastinate GmbH, Guben, Germany. The donor gender of 20 full pelvises was estimated by examining the pelvic girdle (176); 11 were female, 9 male. The remaining 4 hemi-pelvis donor genders were unknown. The source of the bones and the age at death were unknown. None of the acetabula were fractured although 5 showed signs of degenerative joint disease.

All morphologic acetabular measurements were performed by one observer (FG) on plaster moulds taken from the left acetabulum on all specimens. Digitised anatomical geometry of each acetabulum was acquired by a 3D laser scanner (Xyris 2000, Taicaan, UK). This system uses a laser triangulation probe with a 30 μm laser spot that is scanned across the mould surface to build up a 3D computer image. A 3D point cloud representing each surface was obtained and converted into a .stl standard format in Solidworks 2010 (Dassault Systèmes Solidworks Corps, France) in order to be output as a processed point cloud (.xyz) (Figure 28). To coincide with current methods (140, 177) of acetabular morphology assessment a MATLAB program (140) containing a nonlinear least-square algorithm to fit a sphere to the nodal co-ordinate data of the acetabular bearing surface, giving the best fitting acetabulum sphere diameter and centre coordinates. The code was adapted to apply a difference threshold of +/-0.5 mm which deleted points outside this range, eliminating data points from the acetabular notch (below the level of the articular surface) and any error points due to air bubbles that were formed during moulding (Figure 28c). The 0.5 mm deviation threshold was selected based on previously reported literature data (177) which suggested that there was a 0.5 mm maximum deviation from spherical of the articular surface. A 3D scatter graph was produced which illustrated the shape of the articular geometry (Figure 28d)

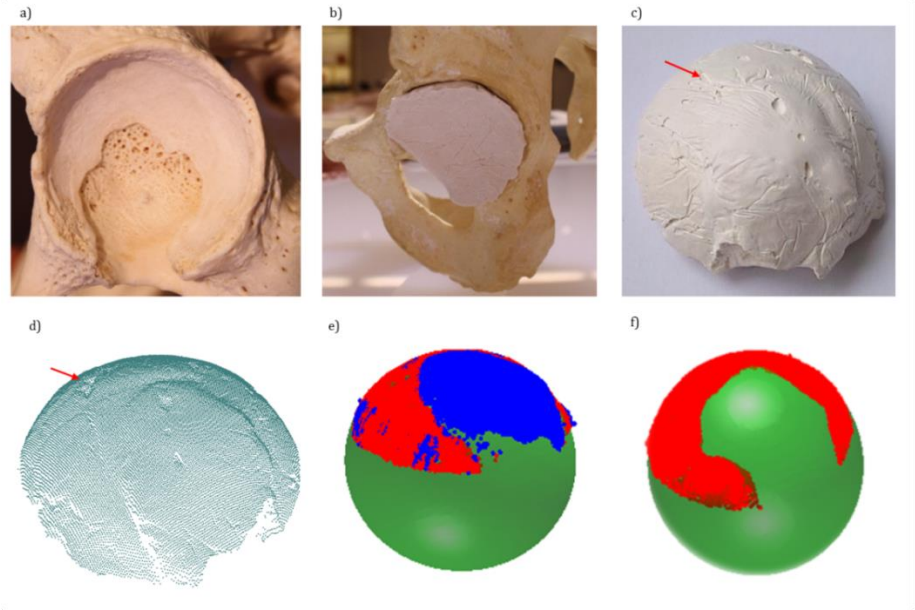

Figure 28: Moulding process of skeleton acetabulum (a) involving insertion of plaster (b) to form mould. An air bubble is highlighted by the red arrow (c), generation of surface point cloud of mould using laser scanner (d), ellipsoid/sphere fitting to point cloud (e) and deletion of points outside of error threshold (f).

To test the hypothesis that the acetabulum is better described by an ellipsoid than a sphere, the MATLAB program was extended to fit an ellipsoid to the point cloud of each specimen. An ellipsoid was fit to the points cloud using the function *ellipsoid_fit.m* by Yury Petrov MATLAB Central File Exchange, June 2012 (178). The algorithm fits the point cloud to a polynomial expression ($Ax^2 + By^2 + Cz^2 + 2Dxy + 2Exz + 2Fyz + 2Gx + 2Hy + 2Iz = 1$) using a

linear least square approach and this was solved to find the centre and radii of the ellipse. The horseshoe shape determined in the sphere fitting procedure was used to mask the original point clouds (including points in the acetabular notch) and delete points located 3 mm inside the acetabular notch outline, enabling an ellipsoid to be successfully fitted to the points on the articular surface.

The ellipsoid axes were aligned along the principal axes of the acetabulae coordinate system (Figure 29) and the radius along each axis was calculated and the ellipsoid centre located. These values were used to calculate the error between the best-fit ellipsoid and each point in the point cloud using the standard ellipsoid equation. To eliminate points within the notch a +/- 0.2 % (~+/-0.5 mm) error threshold was implemented which deleted points outside of this range and exposed the shape of the articular geometry (Figure 28e).

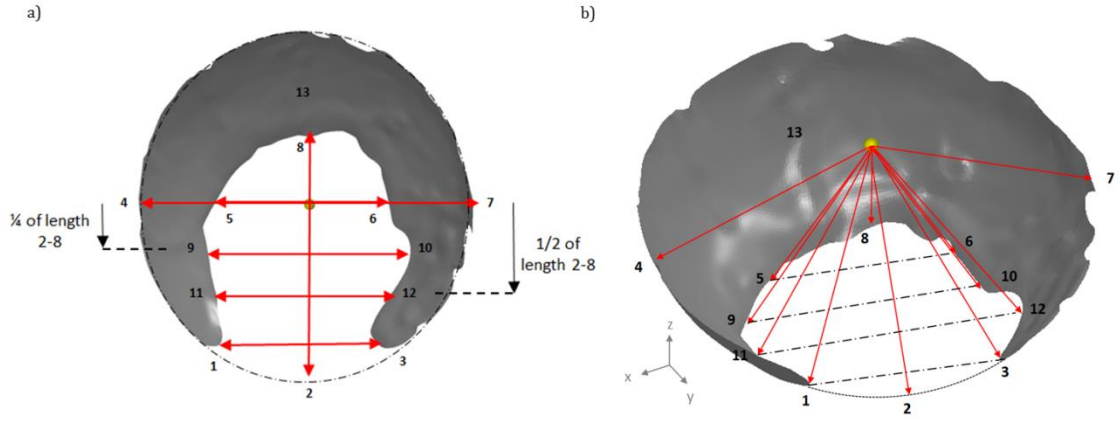

Figure 29: a) Location of points on acetabulum to generate cartilage geometry and b) Angles between location points.

The closeness of the fit of the best-fit sphere and ellipsoid was assessed by calculating the mean deviation between the best-fit sphere/ellipsoid surface and all the points within the point cloud for each acetabulum.

Nine 'landmark' points were picked around the acetabular notch and two from the bony edge of each point cloud produced using the sphere and ellipsoid fitting techniques which eliminate data from the original points that fell within the acetabular notch. All points referenced the best-fit sphere or ellipsoid centre (Table 1, Figure 29).

Table 1: Dimensions and Angles analysed

Acetabulum Points:	Landmarks:
1-3	Notch opening length
2-8	Notch height through centre
4-7	Cartilage width through centre
5-6	Notch width through centre
9-10	Notch width at a distance equal to quarter of the notch height along y-axis
11-12	Notch width at a distance equal to half of the notch height along y-axis

In three acetabula the notch did not extend past the centre so points 5 and 6 could not be picked. Vectors between the points and the best-fit sphere or ellipsoid centre were calculated. The distance and angle between corresponding pairs of points (as defined in Table 1), on the outline of the acetabular notch exposed by the best-fit sphere and ellipsoid were then calculated.

The notch opening width, notch height, notch width through the centre and the notch width at set distances from the centre were characterised for each acetabulum and fitting technique. The angle and distance between corresponding points were calculated to give the total angle between points through the sphere or ellipsoid centre.

Reproducibility of the measurement technique was assessed by 5 repeat mouldings on a single acetabulum. For comparison against published literature (140), differences between male and female groups were assessed using a two-tailed Student t-test assuming unequal variances. The left acetabulae from the hemi-pelvises were excluded from this section of the study as the gender could not be evaluated using the pelvic girdle technique.

Results

The repeatability study of the casting and scanning process showed that the best-fit acetabulum sphere diameter approximation exhibited a range of +/- 0.1 mm whilst on average the range of the length and angle measurement was +/- 0.5 mm and 2.1 ° respectively when the process was repeated on the same acetabulae. The best-fit ellipsoid approximation exhibited slightly higher deviation with the x, y and z radius exhibiting a range of +/- 0.4, 0.4 and 1.2 mm whilst on average the range of length and angle measurement was +/- 0.7 mm and 3.5 ° respectively.

Table 2 shows the mean diameter of the fitted spheres and ellipsoids and compares the overall mean male and female diameters. The mean diameter of the spheres fitted to the acetabulae was 50.7 mm (standard deviation (S.D) of 2.5 mm, range 45.1 mm to 55.9 mm). Males exhibited a larger acetabulum than females averaging 51.6 mm (SD: 2.1 mm) compared to 49.6 mm (SD: 2.5 mm). This difference was not significant ($p>0.05$) (Table 2).

The mean diameter along the x y and z axes of the fitted ellipsoid were: x axis 56.4 mm (standard deviation (S.D) of 6.2 mm, range 47.3 mm to 74.7 mm); y axis 57.2 mm (standard deviation (S.D) of 6.8 mm, range 47.7 mm to 77.1 mm) and for the z axis the average radius was 70.0 mm (standard deviation (S.D) of 16.8 mm, range 47.7 mm to 90.2 mm). The difference between the x and z and y and z axes were significant ($p<0.05$) (Table 2).

Male and female x and y ellipsoid diameters were similar averaging 56.2 mm (SD: 3.0 mm) compared to 56.4 mm (SD: 8.0 mm) in the x axis and 57.0 mm (SD: 3.0 mm) compared to 57.2 mm (SD: 8.8 mm) in the y axis. There was a greater difference in the z axis in which the males average was 70.0 mm (SD: 8.2 mm) compared to the female average which was 68.2 mm (SD: 18.4 mm). These gender differences were not significant ($p>0.05$).

The mean deviation of all surface points from the best-fit sphere and ellipsoid surface was 1.3 mm (SD: 0.3 mm) and 0.4 mm (SD: 0.2 mm) respectively. This decrease in deviation was significantly different.

The results for the lengths and angles between the selected points for both the sphere and ellipsoid analyses are shown in (Table 4). In both cases the only angle larger than 90 ° was the cartilage width angle. Three acetabulae were excluded from each study as the notch width and angle through the central axes as the notch did not extend past the sphere centre; these were all females.

Both analyses demonstrated a difference between the mean notch opening length and the notch width through the centre but this was not significantly different (Sphere $p = 0.40$, Ellipsoid $p = 0.84$). In both cases the mean notch width and angle at a distance away from the centre equal to a quarter and half of the overall notch height were both significantly larger than the mean notch width through the centre ($p<0.05$) and the notch opening length ($p<0.05$) (Table 4). The width geometry calculated for the best-fit sphere were calculated on average to be smaller than the best-fit ellipsoid (Figure 30), although these differences were not significant ($p>0.05$). The calculated angles and notch heights for the best-fit sphere and ellipsoid were all significantly different (Figure 30 and Figure 31).

Males exhibited larger width dimensions than the female group, for both the sphere and ellipsoid analyses (Figure 32, Figure 33). For the best-fit sphere analysis these were all significantly difference except the cartilage width and notch height (Figure 32a, Figure 33a). However, only the notch width at half the notch height was significantly different for the best-fit ellipsoid (Figure 32b, Figure 33b). Females exhibit longer notches than males for both analyses however the difference was not significant.

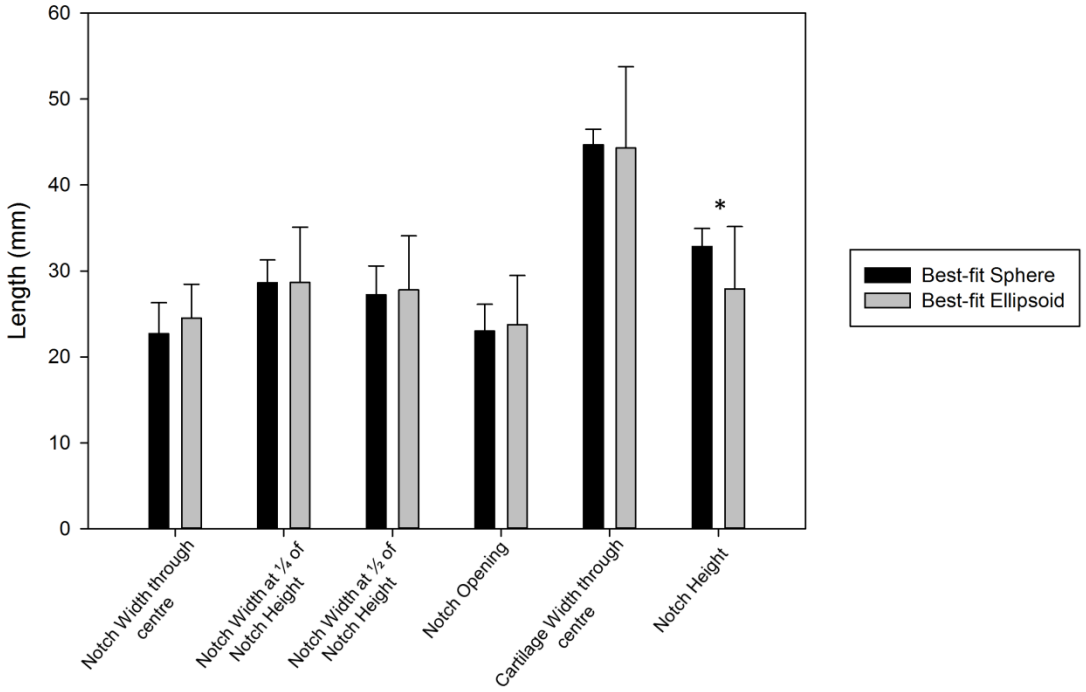

Figure 30: Mean Acetabulum dimensions between six points for best-fit sphere and ellipsoid, (* indicates significant difference between values)

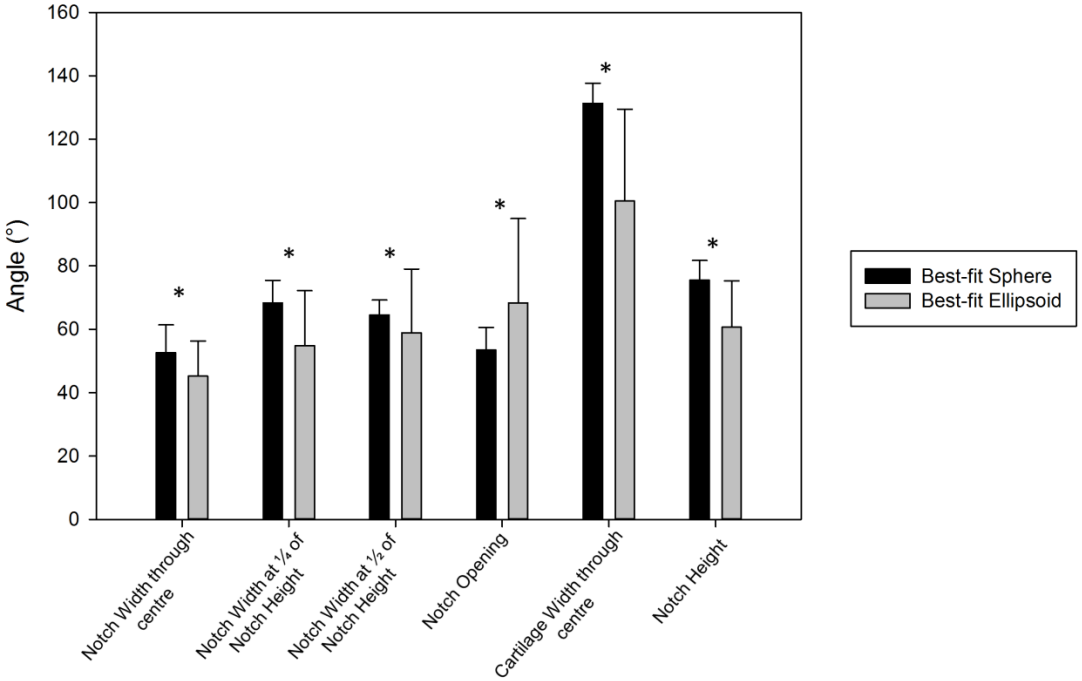

Figure 31: Mean Acetabulum Angles between six points for best-fit sphere and ellipsoid, (* indicates significant difference between values)

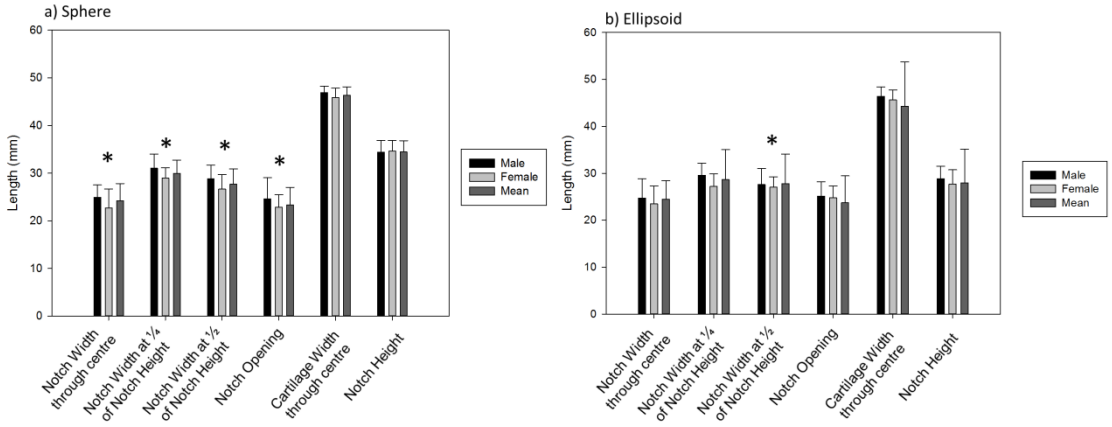

Figure 32: Width between chosen points in acetabulum of best-fit sphere (a) and best-fit ellipsoid (b). Overall mean and mean male and female are compared. (* indicates significant difference between values)

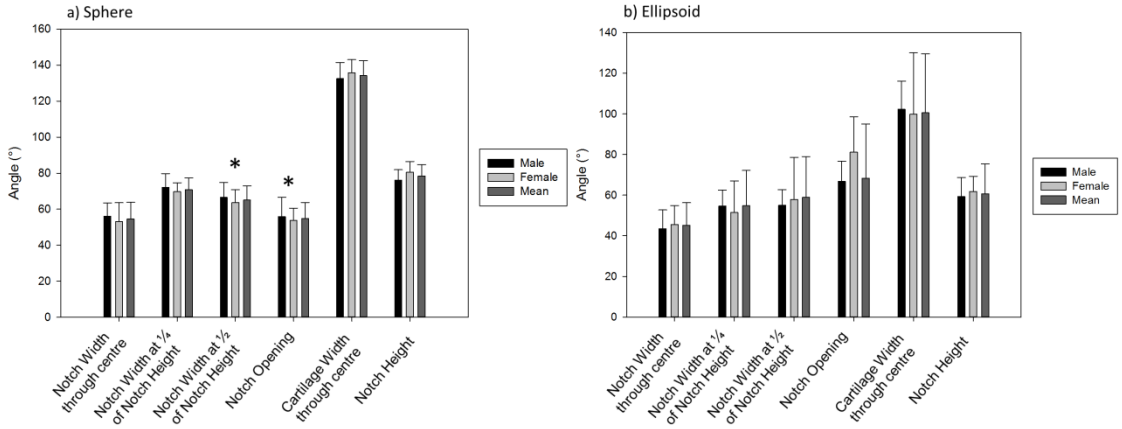

Figure 33: Angles between chosen points in acetabulum of best-fit sphere (a) and best-fit ellipsoid (b). Overall mean and mean male and female are compared. (* indicates significant difference between values)

Table 2: Mean diameter of best-fit sphere and ellipsoid and comparison between male and female.

	Axes	Mean best-fit sphere diameter (mm)	Mean best-fit ellipsoid diameter (mm)
Mean	x	50.7 ± 2.5	56.4 ± 6.2
	y		57.2 ± 6.8
	z		70.0 ± 16.8
Males	x	51.6 ± 2.1	56.2 ± 3.0
	y		57.0 ± 3.0
	z		70.0 ± 8.2
Females	x	49.6 ± 2.5	56.4 ± 8.0
	y		57.2 ± 8.8
	z		68.2 ± 18.4

Table 3: Mean calculated values for acetabulum points fitted with best-fit sphere and ellipsoid.

Acetabulum Points	Best-fit Sphere		Best-fit Ellipsoid	
	Length between points (mm)	Angle (°)	Length between points (mm)	Angle (°)
1-3	23.0 ± 3.1	53.5 ± 7.0	23.8 ± 5.7	68.3 ± 26.6
2-8	32.8 ± 2.1	75.6 ± 6.2	29.3 ± 3.0	78.4 ± 9.4
4-7	44.7 ± 1.8	131.3 ± 6.4	44.3 ± 9.4	97.6 ± 31.6
5-6	22.7 ± 3.6	52.6 ± 8.8	24.5 ± 3.9	45.2 ± 11.1
9-10	28.7 ± 2.6	68.3 ± 7.1	28.7 ± 6.4	54.8 ± 17.4
11-12	27.2 ± 3.7	64.6 ± 7.7	27.8 ± 6.3	58.9 ± 20.1

Discussion

Characterisation of the articular cartilage was one of the main focuses of this investigation due to the indication that cartilage formation and shape is related to the contact stresses across a joint (146, 147). It was hypothesised that if this shape could be determined then a more biomechanically compliant component could be designed which would aim to more naturally load the acetabulum; a key objective of Aurora Medical Ltd. Further to this, and based on existing techniques (12, 140-142), two shape fitting techniques (sphere and ellipsoid) were employed to determine whether the acetabular geometry varies with gender. Both techniques allowed the horseshoe shape of the acetabulum to be exposed, but it was clear that the ellipse fitted more closely to the data: firstly the ellipsoid had more points located closer to its surface than the sphere. Secondly, the ellipsoid radii along the x and y principle axes were similar with an average difference of 0.6 mm. However, the radius along the z-axis was significantly larger than the other axes which confirmed the suggested non-spherical nature of the acetabulum. The relationship obtained between the ellipsoid radii proposes that the acetabulum roughly fits a prolate spheroid as the polar axis (z-axis) is greater than the equatorial diameter (x & y axes).

The height, width and corresponding angle measurements revealed new information relating to the acetabular notch morphology and highlighted differences between fitting a sphere and an ellipsoid to the data. For each analysis, regardless of gender, the notch opening width and the width through the centre of the sphere/ellipsoid were not significantly different. Instead the width increased to a maximum at a distance approximately a quarter of the notch height below the best-fit shape centre. This equated to a subtended angle of 16.7 ° +/-1.6 ° and 19.7 ° +/-1.5 ° in front of the ellipsoid and sphere centre respectively. This is consistent with the study by Oberländer & Kurrat (179) which concluded that the widest region of the notch was about 15 ° degrees away from the acetabular roof.

The significant differences between the geometry obtained from fitting an ellipsoid and a sphere were observed when assessing the notch height and angles between points. The

height of the notch was on average larger for the sphere fit which may be attributed to the sphere fitting technique removing more data points from the acetabular notch near the pole of the acetabulum. The angles are generally smaller for the ellipsoid than for the sphere due to the larger z-radius of the ellipsoid. This means the centre of the ellipsoid is located further away (along the z axes) from the pole of the acetabulum compared to the sphere's centre location. This difference does not significantly affect width calculations due to similarities in x and y centre coordinates of the ellipsoid and sphere. However, for accurate angle calculations which reference to the centre of an ellipsoid should be fitted to the acetabulum morphology.

The implications of these findings are relevant for the design of acetabular components for a number of reasons. Firstly, the ellipsoid nature of the articular surface could imply the kinematics of the hip joint may be more complex than purely rotational motion exhibited by a ball-and-socket joint. Secondly, the determination that the ellipsoid centre is further away from the articular surface than previously suggested by the sphere could have implications on joint replacements. It is critical for the hip centre to be correctly reconstructed after a replacement in order to restore the normal biomechanics of the joint and avoid impingement between the proximal femur or femoral component (109). Based on these findings the traditional ball-and-socket replacement joint may need to be updated to ensure correct joint biomechanics are achieved, however this is a suggestion and requires further investigation.

The influence of gender on acetabulum morphology was also explored in this study. The study showed that males exhibited larger acetabulae than females when fitted with a sphere and ellipsoid. Although this result was not statistically significant, similar sphere fitting studies (140, 180) have shown a significant difference between genders. In addition to acetabulum size, both the sphere and ellipsoid analyses observed differences to suggest males exhibit wider, shorter and deeper acetabular notches. All differences were significant for the best-fit sphere except the cartilage width and notch height. However, only the notch width at half the notch height was significantly different for the best-fit ellipsoid. Köhnlein et al. (2009) (142) reported wider notches in females, however our data correlates with that of Oberländer & Kurrat (1978) (179) which suggests no gender dependency enabling an average acetabulum to be calculated. The difference in outcomes between this study and similar acetabulum morphology studies (140, 142, 180) could be attributed to a number of factors. Firstly, this study adopted a computational approach for measurement whereas Köhnlein et al. (2009) (142) used manual measurement techniques. Secondly, different centres were used to obtain moulds and no patient ethnicity details could be obtained for the specimens used in this study (although 84% of the centre's donors are of German nationality (181)). Previous morphological studies have shown that ethnicity affects anthropometric dimensions (182-184). Similar sphere fitting studies have been conducted on Caucasian, Afro-Caribbean (180) and western European donors (140, 142) although the latter were obtained from archaeological sites and the actual ethnicity can only be presumed. An

extension of this work would be to conduct a repeat of this investigation on acetabulae of known ethnicity to assess this relationship.

Although the gender study established a difference between acetabulum size, no significant difference between male and female acetabulum cartilage geometry was established for the ellipsoid study. This supports the use of acetabulum models in anatomical studies that exhibit average notch geometries for a given acetabulum size regardless of gender.

The determination of the outline of the acetabular notch in this study was useful for the development of novel horseshoe shaped components (68, 102) which aim to more effectively load the acetabular structures (64). Studies on the MITCH PCR cup (67, 68) have illustrated that the cup loaded the acetabulum more effectively and without pole contact compared to the hemispherical design. This was partly due to the material which exhibited a modulus closer to bone, however it was also due to the design restricting the areas of bone through which load was transferred. The horseshoe shape ensured load was transferred onto the cranial region of the acetabulum, the posterior-inferior region at the ischial facet and the anterior region, each an area outside of the acetabular notch. Although the studies assessed load transfer in the acetabulum they did not quantify the horseshoe shape which was the basis of their biomechanically compliant implant. The reasons for the inclusion of a raised horseshoe section in the CFRPEEK component developed in this thesis follows the rationale previously described for the MITCH component, although the component would take on a full hemispherical shape to provide additional component stiffness. It has been shown that the notch's geometry contributes to a more uniform articular contact stress distribution over the horseshoe section (148) but its size and shape can shift the stress pole and increase the peak contact stress in the joint if not correctly determined. This study provided the necessary details to allow the preliminary design shown in Figure 27 to be updated based on the data obtained from characterising the shape of the articular surface. Figure 34 shows that the original bearing surface design had a cut out section which contained a circular region that did not extend bearing centre with a small parallel opening at the rim. Based on the outcomes of this study, the original design was not deemed to mimic the natural geometry and the bearing surface was updated to possess a cut out section with two parallel sides joined with a semi-circular feature (Figure 34). The distance between the parallel sides was determined from the notch width measurements taken in this study in relation to bearing size. Unlike the original design the cut out section extends past the bearing centre of the cup which was determined by examining Dimensions 2 & 8 in Figure 29 which allowed the overall height of the notch to be obtained.

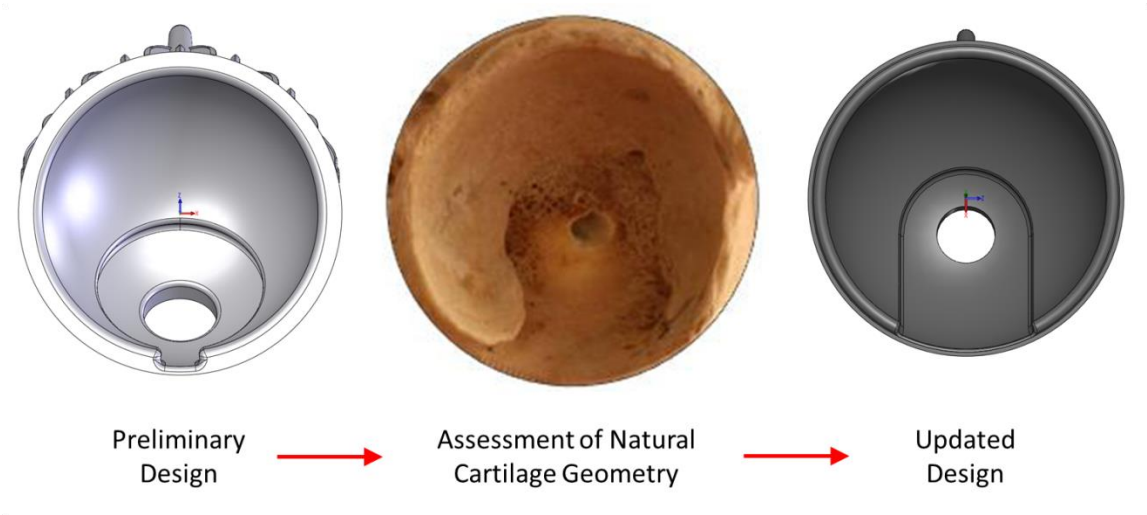

Figure 34: Determination of the bearing geometry (right) from alterations made to the original bearing geometry (left) through the assessment of the natural cartilage geometry in this investigation.

The study and the results must be interpreted with consideration of their strengths and limitations. The plaster moulding technique was adopted in this study as it was considered the gold standard in orthodontic treatment due to its high accuracy and reliability (142). This was reflected by the results of the repeatability analysis performed in this study. In addition the study was carried out by one observer who performed the mould preparation and conducted the computational analysis, eliminating interobserver effects.

A novel aspect of this investigation was applying both spherical and ellipsoid geometries to the acetabulum surface and using vectors to calculate the angles and corresponding lengths. Each vector referenced the best-fit ellipsoid or sphere centre which compensated for any difference in mould orientation during scanning.

The number and form of the acetabulae used in this study limits the strength of the relationships obtained as data was ignored for the acetabular cup groups that contained one sample e.g. extreme sizes. A larger cohort should avoid this limitation and generate results over a larger size range. With sufficient input samples, statistical shape modelling (SSM) and principal component analysis (PCA) could be applied to the current data set (185-187) for further analysis. The repeatability of the plaster cast method was analysed, concluding a small amount of variation which could be due to the operator. Nevertheless, comparative studies have suggested no differences between computer-guided and manual measures (188). A factor which was not investigated in this study was the effect of the number of digitalised points taken over the surface of the plaster mould. In this study a spacing of 0.33 mm was selected between points and it is suggested that a smaller spacing between points could improve the accuracy of the results. An extension of this work would be to conduct a repeat of this investigation and varying the number of points on the surface of the mould.

Shrinkage of bone during the drying process has been identified in a number of studies on the skull (189), femur (190), radius and ulna (191). It is possible that the dry acetabulae used in this study contracted during the drying process, but there is precedence for the use of dry bones for acetabular analysis (140, 142), and if shrinkage is relatively uniform, the relative anatomic trends observed in this study would still hold.

In addition to aiding implant design it has been suggested that characterising the acetabulum cartilage morphology could aid cartilage regeneration techniques (192). Current methods are limited by availability of donor tissue sources, donor site morbidity and prolonged rehabilitation times. Therefore second-generation tissue-engineered cartilaginous constructs which match the complex surface geometries of larger articular cartilage defects have been suggested to improve healing (192). Recently the hip has been suggested as a potential site for biologic resurfacing using shaped cartilaginous constructs in which a concave impression would be used to reconstruct the degenerated acetabulum (193). The main complication is that any surface incongruity between these grafts and the surrounding native cartilage surface has been shown to result in local mechanical stresses that may be unfavourable to the success of the graft treatment. Therefore the graft must be anatomically shaped (192, 193) and based on quantified geometrical data of the hip joint in order to promote their success. In conjunction with cartilage thickness studies, the methodology outlining the acetabular notch described in this study could be extended to surface models generated from medical images to provide the geometrical data required to produce more anatomically shaped constructs.

In conclusion this study has confirmed that while the sphere fitting technique can be used to calculate distances between points in the acetabulum, the best-fit ellipsoid improved characterisation of the acetabulum geometry. This analysis established relationships between the acetabulum geometry and supports the use of acetabulum models in anatomical studies that exhibit average notch geometries regardless of gender. The study also characterised the outline of the acetabular notch allowing the bearing surface of the CFRPEEK component to be updated to reflect the natural geometry. With the basic geometry of the prototype component determined the next stage of analysis relates to the injection moulding process which will be used to produce the component.

3.2 Study 2: Component Manufacturing

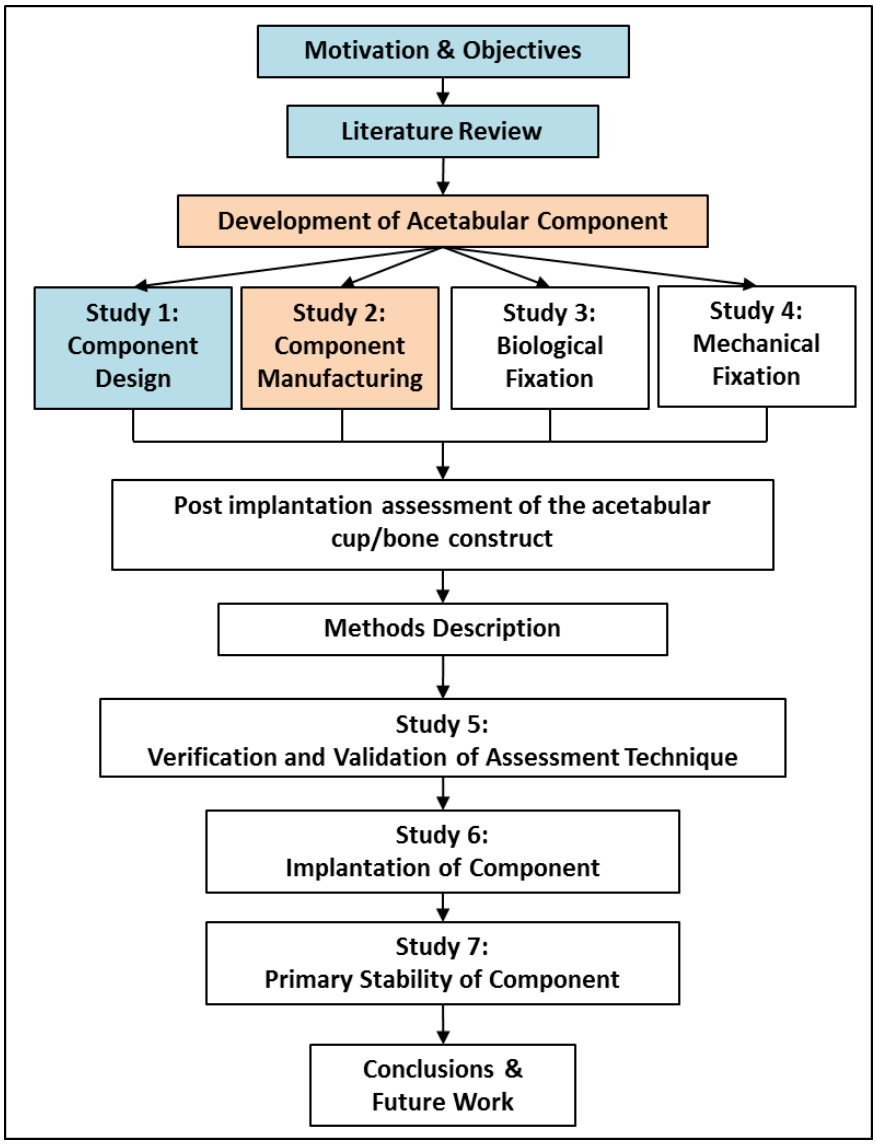

3.2.1 Effect of the injection moulding process on fibre orientation on CFRPEEK

A novel ceramic-on-CFRPEEK bearing combination has been identified by Aurora Medical Ltd to address the limitations of current devices highlighted in Section 2.3.3. Existing large diameter bearing acetabular cups can be made from CoCrMo; however cases of patient sensitivity to metallic ions and component loosening have led to alternative biomaterials being investigated.

The overview of CFRPEEK in Section 2.4.2 indicated its suitability for use as a large diameter bearing acetabular component, with the CFRPEEK MITCH PCR component currently undergoing clinical trials (104). The addition of fibres into the PEEK matrix enhances the mechanical properties and wear resistance of the material as highlighted in Section 2.4.2. However, this section also described how the injection moulding process can influence these properties by altering fibre distribution and orientation but also by introducing defects such as voids. Certain parameters such as pressure, temperature and time of moulding can be

controlled to minimise defect population and optimise material properties but certain aspects such as fibre orientation and distribution are more difficult to control.

Fibre distribution is important as an inhomogeneous distribution of the fibres within the matrix can lead to weak resin rich areas and fibre clumping which are susceptible to micro-cracking (85). Fibre orientation is important as it can affect the mechanical and wear properties of a composite, fibres orientated parallel to the load direction have been shown to enhance strength and wear resistance (194-196).

The key injection moulding processing conditions provided by Invibio Biomedical Solutions (79) were outlined in Section 2.4.2.2. A requirement set out by Aurora Medical Ltd was the development of a quick and efficient method for assessing fibre orientation within the moulded components. This would aim to highlight how certain processing conditions such as melt flow, holding pressure and mould design influenced fibre orientation within the acetabular component. This investigation outlines the methods development; applying it to simplified geometry to obtain fibre orientation, which as well as informing Aurora Medical Ltd could also be adopted by Invibio Biomedical Solutions to inform them further on the injection moulding process. There were several objectives to this investigation. The first was to use the polished sections to analyse the internal morphology of the injection moulded specimens in terms of fibre distribution and orientation. In addition the sections were analysed for defects in the form of voids and inclusions. A method to quantify the orientation of the fibres in CFRPEEK injection moulded standard dog-bone specimens was realised that can be used to assess more complex specimens. The method aimed to accurately identify the fibre edges from polished sections by eliminating any areas that compromised the result in order to calculate the orientation of the fibres. The method was improved by applying the inclined section angle technique in order to identify orientation distribution more accurately in the randomly orientated reinforced fibre composite.

Materials & Methods

Specimen Preparation

5 dog-bone shaped CFRPEEK MOTIS specimens (Invibio Biomedical Solutions) with dimensions according to BS EN ISO 527-2:1996 test specimen 1B (4 mm thickness and 10 mm width at the thinnest section were used. Each specimen was cut in the centre of the injection moulded specimen perpendicularly to the direction of melt polymer flow (Figure 35).

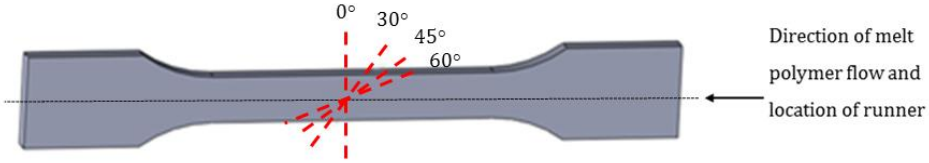

Figure 35: Dog-bone specimen sectioned at 0 °, 30 °, 45 ° and 60 ° for fibre analysis.

A further 9 specimens were cut at 30 °, 45 ° and 60 ° to the direction of melt flow.

The specimens were mounted in cold epoxy resin and polished to a 1 μm finish for microscopy analysis. The polishing procedure exposed the elliptical foot prints left by fibres

cut by the sectioning plane. An InfiniteFocus microscope was used to scan the prepared CFRPEEK specimens, stitching each image together to make a complete reconstruction of the surface (Figure 36).

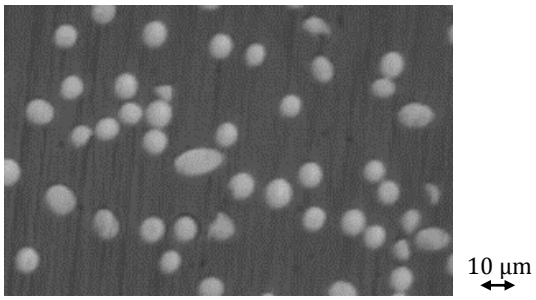

Figure 36: Polished specimen with foot prints of cut fibres.

Characterisation of Fibre Orientation

In components of irregular geometry, the fibre orientation pattern and distribution of fibres is complex and may differ from standard specimens as the influence of shear and extensional flow may vary. Therefore it is necessary to correctly evaluate and account for these differences when testing complex components by finding a suitable method to evaluate standard injection moulded dog-bone shaped specimens.

Short fibres can be analysed by two methods: single or two sections. Single section implies that only in-plane fibre rotations are permitted (197) and they are naturally defined by a single angle. Data can be derived from a polished section of a specimen by reflective microscopy or from microtomed specimens by contact microradiography. A method to describe the 3D orientation of an individual fibre has been suggested by Zhu et al. (1997) (198) and is described by two angles: misalignment (Θ_n) and azimuth (ϕ_n) (Figure 37). Assuming the fibres are smooth and circular in cross-section, a single 2D section through the specimen would produce a series of elliptical footprints on the surface. The *nth* fibre can be represented uniquely by a set of parameters (x_n, y_n, z_n, A_n, d_n, Θ_n, ϕ_n) and is shown in Figure 37 (199).

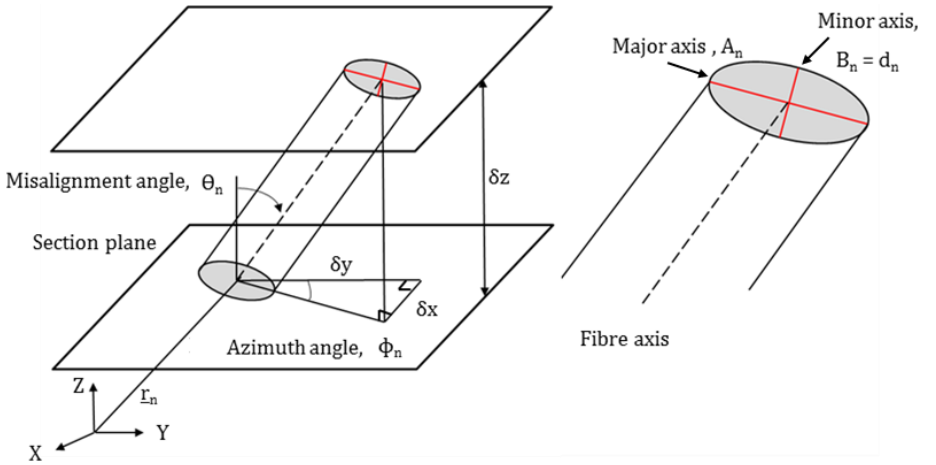

Figure 37: Fibre orientation defined by two angles: Misalignment (ϕ_n) and Azimuth (Θ_n) Adapted from Clarke and Eberhardt (2002) (200).

The elliptical image of the fibre yields estimates of fibre diameter d_i and the orientation angles, Θ_n and ϕ_n. The diameter d_n is equivalent to the minor axis, B of the elliptical image. The azimuth angle ϕ_n, is given by the orientation of the major axis, A of the elliptical image in the XY plane. The x_n, y_n and z_n coordinates locate the fibre at the intersection point of the major and minor axes. The misalignment angle Θ_n between the fibre axis and the direction perpendicular to the cutting plane can be inferred from the eccentricity of the ellipses and the relationship:

$$\boldsymbol{\theta_n = \cos^{-1}\frac{B}{A}} \quad [2]$$

Where A is the major radius and B is the minor radius of the ellipse. Equation [2] is generated when converting polar coordinates to Cartesian coordinate by trigonometric functions sine and cosine. This value can range between 0-90 ° to the section plane if 0 ° is considered along the z-axis. The second angle refers to the rotation about the section-plane, or azimuth angle ϕ_n and is defined by the direction of the major axis of the ellipse. This angle can have values between -90 and 90 ° if 0 ° is considered to be along the y-axis.

The single-section method has limitations; the main being the existence of two equally possible alternative orientations for each elliptical cross section i.e. the orientation duality problem and the second is the near-zero bias introduced by elliptical footprints that are nearly circular.

The orientation duality problem is illustrated in Figure 38 in which two fibres possess the same misalignment angle Θ_n but differing azimuth angles due to the elliptical footprint possessing the same major and minor axes.

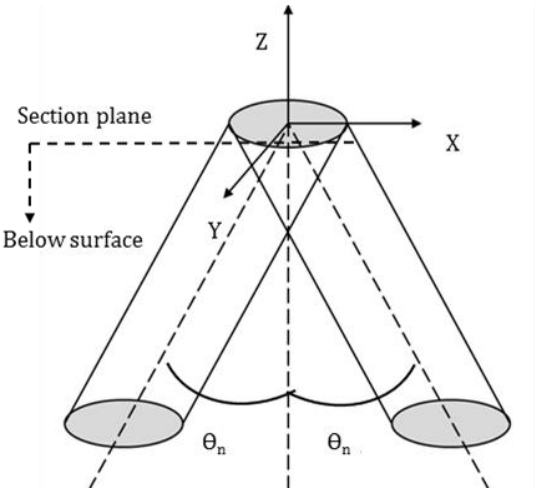

Figure 38: Two possible fibre orientations based on the same elliptical cross-section. Adapted from Davidson et al. (1997) (201).

The orientation duality problem can be overcome by successive sectioning (197), combining data from two or three orthogonal plane sections. This technique requires an adequate fibre length to allow sections 1/10th of the fibre length apart to be achieved. This separation distance is a empirically determined number which was found to be a reasonable compromise between two conflicting requirements (197): a small distance between sections

decreases the accuracy of the estimate, whereas in a large separation distance too few fibres will be crossing both section planes. Only a few studies have used successive sectioning as the experimental implementation is practically difficult and time consuming meaning other more favourable techniques including confocal scanning laser microscopy and X-ray have been used.

The second limitation introduced by nearly circular ellipse footprints exists due to the significant bias and noise sensitivity in the estimation of the near-zero misalignment angles. This bias causes consistent errors in the misalignment angle estimates due to noisy observations which make it difficult to correctly select the major and minor radii of the nearly circular ellipses. By choosing the smaller measured radius as the minor radii undercounting of fibres occurs when determining Θ_n at very small angles.

A section taken perpendicularly to the flow direction through a randomly orientated composite will display more fibres that are perpendicular to the section than those that are parallel. Therefore the section is more likely to intersect a fibre with a large misalignment angle. Consequently a count of the number of fibres using the major axis A will be biased towards counting fibres at large values of Θ_n more frequently than fibres with small of Θ_n (202). A number of investigators (201, 203) have suggested taking sections at a range of angles to the flow direction to reduce amount of near circular ellipses, consequently reducing the near-zero bias. These sections are then mathematically transformed back to the original reference plane, which is perpendicular to the main fibre direction to calculate the misalignment angle.

For a section y' taken at an angle to the Z axis, Figure 39 describes the angle between the normal to the sectioned surface z' and the z axis as α. The orientation angles (ϕ_n, Θ_n) will require a transformation to give the true values of Θ and ϕ with respect to the XYZ axes.

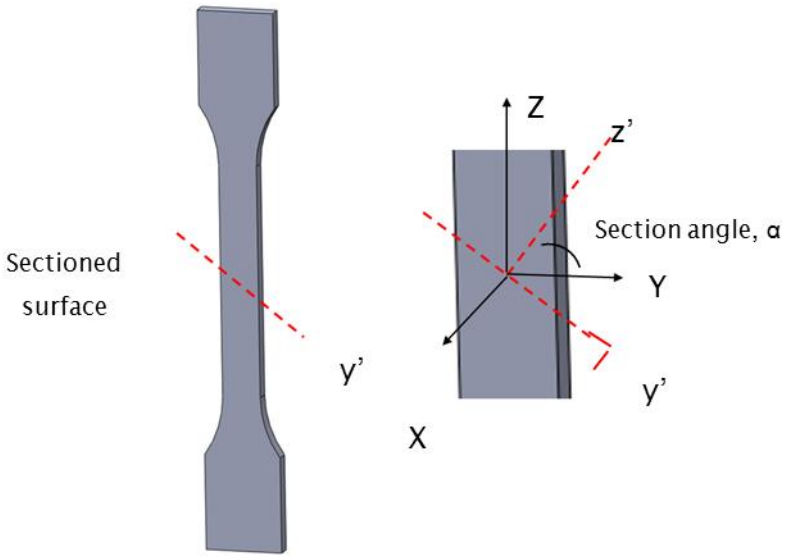

Figure 39: Definition of the section angle α to calculate the true value of the orientation angles Θ and ϕ.

The section is mathematically transformed back to the reference plane which is perpendicular to the main fibre orientation direction. The appropriate transformation equations are in equation [3] and [4] the reader is directed to Diebel (2006) (204) for their derivations.

$$\boldsymbol{\theta} = \mathbf{cos^{-1}}(\mathbf{sin}\,\boldsymbol{\alpha}\,\mathbf{sin}\,\boldsymbol{\theta_n}\,\mathbf{sin}\,\phi_n + \mathbf{cos}\,\boldsymbol{\alpha}\,\mathbf{cos}\,\boldsymbol{\theta_n}) \quad [3]$$

$$\phi = \mathbf{tan^{-1}}\,\frac{(\mathbf{cos}\,\boldsymbol{\alpha}\,\mathbf{sin}\,\boldsymbol{\theta_n}\,\mathbf{sin}\,\phi_n - \mathbf{sin}\,\boldsymbol{\alpha}\,\mathbf{cos}\,\boldsymbol{\theta_n})}{\mathbf{sin}\,\boldsymbol{\theta_n}\,\mathbf{cos}\,\phi_n} \quad [4]$$

The study by Hine et al. (1993) (203) implemented this technique and assessed the improvement in the near bias error by observing the fibre orientation using specimens that were taken at 0 °, 30 °, 45 ° and 60 ° to the flow direction. The study concluded a 5 % error for a near circular image (i.e. Θ_n~0) in the ratio of B/A which was improved to 3 % by taking sections at a 45 ° angle to the flow direction.

Although the error in the misalignment angle is shown to decrease by altering the section angle, the technique is a one sectional approach meaning the 180 ° ambiguity problem will still be present. In addition, the study by Hine et al. (1993) (203) was performed on a well aligned short fibre composite and the degree of improvement is unknown for a randomly orientated composite such as CFRPEEK.

Orientation Measurement

A MATLAB code was written to process each image and calculate the fibre misalignment distributions. To be compatible with MATLAB's vector solving ability the image was converted to binary and a median filter applied to reduce 'salt and pepper' noise. Pixels within a fibre image are white and were assigned a value '1', black pixels are the matrix and were assigned a value of '0' (Figure 40). Image segmentation using the watershed feature identified the contours provided by the fibres against the black background. Each fibre was located within the image by a process called pixel connectivity, where groups of pixels were 'grown' until all the pixels within the object had been added to the group.

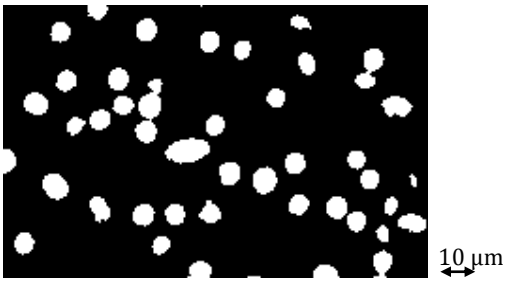

Figure 40: Image is converted to binary (Left) which changes the fibres to white.

To fit an ellipse around each fibre, MATLAB's second moment of inertia measurement technique was employed (205). The second moments were used to find an equivalent ellipse to each fibre and were plotted onto the outline of each fibre as shown in Figure 41.

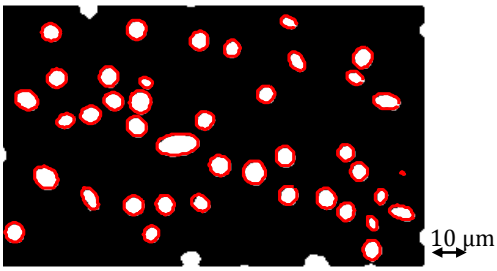

Figure 41: Image Segmentation identifies the contour and ellipses are plotted onto the outline of each fibre.

The orientations of the fibres were then calculated using equation [2] or [3] depending on the angle at which the section was taken from the flow direction.

The second moment technique considered all the pixels within the object in order to calculate the major and minor axes, azimuth angle, eccentricity and the x and y coordinates of each ellipse centre (Figure 41). However, the technique relied on the fibres having a circular cross section which were not always present.

To improve the accuracy of the MATLAB programme a filter was applied to clumped fibres, which the MATLAB programme was unable to separate during the threshold process. It was assumed that the inclusion of such data would give a false conclusion and therefore should be eliminated from the study. To remove unwanted fibres the accuracy of the elliptical fit to the original fibre image data was recorded. This parameter is called the 'fit factor F_f' and has been incorporated into similar studies (200, 206) to evaluate the quality of the elliptical fit to the original pixel area. The fit factor is defined by equation [5] (206).

$$\boldsymbol{F_f = \frac{Pixel\ Area}{\pi AB}} \qquad [5]$$

where A is the major axis and B is the minor axis.

The fit factor improves the performance of the second moment technique by filtering the data to remove the fitted ellipses that possess the most deviation from the area calculated by MATLAB. If $F_f \approx 1$ the object (fibre) is highly elliptical and has the same area as its fitted ellipse. If $F_f << 1$, the fibre cross section is irregular and the fitted shape is dissimilar to an ellipse. This usually symbolises an area where the MATLAB programme cannot fit an ellipse around an individual fibre due to it being in contact with another fibre or that the fibre itself is non-elliptical. The effect of altering the fit factor threshold on the misalignment angle and the method of identifying the critical threshold value to apply to this study was addressed in Investigation A. The application of the critical threshold value was then applied to calculate the misalignment angle distributions for the angled sections in Investigation B.

An overview of each investigation and the method is described below.

Investigation A: Determination of Fit Factor Threshold

To determine the appropriate fit factor threshold, the fit factor equation (equation [5]) was integrated into the MATLAB programme which selected the ellipses depending on the

accuracy of the fit around the fibre. Firstly the 0 ° sections were analysed and the threshold was altered between 0.30 and 1.000 to calculate the number of fibres above the threshold value. Any fibre fitted with an ellipse below the fit factor was eliminated. The number of fibres at each threshold was recorded and a graph was plotted accordingly.

Investigation B: Effect of Section Angle on Misalignment Angle Distribution.

The same method was applied to fit ellipses to the sections cut at 30 °, 45 ° and 60 °, ellipses with the fit factor found in Investigation A (<0.909) were removed from the analysis. The misalignment angle of the fibres was calculated using equation [5] and the fibres were put into groups of 10 ° degree increments and graphs plotted accordingly. Attempts were made to produce second sections at a distance $1/10^{th}$ of the fibres length (≤15 μm) from the first; however complications such as inaccuracy in the separation distance between the first and second section due to the polishing equipment resulted in only one section being taken. The consequences of using one section are outlined in the discussion section.

Fibre Distribution and Defect Characterisation

Image processing was used to assess fibre distribution and identify voids and inclusions in the polished sections. Areas of fibre clumping were identified using the fit factor described previously as the MATLAB programme was unable to separate fibres during the threshold process. Voids were identified prior to thresholding as black regions present on the polished section. Inclusions were identified from ellipses with dimensions that were larger than the carbon fibres.

Results:

Identification of fibre distribution, void content and inclusion in injection moulded CFRPEEK specimens.

Figure 42 illustrates the typical fibre distribution for sections taken at an angle of 0 and 60 ° to the flow direction. It can be seen that the distribution is fairly homogeneous but there are small resin rich and fibre dense regions as highlighted by the black and red circles.

Figure 43 shows inclusions within the injection moulded specimens; these were randomly located in the material. Figure 44 identifies that voids were present in the injection moulded components. From the 9 specimens analysed, voids were present in 3 of the specimens.

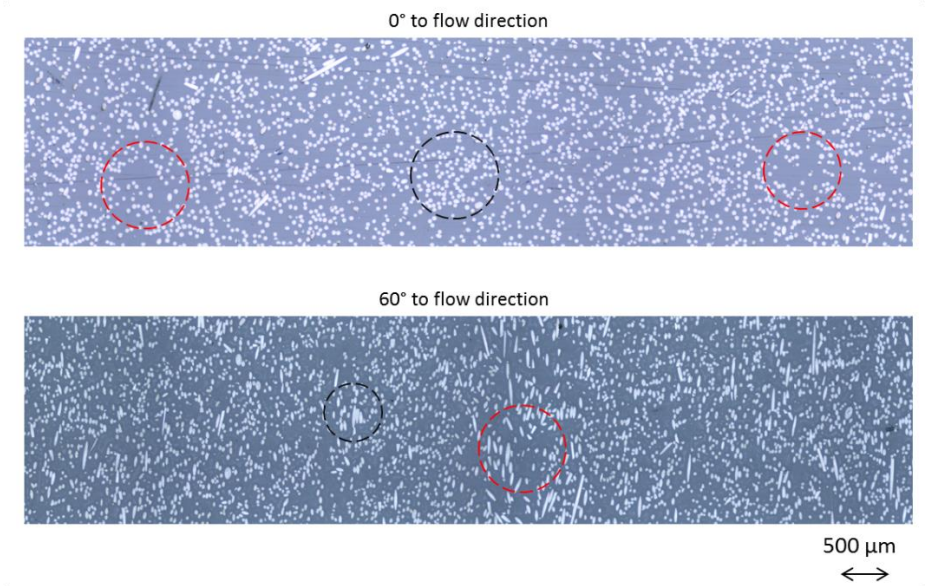

Figure 42: Typical fibre distribution observed in the injection moulded CFRPEEK dog-bone specimens. Red circles indicate resin rich regions whilst the black circle shows a region dominated by fibre presence.

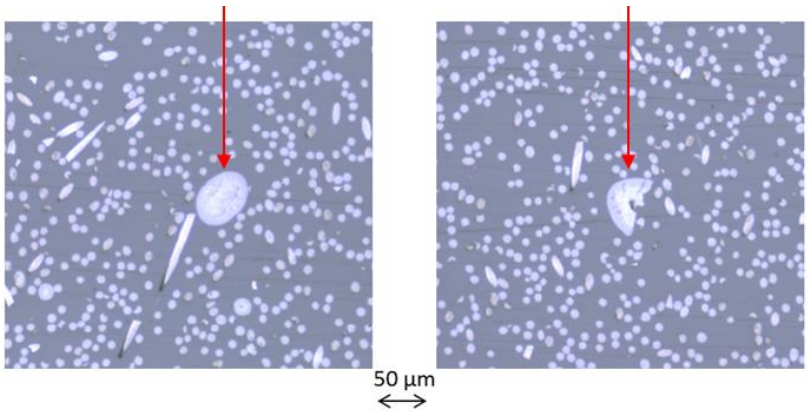

Figure 43: Inclusions present in the injection moulded CFRPEEK dog-bone specimens.

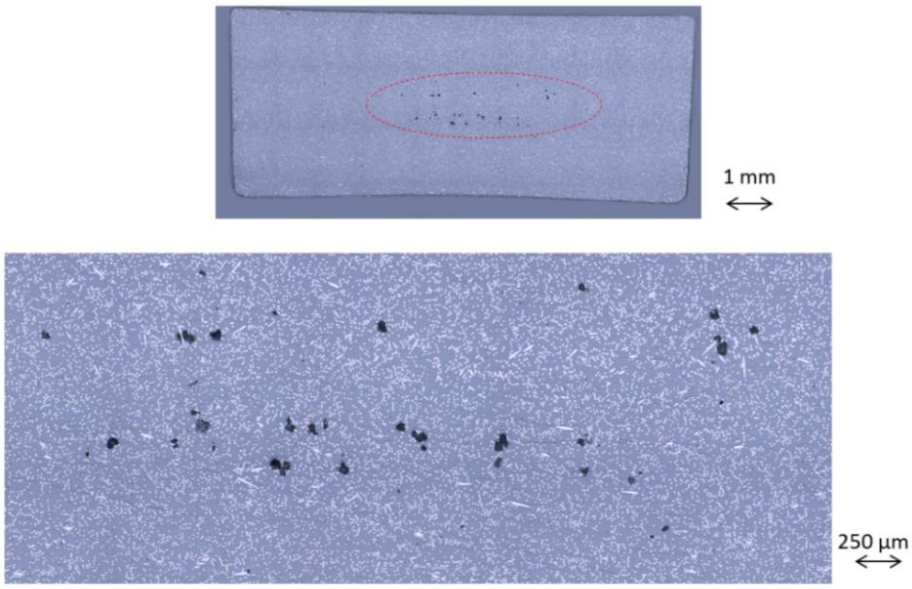

Figure 44: A section through the injection moulded CFRPEEK dog-bone specimens shows the presence of voids and warped edges.

Investigation A: Determination of Fit Factor Threshold

Figure 45 shows the effect of varying the fit factor on the number of fibres selected for orientation analysis. It is evident that there was an inverse relationship between the number of fibres selected and the accuracy of the ellipse fit. The graph shows that the number of fibre selected dramatically decreased above a fit factor of 0.800 with no fibres selected at a value of 0.999.

Figure 46, Figure 47 and Figure 48 show the ellipse fitting procedure with decreasing accuracy. Figure 46 used a strict fit factor (0.995) highlighting that only a small percentage of fibres were selected and these were generally orientated perpendicularly to the section surface. The number of fibres included in the analysis significantly increases when a fit factor of 0.909 is applied (Figure 47). This value incorporated fibres orientated parallel to the section's surface but avoided selecting clumped fibres. Figure 48 shows the section analysed with a fit factor of 0.800 where 99 % of the fibres were selected. As well as including the fibres seen in Figure 46 and Figure 47, ellipses were also fitted around clumps of fibres. These poorly fitted ellipses introduced false readings in the analysis and therefore a fit factor equal to or below 0.800 was unacceptable for an accurate analysis.

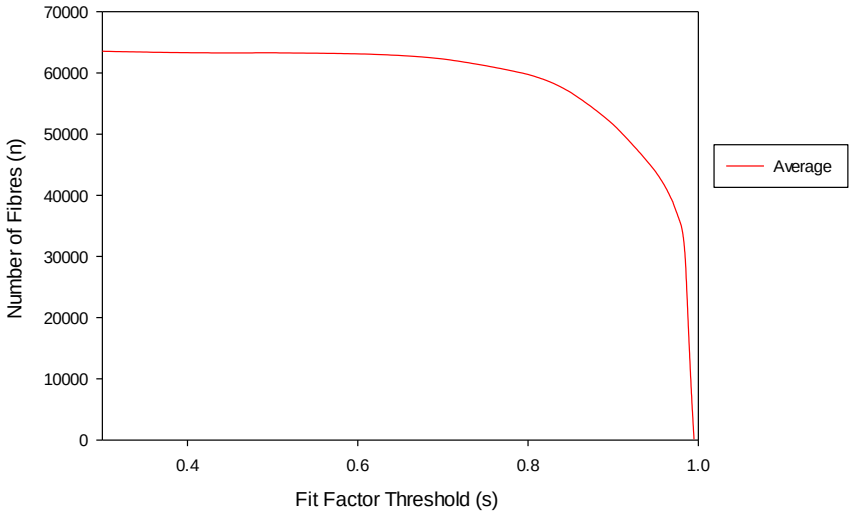

Figure 45: Number of fibres versus fit factor threshold.

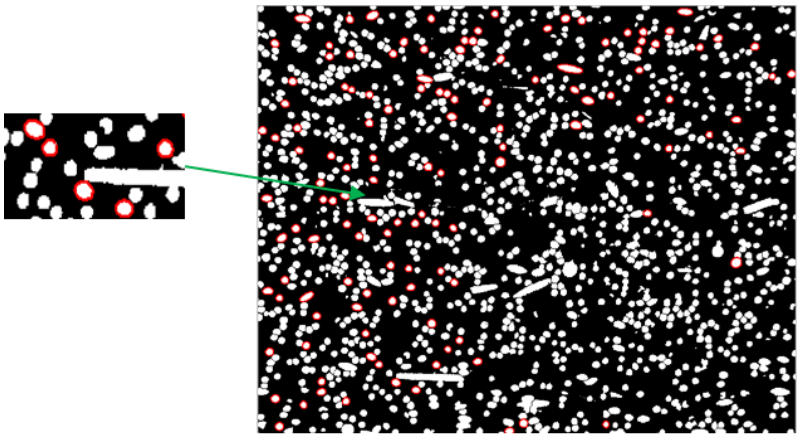

Figure 46: Fit factor 0.995 analysing 10 % of all fibres in section which possess a close fit between the fitted ellipse and fibre area.

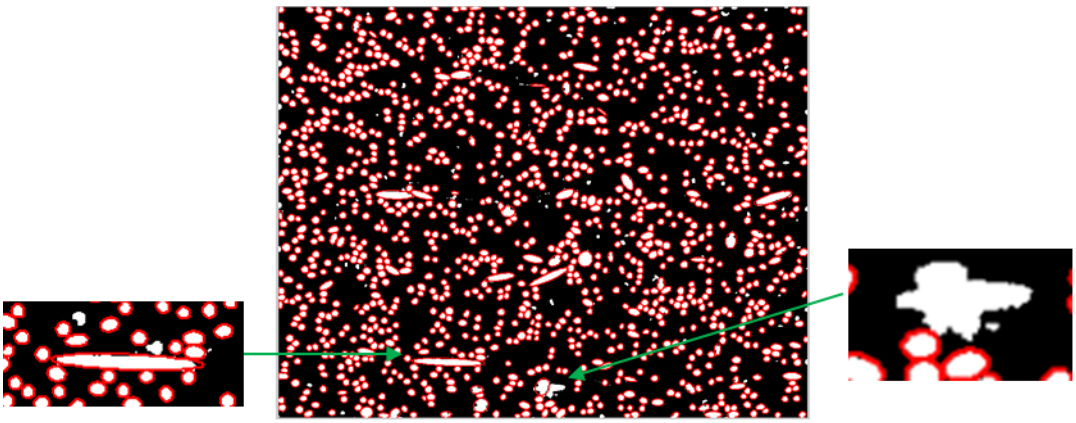

Figure 47: Fit Factor 0.909 analysing 94 % of all fibres in section.

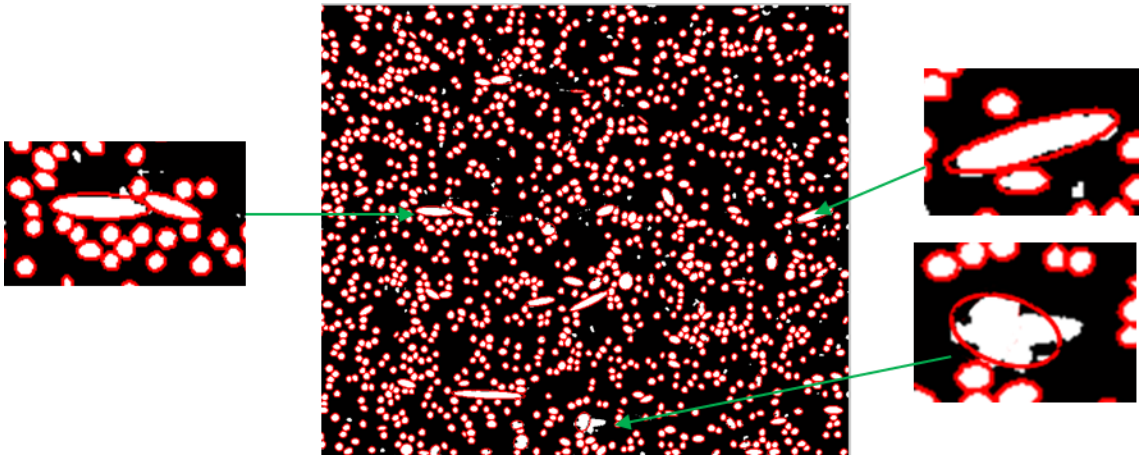

Figure 48: Fit Factor 0.800 analysing 99 % of all fibres in section which has introduced fibres with poor fitting ellipses.

Investigation B: Effect of Section Angle on Misalignment Angle Distribution.

Figure 49 shows the effect of altering the section angle on the fibre misalignment distributions calculated. The red vertical lines show the angle where the majority of the fibres were orientated.

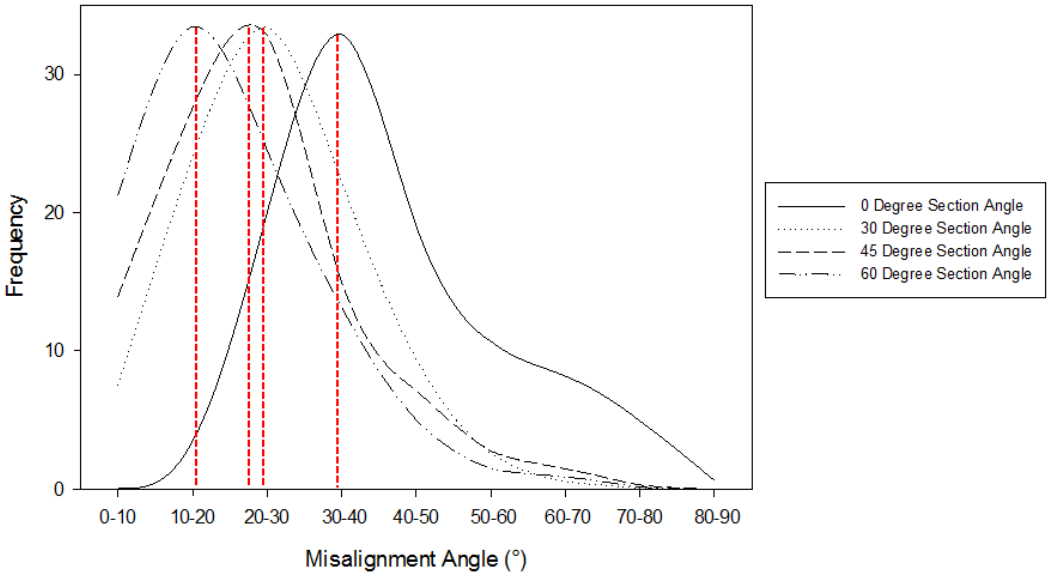

Figure 49: The effect of the section angle α on the misalignment distributions with a fit factor of 0.909 applied.

Discussion

Micrographs from the polished surfaces of the injection moulded CFRPEEK specimens showed the fibre distribution was fairly homogeneous with only minimal amounts of fibre clumping and resin rich areas (Figure 42). This was a positive outcome as it suggested that the rotation speed of the screw in the barrel was optimum for effective mixing of the fibres within the matrix. It also suggested that the channels from the barrel to the mould were large enough and did not compromise the carbon fibre and PEEK matrix mixture. Although

sections were taken at a range of angles to the flow direction it was difficult to gain a true perspective of the extent of the resin rich areas as each cross section represented the distribution at a particular location. Quantification of fibre distribution was difficult due to the random orientation of the fibres within the component. In unidirectional composites, the distance to the nearest neighbour is used to quantity the distribution and separation of fibres from a cross section taken through the specimen (207, 208). This method has been proven successful for unidirectional composites as it is assumed that there is no significant change in the distance between the fibres throughout the specimens. Although the nearest neighbour method could be used to analyse the distance between short fibres in this material, it may not provide a true indication of the distribution of the fibres as they are randomly orientated and the nearest distance between fibres shown on the polished surface may overestimate this quantity.

A negative finding was the presence of voids and inclusions within the material. Figure 43 shows the types of inclusions that were present in the specimens. From the micrographs it was difficult to determine the nature of the inclusions or where they may have been introduced. These inclusions could be present due to contaminants in the injection moulding equipment e.g. from wear of the screw or inadequate cleaning as it was unknown whether the injection moulding equipment was purged prior to moulding as instructed in the material suppliers guide (79). Inclusions could have also been introduced onto the surface of the material in the grinding process although efforts were made to avoid contamination with new grinding wheels used for each specimen together with washing and drying of the specimens between each grade step. However, a possibility still exists that cross contamination could have occurred. As it was difficult to determine the source of the inclusion it is recommended that a further analysis is conducted where the internal morphology is assessed using an alternative method which does not involve sectioning the material.

It can be seen that voids were present in the centre of the specimen and the bottom edge of the specimen is warped (Figure 44). There was also slight warping to the top edge and these shrinkage effects have caused the cross-section of the dog-bone specimens to take a trapezium outline rather than the intended rectangle. The voids and surface sinking indicate that the injection moulding settings were not optimised for forming this component successfully.

Sink marks form when the outer surface of the part cools too quickly in comparison to the internal section. As the internal section cools its shrinkage pulls the surface of the main wall inwards. Sinking can be avoided by increasing the time and the pressure which is applied after filling the inside of the mould (holding time and pressure) (83). The voids are most likely caused by lack of material in the mould meaning either the holding pressure which was used to pack out the part during the holding time was inadequate or the holding time was not long enough to ensure adequate packing had occurred. Voids were present in 3 out

of the 9 specimens but it cannot be assumed that voids were absent in the other specimens as the section taken may not have exposed voids in a different area of the specimen. Further analysis using μCT could be conducted to determine if these specimens and future samples contain voids.

Figure 45 shows the relationship between the fit threshold and number of fibres recorded for each specimen. The graph showed little variation in evaluated fibres up to a threshold of 0.70. Between threshold values of 0.700 and 0.950 the number of fibres reduced considerably as the requirement for a more accurate fit between the recorded area for the fibre and fitted ellipse increased. This effect is highlighted in Figure 46, Figure 47 and Figure 48 in which the same area is analysed using different threshold values. Figure 46 was evaluated using a very high fit factor of 0.995 and showed that the ellipses fitted must have a nearly identical area to the fibre. Consequently this eliminated a large proportion of the total fibres and left ~ 10 % of the total fibres to be available for the misalignment angle evaluation. It was evident that the ellipses were fitted to fibres that possessed a major and minor axis which were similar, resulting in a small misalignment angle, consequently resulting in the analysis not providing a true representation of the entire fibre orientations.

Figure 47 was processed with a slightly lower threshold (s = 0.909) which introduced a considerably larger number of fibres (~ 94 %). This was due to the fitted ellipses possessing a greater dissimilarity to the fibre outline; nevertheless fibres which could not be separated by the programme and would produce an incorrect misalignment value remained eliminated from the evaluation. A lower threshold of 0.800 introduced 99 % of the total fibres for evaluation and the fibres which have been included are shown in Figure 48. The high proportion of analysed fibres has resulted in the introduction of ellipses that have been fitted around fibre clumps and non-elliptical fibres. These inclusions would reduce the accuracy of the analysis and therefore a threshold of 0.800 or below was considered inappropriate for this study.

The evaluation of a large number of fibres which are assigned ill-fitting ellipses resulted in a misrepresentation of the misalignment angle distribution. Therefore the chosen threshold value should be a compromise between the number of fibres analysed and the amount of error introduced. It is unlikely that a standard fit factor threshold can be used to analyse all composite types due to differences in fibre size, content, alignment and processing method. This study has highlighted that removing ~ 6 % (fit factor 0.909) of the fibres in the section produced the optimum compromise and did not introduce a large degree of error. This percentage of fibres was higher than the study by Hine et al. (1993) (203) and it is assumed that this variance was due to differences in material characteristics and manufacturing methods of the two studies. The study by Hine et al. (1993) (203) analysed a well aligned short fibre reinforced epoxy compared to CFRPEEK investigated in this study which contained randomly orientated fibres. A well aligned composite will only exhibit misalignment angles over a small range (e.g. 0-30 ° (203)) compared to the 0-90 ° angles seen

in CFRPEEK. This could influence the accuracy of the fitted ellipses as Figure 46, Figure 47 and Figure 48 have previously shown, as the programme can more precisely fit ellipses to fibre orientated at low misalignment angles.

The misalignment distributions for all the sections analysed are shown in Figure 49 in which a fit factor of 0.909 was applied. The majority of fibres for 0 ° specimens were aligned between 30-40 ° and as the section angle varied the shape of the distribution sharpens with increasing section angle. This was assumed to indicate a reduction in systemic errors as a result of the reduction in the amount of fibres with a near circular footprint as the section angle increased.

Although the accuracy of the analysis improved with section angle, the misalignment ambiguity problem remained. A two sectional approach has been implemented in other studies (197, 198) where longer fibres were used allowing the section planes to be further apart. Nevertheless, the technique was labour intensive and time consuming due to the preparation of two sections and the computational processing time required to align the two sections. In this investigation lack of controllability in the polishing process meant attempts to create a second plane would frequently remove a depth of material more than $1/10^{th}$ of the fibres length (e.g. 15 μm) and led to a second image that could not be related to the first. Additionally, any fibres that had been damaged due to the narrow die openings used in the injection moulding process would be shorter than 150 μm, ultimately reducing the likelihood of their presence in the second section.

Even if a second image was achievable, there are limitations associated with the technique. Firstly the x-y coordinates observed by examining each section plane are likely to be translated and rotated with respect to each other, since the specimen must be removed from the setup for re-polishing and the section-to-section separation distance is unknown. Therefore, to calculate the fibre's 3D orientation, one must find a precise spatial relationship between the two specimen sections. A second problem would be caused by the short PITCH fibre length meaning a significant fraction of fibres would not extend from one section to another, and therefore no matching cross-sections would exist (197). A suggested solution would be to use an auto-polishing device which could more accurately control the thickness of material removed from the specimen; however the section correlation problem would still remain.

The MATLAB technique itself possesses a series of limitations. Firstly, one should consider that there was basic noise in these pixelated images as the square array of pixels cannot reproduce a perfectly circular image of a fibre cross section. Therefore, a perfect circular ellipse and a fit factor of 1 could never be achieved.

Although the absence of a second plane did not allow the full 3D orientation of the fibres to be realised, the results were simple and quick to achieve once the specimens were prepared. This study has assessed the internal morphology of injection moulded dog-bone CFRPEEK specimens and determined that although the distribution of fibres was fairly homogeneous

in the specimens the presence of voids and inclusions indicated that the process was not fully refined for successful component moulding. For successful moulding, it is suggested that the holding time and pressure is reassessed in order to reduce sinking marks and eliminate void formation. Fibre orientation was shown to dominate in the direction of the flow and it was proven that the accuracy of the orientation distribution can be improved by studying section inclined at various angles to the flow which reduced the near bias error. In order to promote improved wear resistance, Section 2.4.2.3 identified fibre orientation normal to the sliding direction to exhibit the greatest wear and the moulding process should aim to achieve this. Mould design, runner location and moulding conditions such as pressure and holding time should be carefully considered to control fibre orientation, distribution and eliminate void presence. The developed methodology for assessing fibre orientation will adopted by Aurora Medical Ltd in future acetabular component studies. In the context of designing useful structural orthopaedic components, composite materials can be described as materials made of at least two chemically different constituents, the matrix and the reinforcement, separated by a distinct boundary, the interface. These components are able to act synergistically to exhibit properties superior to those provided by either component alone. The reinforcement, normally in the form of fibres can be directionally aligned in the matrix that binds it producing the typical characteristics of heterogeneity and anisotropy. This flexibility can be exploited in orthopaedic component design.

By the variation of fibre orientation and volume fraction, within the composite, it is possible to obtain a wide range of mechanical properties, and hence optimise the structure of the component and its interaction with the surrounding tissues. Indeed many biological natural tissues, including bone, employ an efficient composite structure to achieve particular combinations of properties whilst minimising their weight, size, or metabolic cost. Because the elastic properties of composites can be accurately varied and controlled, they can be designed as part of an integrated structure in the body to reproduce the beneficial loading into adjacent host tissues, in terms of compliance, modulus gradient and anisotropy at any given implantation site. This anisotropy can be exploited in biomedical structures, which require specific physical properties, for example in bone replacement applications where longitudinal and transverse rigidities need to be varied.

3.3 Study 3: Biological Fixation

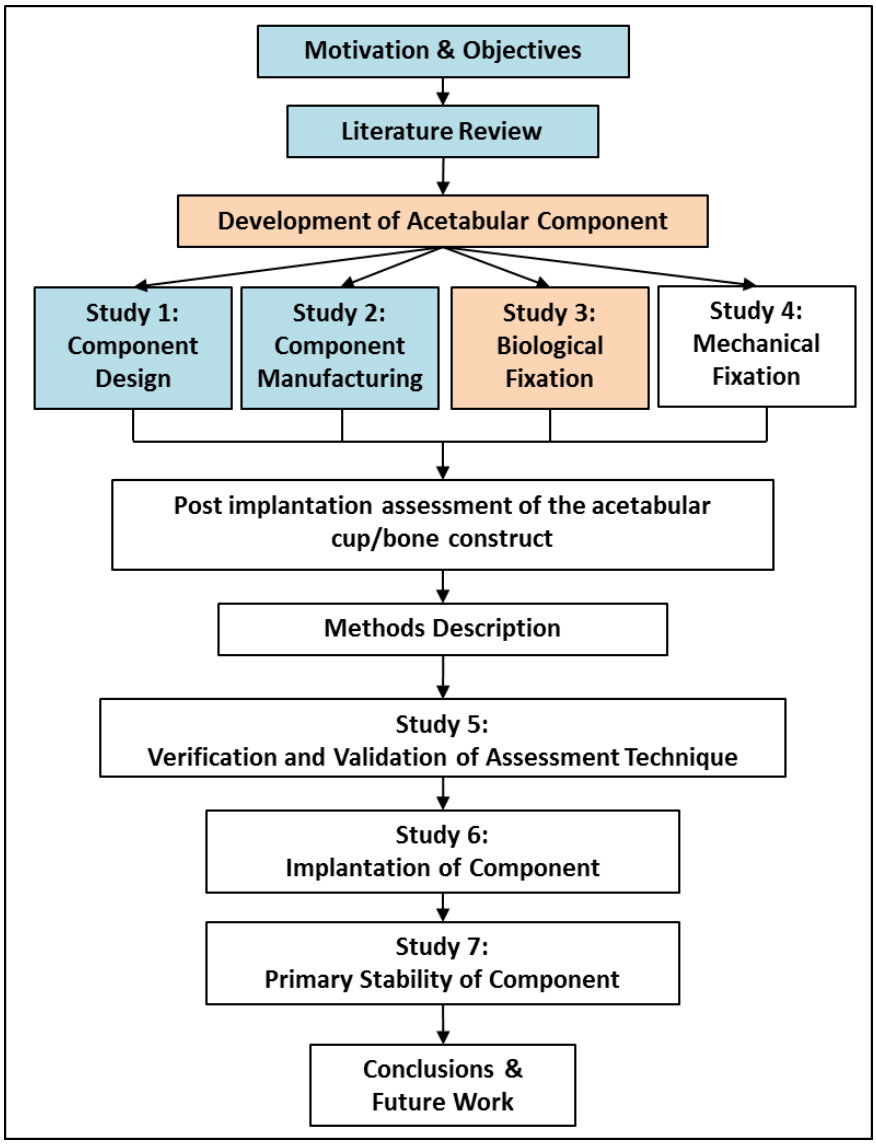

Section 2.5 reviewed the fixation options used in current large diameter bearing hip prostheses. It was shown that mechanical fixation methods are commonly aided by the application of a plasma coating which aims to enhance biological fixation. From this point forwards mechanical and biological fixation methods will be referred to as primary and secondary fixation methods respectively.

PEEK is an inert biomaterial. Therefore an osseointegrative coating should be applied to the surface in contact with the bone to enhance bone growth. Section 2.5 demonstrated that hydroxyapatite (HA), titanium (Ti) or a combined TiHA coating were the most commonly used coatings in hip arthroplasty. HA possesses the longest clinical history (131) but concerns relating to the degradation of the HA layer and its detachment from the components surface has led to the application of dual layered coatings (e.g. TiHA) with stronger adhesion to the component. The review chapter highlighted the potential for the coating process to negatively affect the mechanical properties of the substrate.

All new thermal spray coated hip prostheses must undergo a series of tests specified by the Food and Drug Administration (FDA). Designs that exceed the pass criteria of these tests are exempt from post-market surveillance. Section 2.5 highlighted the importance of a coating to aid primary fixation (103, 131) and it was proposed that either a coating of pure hydroxyapatite (HA) or a combination of titanium and HA would be used on the new CFRPEEK acetabular cup to promote osseointegration. The FDA pass criteria were developed for metallic implant substrates and are not intended for new materials e.g. CFRPEEK. However, a lack of specific tests designed for polymer composite materials has meant that researchers are adopting metallic test procedures (9, 209, 210).

The effect of the plasma spray process upon substrate bulk properties were investigated in the next section via tensile and fatigue testing of HA and TiHA coated CFRPEEK. Aside from the effect of the plasma spraying process on the mechanical properties of the substrate, the adhesion strength of the coating is another important factor. Studies (131, 132) have shown that failure mainly occurs between the implant and coating interface; the integrity of the coating and its bond therefore plays an important role in the longevity of the implant. Assessment of the adhesion strength and the integrity of HA and TiHA coatings are presented in Section 3.3.2 using standard FDA test methods.

Figure 50 displays a typical cross-sectional optical micrographs of the TiHA and HA coatings produced by Medicoat AG (Mägenwil, Switzerland) for the specimens investigated in this thesis. The specimens were prepared with a slow speed saw to reduce the likelihood of coating decohesion. To assess coating thickness, each individual specimen was mounted in epoxy resin for surface preparation and polished to a surface finish of 1 μm. Visual analysis of the surfaces was performed using an Olympus BH2-UMA microscope. Typical thicknesses for the TiHA coatings were between 70 - 90 μm whilst HA coating thicknesses were between 60 - 80 μm. The TiHA micrograph shows that the thickness of titanium and HA layers are similar but gaps exist in the titanium layer. This is likely to affect the local adhesion strength of the coating. A noticeable difference between the micrographs is the surface roughness between the titanium layer and the CFRPEEK. The CFRPEEK surface was identical for both coatings, and had undergone grit blasting to roughen the surface in order to promote interlocking between the coating and the material. But the addition of the titanium layer enhanced the surface roughness further which should promote better mechanical interlocking with the HA (9).

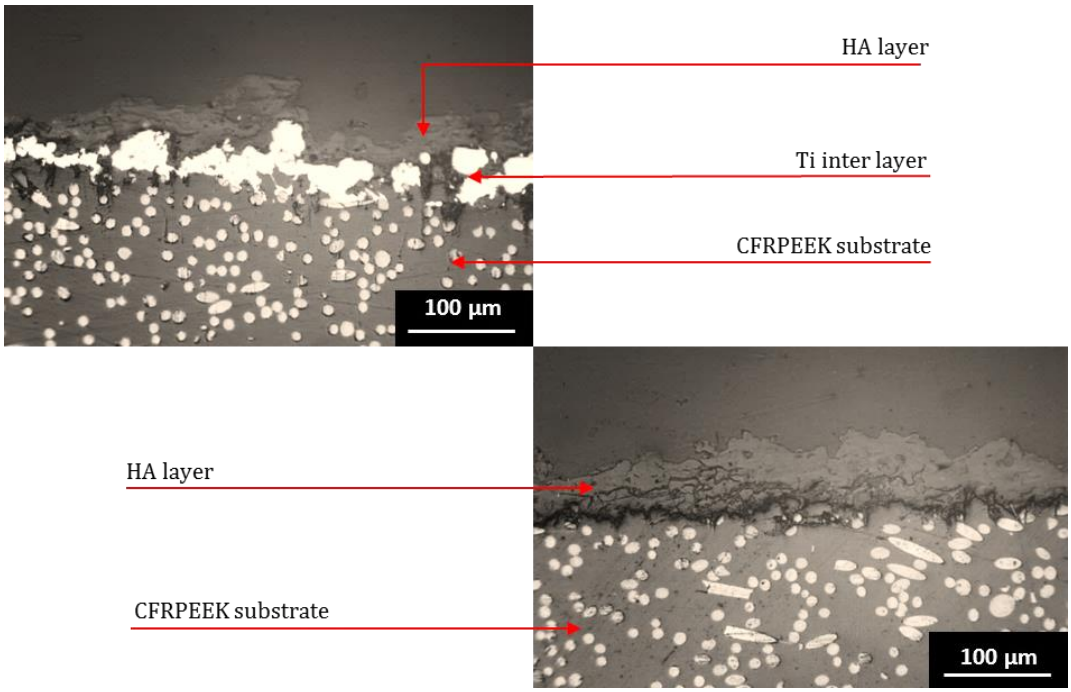

Figure 50: Typcial cross-sectional micrographs of TiHA (top) and HA (bottom) coatings on CFRPEEK MOTIS.

3.3.1 Investigation 1: Effect of the plasma spray coating process on static and fatigue strength of HA and TiHA coated CFRPEEK.

In this section the bulk tensile and fatigue properties of simple dog-bone CFRPEEK specimens coated with TiHA and HA are compared to uncoated and grit blasted specimens as an initial step to understand whether the coating application process affects mechanical parameters.

Materials and Methods

Static Tensile Test:

10 dog-bone shaped CFRPEEK MOTIS (Invibio Biomedical Solutions) specimens with dimensions according to BS EN ISO 527-2:1996 test specimen 1B (4 mm thickness and 10 mm width at the thinnest section) were used (Figure 51). Two specimens were left uncoated, two grit blasted, two coated with a combination of titanium and hydroxyapatite and the remaining two were only coated with hydroxyapatite.

Each specimen was tested using an electromechanical 5569 test machine with a 50 kN load cell. The tensile test apparatus setup followed the guidelines set out in BS EN ISO 527-1:1996, Plastics. Determination of Tensile Properties – General Principles and 527-2:1996, Plastics. Determination of Tensile Properties – Test conditions for moulding and extrusion plastics. The test was run under displacement control, with a load rate of 2 mm/min for all of the specimens. Differences between the uncoated and coated groups were assessed using a two-tailed Student t-test assuming unequal variances.

Fatigue Test

52 dog-bone shaped CFRPEEK MOTIS (Invibio Biomedical Solutions) specimens with dimensions according to BS EN ISO 527-2:1996 test specimen 1B (4 mm thickness and 10 mm width at the thinnest section) were used (Figure 51). 13 specimens were left uncoated, 13 grit blasted, 13 coated with a titanium and hydroxyapatite and 13 were coated with hydroxyapatite.

The apparatus was setup following the guidelines set out in BS EN ISO 527-1:1996 and 527-2:1996. The same Instron 5569 test machine was used, with a 25 kN load cell. Testing was carried out at 21°C under tension-tension fatigue at a frequency of 5 Hz and R-value - the ratio of minimum to maximum cyclic load of 0.1. To evaluate the mechanical durability of the composite, 16 specimens were subjected to 130 MPa (~85 % UTS), 16 the specimens were subjected to a maximum stress of 120 MPa (~75 % UTS), 16 specimens were subjected to 110 MPa (~70 % UTS) and 4 specimens were subjected to 100 MPa (~65 % UTS). The specimens were tested until failure or 1 million cycles, similar to the approach of Kurtz et al. (2012) (9).

Figure 51: CFRPEEK MOTIS tensile and fatigue specimens according to BS EN ISO 527-1:1996.

Results

Static Tensile Test

The results of the static tensile load tests are shown in Figure 52. The uncoated specimens possessed the greatest tensile strength at 157.4 MPa (SD: 0.5 MPa), followed by the TiHA coated specimens (157.0 MPa, SD: 1.9 MPa) and HA coated specimens (156.4 MPa, SD: 0.8 MPa). The grit blasted specimens possessed the lowest tensile strength with an average strength of 155.3 MPa (SD: 0.6 MPa). There was no apparent evidence of debonding on either specimens (Figure 53).

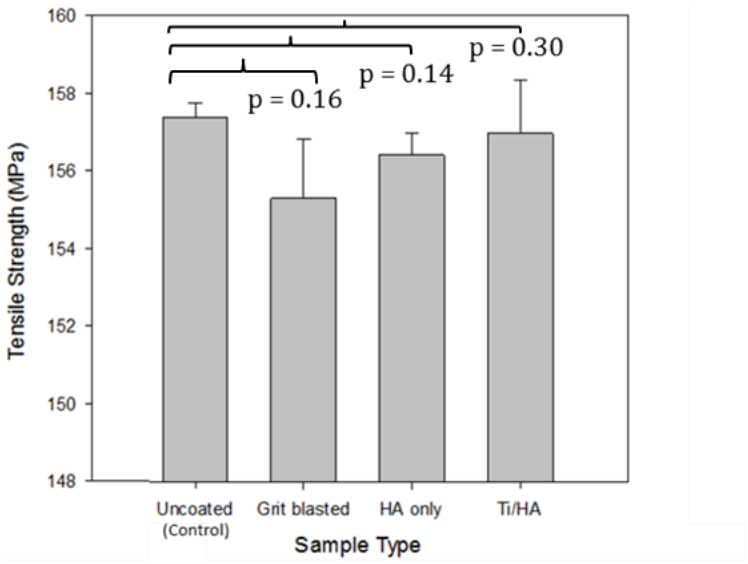

Figure 52: Average tensile strength of CFRPEEK specimens with different surface treatments. Error bars are one standard deviation.

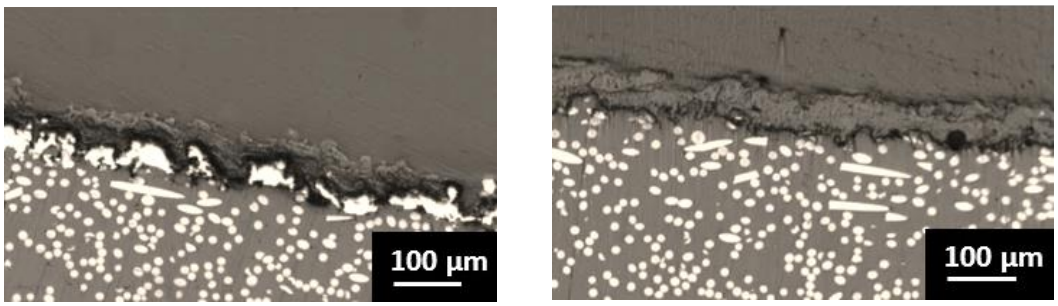

Figure 53: Optical micrographs of the TiHA (left) and HA (right) coatings after tensile testing taken from a section 2 mm from the fracture surface.

Fatigue Testing

Table 4 and Figure 54 show the average number of cycles to failure for each sample tested at each load level. Figure 55 shows optical micrographs taken near the fracture surface of the coatings after fatigue testing; there was no apparent evidence of debonding of the TiHA coating in contrast to the HA coating.

Table 4: Average number of cycles to failure for each sample tested at 85, 75, 70 and 65% ultimate tensile strength. Number of samples tested in brackets.

Sample Type	130 MPa (~85% UTS)	120 MPa (~75% UTS)	110 MPa (~70% UTS)	100 MPa (~65% UTS)
	Average no. cycles to failure	Average no. cycles to failure	Average no. cycles to failure	Average no. cycles to failure
Uncoated	1936 ± 451 (4)	18209 ± 9854(4)	666746 ± 162630 (4)	No break
Grit Blasted	870 ± 128 (4)	14873 ± 2578 (4)	401304 ± 89146 (4)	No break
HA	1594 ± 594 (4)	18063 ± 9766 (4)	213506 ± 80352(4)	No break
TiHA	1952 ± 698 (4)	15589± 2910 (4)	72533 ± 20349(4)	733449 (1)

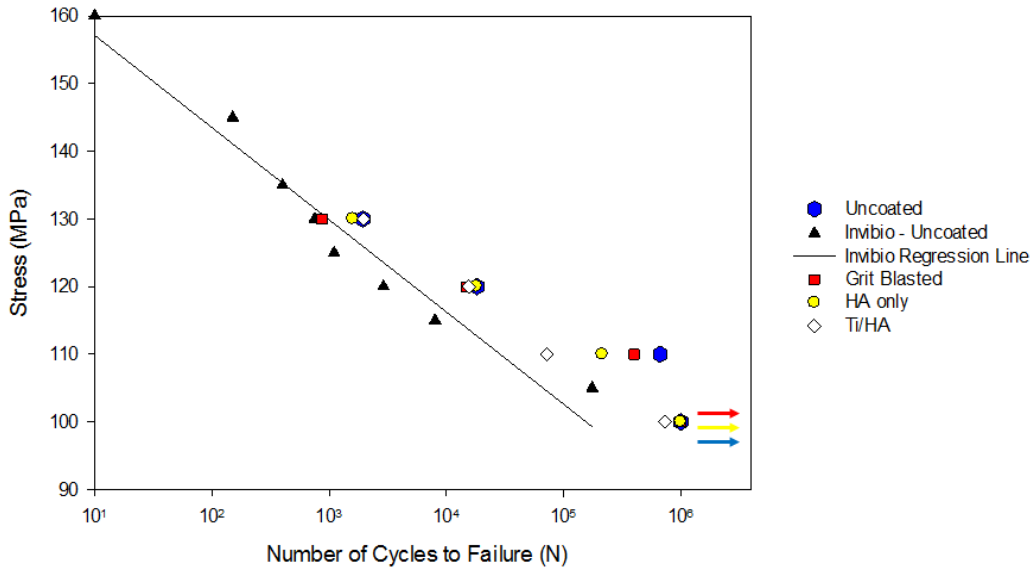

Figure 54: Plot of alternating stress against number of cycles to failure CFRPEEK specimens with different surface treatments.

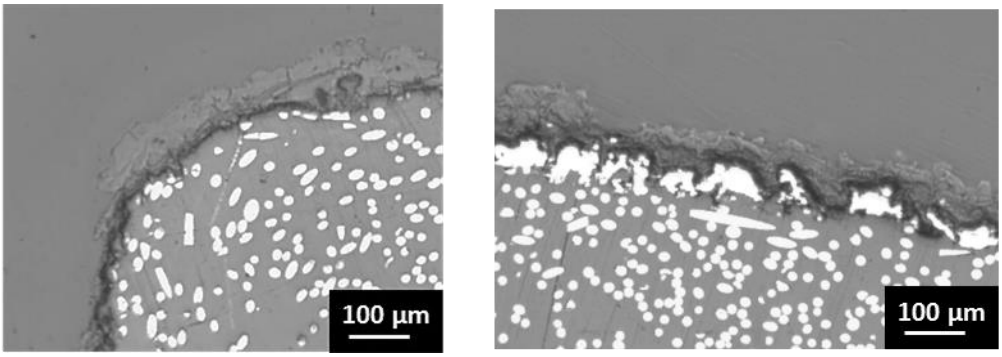

Figure 55: Optical micrographs of the HA (left) and TiHA (right) coatings after fatigue testing.

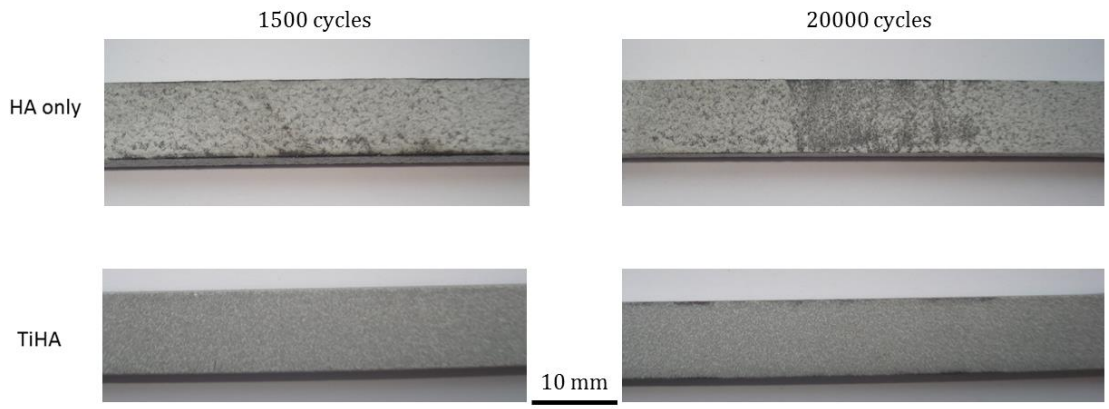

Figure 56: Appearance of specimens after 1500 and 200000 cycles (top HA coated, bottom TiHA).

Discussion

Static Tensile Test

Figure 52 illustrates that there was no statistical difference ($p>0.05$) in bulk tensile strength between the coated and uncoated specimens, as observed in previous tensile studies (9, 211). Figure 53 shows optical micrographs of HA and TiHA coated specimens respectively. Both micrographs showed debonding between the substrate and the coating. No physical deterioration of the PEEK matrix in the form of dimension or colour variation could be seen. These results are consistent with previous studies (209, 211) where it was concluded that the bulk strength of CFRPEEK was maintained after the coating process and that substrate failure was related to the material itself and did not initiate from within the coating (209, 211).

Fatigue Test

Figure 54 shows CFRPEEK's fatigue life is sensitive to grit blasting and the application of a coating. In all instances except TiHA at 130 MPa, a lower number of cycles to failure was recorded for the coated and grit blasted specimens. At 130 MPa and 120 MPa all differences were not statistically significant ($p>0.05$) with the exception of grit blasted at 130 MPa ($p=0.01$).

At 110 MPa all differences between the coated and uncoated specimens were statistically significant indicating that a coating had an adverse effect on fatigue life at this load level.

In this investigation aside from the 130 MPa case, the TiHA specimen showed the poorest fatigue resistance which is in contrast to previous findings (212-214). These fatigue studies have examined the effect of the titanium interlayer on crack propagation but only on a titanium substrate in four point bending (212-214). These results showed that cracks initiate early in the HA layer but a lower number of cracks nucleated in the HA coating when a titanium interlayer was present. This was attributed to the titanium layer reducing the mismatch between the coefficient of thermal expansion of the HA coating and Ti substrate,

consequently reducing the residual stresses in the HA top coat and the number of cracks present in the coating prior to testing.

According to Invibio Biomedical Solutions (79), CFRPEEK has a thermal expansion of 8.0 x 10^{-6} $°C^{-1}$. Although the thermal expansions for the coatings used in this thesis were not supplied by the manufacturer, Laonapakul et al. (2012) (212) and Xue et al. (2004) (215) have documented expansions of 15.2 x 10^{-6} $°C^{-1}$ and 8.6 x 10^{-6} $°C^{-1}$ for HA and Ti respectively. The larger difference between the CTE of HA and CFRPEEK has been suggested to generate residual stresses within the HA layer during cooling (212). These residual stresses could then promote micro-cracking and coating de-bonding. In contrast, the structured Ti layer has a CTE closer to PEEK which could limit the effect of these residual stresses (212). Poor adhesion and coating de-bonding were visually evident (Figure 56) in this study between the HA and CFRPEEK, as the coating detached from the substrate early in the fatigue test. Similar findings were observed by Zappinin and Robotti (2010) (209) who hypothesised that as the brittle ceramic coating was easily removed the resultant fatigue life was similar to that of the substrate material.

There was no visual evidence of debonding on the TiHA specimen (Figure 56) indicating a greater adhesion strength between the titanium interlayer and the CFRPEEK substrate than at the HA/CFRPEEK interface. This factor in partnership with the difference in stiffness between the two materials is suggested to affect the fatigue limit of the specimen. CFRPEEK's lower stiffness may allow the substrate to deform more elastically than if the titanium was tested alone. Whilst the substrate can recover from large deformations during the test, the well adhered stiff thin titanium layer cannot. To the author's knowledge there are no fatigue analyses conducted on coated CFRPEEK which perform sectioning throughout the test. The closest studies either analyse the tensile failure (216, 217) or analyse fatigue failure on alternate substrates (212-214) meaning the damage accumulated within these specimens can only be speculated. However, similar failure is known to occur in flexible electronic devices (218, 219) which use polymer materials to support thin metal films/coatings. These studies show that the stiffer films are susceptible to fatigue damage because they experience plastic deformation, whilst the polymer remains fully elastic. This stiffness difference then initiates fatigue damage in the metal film/coating in the form of voids which act as stress concentration sites, leading to crack initiation and propagation into the substrate causing ultimate failure. It is hypothesised that a similar failure mechanism was experienced for the TiHA coated CFRPEEK specimen. However, as this explanation is speculative future analyses are recommended in which the test is interrupted so fatigue damage can be observed in the titanium interlayer and at sites on the HA specimens where the coating has been removed. This could be achieved with μCT, ultrasound or acoustic emission testing.

3.3.2 Investigation 2: Determination of Adhesion Strength between plasma spray coatings and a CRRPEEK substrate.

In-vivo studies have highlighted that component loosening mainly occurs at the implant/coating interface (220); the integrity of the coating and the bond to the substrate therefore play an important role in the longevity of the implant. There have been indications from previous studies that TiHA has a superior interlock with CFRPEEK compared to HA alone. The following investigations explore the adhesion strength between the coatings and CFRPEEK surface under shear and tensile forces using standard test procedures outlined by the FDA. These tests were conducted to determine whether the adhesion strength of the coatings was sufficient to remain intact under *in-vivo* loading.

Materials & Methods

Shear Adhesion

A single-lap joint specified in ASTM F1044-05 was used. Each lap joint consisted of two rectangular sections made from CFRPEEK specimens and aluminium mating plates, bonded together at the coated region. 24 lap shear CFRPEEK MOTIS (Invibio Biomedical Solutions) specimens with dimensions according to ASTM F1044-05 (76.2 x 25.4 x 6.35 mm) were used. At the end of each specimen an area of 25.4 x 25.4 mm was grit blasted or coated with TiHA, HA or Ti (Figure 57). The surfaces were roughened with sandpaper to encourage a strong interlocking bond with the glue and ensure failure occurred between the coating and CFRPEEK.

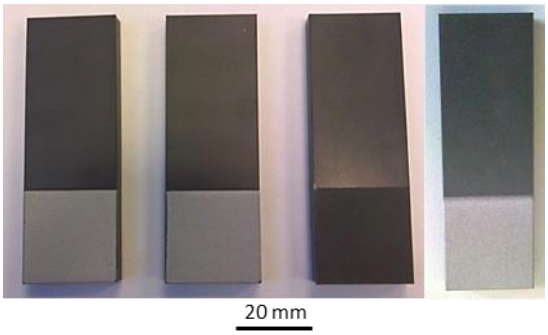

Figure 57: Lap shear specimens. L-R TiHA, HA, grit Blasted and titanium only.

Film Epoxy FM1000 (Cytec Engineered Materials Inc., Havre de Grace, MD, USA) was used to bond the CFRPEEK specimen (thickness 0.25 mm) to the aluminium mating specimen (Figure 58).

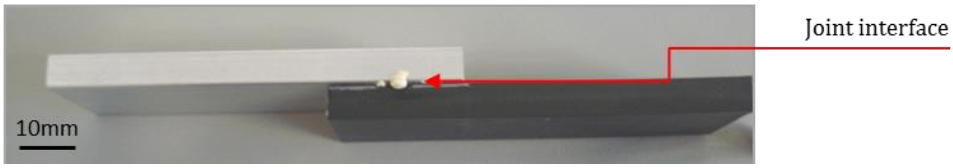

Figure 58: Bonded lap shear specimen.

Each lap shear specimen was mounted on an Instron 5569 electromechanical test machine and subjected to a ramped displacement of 2.5 mm/min until the bond failed. The peak load

(F) applied was recorded by the BlueHill software (Instron). The adhesion strength (S) was calculated by using the coating cross sectional area (A) and the relationship:

$$S = \frac{F}{A} \quad [6]$$

Visual analysis of the surfaces was performed using an Olympus BH2-UMA microscope to assess the failure modes.

Tensile Adhesion

The tensile adhesion strength between the coatings and CFRPEEK surface was tested according to ASTM standard F1147-05. Test specimens were disc shaped, with diameter 25.4 mm and thickness 6.35 mm. 14 injection moulded CFRPEEK MOTIS specimens (Invibio Biomedical Solutions) were coated on one side with a combination of TiHA and HA (Figure 59). The disc specimens were mounted onto aluminium mating cylinders bored with M16 screw threads to allow attachment to the test machine (Figure 60).

Figure 59: Coated test coupons (Left HA, Right TiHA).

Figure 60: Aluminium mating cylinders for specimen mounting. Coating face cylinders on the left and back face cylinders on the right (Note recess for specimen alignment).

The disc specimens were mounted onto cylinders using 300 g/m^2 FM1000 film adhesive (Cytec Engineered Materials Inc., Havre de Grace, MD, USA). Adhesive bonding was conducted under a pressure of 0.138 MPa (20 psi) and in an oven at 177 °C (350 °F) for 3 hours. Alignment was ensured by mounting one of the CFRPEEK faces within the circular recess on the aluminium mating cylinders. A bonding jig was manufactured which allowed bonding of specimens in batches of 6, aligning the specimen cylinders and exerting the desired pressure upon them using springs. The curing jig is shown in Figure 61. To minimise the effects of elevated temperature on the springs, they were re-calibrated before each use. The six screws holding the assembly together were tightened until the springs were compressed to the length corresponding to the desired force. The jig was placed in a pre-

heated oven for 2-3 hours and removed. Specimens were removed from the jig once it had cooled (approximately 1 hour). An example of a batch of 6 bonded specimens is shown in Figure 62.

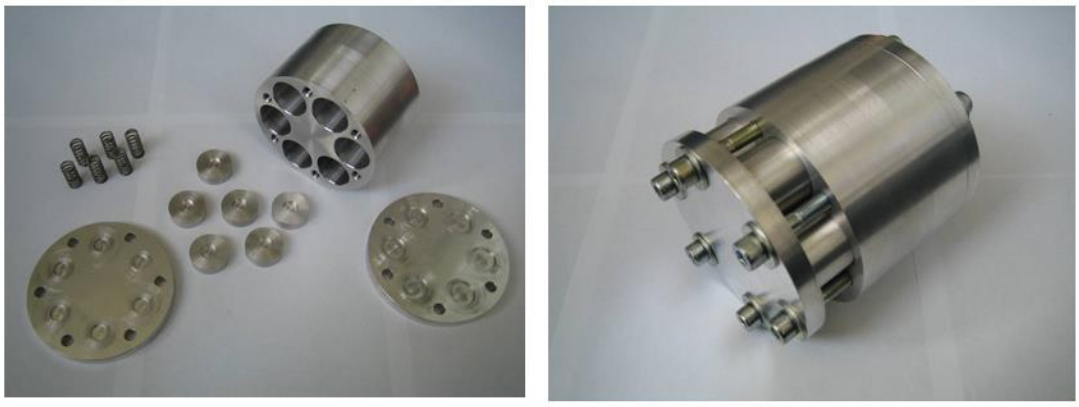

Figure 61: Sample bonding curing jig shown disassembled (left) and assembled containing specimens and mating cylinders (bottom).

Figure 62: A batch of specimens bonded using FM1000 to aluminium mating cylinders.

Each specimen was mounted on an Instron 5569 electromechanical test machine using test fittings outlined in ASTM standard 1147-05 and a ramped displacement of 2.5 mm/min was applied until bond failure. The peak load (F) applied was recorded by BlueHill software (Instron). The adhesion strength (S) was calculated using equation [6]. Visual analysis of the surfaces was performed using an Olympus BH2-UMA microscope to assess the failure modes.

Results

Shear Adhesion

Table 5 illustrates the lap shear strength results, the Ti specimen showed a significantly higher shear adhesion strength ($p<0.05$) than the other specimens. A significant difference was also found between the HA specimens and the grit blasted and TiHA specimens ($p<0.05$). No significant difference was found between the grit blasted and TiHA specimen. Figure 63, Figure 64 and Figure 65 are optical micrographs of the typical failure of each coating type. Whilst the HA and Ti coatings failed at the interface with the substrate, the TiHA coating failed between the Ti and HA layers.

Table 5: Average shear adhesion strength for grit blasted and each type of coated specimen.

Coating	*Average Adhesion Strength (MPa)*	*Standard Deviation*
Grit Blasted	9.8	0.8
TiHA	9.6	1.0
HA	8.5	1.3
Ti	14.2	1.4

Microscope Images:

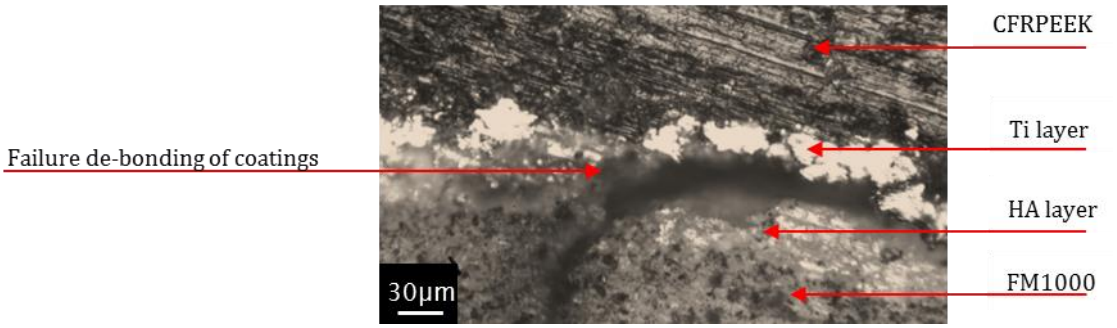

Figure 63: TiHA specimen exhibiting the lowest adhesion strength showed failure between the Ti and HA layers in an area where FM1000 adhesive remained.

Figure 64: Ti coated specimen where no FM1000 adhesive remained on the surface. The Ti layer partially remains on the surface.

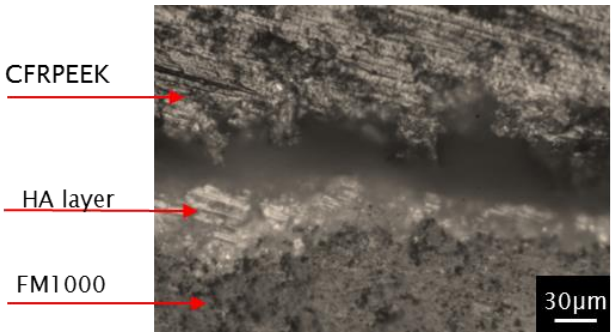

Figure 65: HA specimen exhibiting the typical coating failure showed failure between the HA and substrate.

Tensile Adhesion

Table 6 illustrates the tensile adhesion strength for the TiHA and HA coatings. The TiHA coating exhibited a higher strength of 20.5 MPa (SD: 1.3 MPa), whilst the HA coating exhibited an average strength of 18.7 MPa (SD: 3.3 MPa). This difference was not statistically significant ($p>0.05$). Figure 67 and Figure 68 are optical micrographs of the typical tensile failures of each coating type. In-line with the shear adhesion study the HA coatings failed at the interface with the substrate, whilst the TiHA coating failed between the Ti and HA layers.

Table 6: Average adhesion strength for coated specimens tested in tension

Specimen Type	Average Adhesion Strength (MPa)	Standard Deviation
HA	18.7	3.3
TiHA	20.5	1.3

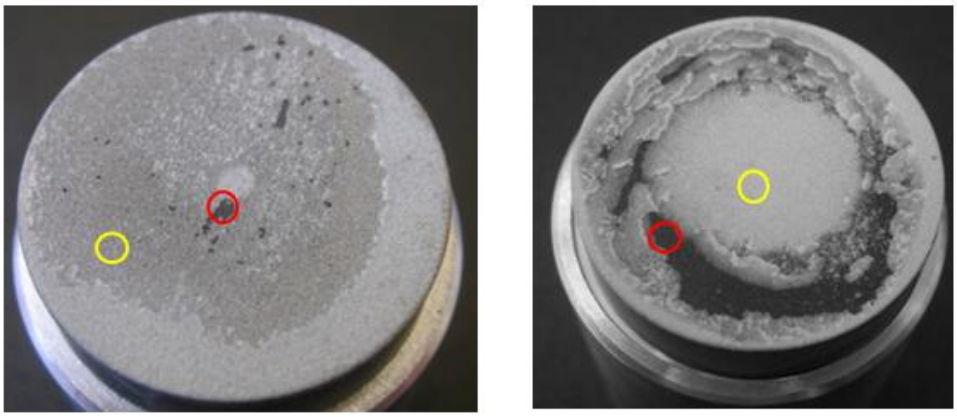

Figure 66: Typical coating surface on TiHA (Left) and HA (Right) specimen after adhesion testing. The red circles indicate areas where the CFRPEEK substrate has been exposed, whilst the yellow indicates areas of coating interface failure.

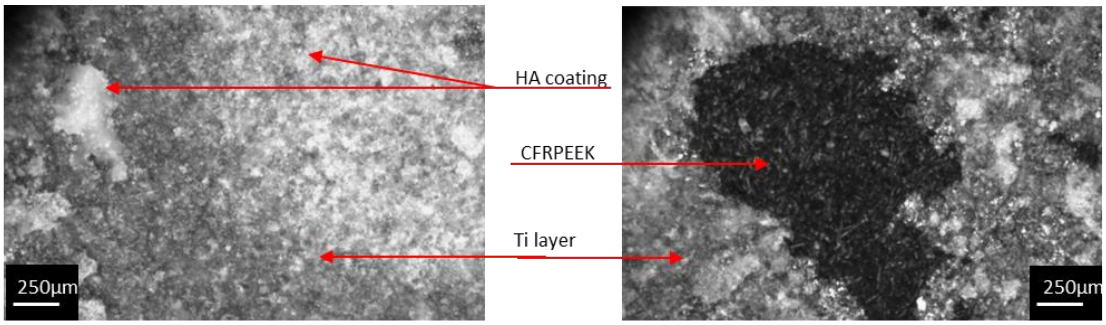

Figure 67: TiHA specimen: Left (Yellow Circle in Figure 66: left) - failure is present between the Ti and HA layers on the majority of the specimen. Right (Red Circle in Figure 66: left) note the titanium layer has de-bonded from the CFRPEEK substrate.

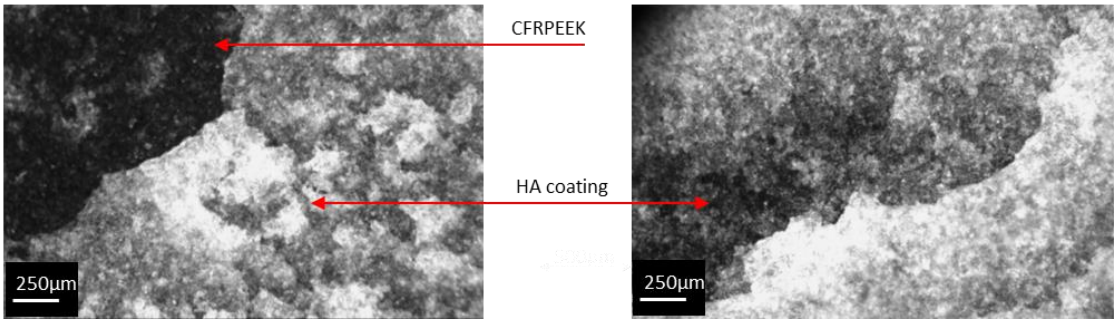

Figure 68: HA specimen: Left (Red Circle in Figure 66: right) - HA layer has de-bonded from the CFRPEEK substrate in the majority of the specimen. Right (Yellow Circle in Figure 66: right) failure is present between the HA layer and the substrate on the majority of the specimen.

Discussion

Shear Adhesion Strength

The titanium specimen exhibited the greatest adhesion strength and the HA/CFRPEEK interface the weakest (Table 5). This proved the hypothesis stated in Section 2.5 that the titanium layer enhances HA adhesion to CFRPEEK.

Figure 63 shows evidence of the HA layer de-bonding from the titanium, with the titanium layer remaining intact. The lack of titanium interlayer caused the HA layer to de-bond from the CFRPEEK substrate (Figure 65). The effectiveness of the titanium interlayer is suggested to be due to the reduced mismatch of thermal expansion between the substrate and the HA top coat (212). The influence of the stiffness mismatch on coating debonding was discussed in Section 3.3.1 where it was related to the residual stresses generated within the coating.

None of the coatings achieved the ASTM pass criterion of 20 MPa which is suggested to be due to the standard's test setup not being suitable for use with a non-metallic material. Aside from the adhesive and processing conditions used, the lap shear test method itself has drawbacks which are evident in the preparation and testing stages.

Firstly, in the preparation stage care must be taken to keep the substrate samples aligned otherwise an extra torque on the bond could occur during the test (221), generating tensile stress at the coating bond, rather than the intended pure shear. Alignment fixtures were used in this experiment to control and minimise these effects. Secondly, the correct volume of adhesive must be used to prevent it running out of the joint and setting on the side of the bond, introducing a bias into the results. It should be noted that a number of additional factors will influence the shear strength including joint geometry and shape of fillet at the overlap end, however, the standard aims to minimise this variability. These factors were controlled by using the same setup of joint geometry and film for each coating.

During the test, the setup configuration changes leading to a non-uniform stress distribution. Figure 69a illustrates the setup prior to testing. It assumes a uniform shear load is applied to the plane of the bond which gives maximum joint efficiency (222). However, as testing proceeds the tensile load increases and the sample begins to deform altering the setup of the

system. The deformity is a result of eccentricity of the tensile axis which gives rise to a bending moment (Figure 69b). The tensile stress by itself may be viewed as acting like a peel stress (223) which is higher at the ends of the overlap joint. At the edge of the bond, shear stresses have been calculated to be as much as six times higher than the average applied stress (224). Figure 69c illustrates the non-uniform stress distribution across the bond length with the ends withstanding the maximum load whilst the mid-area withstands the minimum. With this understanding, failure is most likely to initiate from cracks which propagate from the ends of the overlap. The load value calculated includes the effects of cohesive strength of the adhesive as well as the effectiveness of surface modification. Therefore the calculated adhesion strength (S) is a characteristic for the joint and not solely for the effect of surface modification or coating adhesion (223).

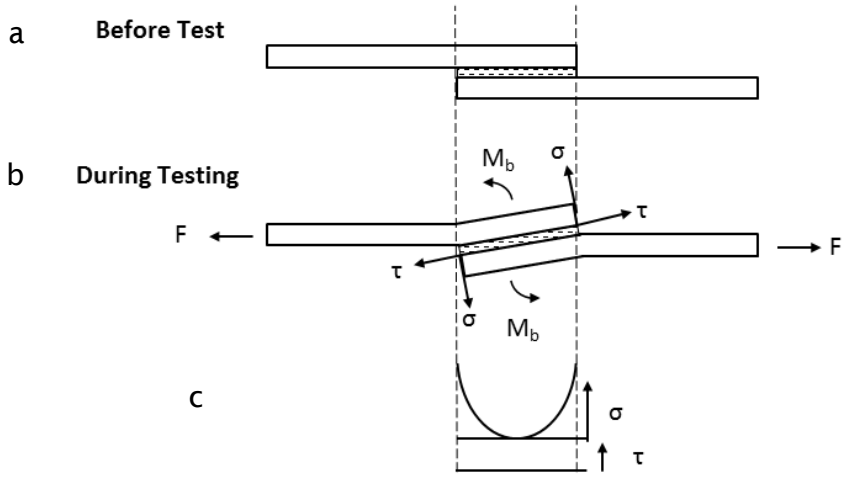

Figure 69: a) Setup prior to testing. b) Deformation of single-lap joint as the tensile load increases illustrating the generation of shear stresses, a bending moment and tensile stresses. c) Stress Distribution across adhesion area. Adapted from Zeiler (1997) (225).

The change in stress distribution is especially relevant when testing and comparing the results of the same coating on substrate materials which possess a range of stiffness values. Due to its lower stiffness CFRPEEK is likely to deform more and produce a larger bending moment in comparison to Ti-6Al-4V or CoCrMo (Ti-6Al-4V 110 GPa (9), CoCrMo 200 GPa (226), CFRPEEK ~15 GPa (9)). In most cases the tensile stress in the adhesive layer controls joint failure and, as a consequence the strength value obtained is unrelated and an unreliable measure of the true shear strength of a bond (227). The consideration of all these points suggest that the shear test setup outlined in F1044-05 may only be useful for coatings applied to metal substrates and either an alternative test setup should be used to compare coatings on polymers or the pass criteria should be adapted to consider the influence of substrates stiffness and the non-uniform stress state across the joint based on the amount of deformation.

Tensile Adhesion Strength

The highest average coating tensile adhesion strength was recorded for the TiHA specimens which also possessed a smaller standard deviation (Table 6). Figure 66 (left) shows a TiHA specimen with failure at two locations: the titanium/HA interface and titanium/substrate interface. The first area is larger suggesting this is the main failure mode which was consistent for all specimens with this coating. Figure 66 (right) shows an HA specimen where failure occurred between the HA/CFRPEEK interface.

Visual analysis performed on the TiHA specimens shows that the HA layer de-bonded from the titanium which was consistent with the lap shear study (Figure 67). The titanium layer remained on the CFRPEEK indicating that this interface had the higher adhesion strength in comparison to the Ti/HA interface. Figure 68 shows images of the HA/CFRPEEK interface; the left image shows an area where the CFRPEEK had been exposed, the right image shows an area in which part of the HA coating had been removed.

The titanium layer served to improve the tensile adhesion strength of the HA coating which is attributed to the layer reducing the inconsistency between the coefficients of thermal expansion (CTE) of the substrate and HA which prevented the coating from spalling (228, 229).

Both coatings did not achieve the ASTM pass criterion of 22 MPa which could be attributed to the standard's test setup not being applicable for use with a non-metallic substrate. Eurocoatings (2010) conducted a similar tensile study using titanium coated CFRPEEK and observed high results (34 +/-4 MPa) (209) whilst Beauvais & Decaux (2007) documented much lower results for HA on unfilled PEEK (7.5 MPa) (210). It is difficult to compare these results to this investigation as the test procedure and coating parameters were unknown. In this study, titanium coated specimens tested in shear produced the highest adhesion strength. The values obtained by Eurocoatings may not be able to be replicated as test images from their work show excess glue protruded out from the coated surface, which may have bonded to the outside of the specimen (Figure 70). ASTM standard F1147-05 advises that this should be carefully removed to avoid introducing damage to the specimen before testing as it could improve the adhesion strength due to additional adhesive bonding to the metal holders.

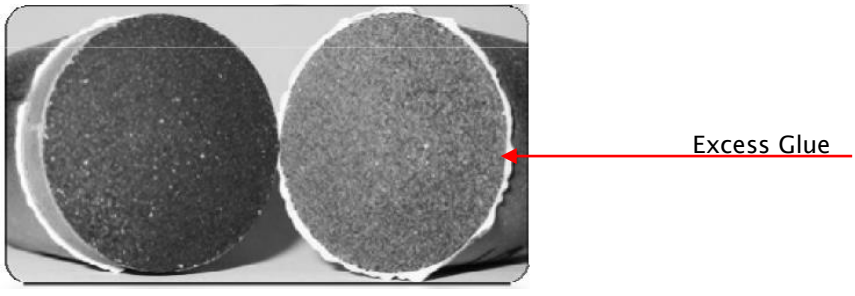

Figure 70: Eurocoating investigation of Ti coating on CFRPEEK displaying adhesive fracture and the presence of excess glue which has protruded from the coated surface (9).

Both studies indicated that the FDA standard tests may not necessarily be optimum for a polymer composite substrate. The shear study showed that the test setup generated an excessive non-uniform stress across the coating surface when the material deformed meaning a true coating adhesion strength measurement may not have been obtained. The stiffness mismatch (230) and the dependency of failure on the presence of flaws at the specimens edge (231) in the tensile adhesion setup may have also affected the results.
Dickinson et al. (2013) (230) performed an FE analysis of the ASTM F1147 test to assess the influence of the stiffness mismatch and predict the coating tensile stress distribution across the specimen for substrates Ti-6Al-4V, CoCrMo, Ceramic (CeramTec BIOLOX Delta) and CFRPEEK MOTIS (Invibio Biomedical Solutions). In addition to the standard specimen setup, two alternative geometries were analysed. Each setup is shown in Figure 71.

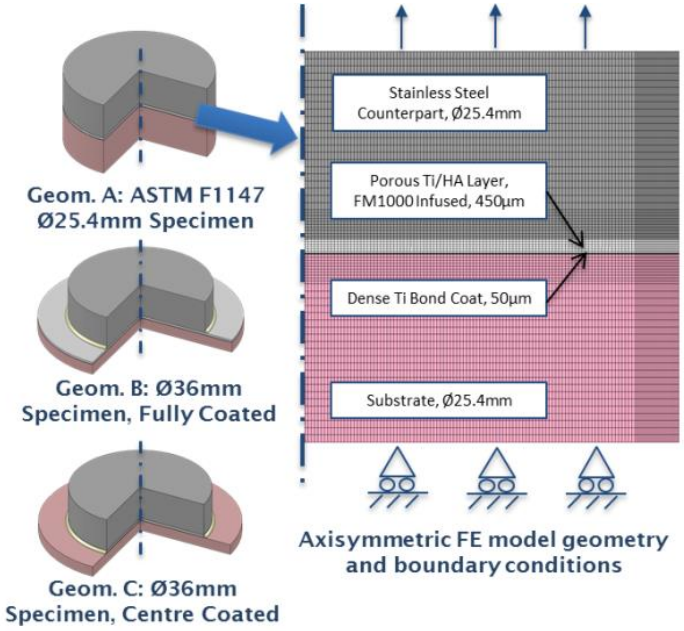

Figure 71: Three different geometries tested in the tensile adhesion test, A - standard geometry from ASTM F1147-05, B – Larger diameter substrate specimen which is fully coated, C – larger diameter substrate specimen which is coated only in the centre (230).

The study suggested that the stiffness mismatch generated a non-uniform stress distribution across the coating surface and it was implied that this would reduce the test failure load for a given interface strength. The tensile test setup assumes that the surface is uniformly stressed but the stiffness mismatch introduces stress concentrations at the interface edge, well in excess of the uniform stress experienced with coatings on similar stiffness metals. Therefore the coatings on non-metals experience non-uniform tension which under-estimates the coating adhesion strength. Changing the setup by oversizing the specimen (Figure 71: Geometry B) brought the distribution closer to the intended uniform stress distribution over the gauge area for ceramic and CFRPEEK substrates. However, the CFRPEEK specimen was not affected to the same extent, suggesting that the strategy of changing the test geometry was not universal and further investigations into the optimum

geometry which produces a uniform stress across the CFRPEEK gauge area should be conducted (230, 232).

At the time of writing, there was only one standard (ASTM F2026-12: Polyetheretherketone (PEEK) polymers for surgical implant applications, 2012) developed specifically for PEEK and its use in medical implant devices. However, this standard only covers PEEK in virgin forms and is not applicable for CFRPEEK nor does it mention the application of osseointegrative coatings onto a PEEK substrate. The findings of these investigations showed that the current ASTM F1044-05 and F1147-05 standards specifically for metal substrates may not be directly applicable for CFRPEEK.

3.3.3 Conclusions of Secondary Fixation Analysis

The conclusions drawn from the secondary fixation studies have outlined the TiHA coating to exhibit the most favourable characteristics meaning it should be applied to the acetabular cup developed in this study. Although the TiHA coated CFRPEEK fatigue results were lower than for the HA coated samples, the greater adhesion strength to CFRPEEK is considered to be more beneficial. This was due to concerns that over time the HA coating would dissolve, leaving the bone in contact with smooth CFRPEEK, hence the problem with achieving direct bone contact would not be avoided but delayed. The inclusion of a bioactive titanium interlayer is advantageous as should the HA debond, the bio-environment would remain in contact with a relatively biocompatible material (Ti) with a rough surface for the bone to mechanically bone onto rather than the relatively smooth CFRPEEK substrate.

Although the adhesion strength of the coating was investigated the failure modes of the coating are yet to be explored. The secondary coating is intended to aid the mechanical (primary) fixation method which is investigated in the next section.

3.4 Study 4: Mechanical Fixation

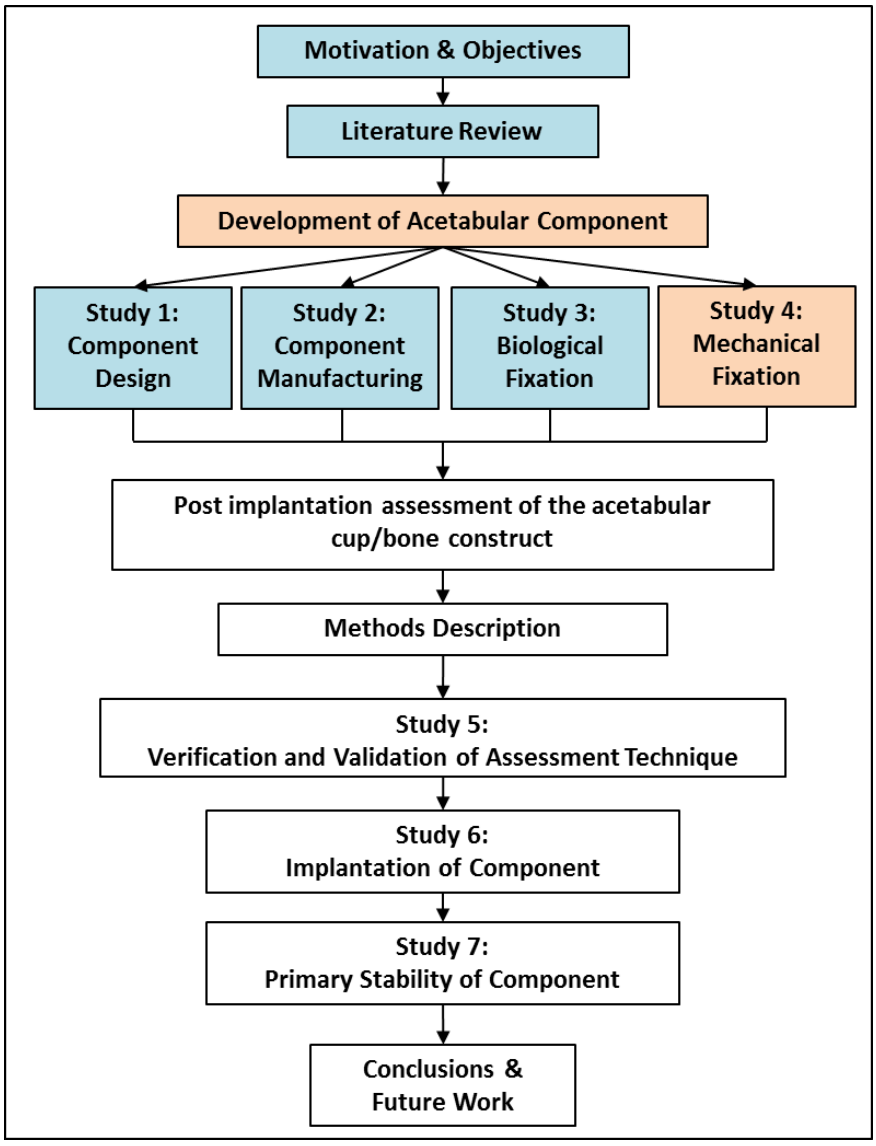

Section 2.5 reviewed the current fixation methods of acetabular components highlighting that secondary fixation aids the primary (mechanical) fixation method. The primary fixation method is more invasive, using screws or compressive forces to anchor the component into the acetabulum. Section 3.3 has investigated the application of an osseointegrative coating onto CFRPEEK concluding that a dual TiHA coating was most suitable for the acetabular component developed in this thesis.

However, the CFRPEEK cup is likely to deform more than a conventional component due to its lower modulus and thin wall thickness which has been documented in previous analyses (68, 167). Therefore, immediately after surgery when bone ingrowth has not occurred the component is likely to deform with the pelvis. If this motion is excessive (> 150 μm (123)) bone ingrowth will be restricted and therefore these micromotions should be kept within a safe range (20 - 50 μm (123)) in order to promote osseointegration. Section 2.5 described several options for augmenting the primary fixation of a cementless implant.

The use of screws for augmented fixation is not an option as the CFRPEEK component does not contain a shell or liner meaning there is an inability to place the screws behind the bearing surface. There is a hole in the CFRPEEK component which is not located on the bearing surface but this is located in the anterior inferior quadrant of the acetabulum (Figure 27). Section 2.5 showed that the bone stock in this quadrant was poor and the insertion of a screw into this area would increase the risk of vascular injury which is unadvisable. A press-fit approach should be aided with an additional fixation method due to the low stiffness of the component allowing it to deform more in the pelvis than conventional components. As a further consideration, MoM large bearing component use as-cast sintered beads and titanium porous material features which are added to their backing surface for fixation purposes. However, this is not a possibility due to complications with bonding the beads and the potential adverse effect on the mechanical properties of CFRPEEK. Due to these restrictions the CFRPBT Cambridge and the CFRPEEK MITCH PCR cups (Section 2.4.2.4) do not use conventional primary fixation methods. Instead the Cambridge cup has six moulded spikes located in the load bearing segment and the MITCH PCR has two parallel fins (Figure 20) to aid primary fixation. There are reports of the six spikes on the Cambridge component failing *in-vivo* and during implantation (68) whilst the clinical outcomes are yet to be reported on the performance of the fins of the MITCH design.

Aurora Medical Ltd have proposed a novel method of micro-interlocking to provide better primary fixation, combined with the more traditional HA based coating for secondary fixation discussed in Section 3.3.

The approach described in this section aims to enhance primary and long term fixation by adopting a novel fixation method. The central innovative concept of this device is the employment of arrowheads located on the backing surface of the component (Figure 72). When the arrowheads are impacted into the acetabulum, in theory, the bone is driven away by the arrowhead and elastically pushed around it (Figure 73). With further impaction the amount of bone surrounding the arrowhead increases until complete encapsulation is achieved (Figure 74). It is anticipated that the flat edge of the arrowhead overhang will stop the implant from backing out of the bone.

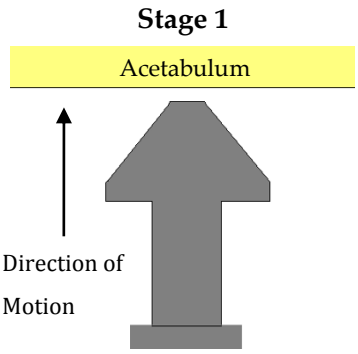

Figure 72: Simplified illustration of one arrowhead before impaction into acetabulum.

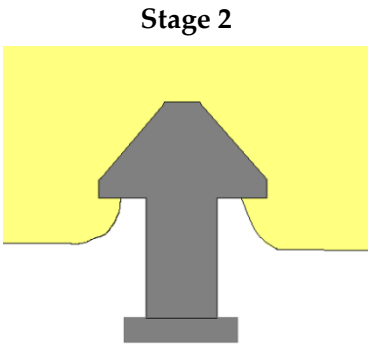

Figure 73: Impaction into acetabulum – bone is pushed around arrowhead as cup is impacted into bone.

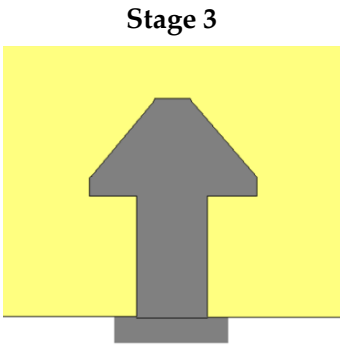

Figure 74: Complete encapsulation of arrowhead by bone resulting in firm primary fixation and reduced likelihood of the cup loosening

The concept originates from a device that uses the concept of bone encapsulation around an arrowhead to fuse the proximal interphalangeal joint. The Arrow-LOK Digital Fusion system (ArrowHead Medical Device Technologies, LLC Collierville, USA) has an arrowhead-shaped head at either end of a 1.5 mm diameter stainless steel bar. Each end has a sharp point and four outwardly facing side surfaces forming a pyramid. Two of the sides have a proximally projecting edge forming an overhang. These overhangs are present to engage tissue and inhibit rotational and axial movement of the fusion device maintaining the primary compression applied at the joint on insertion. Figure 75 shows the design of the Arrow-LOK device and its implantation into the interphalangeal joint in the foot.

This device has been in clinical use since 2009 meaning there is limited data available. However, mechanical tests have shown that the arrowhead features are able to resist a pull-out load of 21.9 N and a rotational load of 19.3 N when removed from bone models (233). These results show the ability of the arrowhead to resist extraction forces highlighting the potential of applying this concept to an acetabular component to provide primary fixation.

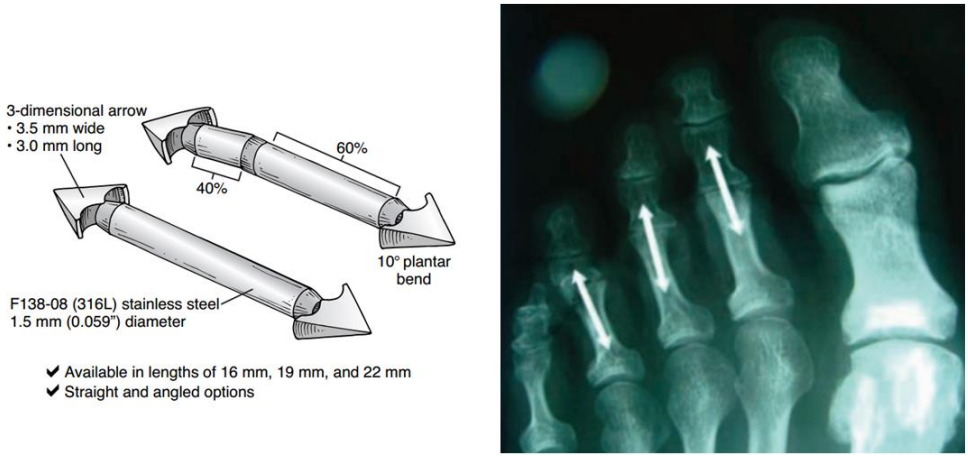

Figure 75: Arrow-LOK implant design (left). Postoperative radiograph of the Arrow-LOK device (right) (233).

The arrowheads present on the back of the acetabular component will build upon the idea adopted by the Arrow-LOK device. However, the conditions to which the arrowheads are exposed are different. The arrowhead features are designed for primary fixation only and are not expected to experience a large amount of shear loading. When the component is implanted into the pelvis at an orientation of 40 ° inclination (from the horizontal) and 20 ° anteversion (forwards), the features will be in-line with the contact force. The loading conditions exposed to the hip during a range of activities have been identified in a number of studies (234-236). During normal gait, the contact force directions in the frontal plane can vary between 12 ° on heel strike to 63 ° during the swing phase (236) (Figure 76). Mean values have been calculated between 13 - 28 ° for static loading and 16 ° for dynamic loading (235). The average peak directions for activities such as stair ascent, stair descent and standing up have been documented as 46.1 °, 38.3 ° and 14.0 ° respectively (234).

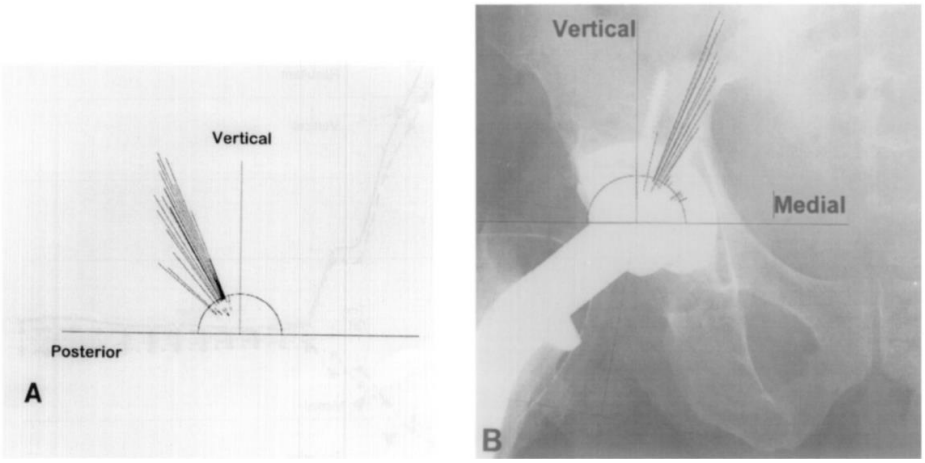

Figure 76: Directions of acetabular contact forces during the gait cycle. The data has been superimposed onto an X-ray of a patient with a telemetered implant to demonstrate the contact force directions (236).

To satisfy these peak directions, the arrowheads are orientated at an angle of 20 ° from the pole of the component to ensure they are exposed to minimal shear forces after implantation and prior to osseointegration.

Figure 77 shows the backing surface of the proposed CFRPEEK component with the arrowhead features intersecting across the surface. The arrowheads are positioned in rows, 7.5 mm apart, with three patterns crossing over at 60 ° angles. Figure 77b shows the 20 ° orientation angle of the arrowheads which coincides with the direction of the contact force. The design features intend to provide maximum opportunity for successful primary fixation of the cup in the acetabulum and the multiple rows aim to restrict movement in shear due to friction.

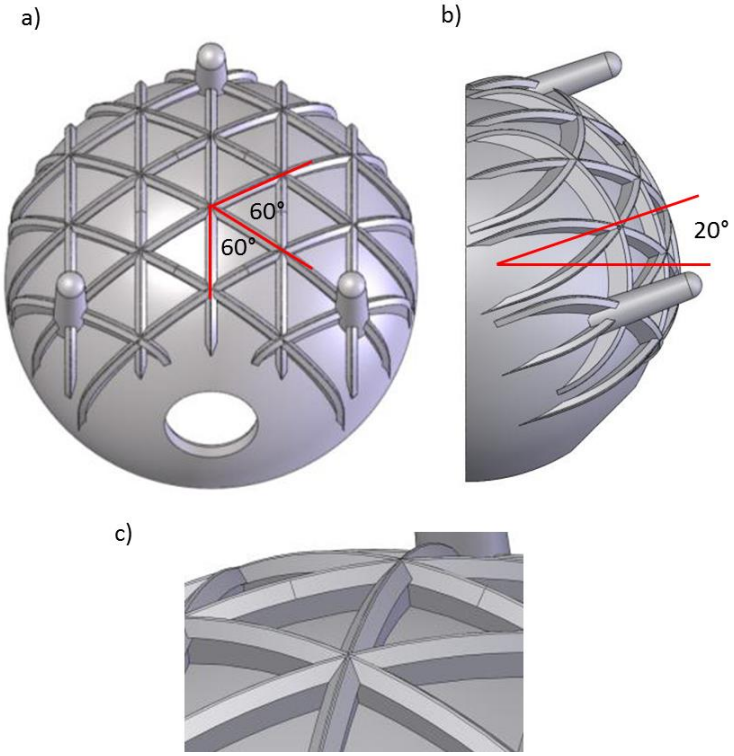

Figure 77: a) Arrowheads coverage on backing surface of the CFRPEEK component b) side view showing the 20 ° orientation angle of the arrowheads c) Close up of arrowhead intersection point.

Due to the novelty of this idea a set of rigorous tests were performed in order to prove the concept and identify if it could be a potential substitute for traditional fixation methods. Two areas of investigation were identified to ascertain the robustness of the proposed arrowhead solution. Figure 78 is a flowchart showing the approach taken towards the development of the primary fixation method.

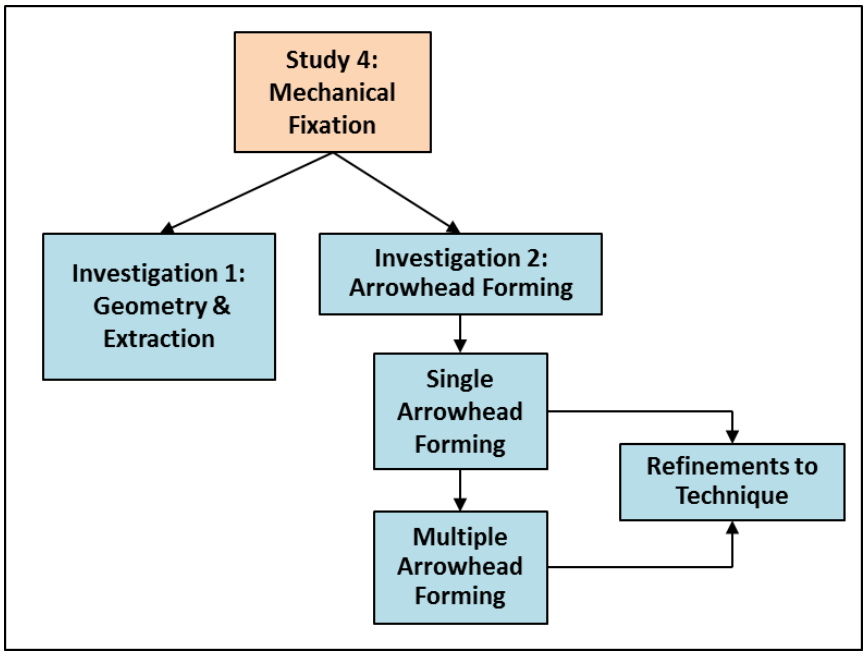

Figure 78: The roadmap described for the development of the primary fixation method.

Figure 78 shows that the mechanical fixation section is split into two main sections. The first investigation (Investigation 1: Geometry & Extraction) aims to confirm the feasibility of the arrowhead concept and ascertain the optimum dimensions of the arrowheads in relation to resistance to an extraction load. The resistance to extraction load was investigated to provide an idea of the achievable primary fixation of the features within the bone. This in turn could be related to loosening resistance as after implantation; the CFRPEEK component would rely purely on these features to withstand *in-vivo* forces experienced prior to osseointegration. There was a risk that arrowheads that were too small would not achieve the primary fixation required, resulting in excessive micromotion and component loosening. Alternatively arrowheads that were too large would be invasive to the patient and may compromise bone conservation. The relationship between geometry and resistance to an extraction load is investigated in Section 3.4.1.

The second area of investigation (Investigation 2: Arrowhead Forming) focuses on the manufacturing technique of the arrowheads. The Arrow-LOK device is manufactured from a solid stainless steel bar by a mechanical metal removal process such as machining (237), however this was not a possible route for the acetabular cup due to the complexity of the shape and instead the component will be injection moulded. This is the primary method of CFRPEEK manufacture and will be used for the acetabular cup as it can rapidly produce complex shapes and is much less labour intensive than machining. However, it is not feasible to generate a mould tool which moulds the component and the arrowhead features in one process as the presence of the overhangs would not allow the part to be released without breaking the mould. If this approach was taken each component would require a new mould tool to be manufactured which would be costly. This was considered to be a non-feasible option by Aurora Medical Ltd as injection moulding was chosen because although the initial

cost outlay is high for a mould tool the subsequent price for individual components on a mass produced scale is low. Machining or wire cutting the arrowhead features from the component after moulding was also not a viable option due to the complex geometry of the arrowhead intersections and the overhangs on the spherical surface. On this basis a novel method of moulding was proposed which moulds the arrowheads from upstanding beams present on the backing surface of the injection moulded component. This method had to be established to make the primary fixation method feasible. Figure 79 shows an example of the outline of the upstanding beam present on the injection moulded component which would be moulded into an arrowhead feature using a secondary technique.

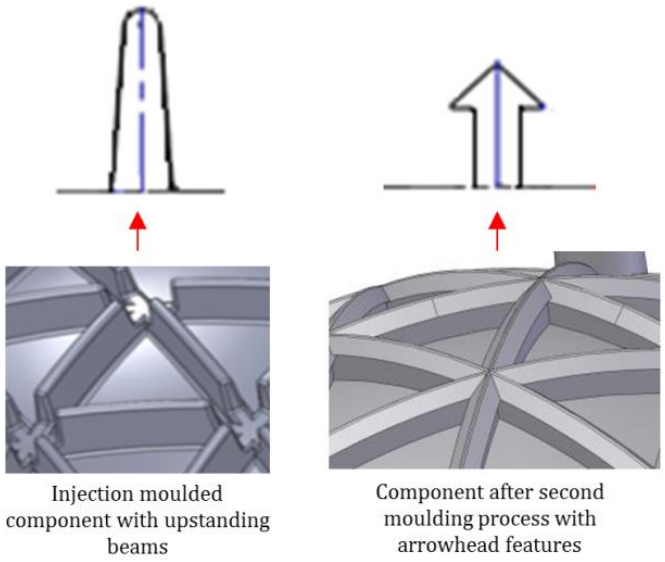

Figure 79: The proposed secondary moulding process will mould upstanding beams on the component (left) into arrowhead features (right).

Figure 78 shows that Investigation 2 is split into three sections. The first section focuses on developing and proving the feasibility of the secondary forming concept on single upstanding beams (Section 3.4.2.1) before extending the technique to multiple sections on the back of the acetabular component (Section 3.4.2.2). The outcomes of each section allowed refinements to be made to the process which improved the state of the reformed material (Section 3.4.2.3).

3.4.1 Investigation 1: Optimisation of arrowhead geometry for augmented fixation

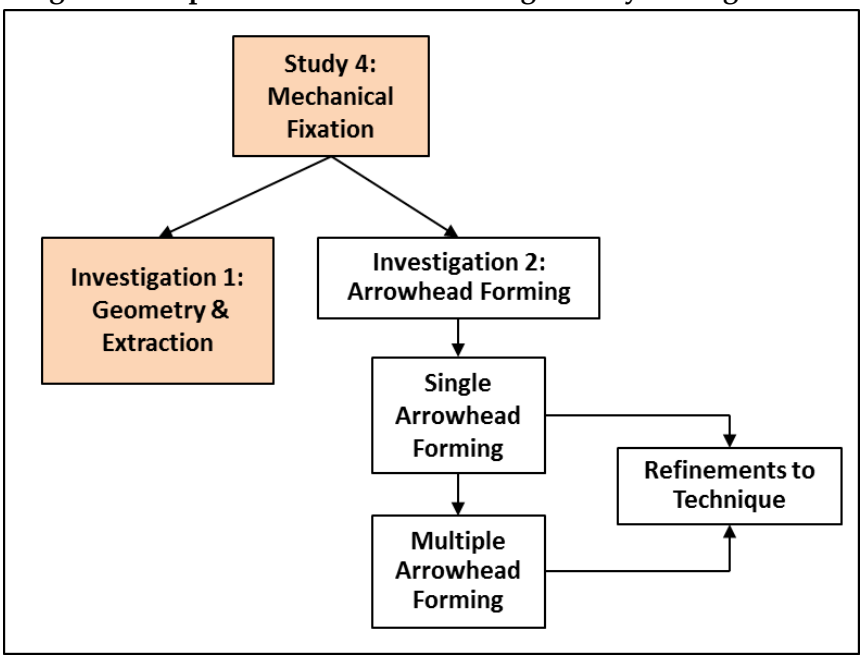

Section 2.3.3 highlighted component loosening to be one of the main causes of revision and it had been suggested that due to the increased deformability of the CFRPEEK component, it would require an alternative approach to achieve adequate primary fixation compared to traditional options. The novel arrowhead concept was described in the previous section and the preliminary design is shown in Figure 77. Aurora Medical Ltd required the optimum geometry of the arrowhead to be determined to maximise degree of fixation.

Materials & Methods

27 CFRPEEK MOTIS cylindrical samples (Invibio Biomedical Solutions) (Ø 30 mm x 7 mm: Figure 80) were machined using diamond tipped tools from extruded rods of CFRPEEK. On the top surface of each sample, four linear arrowheads were machined at a distance of 7.5 mm.

A sample holder was manufactured by Hinkell Ltd (Chessington, UK) to attach the samples to the Instron 5569 electromechanical test machine (Figure 80) which ensured the arrowheads were implanted vertically into the bovine bone.

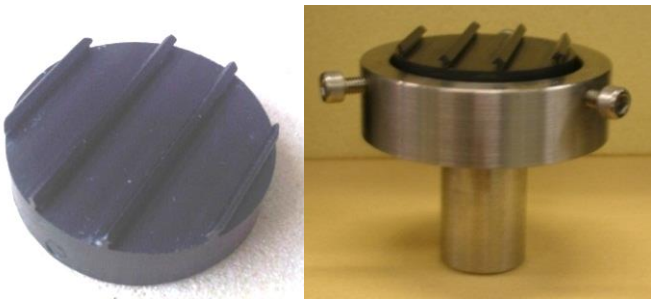

Figure 80: CFRPEEK sample with arrowheads (Left) and sample in holder (Right).

The height (A) and width (B) of the machined arrowheads were varied between 1.2-2.0 mm and 1.5 - 2.0 mm respectively whilst the remaining dimensions remained identical between samples (Figure 81). These ranges were chosen based upon the geometry of the laser sintered beads which are used to aid primary fixation on the ADEPT (MatOrtho Ltd) acetabular component. Table 7 shows these 9 variations. Three samples of each design were tested. To test the concept and due to ease of manufacturing a linear arrowhead pattern (Figure 81) was utilised in the initial programme.

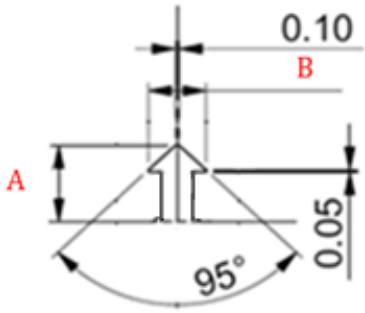

Figure 81: Dimensions of the arrowheads. Dimensions A (height) and B (width) were altered to generate 9 different samples to be tested.

Table 7: Variation in height (A) and width (B) for each sample.

Sample No.	Dimension (mm)	
	A	B
1	1.2	1.5
2		1.7
3		2.0
4	1.6	1.5
5		1.7
6		2.0
7	2.0	1.5
8		1.7
9		2.0

Six bovine pelvises from ~24 month old steers were prepared using a band saw to expose the trabecular bone. Samples with a thickness of at least 25 mm were cut to provide a flat area for sample impaction and to ensure even coverage of arrowheads during testing.

The samples were implanted into the clamped bovine samples under a displacement rate of 0.5 mm/min until the surface of the cylinder was flush with the bone's surface. Once implanted, the sample was fully extracted at a displacement rate of 1 mm/min and the maximum load was recorded. This technique was repeated for each sample. Figure 82 shows the experimental setup.

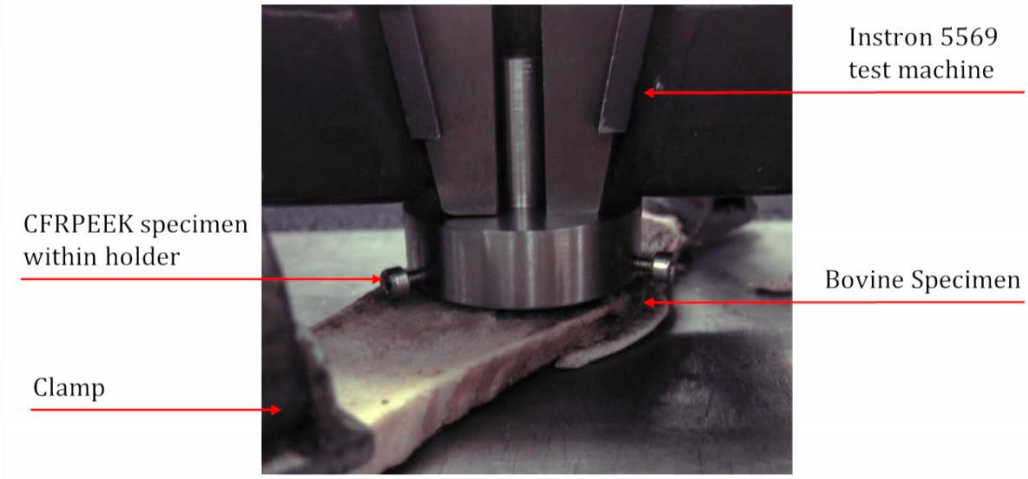

Figure 82: Experimental testing of the arrowhead extraction load.

Results

Table 8 shows the extraction load results for the arrowhead samples. Sample 7 exhibited the greatest extraction load at 131.4 N (S.D +/- 18.1 N) whilst Sample 2 and 3 exhibited the lowest extraction load of 39.4 N (S.D +/- 12.8 N) and 39.4 N (S.D +/- 12.8 N) respectively. Figure 83 graphically represents the average extraction load for each sample. A significant difference was seen between Sample 7 and Samples 1, 2, 3, 4, 6 and 9. No significant difference was seen between Sample 7 and Sample 5 or 8.

Table 8: Extraction load test results.

Sample No.	Impaction result (N)	Standard deviation
1	63.0	14.2
2	39.4	12.8
3	39.4	15.3
4	64.8	10.6
5	85.0	14.2
6	69.3	7.21
7	131.4	18.1
8	101.2	19.0
9	73.9	10.2

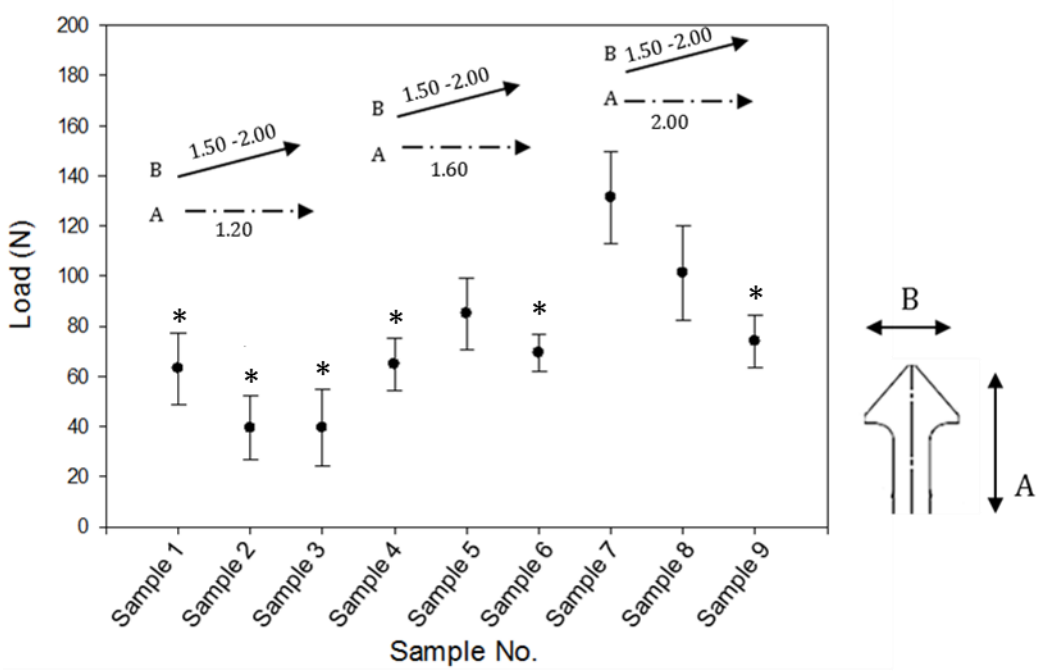

Figure 83: Maximum load results for CFRPEEK arrowheads. Error bars based on one standard deviation where A is the height and B is the width. * indicates a significant difference with Sample 7 which recorded the largest extraction load.

Discussion

Sample 7 (height 2.0 mm, width 1.5 mm) had the highest extraction load within the design constraints set by Aurora Medical Ltd. Sample 7 arrowheads had the largest height (2.00 mm) and the smallest overhang (1.50 mm) (Figure 83). It might have been anticipated that arrowheads with the largest overhangs would have produced the highest extraction load. Samples with smallest overhang generally performed better for each height, suggesting that these samples were easier for the bone to encapsulate.

There were two instances of arrowhead failure (Figure 84) and these were probably due to non-parallel impaction imparting a shear force on the arrowhead. In both cases failure initiated at the arrowhead root where the small 0.25 mm root radius generated a stress concentration. This finding was important as variability in surgical technique may result in off-axis impaction forces which would expose the arrowheads to shear forces. As a result, design alterations were made to the sample and are shown in Figure 85.

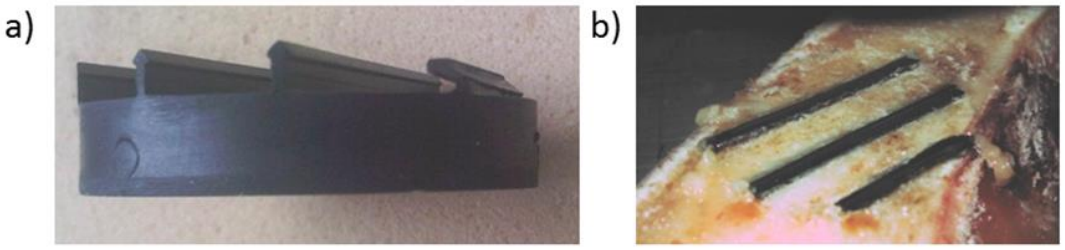

Figure 84: Arrowheads prior to (a) and after implantation (b). Arrowhead failure is shown when the main body of the arrowhead fractures away from the cylindrical base.

The first design modification involved reducing the area of arrowhead coverage on the cup to the load-bearing segments in order to ensure the arrowheads were implanted into a region of adequate bone stock (Figure 23). Section 2.5 outlined the posterior superior and posterior inferior quadrants of the acetabulum as safe areas for placement of fixation features and the design was updated to reflect this placement. In addition, to reduce the likelihood of shear failure, the connected linear design was removed to enable each arrowhead to be its own entity. Therefore if one of the arrowhead sections failed it should not influence or prompt failure in a surrounding feature.

To strengthen the individual sections the arrowhead bodies were tapered. The tapered body of the arrowhead should provide additional support at the root and aimed to reduce the stress concentration with the addition of a larger radius. Figure 85 shows the decrease in area coverage and the individual arrowhead sections. Due to injection mould tool design restrictions, the arrowhead features could not be moulded directly onto the component. In addition, the machining processes necessary to produce these features would be too complicated for a large scale manufacturing process. A secondary moulding process is developed in Section 3.4.2 whereby the arrowheads are moulded from upstanding beams present on the component after injection moulding. Figure 85 shows the updated component design with the upstanding beams present on the backing surface.

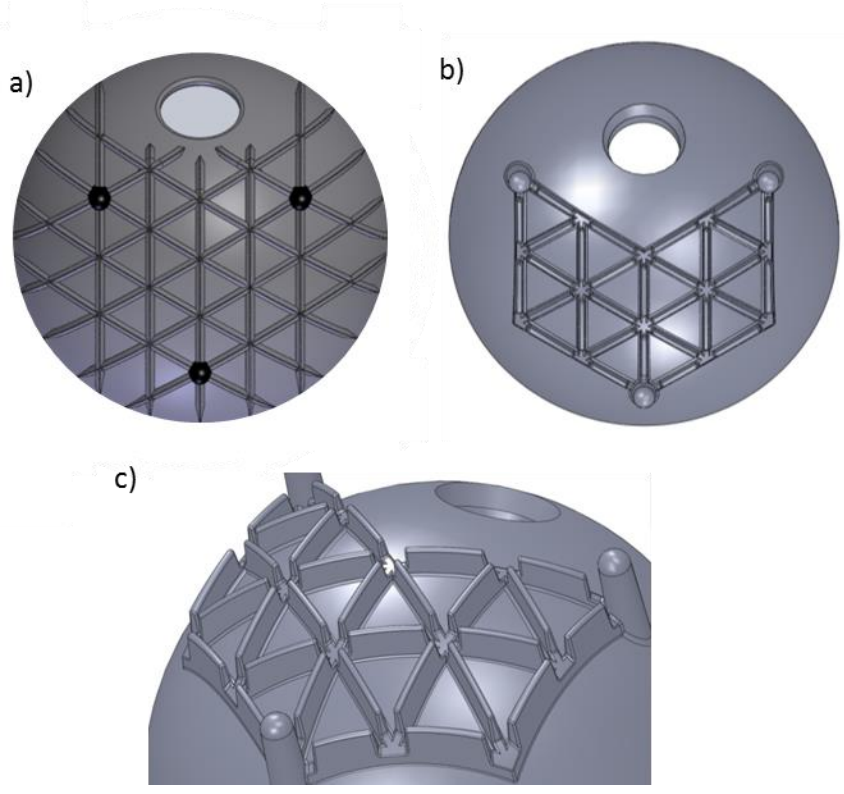

Figure 85: Original coverage of arrowheads (a) and updated model with reduced area of arrowhead coverage and removal of cross-overs (b) and close up of individual tapered upstanding beams (c).

The geometry of the upstanding beams required to form the arrowhead geometry obtained in this investigation (Sample 7) are shown in Figure 86.

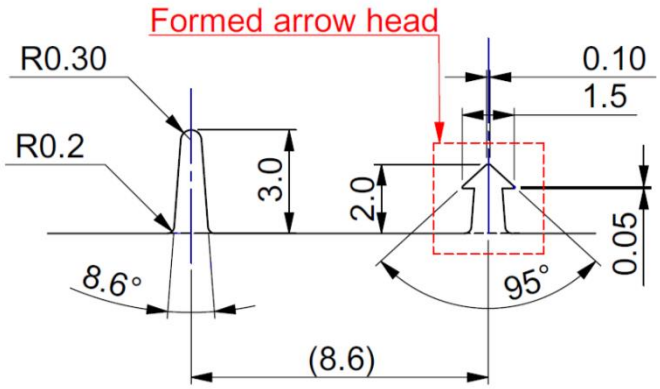

Figure 86: Dimensions of tapered upstanding beam (left) that will undergo a secondary manufacturing process to form the arrowhead (right)

A further objective of this investigation was to confirm that the bone elastically deformed around the arrowheads during implantation. Although visual analysis was not performed after implantation, the recording of an extraction load implied that arrowhead encapsulation had occurred. This was supported by the fact that, bone was present underneath the flat edge of the arrowheads on removal (Figure 87). Nevertheless, this is speculative and to confirm μCT was used in Section 4.5 on an implanted CFRPEEK cup with the design alterations made to the upstanding beams.

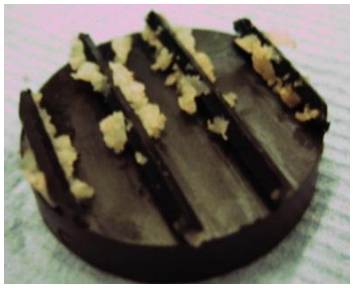

Figure 87: One of the CFRPEEK samples after extraction.

The study and the results must be interpreted with consideration of their strengths and limitations. The analysis was performed using a linear arrowhead arrangement due to ease of machining. However, Figure 85 shows that the arrowheads would be arranged in a cross over pattern on the back of the acetabular cups surface. It is suggested that the linear setup in this study provided the lower bound of extraction resistance as in the full component additional arrowheads would exist at 60 ° angles to the linear pattern. The use of bovine bone as the implantation medium could be considered a limitation as stiffness variation exists in the properties of bone between individual specimens (238). This could explain the large standard deviations observed. Nevertheless, implantation into bovine bone generated a worst-case implantation scenario as bovine stiffness is considerably higher (~2380 MPa (239, 240) than human bone (~552 MPa) (240-242).

This investigation has provided information on the potential of a novel primary fixation method for the CFRPEEK acetabular component proving the feasibility of the idea. The outcomes have indicated the optimum dimensions required and led to specific design alterations to the backing surface of the component. Section 6 investigates these design alterations with particular focus on the response of the bone to the tapered arrowheads. The next section focuses on the secondary manufacturing technique (Figure 78: Investigation 2) employed to produce the tapered arrowheads from the upstanding beam features present on the injection moulded component (Figure 79).

3.4.2 Investigation 2: Arrowhead Forming

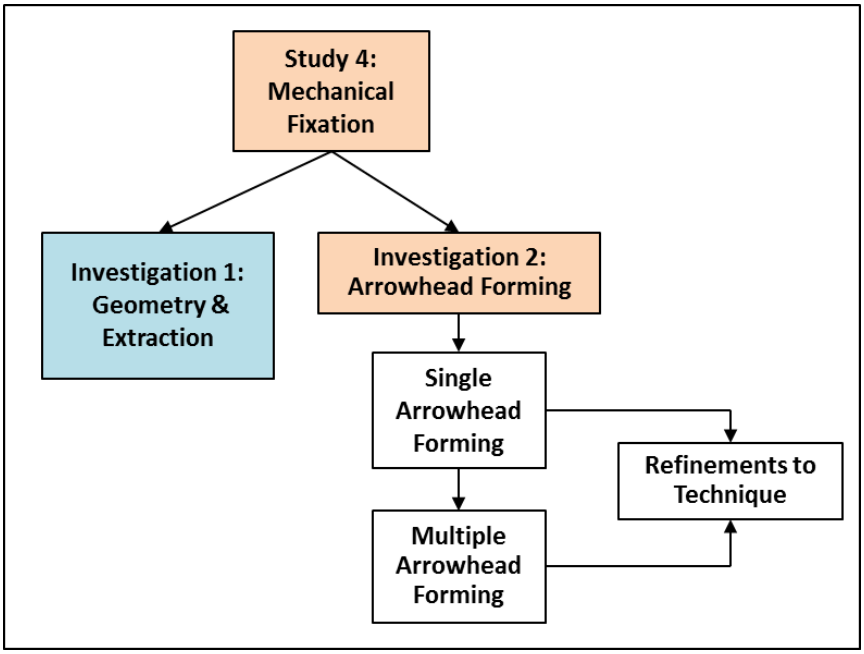

The previous investigation confirmed that the arrowhead features resisted an extraction load; however the method to form the arrowhead from an upstanding beam is yet to be investigated. PEEK is a thermoplastic polymer that can be reprocessed through post-thermoforming. Furthermore under the correct processing conditions, its material properties can be maintained. The response of CFRPEEK to reprocessing is unknown but there is evidence that suggests the mechanical properties of a thermoplastic matrix composite may deteriorate after thermal processing if the processing conditions are not correct (80, 81).

The first part of this investigation explores the reforming technique on individual upstanding beams to identify the optimum processing conditions, before extending the process to reform multiple upstanding beams simultaneously. The final part of this section refines the reforming process based on the outcomes of the previous studies.

3.4.2.1 *Evaluation of the feasibility of the secondary forming technique to produce an arrowhead from an upstanding beam.*

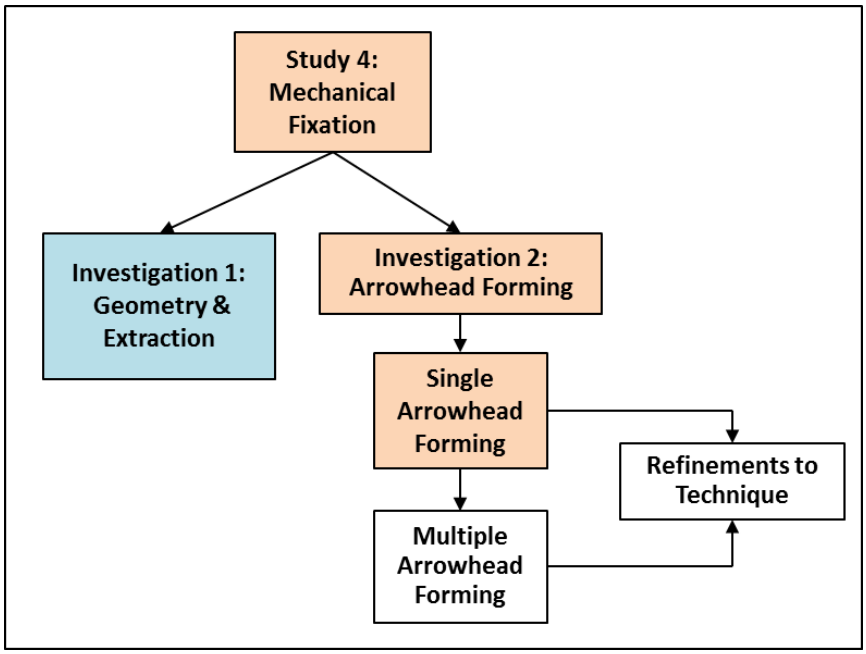

In this investigation, a metal component containing a 'v-shaped' notch was heated to a temperature above the melt temperature of CFRPEEK (~343 °C) and placed on an upstanding beam. It was proposed that to form the arrowhead, the heated metal component would be pressed against the upstanding beam, re-melting its outer surface (Figure 88: Stage 1). When the sample was driven further into the notch, the melted material would be compressed and forced to fill the free space within the notch forming an arrowhead shape (Figure 88: Stage 2 & Stage 3). This type of process is already used in industry to mould tips onto catheters. In this application the tip of the catheter is formed by heat treating the end of a thermoplastic catheter tube until it begins to soften. The softened end is then pressed into a mould which is shaped similar to the end of a sharpened pencil (243). The resulting shape of the tip allows the device to be inserted into the human body with the least amount of trauma to the tissue.

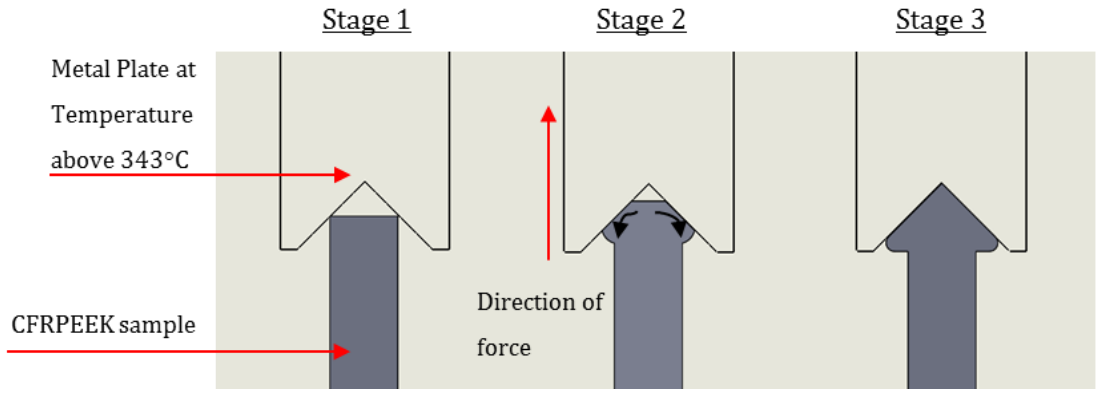

Figure 88: Process of arrowhead formation by re-melting against a 'v-shaped' notch.

This section investigated the proposed reforming technique with particular focus on the effect of varying the temperature of the reforming metal part on the geometry and internal morphology of the reformed features. The wire cutting and machining processes used to manufacture the CFRPEEK samples in the previous investigation (Section 3.4.1) could generate an arrowhead pattern that was within the tolerances specified on the drawings. The two stage manufacturing process for the CFRPEEK arrowheads is unpredictable due to the operator having little control as to how the material reacts to the heated mould tool. It is unlikely that the arrowheads would appear as shown in Figure 79. Any inconsistency between shapes would affect their functionality and therefore the secondary process should be tailored to accurately produce repeatable shapes.

Materials & Methods

Injection moulded CFRPEEK MOTIS upstanding beam specimens were provided by Invibio Biomedical Solutions. Each upstanding beam specimen was cut with a slow speed saw into 7.5 mm wide specimens to replicate the length of each individual upstanding beam sections moulded onto the back of the cup as shown in Figure 89.

Figure 89: Upstanding Beam MOTIS CFRPEEK specimen cut into 7.5 mm wide specimens.

To reform the material, a thermistor controlled digital soldering iron (ST-1000 100W, Toolcraft, UK) was used to heat and control the temperature of a customised copper v-shaped adaptor which attached to the soldering iron (Figure 90) by another customised copper attachment piece which ensured the adaptor's temperature was kept stable by the thermistor.

To control the placement of the notch on the beam each individual specimen was mounted within a 3 mm thick stainless steel sheet with a rectangular cut out. Two separate sheets were placed on top; firstly a 1 mm sheet with oblong cut out and secondly a stopper plate with a circular cut out. The oblong cut out sheet acted as a stopper to control the vertical distance the soldering iron could move on to the beam whilst the circular cut out sheet controlled the placement of the circular v-shaped adaptor on the beam. A mould release agent (227CEE, Marbocote, Cheshire UK) was applied to the v-shaped adaptor as specified in the supplier's technical data sheet to prevent the remelted material from adhering to the adaptor.

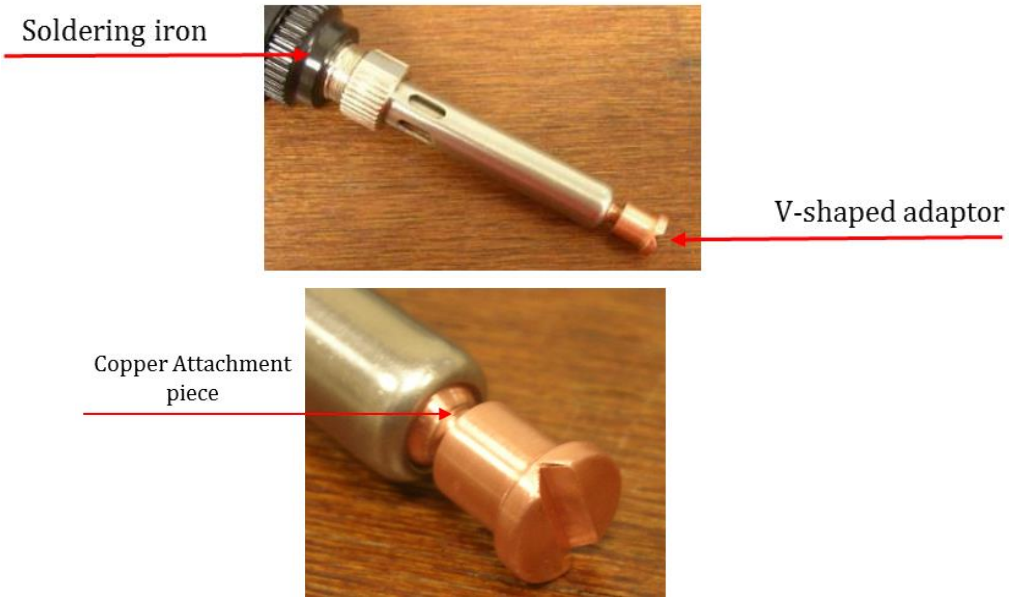

Figure 90: Reforming equipment – Soldering iron with specifically design connector and v-shaped adaptor (bottom).

For reprocessing, the soldering iron temperature was set to the required temperature and left to stabilise. Once stabilised by the thermistor, the v-shaped adapter was aligned with the circular cut out in the top plate and the soldering iron was lowered until the base of the adaptor was flush with the underlying plate. The soldering iron was held for 5 seconds and then removed. The reformed material was left to cool and removed from the holding plates. The height, base thickness and width of the formed arrowhead were measured with digital callipers. These dimensions were compared to the optimum arrowhead width (1.5 mm) and height (2.0 mm) dimensions determined in Section 3.4.1 and shown in Figure 86.
The presence of the thermistor adjacent to the copper adaptor adjusted and maintained the temperature of the v-shaped adaptor allowing the upstanding beams to be reformed at the following temperatures:

i. 343 °C melt temperature of CFRPEEK MOTIS.
ii. 365 °C recommended starting temperature of the rear section of the barrel in the injection mould machine as described by Invibio Biomedical Solutions MOTIS processing guide.
iii. 380 °C recommended starting temperature of the middle section of the barrel in the injection mould machine as described by Invibio Biomedical Solutions MOTIS processing guide.
iv. 390 °C recommended starting temperature of the front section of the barrel in the injection mould machine as described by Invibio Biomedical Solutions MOTIS processing guide.

To determine the internal morphology of the reprocessed specimens, each individual specimen was mounted in epoxy resin for surface preparation and polished to a surface

finish of 1 μm. Visual analysis of the surfaces was performed using an Olympus BH2-UMA microscope.

Results

Table 9 shows the average geometry of the arrowheads produced at each reforming temperature. The most accurate height (2.0 mm) was generated at 380 °C and the most accurate width (1.5 mm) was produced at 343 °C. In all instances, a higher error was seen for the width dimension compared to the height dimension. Figure 91 shows micrographs of a section taken through the centre of each arrowhead. Voids were present in all the specimens although the number of voids increased with reforming temperature. The limited repeatability of the technique was shown by the large variability in geometry and the generation of unsymmetrical arrowheads.

Table 9: Measured height and width of arrowheads reformed at 343, 365, 380 and 390 °C and compared to optimum dimensions determined in Investigation 1 (Section 3.4.1).

Reforming Temperature (°C)	Number of Specimens tested	Reformed Arrowhead Height (mm)	Difference from required height of 2.0 mm (mm)	Reformed Arrowhead Width(mm)	Difference from required Width of 1.5 mm (mm)
343	4	2.30 (SD: 0.11)	0.30	1.65 (SD: 0.12)	0.15
365	4	2.08 (SD: 0.04)	0.08	2.12 (SD: 0.39)	0.62
380	4	1.99 (SD: 0.11)	-0.01	2.30 (SD: 0.18)	0.53
390	4	2.14 (SD: 0.11)	0.14	2.08 (SD: 0.10)	0.58

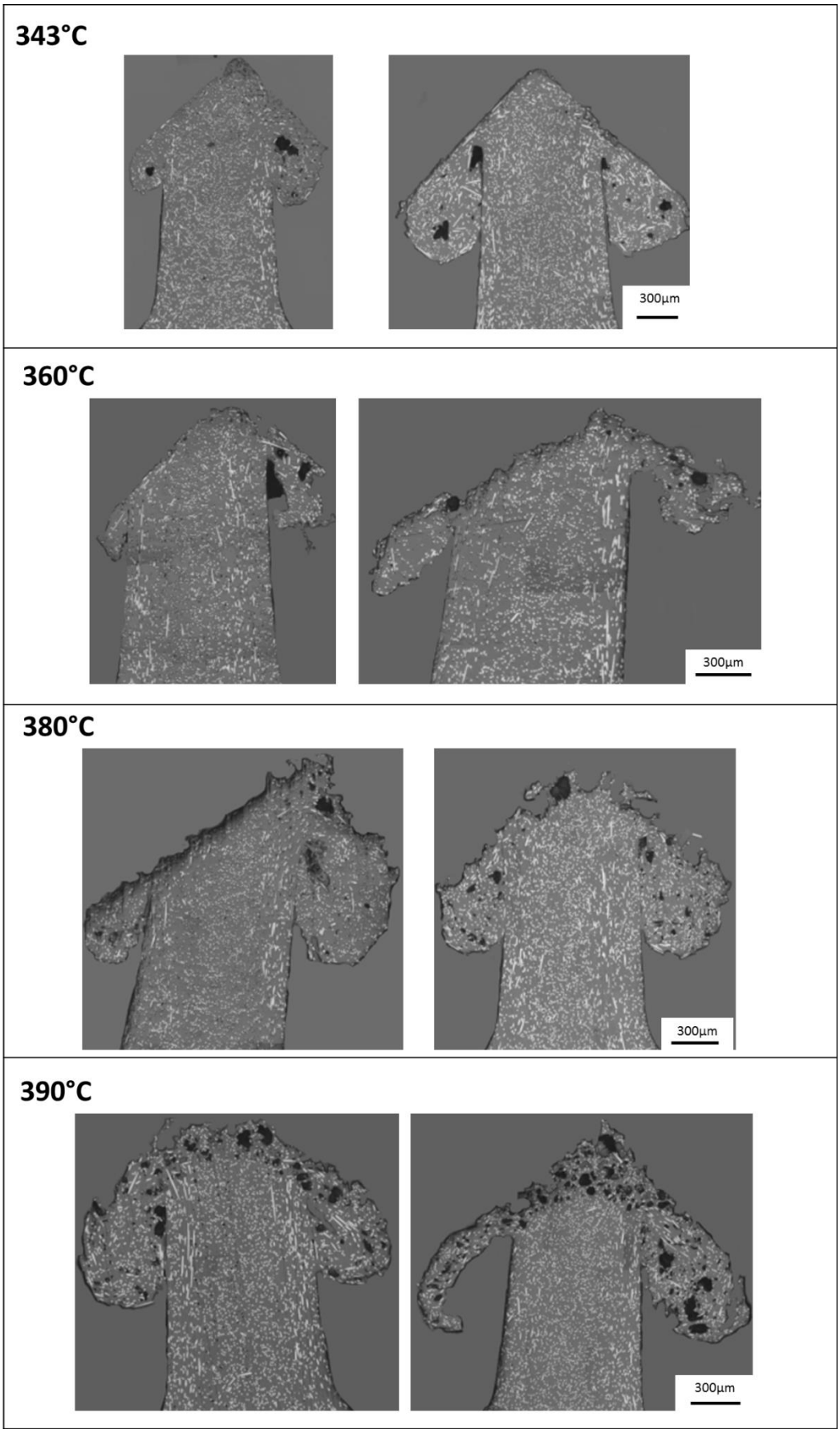

Figure 91: Reformed arrowheads at varying reforming temperatures.

Discussion

Figure 91 illustrates that at all temperatures, the beams were reprocessed into approximately arrowhead shaped features. Table 9 evaluates the accuracy of these features in comparison to the ideal arrowhead outlined in Section 3.4.1 (Figure 86: height - 2.0 mm, width - 1.5 mm). The most accurate arrowheads in terms of the width were produced at a temperature of 343 °C, while arrowheads reformed at 380 °C exhibited the most accurate height. Generally, if the height was close to the ideal arrowhead dimension the width dimension was over 0.50 mm larger than the target width.

The width dimensions exhibited the most deviation from the target geometry and it is suggested that this was due to the current setup not restricting the flow of the melted material in all directions. The stopper plate restricted vertical movement (Figure 92 movement in z direction). However, as the v-shaped notch was open-ended the reformed material could flow along the notch length (Figure 92 in the y direction – red arrows) and was unconstrained in the x-direction ((Figure 92 in the x direction – white arrows). The movement of material along and within the notch meant the material spread out. To constrain the material it is advised that the ends and sides of the notch are closed which should improve the accuracy of the width dimension.

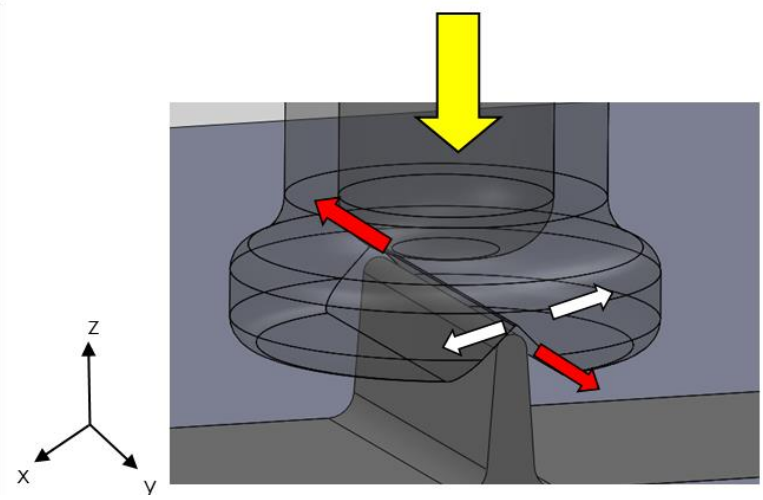

Figure 92: Reformed CFRPEEK is free to move along the x and y-axes but is constrained in the z-axis due to the design of the reforming component.

The target arrowhead dimensions shown in Figure 86 have been selected in order to successfully achieve augmented and micro-interlock fixation. Figure 91 highlights that the reformed arrowheads were often unsymmetrical. It is assumed that this would negatively affect the primary fixation of the arrowhead and it is evident that the current processing method requires refinements to improve the accuracy of reformed shape.

To improve repeatability and accuracy of the reformed features, it is suggested that the thickness of the plate with the circular cut is increased to ensure the adaptor is fully engaged and aligned within the plate prior to initial contact with the upstanding beam. In addition,

an automated method of lowering the reforming piece e.g. with a test machine may generate more accurate results compared to the operator.

As well as the unsymmetrical nature of the arrowheads, voids were observed within the reformed sections at all temperatures. A requirement of the secondary process was to maintain the internal integrity of the material as the presence of voids is known to have detrimental effects on the mechanical properties of polymer composites (80, 81). On this basis, temperatures above 380 °C were considered unsuitable for this application.

Void formation could be due to two main factors; thermal degradation of the PEEK matrix or thermal deconsolidation.

Voids were unlikely to be formed due to thermal degradation as PEEK has superior thermal resistance up to 575-580 °C (9) and this range is significantly higher than the processing temperatures used in this investigation. In addition, the voids in the specimens were irregularly shaped; voids due to matrix thermal degradation would usually take a more circular form as they are generated when gaseous products such as carbon dioxide and carbon monoxide are released from the matrix (244).

Therefore the most likely explanation for void formation is thermal deconsolidation. Deconsolidation is a microstructural deterioration of the originally consolidated composite (81) and can increase interior void content resulting in a deterioration of the mechanical properties of a composite (80, 81). Void growth in thermal deconsolidation can be primarily attributed to three sources: (i) growth of microscopic voids under thermal pressure inside the voids due to an increase in temperature known as thermal expansion of voids, (ii) coalescence of smaller voids into larger ones, and (iii) growth of microscopic voids under the traction of decompaction of fibre reinforcements, which includes the contribution of cavitation (81).

Residual stresses are known to be a factor driving deconsolidation because after the matrix cools, elastic energy of the fibre reinforcement network is stored in the solid injection moulded matrix in the form of residual stresses (81). These stresses result from the higher shrinkage of the matrix compared with the fibres and they are present in all fibre-reinforced polymers, due to their inherent inhomogeneous nature (81). During reprocessing when the material reforms, the stored elastic energy in the fibre reinforcement network tends to be released; this is thought to be one of the driving forces for void formation. Residual stresses can be removed from polymer composites by annealing the material prior to reprocessing (245). Annealing involves raising the composites temperature above the glass transition temperature of the matrix to allow relaxation of the residual stresses to take place (81). It is hypothesised that by refining the reforming technique to include an annealing step prior to reforming, void formation in the arrowheads would decrease. To test this hypothesis, Section 3.4.2.3 investigated whether this pre-treatment reduced the effects of deconsolidation.

Although this investigation showed the ability of reforming individual CFRPEEK beams into arrowhead shapes using the proposed secondary reforming technique, there were aspects to

this study which require further investigation. Firstly, the accuracy of the features was relatively poor and based on the suggestions provided, additional control over the movement of the melted material within the notch should improve the accuracy and repeatability of the shapes produced. Secondly, as discussed previously, refinements to the process should be made to reduce void formation in the reformed material. Finally, the CFRPEEK component has 30 upstanding beams on its backing surface and the current technique would not be viable in terms of time and cost.

3.4.2.2 *Evaluation of the feasibility of the secondary forming technique to reform multiple upstanding beams on an injection moulded cup.*

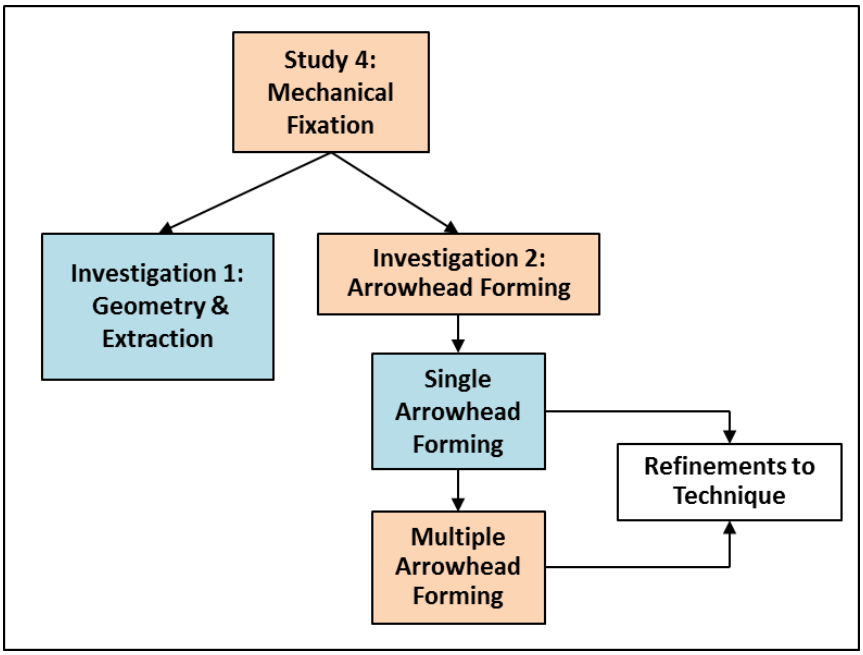

In the previous analysis a v-shaped copper adaptor was used to reform individual upstanding beams, to confirm the feasibility of the reforming technique; however this was considered an unviable option in terms of time and cost for reforming all the upstanding beams on the backing surface of the moulded cup. Therefore, the part shown in Figure 93 a was designed to reform all the upstanding beams in one instance. The reforming procedure remains the same as in Section 3.4.2.1 and involves heating the part and pressing it onto the upstanding beams. However, the part contains a series of interconnected v-shaped notches present on the underside of the part which coincide with the upstanding beam positions on the component (Figure 93 b). It is proposed that the part is placed onto the component with the upstanding beams resting within the v-shaped notches and externally heated (Figure 93 c). Once the part reaches the ideal reforming temperature it can be pressed down onto the beams and the remelted material reforms into arrowheads within each notch. External heating is required as the part cannot be heated using the soldering iron due to its large size. Induction heating is proposed due to its rapid and repeatable heating cycles. This study investigates the heating conditions required to reform the upstanding beams using induction

heating and assesses the internal morphology of the reformed structures produced using this method.

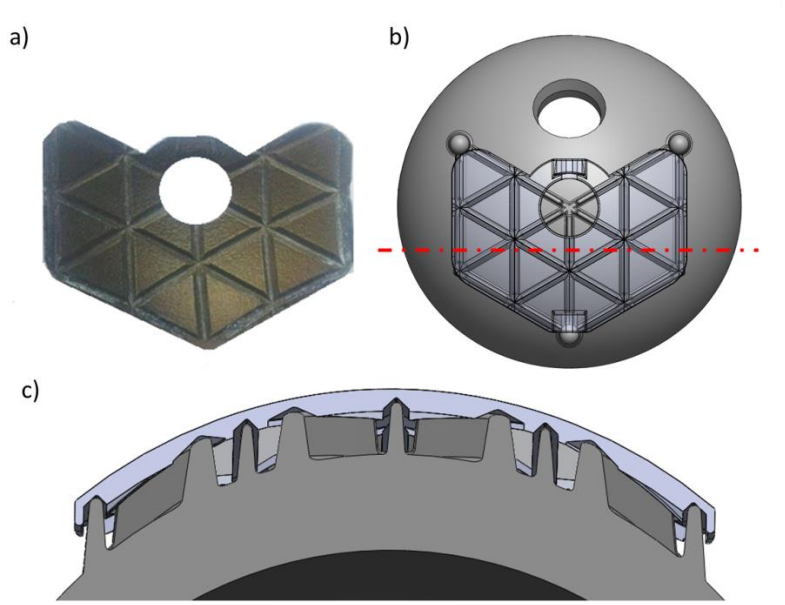

Figure 93: a) Reforming part designed to reform all upstanding beams simultaneously. b) Reforming part placed upon the upstanding beams on CFRPEEK cup. c) Cross section through the component and reforming part showing the upstanding beams within the v-shaped notches on the reforming part. (Red line indicates location of cross section)

Materials & Methods

Three CFRPEEK MOTIS acetabular cups with geometry shown in Figure 85 were injection moulded by Ensinger Ltd (Nufringen, Germany). The reforming part was manufactured by 3T (Newbury, UK) using direct metal laser sintering due to the complex design of the part. It was made from maraging steel 1.2709 which is used in contemporary injection mould tool materials.

A trial test was conducted to determine the approximate induction heating settings which raised the temperature of the part to 343 °C. This was conducted by applying three different heat sensitive paints to the outer surface of the reformed part and altering the heat ramp and exposure time until the paint reacted. The indicating temperatures chosen were 274 °C, 316 °C and 343 °C (Tempilaq, Tempil, Illinois, USA). The part was heated with an EASYHEAT 0224 (Ambrell Ltd, UK) induction heater. Two power ramps were applied to the part in order to first achieve the required reforming temperature and the second to hold the part at the required temperature whilst upstanding beam reforming took place. The settings were adjusted until the 343 °C paint reacted. The successful settings for the first and second ramp were found to be 300.51 A for a time period of 4 seconds and 170 A for a time period of 4 seconds respectively.

Once the initial induction heating settings were established a cup was mounted onto an inclined base plate to ensure the upstanding beams were vertical and this was placed inside the induction heater coil (Figure 94). Ceramic spacers 1 mm thick were placed between the

upstanding beams to control the height that the reforming part could press down onto the upstanding beams. A mould release agent (227CEE, Marbocote, Cheshire, UK) was applied to the reforming part as specified in the supplier's technical data sheet. The reforming part was placed over the upstanding beams and the induction heater was set to apply the power outlined in the trial investigation. Once the heating cycle was applied, the reforming part was removed from the reformed upstanding beams. The power settings were then altered depending on the extent of reforming.

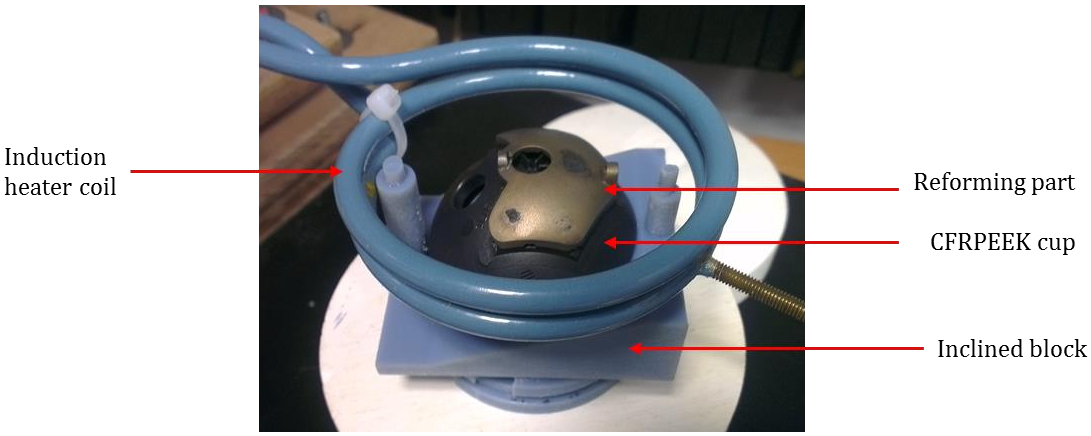

Figure 94: Reforming assembly within the induction heater coil.

To investigate the upstanding beams internal morphologies, Microfocus computed tomography was used. The parameters are described below and the reader is directed to Section 4.1.1 for a description of microfocus computed tomography. Micro X-ray computed tomography measurements were carried out using a custom 225 keV Nikon/Metris HMX ST scanner (Nikon Metrology NV). An X-ray tube potential of 115 keV with a tungsten reflection target was found to satisfactorily penetrate the samples, with a reasonable contrast-to-noise ratio being achieved between the air and CFRPEEK component. A voxel resolution of 32 µm was achieved, implying reasonably confident detection of voids > 64 µm (i.e. being two order of two or more voxels across (246)). The projection data for each scan consisted of 3142 projections taken over approximately 4 hours. Projections were reconstructed into 3D volumes using CTPro via filtered-back projection (simple Ram-Lak filter). In addition to obtaining µCT images of the three reformed components an unreformed injection moulded component was also imaged for comparison.

Void content was analysed on the reconstructed 3D volume using the commercial package VGStudio Max 2.1 (Volume Graphics, Heidelberg, Germany) and features of interest were identified and segmented. Semi-automatic techniques were used to analyse the voids. An automatic 3D seed growth tool was used to outline the voids and each acetabular component (Figure 95b). This process is called region growing and it groups neighbouring pixels or a collection of pixels of similar properties into larger regions (247). The 3D tool segments voxels by adding all adjoining points of a defined seed point that are within a tolerance with respect to the mean grayscale value of the selection (248). As the grayscale values for the

surrounding air and voids were similar, each component was segmented from the air using an erode/dilate operation (249). The outline obtained in the region growing command was expanded (dilated) by a specified number of voxels until all the voids within the component were selected (Figure 95c). Once the voids were bound within the enlarged component outline, the erosion command was implemented which contracted the outline by a specified number of voxels to reduce it back to outline of the component. The component and the voids were then extracted as a separate volume of interest. The voids were extracted from this new volume using the exact minimum in the greyscale histogram between the void and the CFRPEEK matrix peaks, this volume was then segmented so the voids remained.

In some instances the sides of the arrowhead did not completely fold over so that they touched the main body of the arrowhead (Figure 95c). The separating distance between these areas was small, between 1-2 voxels and during dilation the outline overlapped at this point and part of the air was enclosed in the outline (Figure 95d). Therefore when the voids were segmented this region was considered a void as the grayscale values between the air and voids were similar. To segment, the air fragments, the region growing command was reapplied using a smaller tolerance which allowed these areas to be segmented and deleted from the region of interest (Figure 95f). Figure 95f shows the voids highlighted in red and the surrounding air enclosed during the dilation steps (blue). The red sections were removed from the analysis when the ROI volume was extracted. Due to the close proximity of the component inside the tube during scanning, parts of the neighbouring component were sometimes enclosed. The purple section in Figure 95f shows this section. These sections were also removed during the region growing stage and eliminated from the main body of the analysis using the same technique as the air segments.

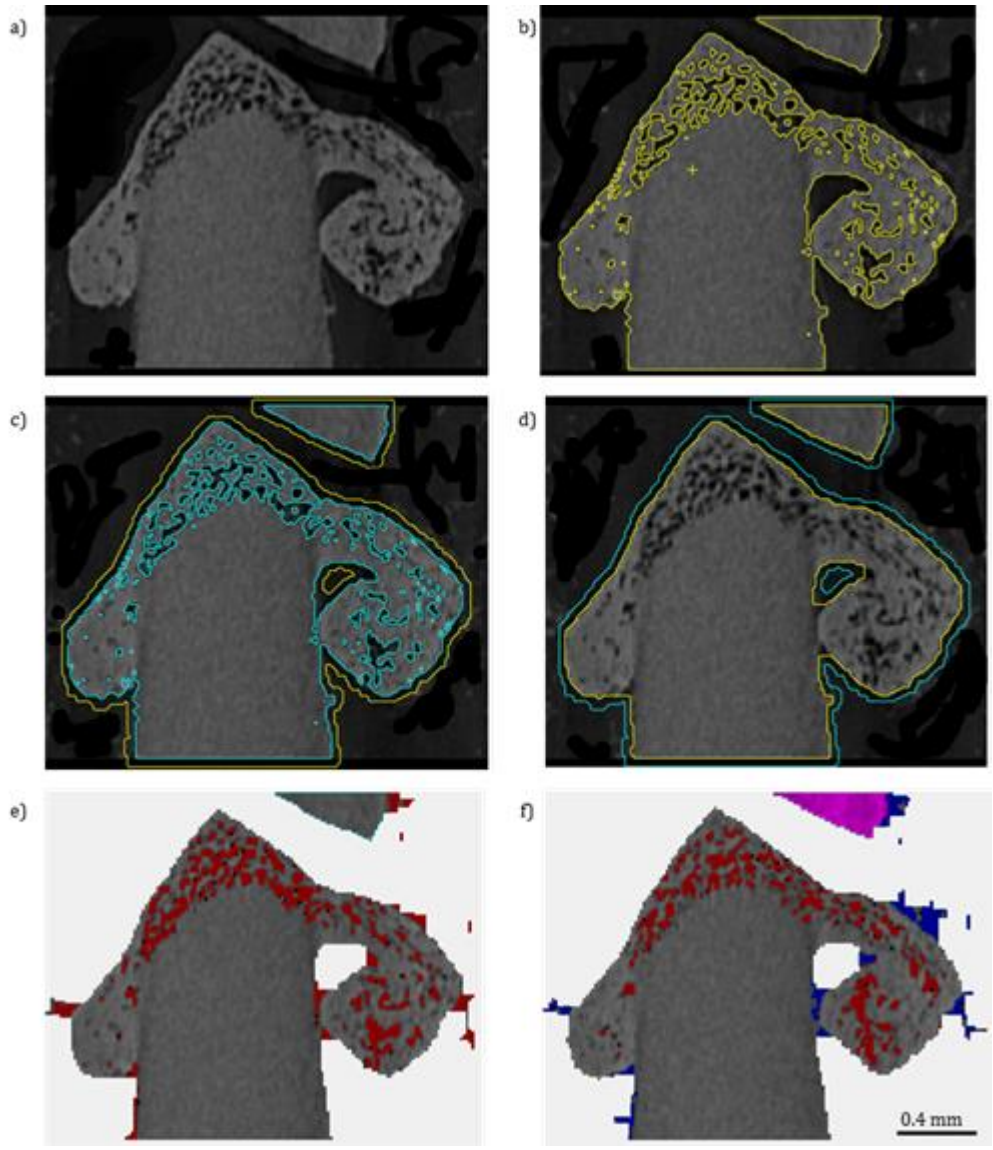

Figure 95: Steps to obtain segmentation of voids from the component. a) Original volume, b) 3D region growing to select outline of component and voids, c) Dilation to contain voids (blue) inside enlarged yellow outline of the component, d) Erosion to return outline to actual component outline, e) Pixel value with a grayscale value close to one (black) are the voids and are highlighted in red, f) Region growing is used to segment out material which are enclosed air segments and neighbouring components (purple and blue).

Once the voids were segmented the fraction of void space within the arrowheads was calculated using equation [7].

$$\boldsymbol{n} = \frac{\boldsymbol{V_v}}{\boldsymbol{V_T}} \qquad [7]$$

where V_v is the volume of void-space and V_T is the total of bulk volume of material including the solid and void components. The volume values were obtained from the number of voxels in each segmented section.

Results

Table 10 shows that the induction heater settings were altered from the original heat paint analysis in order to reform the upstanding beams and this was proposed to be due to heat being transferred from the part into the CFRPEEK component. Therefore to keep the component at 343 °C additional power was required.

Figure 96: Test 1 highlights that reforming was restricted to the outer beams whilst the remaining beam remained unaffected. The cross section taken illustrated that these reformed sections did not take an arrowhead form and contained voids.

Exposure to additional heating in Test 2 increased the region of reforming coverage, although most of the central beams were not affected. The outer beams were reformed into a shape which more closely represented an arrowhead, although voids were present in all of the reformed material.

Figure 96: Test 3 shows that the area of coverage increased further when the component was exposed to a prolonged heating cycle and an arrowhead outline was more prominent in the reformed features. Nevertheless, void formation was dominant in all the reformed structures and the central beams were still unaffected.

Table 10: Heating cycles settings.

Test	Heating cycle		Outcome
	Ramp	Power (V) and Time (s)	
Initial heat paint analysis	*1*	300.5 for 4 s	*Reaction from 343 °C paint*
	2	170 for 4 s	
1	1	300.5 for 4 s	Minimal reforming only outer upstanding beams slightly reformed.
	2	170 for 4 s	
2	1	300.3 for 5 s	Slight increase in area of reforming, central beams remain unreformed
	2	190.4 for 5 s	
3	1	305.5 for 5.3 s	More upstanding beams reformed and arrowhead geometry more evident.
	2	180.7 for 7.5 s	

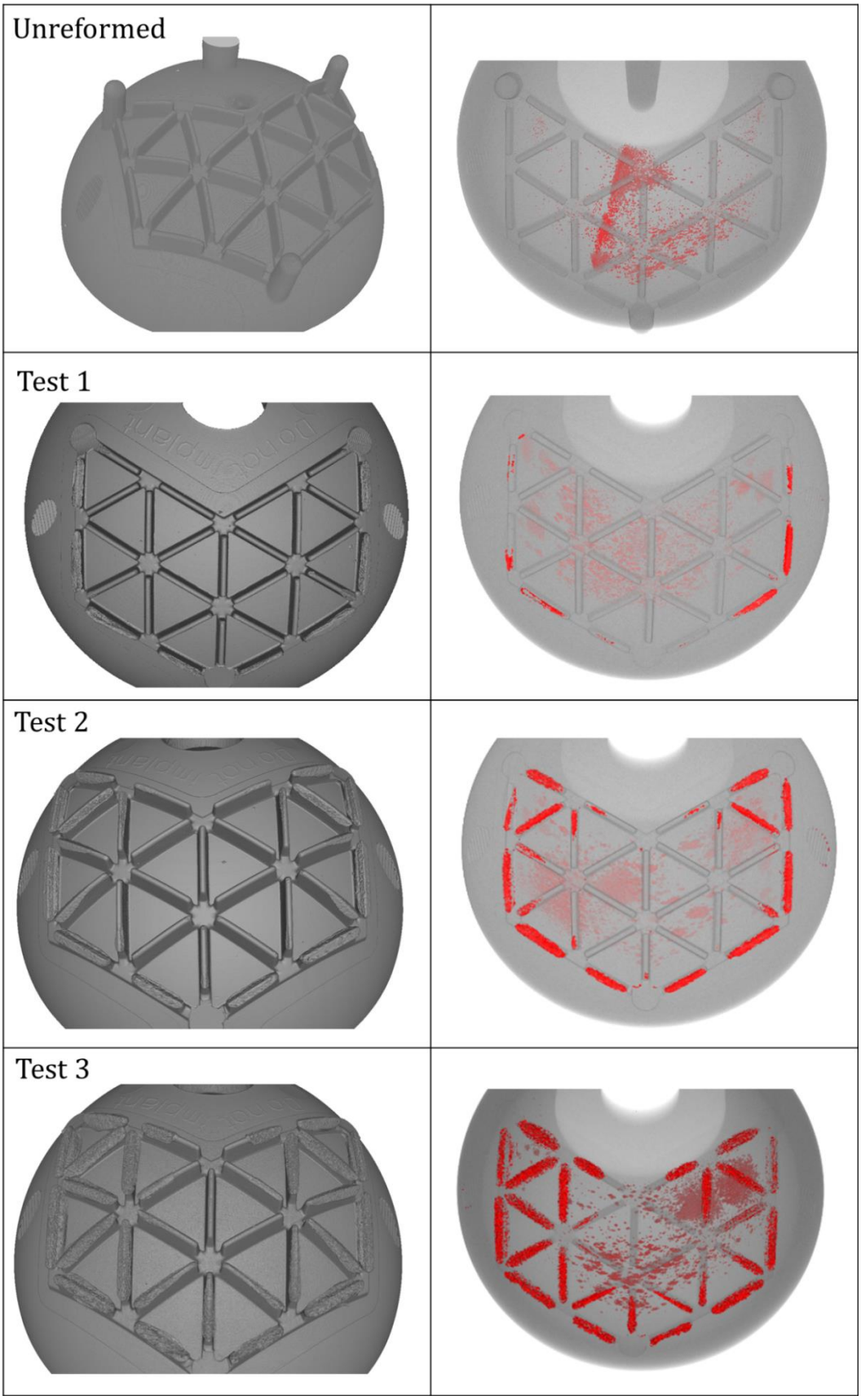

Figure 96: The extent of upstanding beam reforming for each test with the voids within the reforming structures highlighted in red (right)

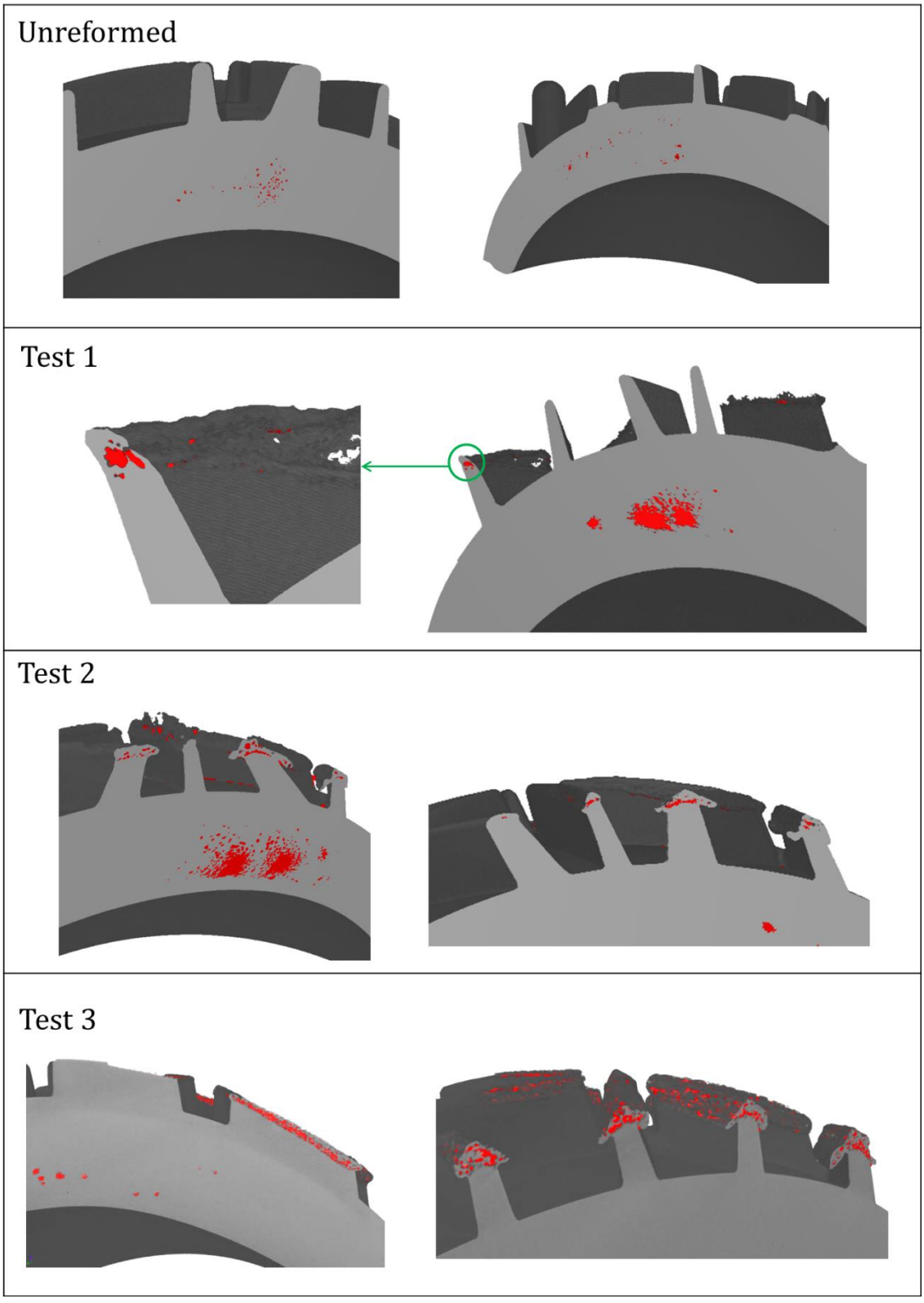

Figure 97: Cross sections taken through the arrowhead features showing the generation of voids within the reformed material.

Table 11: Volume of voids within each component.

Component ID	Volume of voids within component (%)
Unreformed	0.12
Test 1	0.27
Test 2	0.61
Test 3	0.76

Discussion

Figure 97 shows that the upstanding beams were reformed into features which resembled arrowheads. This highlighted the potential of the secondary reforming technique; however refinements are required due to void presence and geometrical inaccuracies.

The figures show that the area of reforming increased as the power and exposure time increased. However, in all instances there was uneven distribution of reforming with the outer upstanding beams reforming before the central beams. Test 1 showed that only the outer sections were remelted and the short exposure time restricted the ability for the material to reform into an arrowhead shape meaning the induction heating settings were not suitable for this application. A longer exposure time in the initial ramp and a higher power and exposure time in the second ramp (Test 2) reformed additional upstanding beams however the central sections remained unaffected. In Test 3, where the power and exposure time of the initial ramp were both extended, 26 out of the 30 beams showed some evidence of reforming.

Voids were present within the main body of the injection moulded component prior to reforming. Section 2.4.2 discussed the negative effects that void presence has on the mechanical properties of a reinforced composite component (80, 81) and it was hypothesised that inadequate holding time or pressure resulted in insufficient material in the acetabular cup mould. Although voids were not identified in the upstanding beams, voids smaller than 62 μm (2 voxels in size) may still be present but the image resolution meant that they could not be confidently segmented.

Table 10 shows the induction heating schedule for the experiment; a higher power and longer exposure time resulted in successful reforming. The change in settings from the trial analysis could be due to heat being transferred into the CFRPEEK component. The absence of paint led to difficulty determining the maximum temperature experienced by the reforming part. The heating cycles should be assessed further with the use of a heat sensitive camera which will allow the temperature profile across the component's surface to be assessed, highlighting any non-uniformity in the heating process.

Increased heat exposure improved the resulting reformed shape with the features shown in Figure 97: Test 3 representing an arrowhead shape more so than the features in Test 1.

Again thermal deconsolidation is thought to be the main cause of void presence in the reformed material. This could have existed if inadequate pressure was applied during reforming meaning insufficient constraint of the material within the notches of the part.
The variability across the reformed surface may be related to temperature gradient effects across the reforming component, with the outer edges being at a higher temperature than the centre. This gradient may have been generated due to the geometry of the part and its orientation within the coil. Additionally, a radius of curvature that was too small on the reforming piece could explain why the outer beams were reformed more than the central ones as they would engage with the reforming part first. This may have occurred if the part was out of tolerance initially or if the repetitive cycles of heating and cooling resulted in the component deforming (250). However, it is difficult to identify which of these is correct as dimensional analysis was not conducted prior to reforming.
Regardless of the number of beams that were reformed or the obtained arrowhead accuracy, voids were still present in the reformed material and this is a critical factor which should be addressed to ensure the material maintains its mechanical properties. Deconsolidation has been identified as one of the main driving factors of void formation due to the release of residual stresses generated when the part was injection moulded. Annealing has been proposed as a method to reduce this effect. The following section investigates the effect of annealing on the void content in the reformed material.

3.4.2.3 *Pre-reforming treatment to reduce void content in reformed specimens*

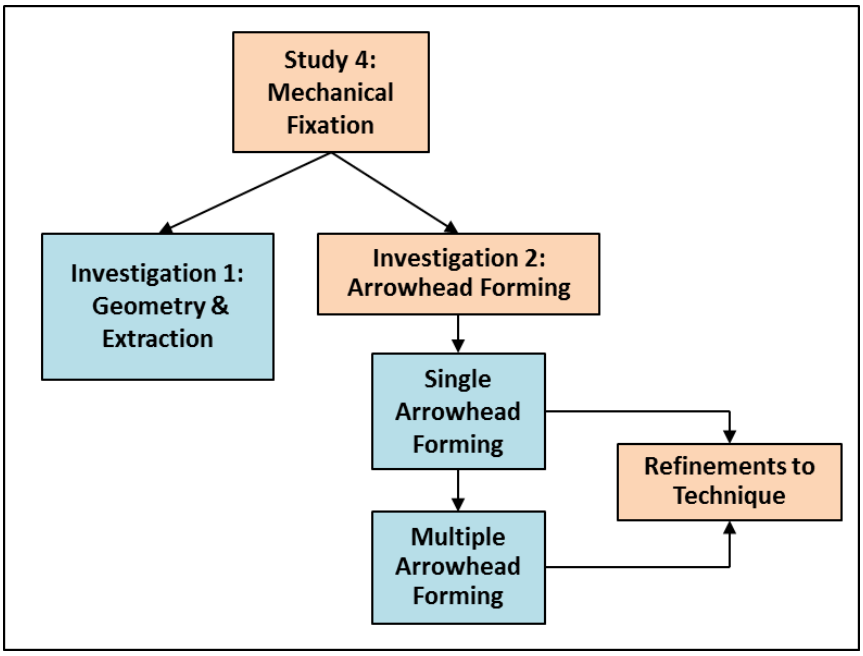

Annealing (206) was identified in the last two investigations as a preconditioning process that could be used to reduce residual stresses in composites. This investigation focuses on identifying whether annealing could be applied to the material prior to the secondary manufacturing technique to reduce void generation in the reformed features.

Materials & Methods

An injection moulded CFRPEEK MOTIS (Invibio Biomedical Solutions) acetabular cup (Figure 98) was provided by Ensinger Ltd. 12 upstanding beams from the outer surface of the component were removed from the main body of the acetabular cup using a slow speed saw.

Figure 98: CFRPEEK acetabular cup from which upstanding beams were individually removed.

Six of the upstanding beams were heated in an air circulating oven (BINDER FED 53) for 3 hours at 150 °C in line with the annealing conditions set out in the Invibio Biomedical

Solutions CFRPEEK MOTIS processing guide. After 3 hours the specimens were slowly cooled. All upstanding beams were reformed using the soldering iron technique described in Section 3.4.2.1. It was observed from reforming of the first 3 annealed beams that the beams were not being reformed successfully. Therefore, the reforming temperature was increased to 350 °C. To investigate void generation the upstanding beams were analysed using μCT. Micro X-ray computed tomography measurements were carried out using a custom 225 keV Nikon/Metris HMX ST scanner (Nikon Metrology NV). An X-ray tube potential of 100 keV was used with a tungsten reflection target was found to satisfactorily penetrate the samples, with a reasonable contrast-to-noise ratio being achieved between the air and CFRPEEK. A voxel resolution of 15 μm was achieved, implying reasonably confident detection of voids > 30 μm (i.e. being two order of two or more voxels across (246)). The projection data for each scan consisted of 3142 projections taken over approximately 8 hours. The systems performance verification methodology is described in Section 4.1.1. Projections were reconstructed into 3D volumes using CTPro via filtered-back projection (simple Ram-Lak filter).

Void content was analysed on the reconstructed 3D volume using the commercial package VGStudio Max 2.1 (Volume Graphics, Heidelberg, Germany) and features of interest were identified and segmented. Segmentation was achieved by applying the techniques used in the previous analysis (Section 3.4.2.2, Figure 95). Once the voids were segmented the fraction of void space within the arrowheads was calculated using equation [7].

Results

Figure 99 and Figure 100 show the rendered volumes of the reformed upstanding beams with the segmented voids highlighted in red for both specimen types. Table 12 illustrates the void fraction for each specimen type. The non-annealed specimens contained on average 6.52 % (S.D: 1.95 %) voids compared to the total volume. The annealed specimens contained on average 0.13 % (S.D: 0.07 %) voids compared to the total volume.

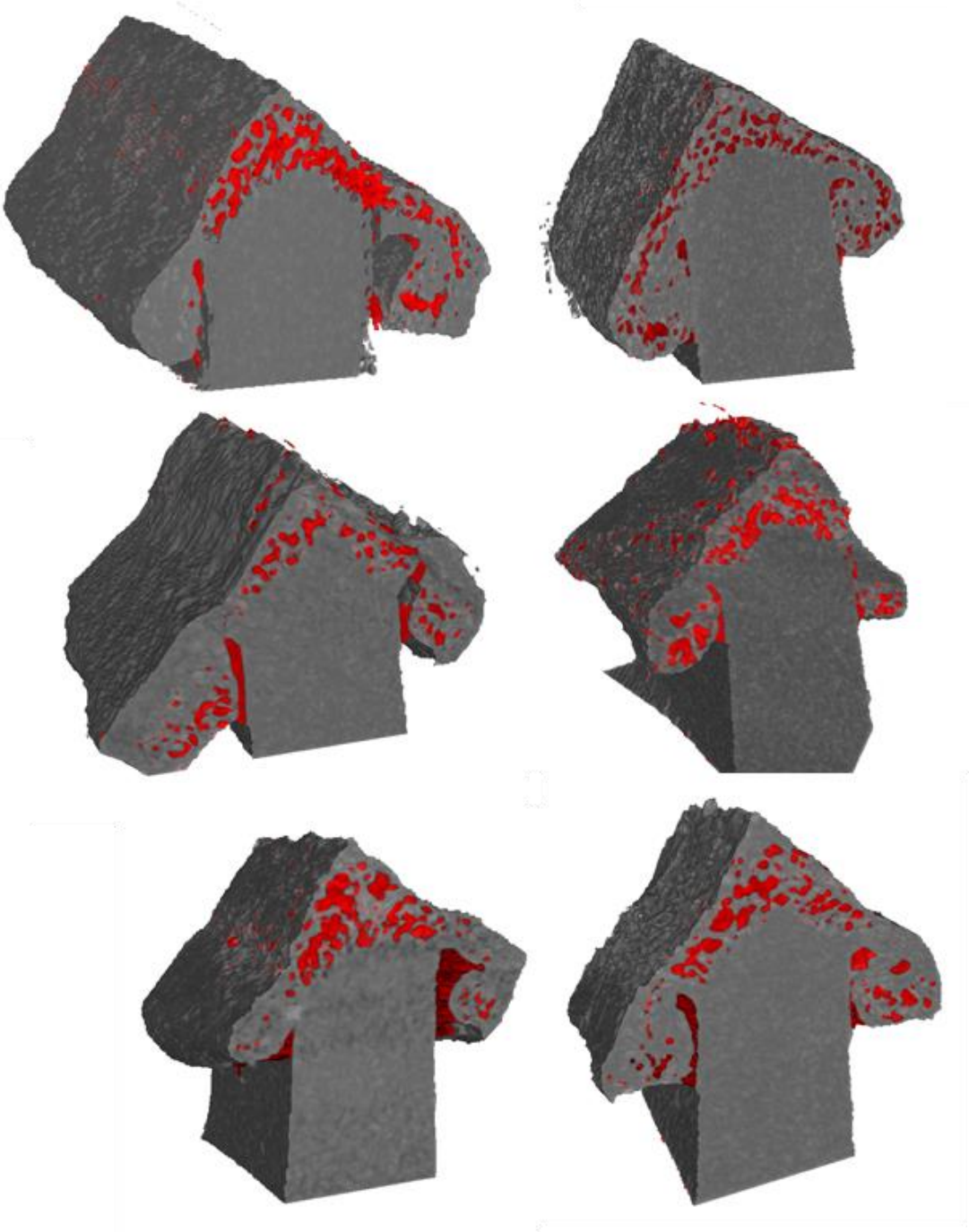

Figure 99: Arrowheads produced from non-annealed upstanding beams.

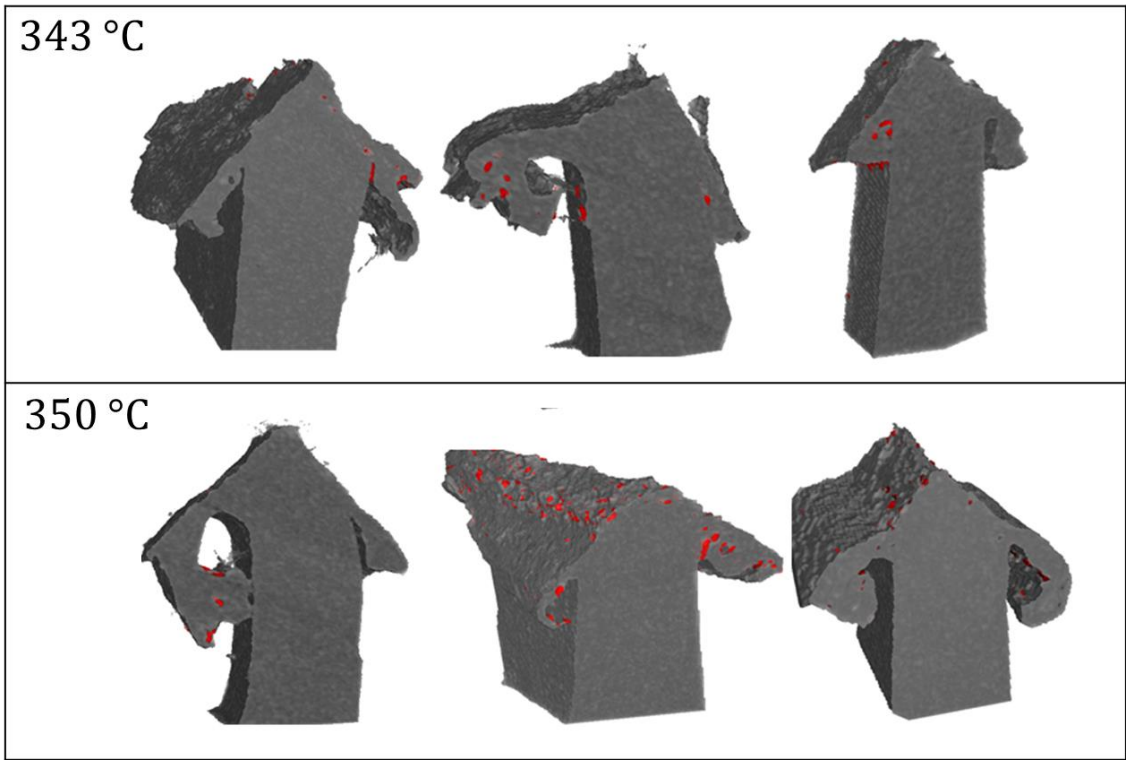

Figure 100: Arrowheads produced from annealed upstanding beams.

Table 12: Percentage Void fraction in the Non-annealed and annealed reformed arrowheads.

Number	Volume fraction (%) for each specimens type	
	Non-annealed	**Annealed**
1	9.39	0.06
2	8.06	0.05
3	3.35	0.17
4	5.80	0.19
5	5.39	0.24
6	7.13	0.09
Average	6.52	0.13
Standard Deviation	1.95	0.07

Discussion

Quantification of average void fraction for the annealed and un-annealed specimens demonstrated that the difference in void content was significant (Table 12: $p<0.05$). This showed that annealing reduced void generation in the reformed material.

Figure 99 shows that the outline shape of the un-annealed specimens resembled an arrowhead with overhangs evident as a result of the upstanding beam pressing into the v-shaped notch. There was a decrease in geometrical accuracy of the arrowheads produced after annealing highlighting unsymmetrical and poorly formed overhangs (Figure 100). This decrease in accuracy could be related to lack of controllability of the soldering iron and the

increased pressure applied to ensure the v-shaped adaptor was flush with the stopper plate during reforming. Certain refinements could be made to the technique to improve repeatability and accuracy of the reformed features and these were discussed in Section 3.4.2.1.

The role of pressure in void generation has been discussed in Section 3.4.2.1; however it was also observed that the temperature was increased for successful reforming of the annealed specimens. It is known that exposure to temperatures above the glass transition temperature can alter the crystallinity and the glass and melt temperatures of a thermoplastic (245, 251). Semi-crystalline polymers generally change their physical properties when they are heated to temperatures near their melting point as there is reorganisation of the chain structure. Studies (251-253) have shown that this reorganisation affects the melting profile of PEEK, increasing the melting temperature (T_m) when the material is annealed quickly and at high temperatures (> 300 °C). It is unlikely that this was the reason behind the need to increase the soldering iron temperature as the annealing temperature was significantly lower (150 °C) and the rate of temperature increase was slow (20 °C per hour). A possible explanation could be that the connection between the v-shaped adaptor and the copper connector was less secure than in the previous study meaning heat transfer was not as effective (Figure 90). This is a hypothesis and to determine whether the need to increase the soldering iron temperature is related to a change in melt temperature, a differential scanning calorimetry (DSC) investigation should be performed to identify T_g and T_m of the un-annealed and annealed material.

This study has shown that void content can be reduced by annealing the material prior to reforming but certain aspects relating to the effect of the annealing process on the melt behaviour of the material should be investigated in future studies. The annealing step is extended to a full acetabular component in Section 4.5.2.

3.4.3 **Conclusion of Primary fixation analysis**

The objective of this section was to develop and evaluate a novel primary fixation approach using the principles of augmented and micro-lock fixation methods. The approach was based on an arrowhead idea which is intended to anchor the cup into the bone when it elastically deformed around the arrowhead features after implantation.

The concept was proven through a series of extraction investigations (Section 3.4.1) in which the machined arrowheads were implanted into animal bone and the extraction load was recorded on removal. The experiment investigated arrowheads with varying heights and widths and it was determined that an arrowhead with 2.0 mm height and 1.5 mm width produced the greatest resistance when removed from the bone. The investigation prompted a series of design changes including reducing the arrowhead coverage area and making the body of the arrowhead tapered.

A secondary manufacturing technique was proposed (Section 3.4.2 which exploited the material's ability to be reprocessed and aimed to melt upstanding beams on the external

surface of the CFRPEEK cup and reform them into arrowhead shapes. A key requirement of the secondary technique was to maintain these properties especially the mechanical performance. Section 3.4.2.1 performed initial reforming experiments on individual beams to identify the ideal reforming temperature which was confirmed to be the material's melt temperature of 343 °C. While arrowhead features were achieved, internal voids were generated, which were known to degrade the mechanical properties of composites (80, 81). The individual process was considered unviable as each acetabular cup has 30 beams on its backing surface making it uneconomical for large scale manufacturing. Therefore, the technique was extended in Section 3.4.2.2 to reform the upstanding beams in a single process using a specifically designed part. However, void formation recurred with this setup. Deconsolidation was identified as a potential driving factor for void generation and annealing was hypothesised as a method to reduce its effects.

The final part of the investigation refined the reforming process by investigating the influence of annealing on void formation in the reformed part. It was found that annealing significantly reduced void formation but at the expense of the geometrical accuracy.

The studies have shown that there is potential for the proposed novel primary fixation technique and the secondary manufacturing technique used to produce the features. The outcomes have also highlighted areas for further refinement of the reforming process to improve the repeatability and accuracy of the reformed features.

4 Assessment of Implantation and Initial Post-operative Conditions of the Acetabular Component

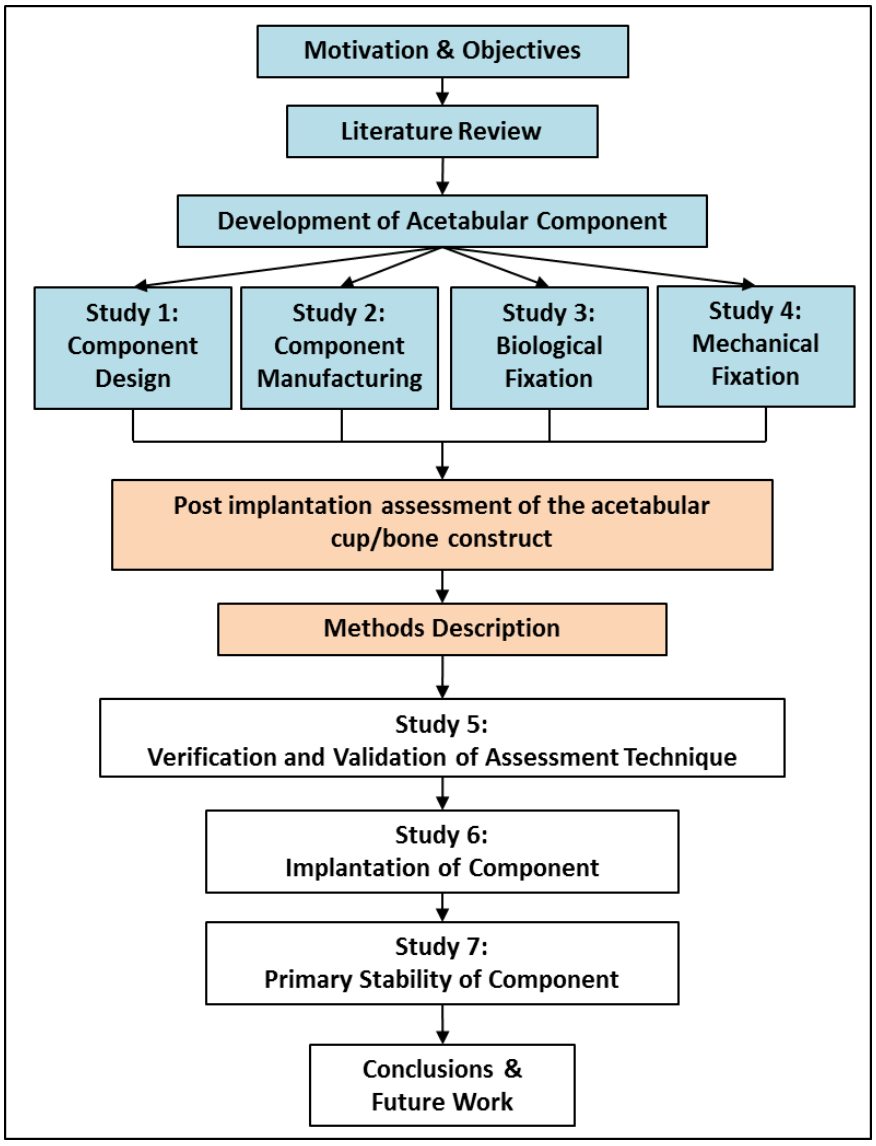

Microfocus computed tomography is central to this part of the thesis as the technique is used to generate the 3D volumes required for strain analysis. This section will outline the principles of microfocus computed tomography, digital volume correlation and the virtual field method prior to their implementation for the assessment of the initial post-operative conditions of the acetabular component.

4.1 Method Description

4.1.1 Microfocus Computed Tomography (μCT)

High resolution X-ray computed tomography (CT) is a non-destructive technique for visualising features in the interior of solid objects and it has been used to investigate a wide range of materials including rock (254, 255), bone (256), metal (257) and composites (246).

The principle involves transmitting an X-ray intensity field through a specimen at different angular positions (Figure 101). X-rays are generated when charged particles are accelerated or when electrons change shells within an atom (258). In microfocus tomography, electrons are repelled and accelerated from a wire cathode (usually tungsten) onto a focussed spot on a metallic anode target (generally a high melting point metal such as molybdenum or tungsten). Upon striking the target, energy is transferred from the electrons to the target. This energy is mainly transferred as heat however a small fraction is converted to X-rays. The X-ray photons emanate from the region where the electron beam hits the target and this is known as the X-ray spot. From this spot X-ray photons are directed through the test subject and onto a scintillation detector. The scintillation detector uses certain materials that emit visible radiation when exposed to X-rays. The materials scintillate in proportion to the incident flux and coupling them with a device that converts optical input into an electrical signal which is usually a charged-coupled device (CCD) generates a radiograph of the subject (259).

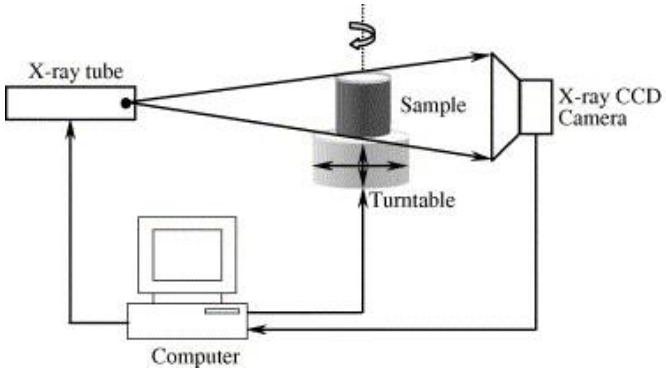

Figure 101: Illustration of X-ray Computed Tomography (260).

Visualisation of features within a specimen depends on the spatial resolution and the contrast that the features have relative to their surroundings. Spatial resolution describes the ability to resolve small details or features located with respect to a reference point (258). It is determined by the ratio of distance between the tube and the target, and the tube and the detector. The important variables that determine how effective an X-ray source will be for a specific task are the size of the focal spot, the spectrum of the X-ray energies and the X-ray intensities. The smaller the spot size, the smaller the penumbral blurring, which helps produce a more accurate projected image (261). A larger spot means that photons hitting a particular pixel can be traced back from the detector through multiple paths in the specimen to the source, adding significant noise to the tomographic reconstruction (261). The energy spectrum defines the penetrative ability of the X-rays as well as the relative attenuation as they pass through materials of different densities (262). A higher energy X-ray penetrates more effectively than lower ones but it is more insensitive to changes in material density and composition. Although higher intensities improve the underlying counting statistics, they often require a larger focal spot meaning image quality is compromised. The enlargement of

the focal spot is a defensive mechanism adopted by the system to avoid the target being exposed to excessive heat which could initiate damage.

The X-ray energy applied by a scanner is usually described in terms of the peak X-ray energy (kVp). However, the beam is actually polychromatic meaning it consists of a spectrum of energies where the maximum intensity is typically less than half of the peak.

To generate a full volume of the subject, computed tomography acquires multiple radiographs of the subject at multiple projections (angles). Unlike medical scanners, lab scanners fix the X-ray source whilst the specimen is rotated around a central fixed axis. For each angular position a series of detectors measure the extent to which the X-ray signal has been attenuated by the object.

Attenuation is the removal of photons from the beam of X-rays as it passes through matter. As the X-ray pass through the object the signal is weakened due to scatter and absorption. The basic equation for attenuation of a monochromatic (same energy) beams of photons is described by Lambert-Beer's Law shown in equation [8] (262).

$$\mathbf{I} = \boldsymbol{I_0 e^{[-\mu x]}} \quad [8]$$

Where I_o is the initial X-ray intensity, μ is the linear attenuation coefficient for the material being scanned, and x is the length of the X-ray path through the material. The linear attenuation coefficient is the fraction of photons removed from a monochromatic beam of X-rays or gamma rays per unit thickness of material. This can be linked to a polychromatic (a broad spectrum of X-ray energies) source by updating the equation to include the X-ray spectrum (E). Equation [9] (262) shows the equation for a polychromatic beam where E is the energy and w(E) is the spectrum of the source.

$$\mathbf{I} = \boldsymbol{I_0 \int w(E)\, e^{-\mu(E)\Delta x} dE} \quad [9]$$

The accumulation of each radiograph in a full 360 ° rotation produces a 3D image of the variation in linear attenuation coefficient in the specimen which is obtained by reconstruction. Reconstruction is the mathematical process of converting sinograms into two-dimensional slice images or 2D radiographs into 3D volumes. A sinogram is the 2D array of data containing the projections. Filtered back-projection is the most common reconstruction technique and involves the data being convolved with a filter and each view successively superimposed over a square grid at an angle corresponding to its acquisition angle (259). The filter is used to reduce the blurring of the true object and usually a ramp filter is applied, this effect is described below (259).

The principle of filtered back projection is shown in Figure 102 with a simple case where the object is an isolated point. The initial projection (a) is an impulse function with its peak centred at the location of the point. However, the precise position of the point is unknown and it is only known that it exists somewhere along the line. We assume a uniform probability distribution for its location (263) and that the entire ray path has the same

intensity. After a slight rotation the next projection is analysed in the same way and again the entire ray path has the same intensity as the measurement but the path is slightly rotated due to the change in projection angle. As the process is repeated for all projections (Figure 102c-i) the procedure essentially reverses the projection process and formulates a 2D object from a set of 1D line integrals (263). When the intensity profile of the reconstructed point is examined it is blurred and degradation of the spatial resolution is evident (Figure 103). To remove blurring a ramp filter is generally applied which limits the frequency domain response.

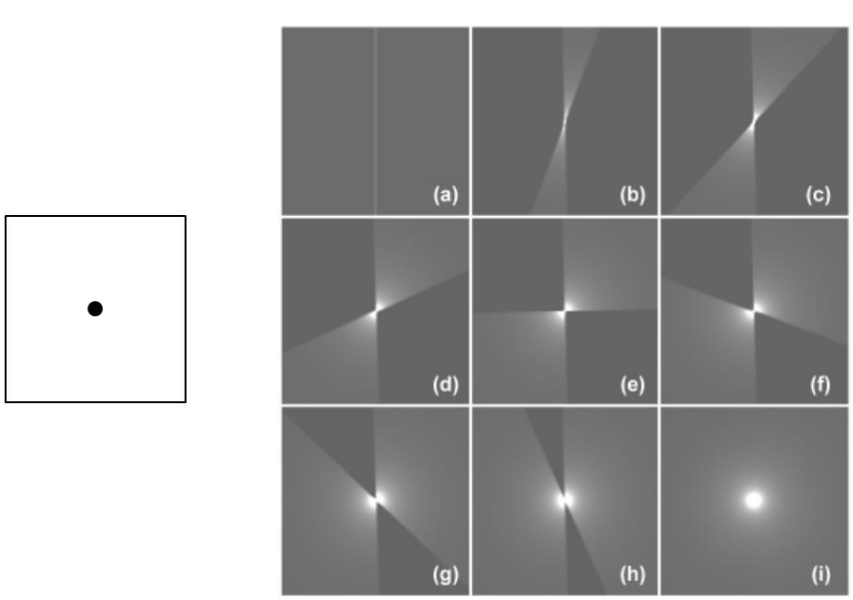

Figure 102: Back projection process of a single point shown on the left. (a) Back projected image of a single projection. Back projection at the following rotations b) 0 to 22.5 °, c) 0 to 45 °, d) 0 to 67.5 °, e) 0 to 90 °, f) 0 to 112.5 °, g) 0 to 135 °, h) 0 to 157.5 ° and i) 0 to 180 ° (263).

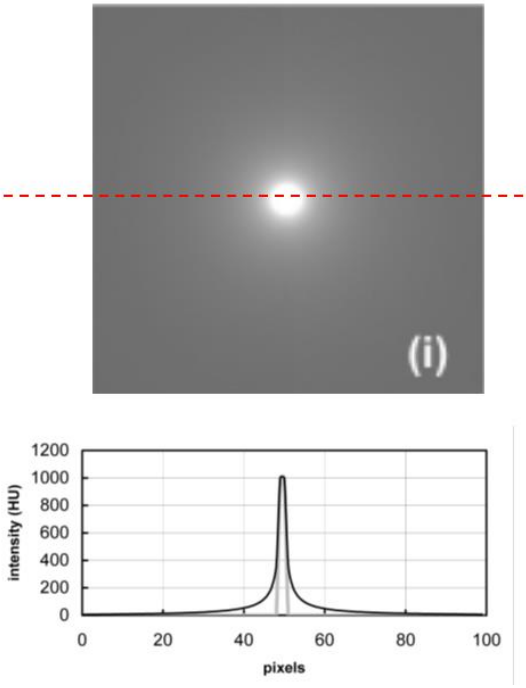

Figure 103: Reconstructed point (top) and intensity profile taken across reconstructed point with solid black line indicating reconstruction with back projection and thin grey line the ideal reconstruction. Adapted from Hsieh (2003) (263).

4.1.2 Microfocus CT scanners

Two scanners are used in this thesis for metrological analysis both located at μ-VIS centre at the University of Southampton. The two scanners are 1) Custom 225 keV Nikon/Metris HMX ST and 2) 225 keV/450 keV HUTCH Nikon/Metris custom design. The following section provides an overview of the two scanners used in this thesis.

1) Custom 225 keV Nikon/Metris HMX ST

This scanner has three different configurations; transmission, standard reflection and rotating target. It was described earlier that in microfocus tomography, electrons are accelerated onto a focused spot on a metal target and the energy transferred from these electrons into the target produce X-rays. The three configurations describe the different ways that the electrons interact with the target. In the reflection configuration the electrons hit the target and photons are reflected. This design provides greater heat dissipation so higher power can be used and shorter measurement times can be obtained. The minimum spot size is a few microns which was sufficient for the measurements conducted in this thesis. Transmission targets are penetrated by the electrons and are thinner than the reflection targets. Unlike the reflection target the photons are propagated in the direction of the electron beam. As the beam is focused through the metal target, it cannot handle the high powers associated with the reflection target as the cooling is much less efficient, but the focal spot is smaller due to the thinner target and thus a higher resolution is achievable. With reflection targets the focal spot depends on the power setting meaning small focal spots are

obtained only at low powers. This is a significant limitation of the transmission target and this type of target is usually applied to micro parts with very high resolution requirements (264). The final configuration is the rotating target and the electron beam falls on a moving surface meaning the power is spread over a greater surface area of target material. This allows a higher power to be implemented without incurring the damaging heating effects; denser and/or larger objects can be therefore measured or objects measured more quickly. A disadvantage of the rotating target is the focal spot is larger than the other two configurations due to the oscillation produced when the target is rotating. Figure 104 provides an overview of the principle of X-ray generation for reflection and transmission targets.

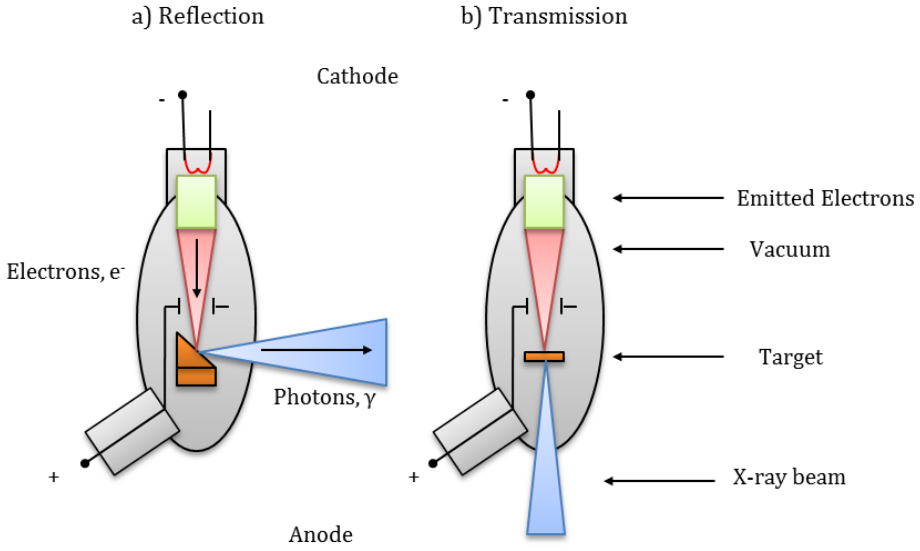

Figure 104: Principle of X-ray generation. The illustration shows the principles behind a a) reflection target and b) transmission target Adapted from Christoph and Neumann (2011) (264).

In the energy range of microfocus CT there are three fundamental ways in which the X-rays then interact with the material; the photoelectric effect, Compton scattering and pair production.

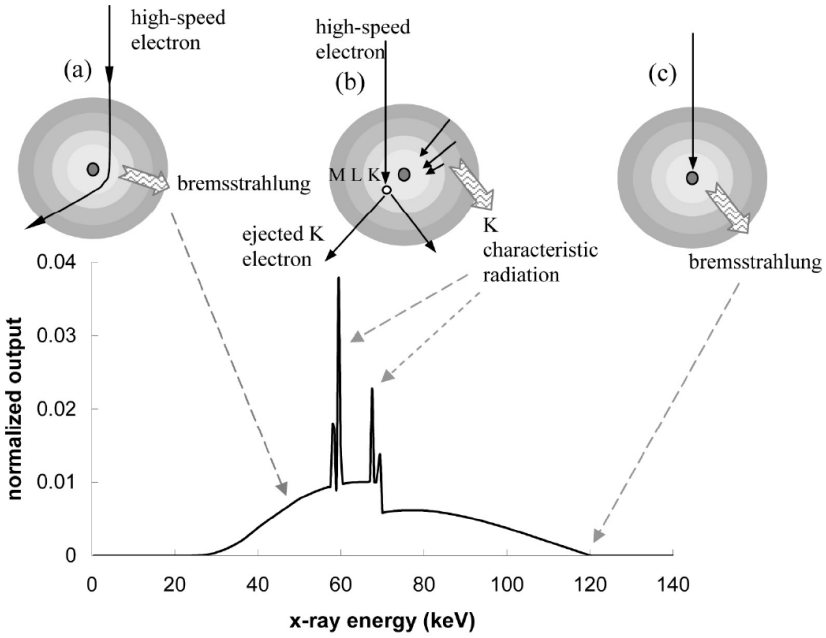

Figure 105: Illustration of electron interaction with a tungsten target and its relationship to the X-ray tube energy spectrum. a) Bremsstrahlung radiation is generated when high-speed electrons are decelerated by the electric field of the target nuclei b) Characteristic radiation is produced when a high-speed outer electron interacts with a target electron and ejects it from its shell. c) A high-speed electron hits the nucleus directly and all of its energy is converted to X-ray energy (263).

The photoelectric effect is when the photon gives up its entire energy to liberate an electron from a deep shell of an atom (Figure 105a) as the energy of the photon is greater than the binding energy of the electron. Once the interaction has occurred a hole is left in the deep shell and this is filled by an outer-shell electron. The movement of the higher energy state electron between the shell results in characteristic radiation (265).

Compton scattering causes X-ray photons to change direction (and energy) (Figure 105b). The Compton Effect occurs when the energy of the incident photon is higher than the binding energy of the electron. When the incident photon strikes an electron part of the energy is used to release it from the atoms whilst the rest is carried away by a new photon which is scattered (266). This scattered photon has less energy than the initial energy with the produced recoil electron carrying the complementary part of the energy.

The third way in which X-rays interact with matter is through pair production. Unlike the previous two interactions, no energy is converted to kinetic energy and ionization does not occur (263). Instead the photon interacts with a nucleus and is transformed into a positron-electron pair. A slightly broadened X-ray beam is produced in the forward direction (Figure 105c) but as there is no energy transfer this type of interaction has historically shown little importance to μCT.

Figure 106 shows that each principal interaction is dominant within different energies ranges. The photoelectric effect predominates at low energies, whilst pair production predominates at high energies (MeV) which is outside the energy range of the X-ray photons generated by a microfocus scanner. Compton scattering predominates at intermediate energies and varies directly with atomic number per unit mass (267); this interactions falls within the photon range generated by an microfocus scanner and this can generate scatter artefacts as discussed in Section 4.1.3.

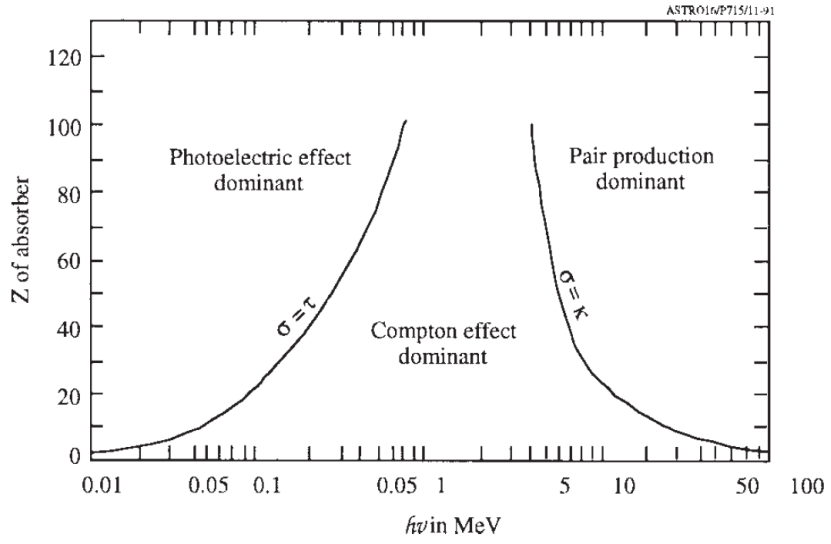

Figure 106: Principal X-ray Interactions. Reprinted with permission, from ASTM E1441-00 Standard Guide for Computed Tomography (CT), copyright ASTM International (267).

This scanner has a flat panel detector (PE1621, PerkinElmer, Massachusetts, USA) to record the incident ionising radiation after sample penetration. The detector consists of an array of individual detector elements known as pixels. The pixels are made of amorphous silicon and arranged in a row and column matrix. The scintillator within each pixel converts the X-rays to visible light and is made from gadolinium oxysulfide (Gadox). The flat panel in this scanner has a 2000 x 2000 pixel array and each pixel is 200 x 200 μm^2.

The system was tested using a performance verification methodology based on VDI/VDE 2630 and was found to be consistent in centroid-centroid distance measurements to within 0.2 % using a pair of ruby sphere test objects whose positioning had been previously calibrated to a white-light optical profilometer. The scanner operates within a thermostatically controlled room, providing a sustained ambient temperature close to 18 ˚C with long term temperature fluctuations of less than 2 ˚C. A further open loop cooling system operated within the scanner. Within these conditions, internal scanner ambient temperature is maintained at a temperature close to 19 ˚C, with temperature fluctuations of less than 0.2 ˚C during sustained operation. The X-ray gun housing ('front' of the main barrel, adjacent to the target housing) operates at around 24.0 ˚C which is sustained between +/- 0.25 ˚C. An initial thermal transient of several ˚C is known to affect the X-ray gun housing when

switching from the off to energised condition: this is known to stabilise to a $\Delta T \leq 0.25\ ^{\circ}C$ within ~60 minutes of operation.

2) 225 keV/450 keV HUTCH Nikon/Metris custom design

This scanner comprises of two energy sources, a 20-225 keV source and a 100-450 keV source. The 225 keV source has reflection and rotation options whilst the 450 keV source is reflection only. This scanner can achieve resolution at low keV of ~3 µm and 50 µm at high keV. Unlike the previous scanner it has two types of detector: a flat panel and a curved collimated line array. The flat panel (PE1621, PerkinElmer Massachusetts, USA) has the same setup as the previous scanner, although the scintillating material is caesium iodide. This detector allows short measurement times as the whole specimen can be imaged in one radiograph. The line array (Curved Linear Diode Array, (CLDA), Nikon) consists of a thin line of pixels meaning the section plane through the object is always perpendicular to the rotary axis. This is advantageous for measuring materials where there is a lot of scatter. When Compton scatter interactions occur, the photons experience a deflection through a small angle. Due to the area covered by the flat panel, these deflections are recorded but this is an undesired detection because it reduces image contrast (265). As the line array consists of only a single line of pixels, photons which have been deflected are filtered out as only photons travelling in the line of sight between the X-ray source and the detector are detected. Consequently image quality is improved as scatter is no longer detected. The main disadvantage of the line array is the requirement for each section plane to be captured individually in every rotary position which significantly increases the measurement time. For this reason, the flat panel detector was used in all the µCT measurements performed in this thesis. Figure 107 is an illustration of the two types of detectors available with the HUTCH scanner.

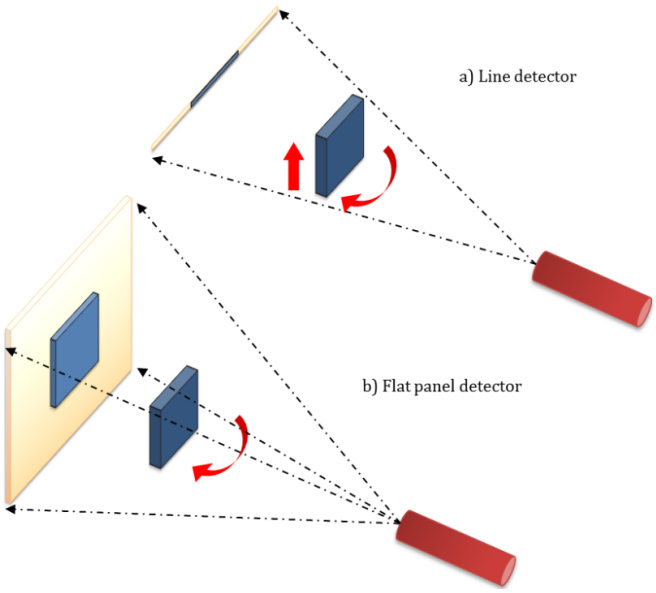

Figure 107: Tomography using a line detector (a) and a flat panel detector (b). Adapted from Christoph and Neumann (2011) (264).

The system was tested using a performance verification methodology based on VDI/VDE 2630 and was found to be consistent in centroid-centroid distance measurements to within 0.2 % using a pair of ruby sphere test objects whose positioning had been previously calibrated to a white-light optical profilometer. The scanner operates within the same thermostatically controlled room as the previous scanner.

4.1.3 Image Quality and Artefacts

Diverse physical effects can affect the tomography results and the imaging system may produce artificial structures which deviate from reality; these are called artefacts. There are many different types of CT artefacts, including noise, beam hardening, scatter, cone beam, ring and metal artefacts. The cause and appearance of the type of artefacts likely to be experienced in this thesis are reviewed in the following section. It is important to identify these features as they are detrimental to image quality and can affect any measurements taken from them.

Reconstruction Artefacts

Artefacts can be generated during reconstruction as prior to this procedure the position of projection on the detector of the specimen rotation axis has been determined accurately (268). Normally the 'actual' position of the rotation axis is decided visually by the user during the software alignment procedure which can introduce errors as the axis selection will vary between experimenters (268).

Ring Artefacts

Ring artefacts are due to defective elements of the detector (i.e. elements that deliver a non-linear pixel response) or inhomogeneity in the X-ray beam. As the name implies, this type of artefact appears as ring shaped contrast centred on the projection axis. The artefact is more pronounced near the centre of rotation due to the higher angular sampling rate (259). To remove this type of artefact, actions can be completed pre and post processing. In the case of post-processing the reconstructed data can be filtered, for the former sinogram processing can be implemented (259).

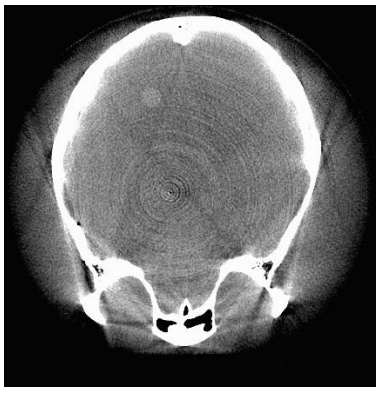

Figure 108: Example of Ring Artefacts in a μCT image (269).

Beam Hardening and Scatter

Beam hardening and scatter are different mechanisms which produce dark streaks between two high attenuating objects. Dark streaks can also be provided along the long axis of a single high attenuating object and bright streaks are seen adjacent to the dark streaks. The artefacts are a particular problem when imaging bone surrounding metal implants.

Beam hardening results when a polychromatic (a broad spectrum of X-ray energies) beam is transferred through a specimen and it loses less energetic photons. Although the overall intensity of the beam is diminished, the average energy of the beam is higher than the incident beam. On reconstructed volumes cupping and the appearance of dark bands or streaks between dense objects in the image can be seen. Cupping occurs as the outer layer of the reconstructed specimens shows a higher attenuation coefficient than the inner part (263) making the centre of a long ray path appear darker whilst the edges appear brighter. Figure 110 illustrates cupping in a roughly circular cross section.

A typical way of reducing beam hardening is by pre-hardening the beam. By placing a metallic foil between the beam and the specimen, lower energy electrons are absorbed, causing the average beam energy to increase prior to specimen penetration. However, the main drawback of beam prehardening is that it reduces the flux which may mean the sample is not be penetrated.

This section has outlined that an important mechanism between photons and materials is incoherent scattering or Compton scattering. Compton scattering predominates in the range of photon energies produced by a microfocus scanner (100-450 keV) and the effect causes artefacts in the examined material. (265). Due to Compton scatter not all the photons which are detected are primary photons. The deflected or scattered photons are detected which deviates the result from the true measurement of the X-ray intensities and causes a shift in CT number and shading (or streaking) artefacts (263).

Figure 109 provides a schematic of Compton scattering during the scan of an object (light grey shape) which contains a highly attenuating structure (grey oval). The dotted arrowheads represent the primary photons generated from the X-ray source and which penetrate the specimen and are collect by the detector. Their intensities are plotted on the thick light grey line in the graph at the bottom of the figure. The thick black arrows show the trajectory of the scatter photons which are deflected by a random angle. This random nature causes the intensity distribution of the scattered photons to be detected as a background signal of low frequencies (dotted black line). When combined with the primary photons, the true signal is distorted and the composite signal is a projection with reduced contrast (dark solid line).

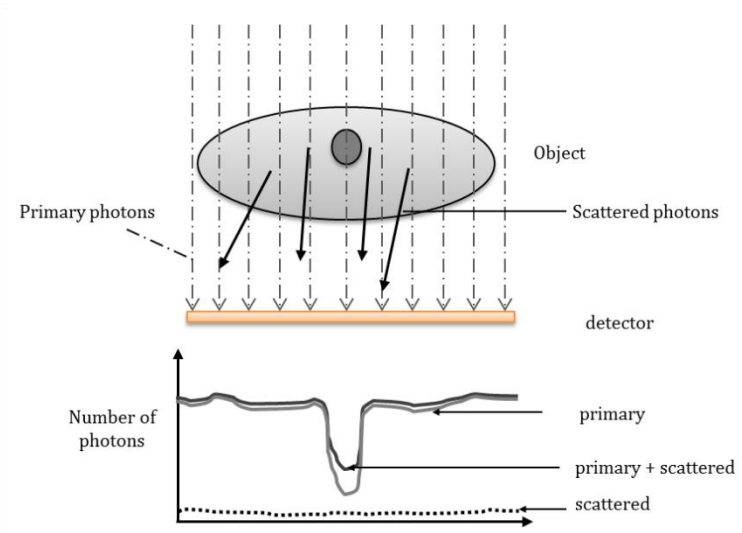

Figure 109: Schematic representation of the effect of Compton scattering. Adapted from Hsieh (2003) (263).

Compton scattering is seen as random thin bright and dark streaks that appear preferentially in the direction of greatest attenuation. The higher level of noise can cause low contrast boundaries to be obscured whilst the high contrast object remain visible.

Metal Artefacts

The presence of metal objects in the scan field can lead to severe streaking artefacts. Figure 110 shows an example of streak artefacts produced due to the presence of a dental filling (257). The streaks occur because the portion of the beam that passes through one of the objects at one projection is hardened less than when it passes through both objects at other projection angles. This is called photon starvation whereby insufficient photons reach the detector. Figure 110 illustrates the detrimental effect beam hardening can have on image quality. Metal artefacts are particular pronounced in high atomic number metals such as iron and platinum, and less pronounced with low atomic number metals such as aluminium (270) or light non-metals.

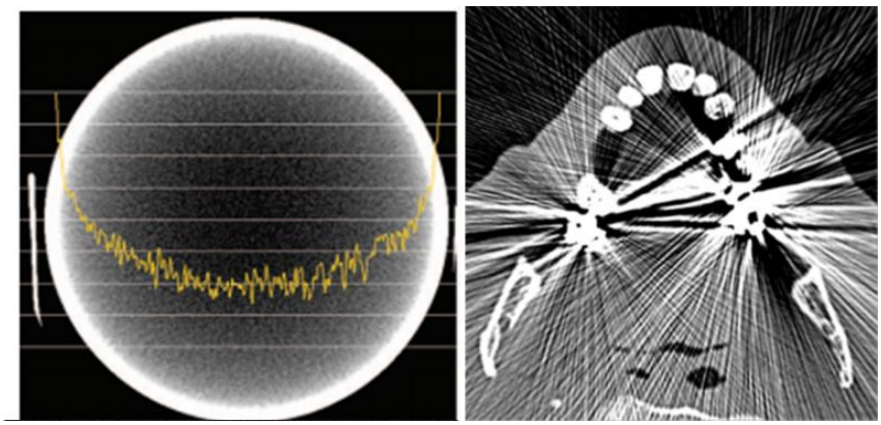

Figure 110: An example of cupping (271) and streak artefacts (257) caused by beam hardening.

Heat Generated Artefact

The final artefact arises from the heat generated from the X-ray tube. It has been discussed that only a small fraction of the energy from the electron beam is transferred to X-rays with most energy dissipated into heat. During scan acquisition, X-ray are continuously emitted which can raise the temperature of the X-ray tube by tens of degrees. If multiple scans are performed successively the tube's temperature will increase with the number of scans. The increase in tube temperature induces a thermal expansion of the tube which can cause small geometric motions of the X-ray emission point. These motions occur in plane or parallel to the X-ray beam. These artefacts can be reduced by running warm-up scans which allow the X-ray gun's temperature to increase and stabilise prior to data collection.

4.1.4 **Summary of application of μCT**

The μCT images taken in this thesis will be used for two main applications. The first to identify void formation in the reformed CFRPEEK material when a secondary manufacturing technique is applied to form the novel primary fixation features. The secondary application will use the reconstructed volumes for digital volume correlation (DVC), a technique used to identify deformation and strain generation within materials. The next section discusses the digital volume correlation technique and its use in research.

4.2 Digital Volume Correlation (DVC)

4.2.1 Technique Description

The mechanical properties of bone have been extensively studied for clinical applications to provide researchers with information relating to fracture, age related conditions such as osteoporosis, and bone and joint replacements. However, measuring and computing full-field strain measurements at a microstructural level is challenging. Traditional experimental techniques include strain gauging, digital image correlation (DIC), shearography, speckle interferometry, thermal stress analysis and reflectometry. Strain gauging is a well understood and reliable technique but it is limited to a few discrete points (170, 272). For spatially richer information, DIC or speckle interferometry can be implemented; these yield spatially dense strain data over an area of material. DIC yields field strain data on the surface of the specimen (170, 272), providing high resolution strain magnitude and direction data. The process involves the surface of the specimen being marked with a speckled pattern which a camera generates images of throughout the loading cycle. The speckled pattern in the field of view is divided into a number of unique correlation areas called facets which typically contain a square subset of pixels (169). Facets track the speckle pattern throughout the loading cycle and provide a measurement of deformation. Figure 111 shows the DIC principle. Strain is averaged over a number of facets and is thought to represent a reading from a rosette strain gauge at that particular location (169).

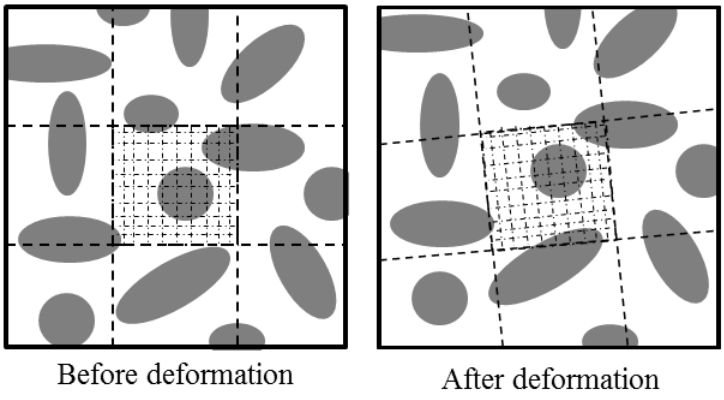

Figure 111: Digital image correlation assesses deformation by tracking a macroscopic speckle pattern consisting of a facet of pixels adapted from Sztefek et al. (2010) (169).

The DIC technique has been used successfully in many fields including medical engineering to assess bone surface strains (169, 170, 273). Speckle interferometry is an optical method which uses a laser impinged onto the surface of the specimen for creating speckle patterns which in turn are processed by a CCD camera. This technique has been successfully implemented to assess the Young's modulus and mechanical strain on a variety of bones including the jaw and femur (274-276). Thermal stress analysis uses the theory of thermoelasticity to relate the temperature distributions in elastic bodies to the mechanical stress and strain (277). This technique has been implemented to assess the surface stress

distribution of loaded canine and bovine femurs (277, 278). Each of the techniques described are well understood and have many non-biomechanical applications, however in all cases strain measurements are restricted to the surface of specimens meaning the investigation of internal strains is not viable.

Methods for measuring internal strains are historically dominated by diffraction approaches (including X-ray (256), and neutron methods (279)). Whilst well established, such methods are complicated by the non-trivial links between atomic and molecular displacements and a longer length-scale continuum mechanics perspective, particularly when either non-linear or yielding processes occur. In this respect, image correlation of volumetric image datasets have emerged as a promising approach for internal deformation mapping, particularly for the larger displacements and strains frequently associated with failure processes. Increased interest in this approach is undoubtedly linked to the improved availability of high resolution 3D imaging, particularly high resolution computed tomography, either by laboratory microfocus methods (μCT) or synchrotron radiation methods (SRCT).

From the strain measurement techniques described above, DIC has emerged as the preferred technique to measure surface strains on deforming bones (66, 169, 280-282). However, these investigations are limited to assessing surface characteristics and frequently only the cortical bone can be assessed. Therefore internal bone deformation on a trabecular level cannot be achieved and in order to predict internal cancellous bone strains finite element (FE) models are commonly used. While the technique is improving and the introduction of micro-FE models captures local strains that represent actual trabecular architecture (283-286), the analyses can only calculate strains as a function of bone loading, architecture and assumed tissue material properties (287). Limitations of micro-FE exist and include the requirement for tissue-level mechanical properties (e.g. Young's modulus and Poisson's ratio) and the prerequisite for these predictions to be validated against experimental data (288). The validation has been fairly successful for linear elastic properties, however, simulation of bone's failure behaviour has been less effective (289). These limitations can be overcome by the attainment of full-field deformation measurements.

Section 4.1.1 has described microfocus computed tomography (μCT) and explained the process which enables slice images and 3D volumes of the internal microarchitecture of a range of materials to be generated, with resolutions now routinely extending to the micrometre level (290, 291). With 3D full volume models of certain materials other applications for the data became apparent when considered in the context of surface strain mapping and texture correlation. Texture correlation (TC) uses the naturally occurring texture of a material to conduct image correlation without the requirement of applying an artificial speckle pattern. TC tracks the displacements of small regions of image content, identified by a reference image and subsequent images generated by manipulation (292). In DIC and TC this small region is a subset of pixels, in 1999 Bay et al. (1999) (256) extended this subset area into a 3D sub-volume. Within each sub-volume the natural material texture exists

which with correlation procedures can be tracked during deformation or loading. This procedure is known as Digital Volume Correlation (DVC) and Bay et al. (1999) (256) applied the technique as a means of determining continuum-level displacement and strain fields in trabecular bone (292). The main advantage of DVC is that it is not limited to the specimens surface which means it is a useful experimental complement to 3D numerical simulations such as finite element analysis (FEA) (293). In particular the 3D displacement and strain field produced by DVC can be used to validate the results or determine the input parameters of FE simulations. Since its introduction, DVC has been used to analyse a range of materials, such as bone (256, 294, 295), rock (255), synthetic foams (296, 297), wood (298) and sand grains (254). The initial measurement technique developed by Bay et al. (1999) (256) followed DIC principles with an objective function used to track displacements of small regions of image data. For DVC to function the image resolution achieved by the 3D imaging device must be good enough to capture the internal natural pattern of the material. Figure 112 illustrates two ideal DVC materials: synthetic foam and trabecular bone which both exhibit the appropriate internal features required for DVC.

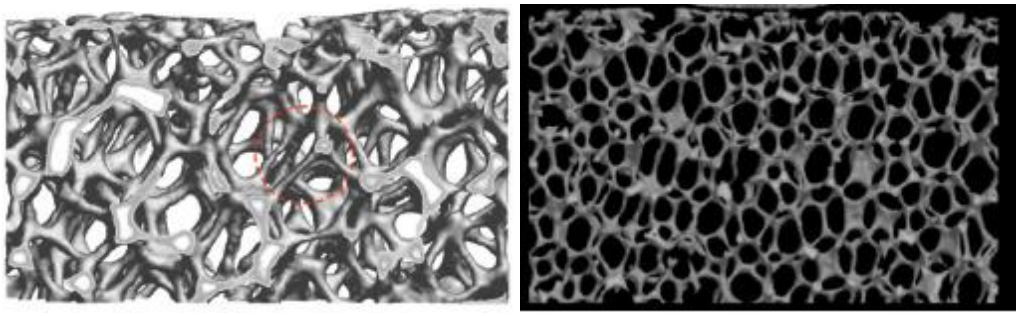

Figure 112: Renderings from μCT data showing porous structure and internal pattern of vertebral trabecular bone (left) and aluminium foam (right) which make the materials ideal for DVC (292).

DVC requires two image sets to perform the correlation procedure which quantifies the extent to which two quantitative variables are matched. An undeformed or reference image is taken of the specimen with a 3D imaging device. A second target image is then taken once a motion or deformation is applied to the specimen.

Volume correlation begins with the 3D volume being subdivided into several smaller and equal sub-volumes. The sub-volumes are registered and represented as a discrete function: $f(x, y, z)$ and $g(x+i, y+j, z+k)$ for the offset (i, j, k) which are assumed to be present in the image volume before and after a continuous mapping. These sub-volumes are shown in Figure 113.

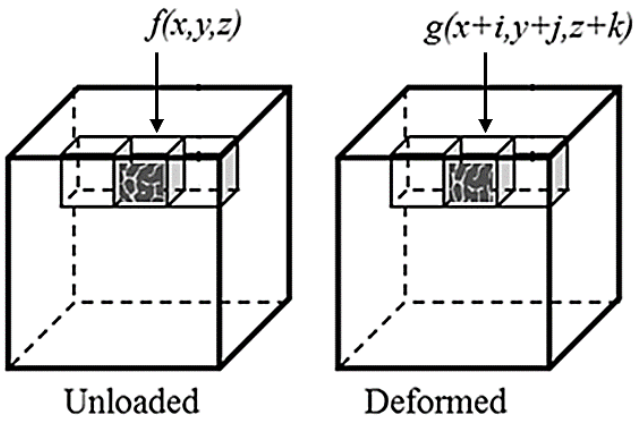

Figure 113: For cross-correlation, the unloaded and deformed image volumes are divided into many small, non-overlapping sub-volumes *f(x, y, z)* and *g(x+i, y+j, z+k)*. An average displacement is computed for each *f(x, y, z)* by finding the offset *(i, j, k)* that maximizes the cross-correlation function. Adapted from Liu and Morgan (2007) (299).

The registration of two gray level volumes in the reference and deformed images is based upon the conservation of the gray levels given by Equation [10].

$$\boldsymbol{f(x,y,z) = g(x+i, y+j, z+k)} \quad [10]$$

where *f* and *g* are sub-volumes of two volumes that are captured at different applied loads, x, y and z represent the coordinates and *i, j* and *k* are the offset in the x, y and z direction respectively.

To map between the reference and deformed images a linear shape function is used to define the degrees-of-freedom (DOF) to be determined at each point. This procedure is a local approach as the shift of the pattern within each sub-volume is considered without dependency upon neighbouring sub-volumes. The alternative approach is the global method and links neighbouring sub-volumes enabling the entire displacement volume to be minimised simultaneously (300).

For the local approach the following mathematical operations are applied to calculate the displacement of the sub-volumes.

a) Both sub-volumes are analysed by evaluating the Fast Fourier Transform (FFT) (301).
b) The cross product of the reference sub-volume *f(x, y, z)* FFT and the deformed sub-volume *g(x+i, y+j, z+k)* FFT conjugate is computed (301).
c) The inverse FFT of the result of b) is determined (301).

LaVision's software uses the normalised cross correlation function *C* to quantify the similarity of paired sub-volumes *f(x, y, z)* and *g(x+i, y+j, z+k)* for the offset *(i, j, k)*. The cross-correlation function is described by equation [11] (301).

$$C = \frac{\sum_X \sum_Y \sum_Z f(x,y,z)) \cdot g(x+i,y+j,z+k)}{(\sum_X \sum_Y \sum_Z [f(x,y,z)]^2 \cdot \sum_X \sum_Y \sum_Z [g(x+i,y+j,z+k)]^2)^{1/2}} \quad [11]$$

where · represents the dot product of the matrices.

The resulting displacement estimate is obtained from the position of the maximum in the correlation graph. A local Gaussian interpolation around the peak value of the map yields the peak position with sub-pixel precision (301). To achieve the maximum correlation the software adopts a multi-pass approach that uses the displacement gradient from the previous pass to deform the sub-volume on the subsequent pass until the highest possible correlation is achieved (300, 302). From the displacement vector of the centre of each sub-volume, all the strain components can be calculated using a centred finite difference scheme (303).

In summary the DVC process has four main stages; firstly the reference and deformed images need to be obtained. Although, in this thesis μCT is the method of acquiring image data other methods included magnetic resonance image (MRI) and optical tomography can be used. To implement DVC on the images measurement points at the centre of the sub-volumes are defined within the specimen allowing an initial estimate for the displacement field to be conducted which is supplemented with information from neighbouring points that have been successfully located (292). Values between the centres must be estimated through some form of interpolation and tri-linear interpolation is the simplest interpolation used and has been proven adequate for most applications (298, 304).

4.2.2 **Previous Work**

Table 13 provides details of examples of DVC research implemented since 1999. Generally there are three main areas of DVC investigation. The first investigates advancements and refinements to the technique with the aim of improving solve time, precision and efficiency. The second area implements the technique to gain a greater understanding of how certain materials react under certain test conditions. The third area assesses the precision and accuracy of the technique especially when new refinements to the technique are introduced. It can be seen from Table 13 that a number of the studies investigate more than one area and the following section provides a brief history of DVC and its development and use.

DVC was introduced in 1999 by Bay et al. (1999) (256) who proposed extending the methods adopted by DIC in order to determine continuum-level displacement and strain fields in trabecular bone. The study successfully mapped full continuum-level 3D strain tensor fields throughout the interior of the specimen using a method with limited displacement degrees of freedom and interpolation properties. However, aside from computational restrictions, the method worked as anticipated and proposed a new method to improve DVC's performance. In addition, the study proposed that certain calibration procedures were required to determine the effects of image quality on the displacement and strain outputs. The study examined specimens under zero strain conditions as it was predicted that these

data sets captured all sources of measurement error except for the relative distortion between the sub-volumes (256).

Subsequent research on DVC focused on improving the technique and quantifying measurement accuracy. Smith and Bay (2002) (294) introduced rotational degrees of freedom which improved the accuracy when local sub-volume rotations are present during loading. Verhulp et al. (2004) (287) extended the DVC technique further and used twelve DOF when analysing aluminium foam. The study intended to determine the precision of the extended technique using foam before analysing individual trabeculae in trabecular bone. The extension enabled deformation of the sub-volume itself to be realised unlike previous studies (256, 294) in which only homogenized strains were calculated.

Table 13: Summary of DVC investigations.						
Author	Year	Material	Test Objective	Development of the technique	Material Analysis	Assessment of Reliability
Bay et al. (256)	**1999**	bone	To assess the DVC technique	**X**	**X**	**X**
Smith and Bay (294)	2002	bone	To assess the influence of adding rotational degrees of freedom into the minimisation problem for DVC	X	X	X
Verhulp et al. (287)	2004	Aluminium foam	To assess the precision of a DVC technique that measures local strain in single trabeculae	X		
Zauel et al. (305)	2006	bone	To compare the linear finite element prediction of deformation and strain of trabecular bone to DVC.	X	X	X
Lenoir et al. (306)	2007	rock	To use DVC to detect the onset of shear strain localisation and to characterise its development in a 3D complex pattern for argillaceous rock		X	
Liu and Morgan (299)	2007	bone	To quantify the accuracy and precision of DVC across a wide range of structures to determine how the accuracy and precision vary with DVC method and structure		X	X
Bremand et al.(307)	2008	bone	To study the mechanical behaviour of human trabecular bone		X	
Forsberg and Siviour (308)	2009	sugar	To study the compaction of sugar using DVC and compare results with DIC		X	
Forsberg et al. (298)	2010	wood	To assess the micro-scale deformations of wood during bending		X	
Hall et al. (254)	2010	sand	To observe and quantify the onset and evolution of localised deformation in sand with grain-scale resolution	X	X	
Gates et al. (293)	2010	PDMS	To assess the performance of an improvement made to the DVC algorithm which will improve the speed and efficiency of the technique	X		X
Hussein et al. (309)	2012	Whole bone	To quantify the accuracy of applying the DVC method to whole bones and to use it to characterise failure patterns throughout entire vertebrae		X	X
Sjödahl et al. (255)	2012	sugar	To study the compaction of sugar using DVC with the application of a finite element smoothing technique to reduce noise	X		
Madi et al. (300)	2013	Bone scaffold	To measure the 3D displacements in a scaffold implant under compression using two DVC methods and compare the results to FE models		X	X

Previously it has been commented that DVC could be used for validation of 3D finite element simulations. At the time of writing there was one study which has attempted to compare the two techniques. Zauel et al. (2006) (305) aimed to use DVC to compare the compression of trabecular bone with a linear finite element model. The limitations of micro-FE have already been discussed with traditional methods of FEA verification involving in-vitro studies which mechanically test bones. The study (305) showed that the displacement and strains in the compression direction were highly related. However, poorer comparisons were seen in the direction perpendicular to the loading direction. It was concluded that the poor results in this direction were a consequence of modulus inhomogeneity something that the FEA model ignored as it assumed uniform material properties.

Measurement precision and accuracy has received more attention since the first initial investigation by Bay et al. (1999) (256) as it is essential that significant material strains can be identified from strains caused by noise artefacts. The noise of a system can be quantified using a term called strain resolution. Strain resolution is defined as the minimum significant strain value that can be extracted from data and regarded as a result of material behaviour and not due to a noise artefact. Section 4.1.3 described artefacts that can be present in the reconstructed volumes generated using μCT and which can have a detrimental effect on image quality. Variations in these artefacts between the reference and deformed volumes will increase the noise and the minimum significant strain that can be identified as being a result of material behaviour. To quantify the noise a series of baseline DVC tests can be performed. These tests perform DVC between two volumes under zero strain (292, 294, 299, 305) and use the mean and standard deviation of the resulting strain maps to calculate the strain resolution. The mean indicates a possible systematic bias and the standard deviation, the random error arising from the imaging noise. It has been found that DVC has a similar measurement fidelity to DIC (292).

The most thorough validation test to date has been performed by Liu and Morgan (2007) (299) and describes the procedures dependence on the material's internal structure and the influence this has on the accuracy and precision of the technique. The study (299) performed DVC on a range of trabecular structures in order to determine how differing material structures affect the DVC performance. Bovine (femur and tibia), rabbit (femur, tibia and vertebral) and human (vertebral) bone were assessed using the same equipment and set up. The material structure was quantified by volume fraction, mean trabecular thickness, mean trabecular spacing, trabecular number and structural model index. Stationary tests were performed and the results indicated that the displacement and strain errors differed among bone types. Specimens with a lower volume fraction and trabecular number but higher trabecular spacing improved the accuracy and precision of DVC. Although this study highlighted that the accuracy of DVC depends on the material structure, the analysis was only performed on undeformed specimens.

A final area of development in DVC has been the introduction of alternative imaging modalities used. Most of the research has been performed on X-ray micro-tomography acquired images. However work is emerging from confocal microscopy (310) and optical slicing of transparent specimens (311).

DVC can be applied to a wide range of materials, provided an adequate internal pattern exists. Trabecular bone has been investigated more frequently than any other material due to its natural internal pattern, however, as the DVC technique has been refined a larger range of materials are being explored. Strain resolution can be affected by many aspects in image acquisition and software parameters and it is critical for any investigator to perform the baseline studies prior to material testing. The DVC principles (e.g. algorithms) will not be investigated in this thesis but the technique will be used to explore two main aspects. Firstly the full-field strain data produced by DVC will be used to extract the Poisson's ratio from compressed bone using an inverse method called the Virtual Fields Method (VFM). The investigation is outlined in Section 4.3.1 and the inverse method explained in the following section.

The second application was to investigate the feasibility of using DVC to assess the deformation and strain generation around different acetabular components including the assessment of the novel CFRPEEK component developed in this thesis. This offers new challenges due to the presence of two materials in the reconstructed volume. Previous investigations have only assessed one material medium meaning the limitations of using DVC for this purpose is unknown. Section 4.5 outlines the component implantation investigations and the results achieved for assessing strain generation in artificial and real bone surrounding implanted CFRPEEK and contemporary acetabular components.

4.3 Extracting Constitutive Mechanical Parameters from Full-field Deformation Measurements

Finite element methods have developed extensively over the last decade. Micro-FE models are frequently used in biomechanical studies to predict displacement, strain and stress distribution at a trabecular and whole bone level. This has contributed to the advancement in the design of hip and knee replacements over the last decade.

Aside from computational methods, experimental models can be used in implant development as they can in some case mimic the response of a structure more accurately; however certain assumptions concerning the model's geometry, load and mechanical response of its constitutive material are required. The specimen geometry is usually known and the load can be measured using a suitable force transducer. The type of constitutive equation used is chosen *a priori* for its relevancy and the main objective is to determine the parameters which govern the constitutive equations (312). For example in a tensile experiment, the mechanical properties of a material can be identified by measuring the cross-sectional area of the specimen, the load and a quantity related to kinematics (generally a strain component at a given point) which allows the stress and modulus to be determined.

However, this approach suffers two major drawbacks. The first is the requirement for stringent assumptions such as a homogeneous field which provides a link between the unknown parameters to the load and strains (e.g. uniform pressure distribution at the specimen ends for uniaxial tensile test) (312). This is especially restrictive with anisotropic materials. The second is the small number of parameters that can be determined from an individual test resulting in the requirement to perform multiple tests when the constitutive equations depend on more than one parameter other than isotropy (312).

The advancement in full-field measurement techniques has allowed measurements to be obtained with increased accuracy and this enables the homogeneous field assumption used in simple tests to be reconsidered. DVC can be used to measure 3D displacement fields inside the solid specimen can be measured with a suitable technique such as μCT; alternatively 2D displacement field can be obtained by suitable optical non-contact methods on the external surface only. Such methods include DIC which has already been identified in Section 4.2 as a method successfully used in biomechanical tests to assess the Young's modulus and mechanical strain on a variety of bones (169, 273, 313).

Strain is obtained by numerical differentiation of the displacement field; however, the main difficulty comes from the fact that the measured displacement or strain components are generally not related to the unknown parameters (314) so no closed form solution between the displacement, strains and stress fields can be achieved (312). However, the stress, strain and displacement can be linked through the well-known equations of continuum mechanics namely the equation of equilibrium, strain/displacement relations and the constitutive equations (314). These equations are verified at any point on or within the specimen but they do not provide the link between the measurements and the unknown parameters and such a problem is referred to as an 'inverse' problem.

Finite element updating models (315) are the most popular solution to the 'inverse' problem although other methods do exist (312, 314, 316-318). The finite element model involves constructing a discretised model of the mechanical test where the model is divided into a number of small subregions (elements) and nodes. The method uses integral formulations to create a system of algebraic equations which are solved to obtain displacement and strain components at nodes. The updating method minimises the difference between numerical and experimental displacements between these nodes with respect to the unknown constitutive parameters to provide the solution of the problem. Although the approach is highly respected, there are shortcomings (312). The method is iterative even for simple linear elastic models and requires a solution of direct calculation for each evaluation. Consequently, initial values of parameters such as Poisson's ratio and Young's modulus must be provided and the loading distribution known to initiate the procedure and these factors will affect the convergence rate and the quality of the results themselves. Another possibility for solving this problem is to consider the basic set of equations of equilibrium in a method known as the Virtual Fields Method (VFM). The VFM method considers the local

equilibrium of subregions within a mesh of a specimen as it is based on the fact that the specimen is at equilibrium. This method leads to the generation of a set of equations from which the constitutive parameters can be obtained (316). The following section provides a brief outline of the VFM and outlines how it is applied in this thesis. For a more in-depth explanation the reader is directed to Pierron and Grédiac (2012) (312).

4.3.1 **Virtual Fields Method (VFM)**

The VFM is based on the principle of virtual work (319). Virtual work is defined as the work done on a particle by all the forces acting on the particle when it is given a small hypothetical displacement or a virtual displacement which is consistent with the constraints present (319), during which the applied load remains constant. This principle can be written as follows (equation [12]), for a given solid volume V which is in a state of equilibrium (320) (Figure 114).

$$-\int_V \sigma : \varepsilon^* \, dV + \int_{\partial S_f} \overline{\boldsymbol{T}} . \boldsymbol{u}^* dS + \int_V \boldsymbol{f} . \boldsymbol{u}^* \, dV = \int_V \rho\gamma . \boldsymbol{u}^* dV \qquad \textbf{[12]}$$

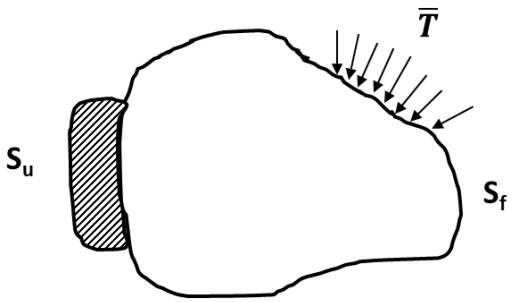

Figure 114: Solid of any shape subjected to mechanical load. $\overline{T}$ is the distribution of loading tractions acting on the boundary, *Sf*, is the part of the solid boundary where the tractions are applied Adapted from Pierron and Grédiac (2012) (312).

where σ is the actual stress tensor, ε^* is the virtual strain tensor deriving from $\boldsymbol{u}^*$, S_u is the surface over which kinetic boundary conditions are prescribed, $\overline{T}$ is the distribution of loading tractions acting on the boundary, S_f, is the part of the solid boundary over which static boundary conditions are applied (Figure 114), u^* is the virtual displacement field vector, f is the distribution of volume forces acting on V, ϱ is the mass per unit volume and γ is the acceleration. '.' represents the dot product between vectors, ':' represents the dot product between 2D matrices (also known as the contracted product) (320).
In statics and the absence of volume forces, (equation [12]) can be reduced to

$$-\int_V \boldsymbol{\sigma} : \boldsymbol{\varepsilon}^* \, \boldsymbol{dV} + \int_{\partial \boldsymbol{S_f}} \boldsymbol{T} . \boldsymbol{u}^* \boldsymbol{dS} = \boldsymbol{0} \qquad [13]$$

A virtual displacement field is a function defined across volume V and the virtual strain tensor is the tensor derived from the given virtual displacement vector (314). The virtual displacement field vector must be continuous across the whole volume. It should also be noted that if a virtual field is selected so that it is zero over the specimen's boundary where

the loads are introduced, the last term in equation [13] disappears.
It has been noted that the VFM can be coupled with full-field measurements to extract unknown parameters such as Young's modulus and Poisson's ratio. Section 4.2 provided an overview of obtaining full-field strain data through the implementation of DVC. Section 4.4 combines μCT measurements with DVC to produce full-field strain measurement data from a trabecular bone specimen under compression. The following section outlines how the Poisson's ratio can be extracted from this data using VFM and the constitutive equations.

4.3.1.1 **Poisson's Ratio Identification**

To derive the Poisson's ratio equation in 3D, it can be assumed that the material is linear elastic isotropic and therefore the stress-strain relationship depends on two independent parameters such as the Lamé coefficients μ and λ (321). Therefore the stress/strain relationship can be written as:

$$\sigma = 2\mu\varepsilon + \lambda\varepsilon_{ii}\mathbf{I} \quad [14]$$

where ε is the recorded strain, **I** is the second order unit tensor.
Using this relationship (equation [14]) the nine stress components to describe the stress state within the specimen can be inserted into equation [13] and by assuming that the material is macroscopically homogeneous the Lamé coefficients can be taken out of the integrals, simplifying the equation to equation [15]:

$$\int_V (\varepsilon_{xx}\varepsilon^*_{xx} + \varepsilon_{yy}\varepsilon^*_{yy} + \varepsilon_{zz}\varepsilon^*_{zz} + 2\varepsilon_{xy}\varepsilon^*_{xy} + 2\varepsilon_{xz}\varepsilon^*_{xz} + 2\varepsilon_{yz}\varepsilon^*_{yz})\, dV + \frac{\lambda}{2\mu}\int_V (3h(\varepsilon)h(\varepsilon^*))\, dV = 0 \quad [15]$$

where h(ε) is the first invariant of strain ($\varepsilon_{xx} + \varepsilon_{yy} + \varepsilon_{zz}$) (the trace).
By relating the Lamé coefficient $\lambda = \frac{\nu E}{(1+\nu)(1-2\nu)}$ and shear modulus $\mu = \frac{E}{2(1+\nu)}$, the resulting expression for $\lambda/2\mu$ can be obtained.

$$\frac{\boldsymbol{\lambda}}{\boldsymbol{2\mu}} = \frac{\boldsymbol{\nu}}{\boldsymbol{1-2\nu}} = \boldsymbol{k} \quad [16]$$

From this relationship the Poisson's ratio can be determined as

$$\boldsymbol{\nu} = \frac{\boldsymbol{k}}{\boldsymbol{1+2k}} \quad [17]$$

Finally, solving equation [15] for k provides

$$\boldsymbol{k} = \frac{-\left(\overline{\boldsymbol{\varepsilon_{xx}\varepsilon^*_{xx}}} + \overline{\boldsymbol{\varepsilon_{yy}\varepsilon^*_{yy}}} + \overline{\boldsymbol{\varepsilon_{zz}\varepsilon^*_{zz}}} + 2\overline{\boldsymbol{\varepsilon_{xy}\varepsilon^*_{xy}}} + 2\overline{\boldsymbol{\varepsilon_{xz}\varepsilon^*_{xz}}} + 2\overline{\boldsymbol{\varepsilon_{yz}\varepsilon^*_{yz}}}\right)}{\boldsymbol{3h(\varepsilon)h(\varepsilon^*)}} \quad [18]$$

where $\overline{\boldsymbol{\varepsilon_{xx}\varepsilon^*_{xx}}}$ is the spatial averaging of the function $\boldsymbol{\varepsilon_{xx}\varepsilon^*_{xx}}$ and h(ε*) is the first invariant of strain ($\varepsilon_{xx}{}^* + \varepsilon_{yy}{}^* + \varepsilon_{zz}{}^*$). Equations [17] and [18] then provide ν. It should be noted that this

derivation does not require any assumption on the stress distribution inside the considered volume and is therefore very general.

The VFM has been successfully applied to investigate the mechanical properties in a range of materials including composites (266, 322), polymers (314, 320) and metals (323, 324). These studies have calculated the volume integrals using surface measurements only so a through-thickness strain distribution assumption was required and the derivation of the Poisson's ratio is limited to 2D. An advantage of using the VFM with DVC is that full-field volume measurements can be obtained and the through thickness assumption is no longer required. The explanation of the VFM to calculate the Poisson's ratio is described briefly in this paper but there are extensions of the technique including the use of piecewise virtual fields to reduce noise. This method and its 2D version are both explained in more detail and with examples in Pierron & Grédiac (2012) (312).

The VFM is used in the present thesis to extract constitutive mechanical parameters from the full-field deformation measurements generated through DVC. Poisson's ratio is an important property when assessing trabecular bone and its accurate determination is a subject of continuing investigation. Literature states a wide range of values between 0.07 and 0.41 for Poisson's ratio (325-329). The use of VFM to extract these parameters is discussed in more detail in Section 5.1.

5 Study 5: Verification and Validation of Digital Volume Correlation to assess the Microstructural Behaviour of Trabecular Bone.

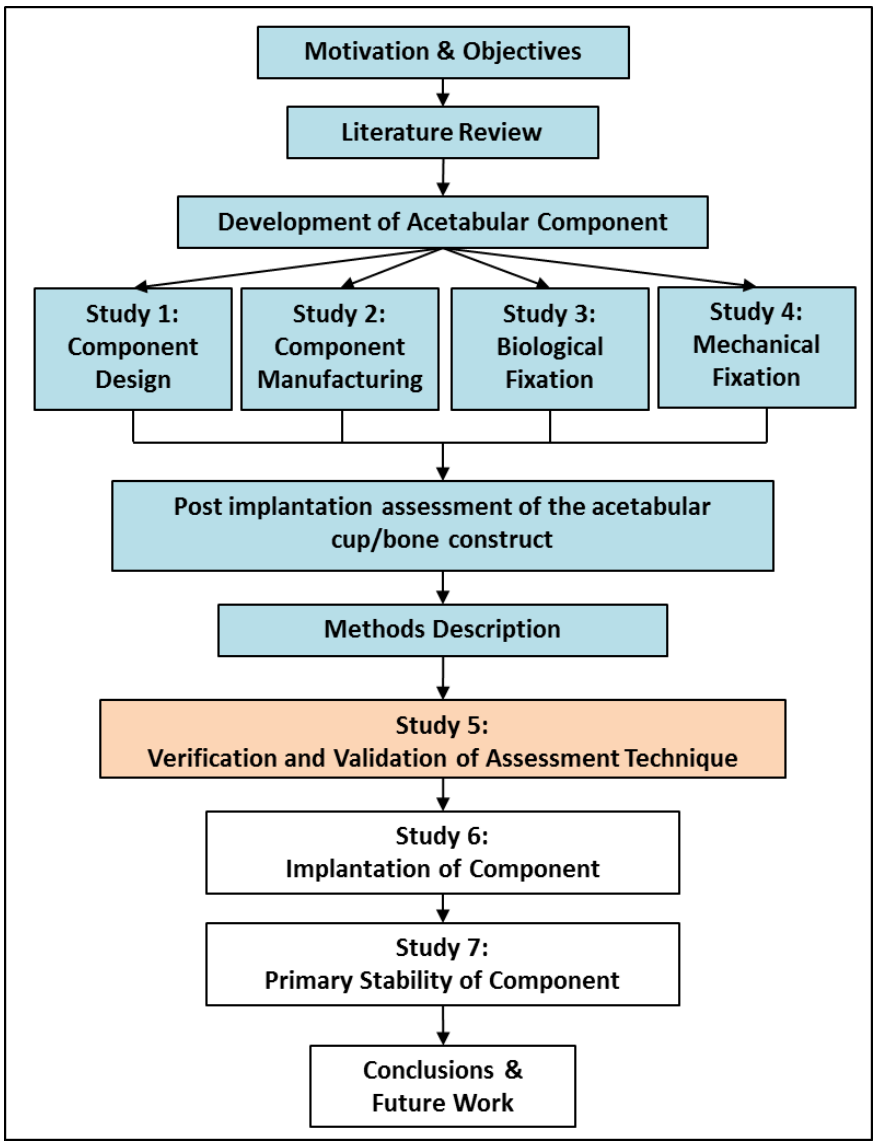

This part of the study has been published in a journal article:
F. Gillard, R. Boardman, M. Mavrogordato, D. Hollis, I. Sinclair, F. Pierron, M. Browne. *The application of digital volume correlation (DVC) to study the microstructural behaviour of trabecular bone during compression.* Journal of the Mechanical Behavior of Biomedical Materials, 2014. 29:480-499.

5.1 The application of digital volume correlation (DVC) to study the microstructural behaviour of trabecular bone during compression.

A key objective of Aurora Medical Ltd was to develop a biomechanically compliant component which promoted more natural load transfer into the acetabulum than current devices. This design rationale was to use CFRPEEK which possesses a modulus closer to

bone and incorporating a raised section on the bearing surface whose shape represented the load bearing horseshoe articular cartilage in the acetabulum (Section 3.1).

Following the design and fixation studies, the present study assessed the response of the component and the bone to implantation as it has been described that the biomechanical bone adaption stimulus can be assessed by measuring the change from pre- to post-operative peri-prosthetic strains (66). CFRPEEK has a stiffness closer to bone and has been predicted through computational simulations (64, 65) to promote less adverse bone adaption compared to excessively stiff components (CoCr and ceramic devices) which can cause loosening by stress shielding and bone resorption (64, 66).

Section 2.7 outlined the current experimental and computational methods employed to investigate the pelvis's response after the insertion of an acetabular component. DIC was identified as one of the primary experimental techniques but it can only yield strain data on the surface of a specimen (330, 331). Therefore full bone models can only draw conclusions which consider the stimulus for cortical bone adaption whereas trabecular bone adaption can only be predicted (66). Computational methods (160, 161) are also limited as they rely on the requirement for tissue-level mechanical properties (Young's modulus and Poisson's ratio) for calculation and the prerequisite for these values to be validated against experimental data (288).

Section 4.1.1 has described how micro-focus computed tomography (μCT) enables slice images and 3D volumes of the internal microarchitecture of a range of materials to be generated, with resolutions now routinely extending to the micrometre level (290, 291). Section 4.2 introduced DVC, a technique that can exploit a material's internal structure to track the displacement of a small sub-volume of interest and produce full-field 3D strain data.

It is hypothesised that the change in strain in peri-prosthetic bone after implantation of acetabular cups of different stiffnesses can be recorded by combining μCT and DVC. This has advantages over current techniques in that internal measurements can be obtained with no assumptions regarding the mechanical properties of the analysed material.

Section 4.2 highlighted that the application of DVC to obtain full-field strain measurements in trabecular bone is an established concept. The majority of published DVC investigations are conducted on this material due to its porous and random structure (256, 294, 295). However, the extension of its use to assess the compressive behaviour of trabecular bone surrounding an orthopaedic implant is a novel concept as previous investigations have only tested small and simple shaped (cylindrical or cubed) specimens (256, 294, 295).

To confirm the feasibility of using DVC, a compression study was performed on a small section of trabecular bone. This would represent the compression which could occur around a component but in a simple stress setup, in order to inform more complex analyses. Secondly, the steps taken to obtain the strain resolution were investigated. Section 4.2 introduced this term as a way of quantifying the noise of the system and the software (e.g.

μCT scanner) used to perform the DVC process. This factor is essential as it enables investigators to identify strains produced as a result of material behaviour and not a noise artefact. This aspect has partly been investigated in previous studies (292, 294, 299, 305) but no consistent method for its calculation has been developed.

A third area of investigation relates to isolating and reducing sources of errors. Certain events such as the onset of crushing at high compressive strains in which the internal structure is lost and edge effects may introduce errors into the calculation. As with DIC, the correlation coefficient can be used to determine how well two volumes are related. A coefficient of 1 means the volume are completely correlated and a value of 0 means they are completely unrelated. It is assumed that a loss of a material's internal pattern will reduce the correlation coefficient and by compressing a simple trabecular bone specimen to an extent that bone crushing is initiated a minimum correlation coefficient value can be determined which ensures reliable strain data is extracted from the analysis.

An additional objective is to use the full-field DVC strain measurements to demonstrate the possibility of identifying the Poisson's ratio of trabecular bone using the VFM. Section 4.3 introduced the VFM and the procedure to identify Poisson's ratio by relating the Lamé coefficient and shear modulus. Poisson's ratio is an important property for foam-like materials and has been shown to vary with the strain level (320). Multiple compression steps were conducted in this investigation in an attempt to measure the evolution of the Poisson's ratio and to show how full-field measurements can be coupled to VFM.

Materials and Methods

A cubic specimen of cancellous bone from the femoral head of a porcine femur with approximate dimensions 20x20x20 mm^3 was prepared using a bandsaw. The specimen was wrapped in polyvinyl chloride film (standard commercial 'plastic wrap') so it remained hydrated throughout testing. It was placed between two polyvinyl chloride platens and compressed under displacement control in the rig shown in Figure 115. The specimen was not bonded to either platen within the X-ray scanner.

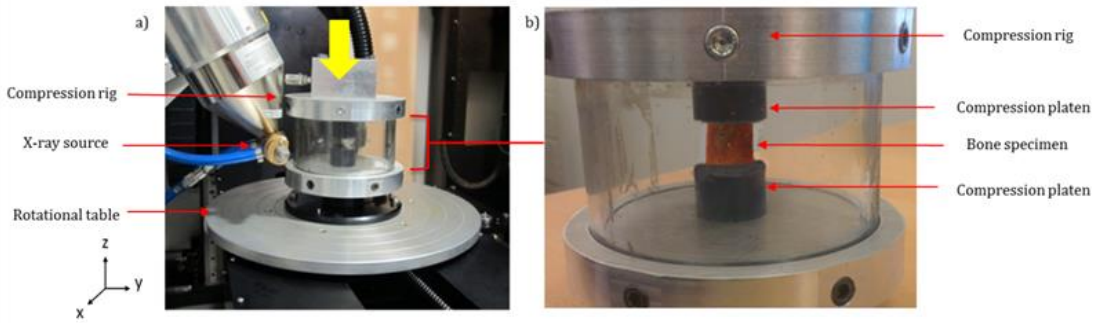

Figure 115: a) Complete experimental test set up with yellow arrow showing compression direction, b) Close up of bone specimen placed between compression platens prior to compression.

Microfocus X-ray computed tomography measurements were carried out using a customised 225 keV Nikon/Metris HMX ST scanner (Nikon Metrology NV). An X-ray tube potential of 105 keV with a tungsten reflection target was found to satisfactorily penetrate the samples, with a reasonable contrast-to-noise ratio being achieved between the air and trabecular bone specimen. A voxel resolution of 24.6 μm was selected which yielded a dataset encompassing the entire specimen. The projection data for each scan consisted of 2001 projections taken over a 71 minute period at a source power of 12 W. Projections were reconstructed into 3D volumes using CT-Pro via filtered-back projection (simple Ram-Lak filter). After reconstruction the bit depth of the volumes were reduced from 32-bit floating point to an 8-bit format. This allowed for faster processing times without any loss in fidelity which was checked experimentally by processing the same volume in a 32-bit floating point and an 8-bit format and comparing the results of the stationary test outlined in 5.1.1.
Digital volume correlation was performed on the reconstructed volumes using DaVis 8.1.3 software (LaVision, Göettingen, Germany) via a proprietary Fast Fourier Transform (FFT) approach (301) described in Section 4.2.

5.1.1 **Evaluation of Measurement Resolution**

The metrological performance of the DVC procedure was investigated through a series of experiments which were conducted prior to the compression study. The first was a stationary test which analysed two subsequent scans of the specimen under zero strain and aimed to quantify any mechanical perturbations in the scanner which may produce rigid body motion and scanner noise. The second was the rigid body translation test which analysed two scans also under zero strain with the latter undergoing a rigid body translation within the scanner. This test aimed to quantify the combined errors of the stationary test as well as interpolation errors caused by the specimen's movement.

Stationary Test

A baseline test was conducted to evaluate the strain resolution of the DVC technique. The specimen was imaged three times under zero strain (Scans A, B and C). A warm-up cycle of 15 minutes was implemented prior to the first scan (the scanner being run through a 'dummy' scan, with the X-ray source energised). DVC was performed between each scan (Scan A & B, and Scan B & C). With scans being run continuously, the initial thermal transient effect detected on the gun may be anticipated to affect Scan A, more so than Scan B and C. The sub-volume size used for analysis is explained later in this section and was 64 voxels with a 50 % overlap meaning measurements were taken at a spacing half of the voxel size and a two pass approach was used. Performing correlation on repeat unloaded data sets aims to capture all major sources of measurement error except for relative distortion (256). Ideally the displacement field computed by DVC for successive static images should be zero, but mechanical perturbations in the scanner may introduce some rigid body motion for example, and scanner noise (photon counting statistics, electrical noise, scattered radiation *etc.*) can affect the result. These baseline scans aim to quantify noise by calculating the strain

resolution from the calculated mean and standard deviation of the resulting DVC strain maps from each slice.

No smoothing was performed during or after the correlation process. The vector fields were exported from the LaVision software and the strain computed in MATLAB using the gradient command. The gradient command computes the first derivative of the vector field in each dimension using equation [19]. For the points on the surface of the 3D vector matrix the first order finite difference approximation was used. For points within the matrix, the command uses the second order central difference approximation to determine the derivative. The spacing refers to the distance between sub-volume centres which was constant in each direction.

$$\Delta \boldsymbol{F} = \frac{\partial \boldsymbol{F}}{\partial \boldsymbol{x}} \hat{\boldsymbol{\imath}} + \frac{\partial \boldsymbol{F}}{\partial \boldsymbol{y}} \hat{\boldsymbol{\jmath}} + \frac{\partial \boldsymbol{F}}{\partial \boldsymbol{z}} \hat{\boldsymbol{k}} \quad [19]$$

where $\Delta \boldsymbol{F}$ is a function of x, y and z.

Rigid Body Translation Test

To test the effectiveness of the DVC analysis when determining displacements and strain fields, rigid body translation was applied to the specimen. Two reconstructed volumes (Scans C & D) were obtained with the second (Scan D) undergoing a vertical rigid body translation within the scanner of 125 μm (~5 voxels). Strain resolution was investigated by applying the DVC algorithm to the volume after rigid body correction and calculating the mean and standard deviation of the resulting strain maps. Strain was calculated using the gradient function described previously.

Influence of sub-volume size

The DVC technique relies on the material's internal pattern to compute correlation between a reference sub-volume and the deformed sub-volume. It is known that the amount of material within each sub-volume and therefore the sub-volume size affects DVC resolution (299, 332). A sub-volume size that is too small is typically susceptible to noise effects, whilst an excessively large sub-volume may result in an inadequate spatial resolution (296).

In order to evaluate the influence of sub-volume size on the correlation resolution in this study, four different sub-volume sizes (24, 48, 64 and 96 voxel edge length) with a 50 % grid spacing were analysed on the two reconstructed volumes of the stationary unloaded specimen (Scans A & B and B & C), and after rigid body translation (Scans C and D). Figure 116 illustrates the typical structural content within different sub-volume sizes. The strain standard deviations for each sub-volume size were compared to the stationary results.

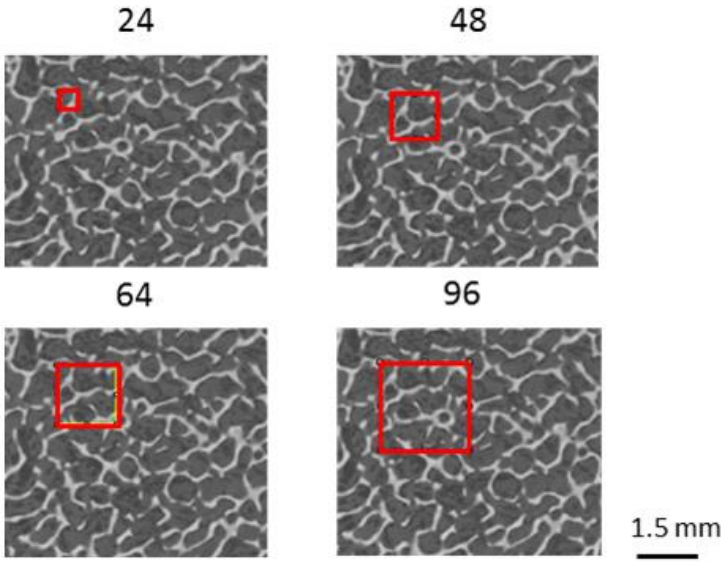

Figure 116: CT slices with sub-volumes of different sizes in relation to features of trabecular bone.

Table 14 provides a summary of the μCT measurements completed in the noise study.

Table 14: Summary of Scans A-D undertaken in noise study.

Scan Number	*Scan Details*
Warm up	Unloaded
A	Unloaded Stationary Scan
B	Unloaded Stationary Scan
C	Unloaded Stationary Scan
D	Vertical rigid body translation of 125 μm introduced in the z-direction

5.1.1.1 *Measurement Resolution Results*

The stationary and rigid body translation test scans were analysed with DVC and the resulting strain maps used to produce the mean strain and standard deviation. These two quantities for each strain component throughout the volume for the two stationary tests are shown in Figure 117a-f. The mean strain between the first and second stationary scans (Scans A & B) varied between 4×10^{-5} and -4×10^{-5} with the z direction exhibiting the most variation between slices (Figure 117a). All the standard deviations of the strain components were below 2×10^{-4} (Figure 117b). The standard deviation and mean strain for the second stationary test (Scans B & C) were lower than the first stationary test with the mean strain varying between 2×10^{-5} and -4×10^{-5} (Figure 117c) and the standard deviations of the strain components all below 1.4×10^{-4} (0.01 %) strain throughout the volume (Figure 117d).
The highest strain standard deviation values were obtained in the rigid body translation test (Scan C & D) due to the combined errors of the scanner, environment changes and also interpolation errors. The mean strain and standard deviation were +/- 2.5×10^{-4} and 7.5×10^{-4} respectively (Figure 117e and f).

Strain maps from a central slice in the stationary test (Scans A and B) showed spatial correlation (Figure 118) with an expected 2x2 sub-volume pattern consistent with the 50 % sub-volume overlap used in the correlation procedure.

Figure 119a and b illustrate the variation of the strain standard deviations calculated using sub-volume sizes of 96, 64, 48 and 24 voxels with a 50 % overlap. Figure 119 highlights that the standard deviation for the stationary test scans correlated with a 64 voxel or smaller sub-volume size increased significantly from below 4×10^{-4} (64 voxels) up to 7×10^{-4} (24 voxels). The standard deviation for the rigid body translated test scans correlated with a 64 voxel or smaller sub-volume size increased significantly from below 2×10^{-4} (64 voxels) up to 4×10^{-4} (24 voxels).

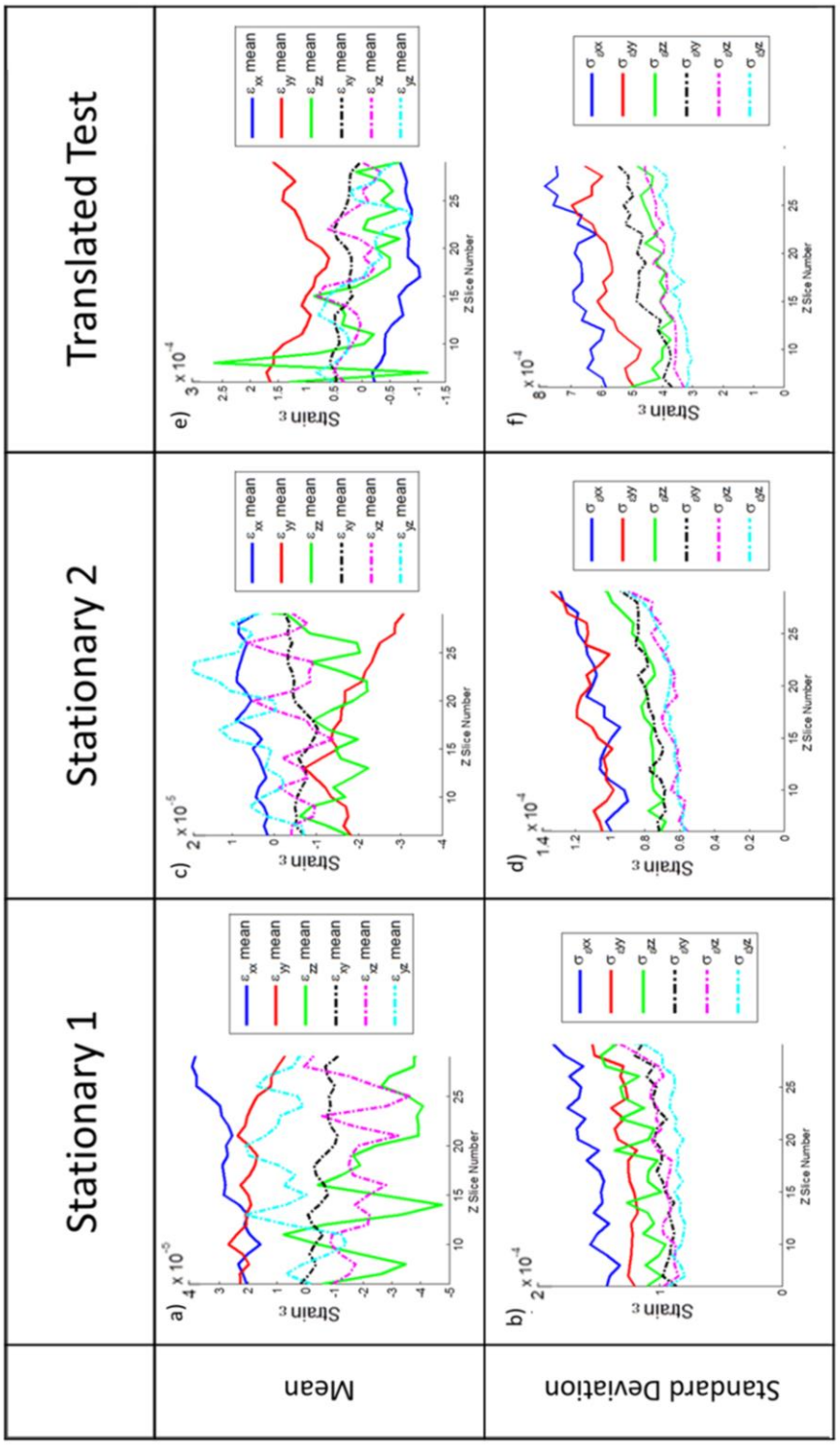

Figure 117: a) Mean strain between the first two repeat stationary scans (A and B). Slice 1 is located at the top of the specimen. b) Standard deviation of the strain maps between the first two repeat stationary scans (A and B). (A 64 voxel size with a 50 % overlap was used in the DVC calculation). c) Mean strain for the second and third stationary scans B & C. d) Standard deviation of the strain maps for the second and third stationary scans B & C. e) Mean strain between the stationary and translated scans (C and D). f) Standard deviation of the strain maps between the stationary and translated scans (C and D).

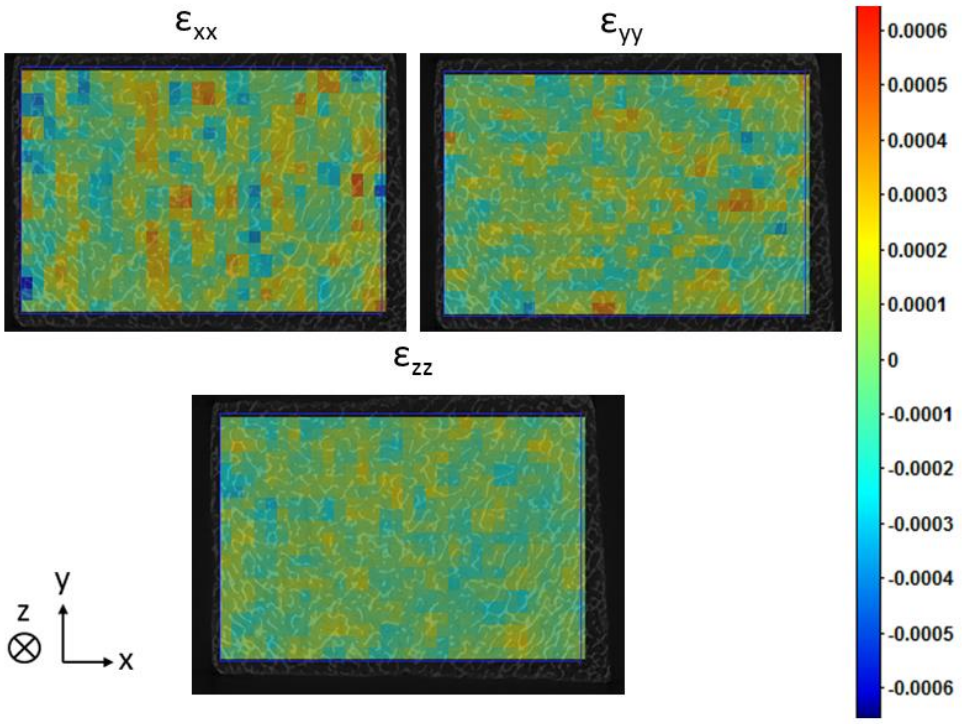

Figure 118: Nominal strain maps in central transverse slice for the stationary specimen test after 15 minute warm up. (Scans A & B).

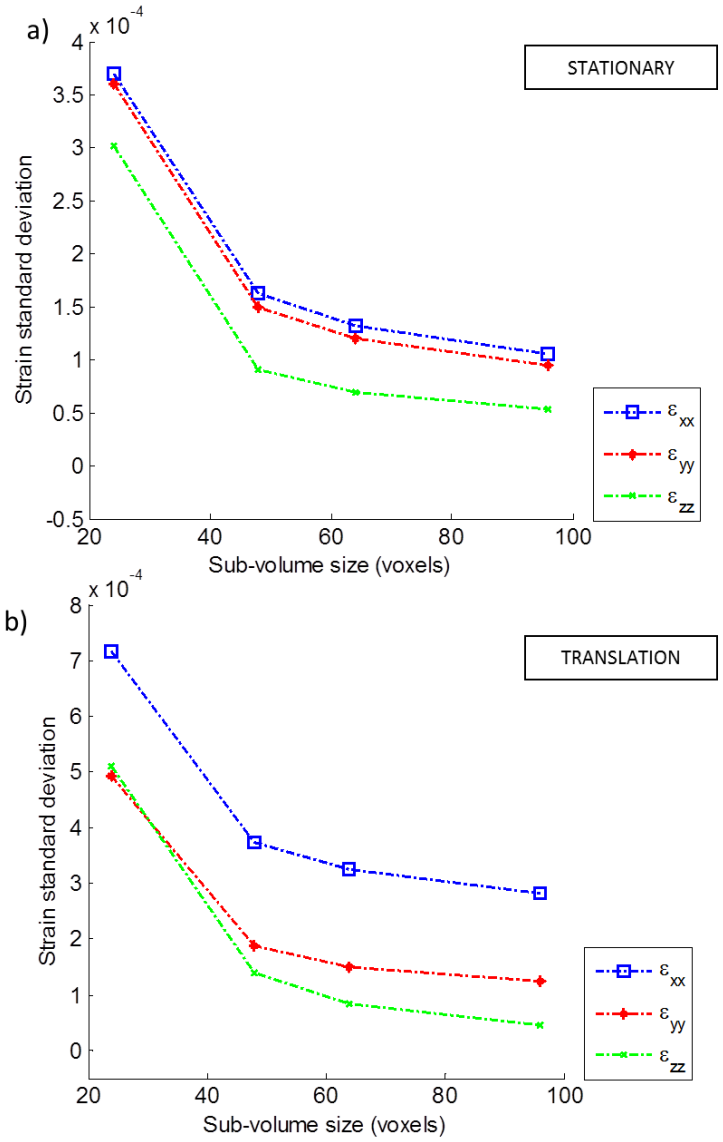

Figure 119: a) Strain standard deviation for stationary test (Scans B & C) and b) translation test for different sub-volume sizes (24 to 128).

5.1.1.2 *Measurement Precision Discussion*

The implementation of the FFT and the multipass approach on μCT images of trabecular bone allowed rapid calculation with strain standard deviation values between 2 x 10^{-4} and 8 x 10^{-4} for a sub-volume size of 64 voxels with a 50 % overlap. The values compare well with data reported in the literature of local DVC approaches (256, 311, 333) where strain standard deviation ranged between 100 – 800 με. Figure 118 illustrates the strain maps for each strain component where the significant heterogeneities apparent in Figure 117 a, c and f are visualised with positive and negative values on the strain map. The results show minimal spatial correlation limited to a 2x2 pattern which is due to the 50 % grid spacing used in the analysis.

The strain resolution improved between the first and second stationary tests suggesting that the gun was affected more by the initial thermal transient in Scan A than in Scans B and C.

Section 4.1.3 reviewed the influence of heating effects indicating that variations can affect scan quality and DVC precision. Therefore it is suggested for future μCT studies using this scanner a longer warm up scan should be completed as well as an initial specimen scan in order to obtain the lowest noise artefacts.

The results of the rigid body translation test showed that the strain standard deviation was higher than for the stationary tests which was in agreement with previous studies (300, 333). This was expected as the rigid body translation test suffered from the same noise and discrepancy sources as the stationary test but it will also suffer from interpolation biases because of the specimen movement.

The evaluation of sub-volume size on the correlation precision indicated that for both the stationary and rigid body translation tests, a 64 voxel sub-volume with a 50 % overlap was an adequate compromise between strain resolution and spatial resolution. The strain standard deviation computed in the stationary test reduced by 2.5 times when the sub-volume increased from 24 to 64 voxels. Figure 116 provides an indication of the typical proportion of trabecular structure contained within sub-volumes of different sizes. It is shown that a 48 voxel or smaller sub-volume contains a small portion of a single trabecula which will make it susceptible to noise effects. In comparison a 64 voxel sub-volume encloses multiple portions of different trabeculae generating a more defined pattern for correlation. An even larger sub-volume (above 65) encloses multiple whole trabeculae which may result in an incorrect approximation of the underlying deformation of each individual trabeculae (334). Therefore a 64 voxel sub-volume size with a 50 % overlap was used in the compression study.

This sub-volume size was selected based on the strain resolution observed in the stationary and rigid body translation tests. Due to the 50 % overlap the algorithm allowed for larger displacements than the sub-volume size to be tracked. In the instance of large deformations which have induced a dramatic change in the material's internal pattern, inaccurate strain calculations would be highlighted with a poor correlation value being reported for the sub-volume.

The completion of the measurement resolution tests has enabled the strain resolution to be determined and is conducted in each DVC investigation performed in this thesis.

5.1.2 Compression Test Methodology

Following the stationary and rigid body translation tests, the specimen was axially compressed within the scanner. Six compression steps were applied under displacement control with μCT measurements taken at each step. The scan parameters were identical to that of Section 5.1.1 scans. The loading platen displacements between each step are shown in Table 15, whilst Figure 120 shows roughly the central section at three compression steps. The specimen was left to relax for 25 minutes prior to scanning to reduce the effects of time-dependent relaxation and specimen motion.

Table 15: Displacement parameters for each compression step.

Scan Number	Compression Step	Incremental Displacement (mm)	Absolute Displacement (mm)
1	*0*	*0*	*0*
2	*1*	*0.8*	*0.8*
3	*2*	*1.0*	*1.8*
4	*3*	*1.9*	*3.7*
5	*4*	*0.9*	*4.6*
6	*5*	*1.3*	*5.9*
7	6	*0.9*	*6.8*

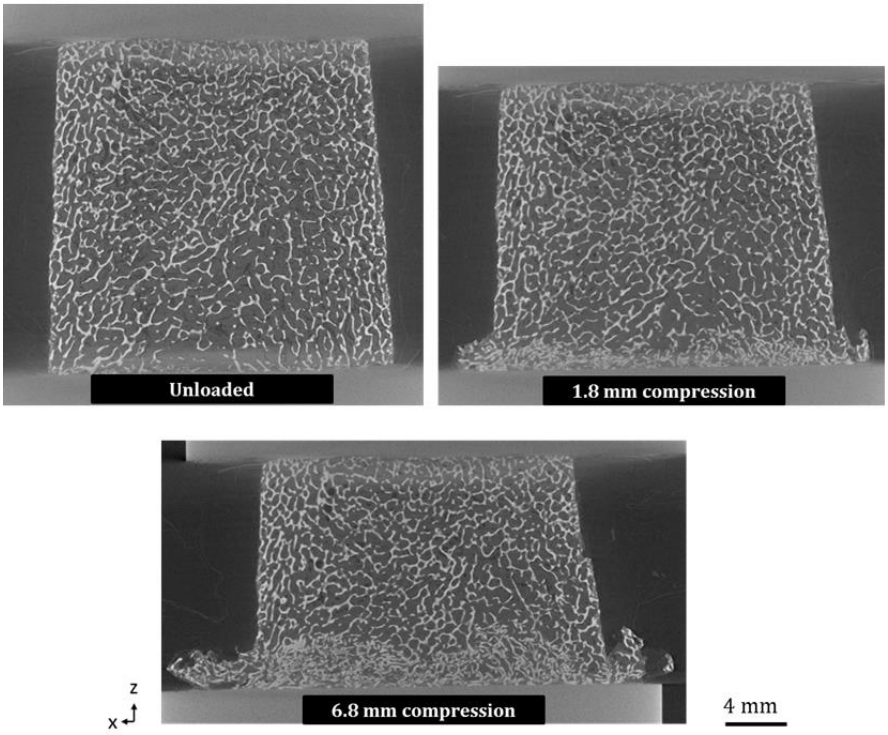

Figure 120: Slice of bone taken from the unloaded specimen and after 1.8 and 6.8 mm compression i.e. 3rd and 6th compression steps.

Each displacement stepwise pair (i.e. 0-0.8 mm, 0.8-1.0 mm, 1.0-1.9 mm) was analysed with DVC using a sub-volume size of 64 voxels with a 50 % overlap, therefore providing a

measurement every 32 voxels. It should be noted however that these measurements are not independent and that the spatial resolution is 64 voxels determined by the sub-volume size analysis performed in Section 4.4.1.1. The same procedure described previously was implemented to calculate the strains using the DaVis software.

For visualisation the strain vector fields were exported into VGStudio Max 2.1 (Volume Graphics, Heidelberg, Germany). VGStudio applies trilinear interpolation to the strain vector field to visually smooth the strain data.

To assess bone morphology, CTAnalyser software (Skyscan, Kontich, Belgium) was used. Bone volume fraction, trabecular separation and trabecular number were calculated for a 6 mm thick section at the crushed end of the specimen where bone collapse was seen to initiate.

Poisson's Ratio Identification

VFM was applied to the specimen to calculate the Poisson's ratio. The Poisson's ratio was identified for a central cube of bone within the main body of the specimen at each compression step which was adjacent to the crushed zone using VFM as described in Section 4.3.1.1 (Figure 121). The analysis was restricted to this section of bone to ensure the VFM functioned correctly as the unreliable data generated by the DVC algorithm in the crushed zone and at the specimen's edges adjacent to the air would restrict the results.

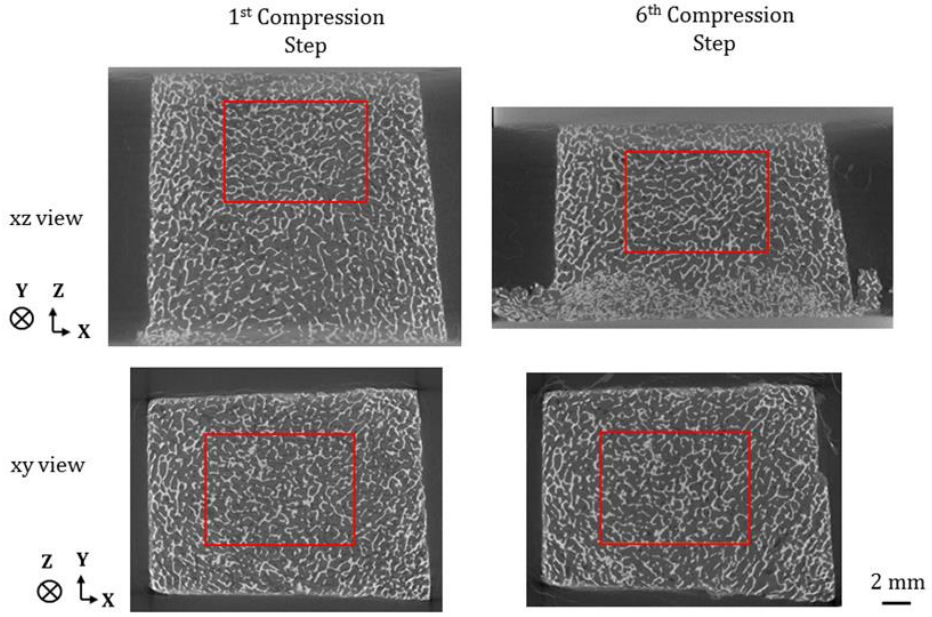

Figure 121: Central slice taken through the middle of the reconstructed volumes in the xz and xy views from the 1st and 6th compression step roughly indicating the cube of bone analysed using VFM.

To ensure there was zero contribution of the loading forces on the faces of the cube (i.e. from neighbouring sub-volumes) and to eliminate the loading term in equation [13] the following polynomial virtual field was set up.

$$\begin{cases} \boldsymbol{u_x^* = 0} \\ \boldsymbol{u_y^* = 0} \\ \boldsymbol{u_z^* = Z(Z - Z_a)X(X - X_a)Y(Y - Y_a)} \end{cases} \quad [20]$$

where u_x^* u_y^* and u_z^* are the virtual displacement components in x, y and z directions. X, Y and Z are the planar coordinates. X_a, Y_a and Z_a are the lengths of the active area in the x, y and z directions respectively. The terms $X\text{-}X_a$, $Y\text{-}Y_a$ and $Z\text{-}Z_a$ ensure that the virtual displacements are zero at the cube edges. The axes are shown in Figure 121.

The virtual strains ε_{xz}^*, ε_{yz}^* and ε_{zz}^* generated from differentiating the virtual displacements are equal to:

$$\begin{cases} \boldsymbol{\varepsilon_{xz}^* = (2X - X_a)Z(Z - Z_a)Y(Y - Y_a)} \\ \boldsymbol{\varepsilon_{yz}^* = (2Y - Y_a)X(X - X_a)Z(Z - Z_a)} \\ \boldsymbol{\varepsilon_{zz}^* = (2Z - Z_a)X(X - X_a)Y(Y - Y_a)} \end{cases} \quad [21]$$

As previously shown the Lamé parameters can be used to derive the Poisson's ratio (equations [15] and [17]) and determined k (equation [22]).

$$\boldsymbol{k = \frac{-\left(\overline{\varepsilon_{zz}\varepsilon_{zz}^*} + 2\overline{\varepsilon_{yz}\varepsilon_{yz}^*} + 2\overline{\varepsilon_{xz}\varepsilon_{xz}^*}\right)}{h(\varepsilon)\varepsilon_{zz}^*}} \quad [22]$$

where the overline indicates spatial averaging over the field of view. Equation [22] was then inserted into the relationship shown in equation [17] to calculate the Poisson's ratio.

Since Poisson's ratio of trabecular bone can vary considerably and is rarely known *a priori*, there is no reference value available to check against that obtained using the VFM. Therefore the constant uniaxial stress approach was used to provide an indication of the expected value as this method has previously been used by researchers for Poisson's value calculation (239, 335). The spatial average of ε_{xx}, ε_{yy} and ε_{zz} were used to calculate the average Poisson's ratio using the constant uniaxial stress approach (equation [23]). The spatial average equations for the x-direction (ν_{xz}) and y-direction (ν_{yz}) shown in equation [23].

$$\boldsymbol{\nu_{xz} = -\frac{\overline{\varepsilon_{xx}}}{\overline{\varepsilon_{zz}}}} \text{ and } \boldsymbol{\nu_{yz} = -\frac{\overline{\varepsilon_{yy}}}{\overline{\varepsilon_{zz}}}} \quad [23]$$

This calculation was performed between consecutive stages of loading, leading to tangent Poisson's ratio values. Aside from generating a baseline value, the constant stress approach was utilised to underline the shortcomings of calculating the Poisson's ratio based on the constant stress assumption.

Platen compression tests are expected to produce a uniform uniaxial stress state within the specimen. However, practical test implementations may lead to deviations and strain concentrations at the contact areas which will violate the uniaxial stress assumption resulting in an inaccurate Poisson's ratio calculation.

To investigate this shortcoming, a finite element (FE) model of a specimen experiencing a uniform compressive load was analysed. As the Poisson's ratio is manually input into the FE

simulation, the idea was to use the strain data obtained from the FE simulation and re-obtain the Poisson's ratio using the VFM and the constant stress approach.

ABAQUS finite element code (336) was used to analyse a 20 x 20 x 20 mm cube solid model. The model consisted of three-dimensional solid elements made up of C3D8R, 8 node linear brick elements. The bottom surface was fully constrained (Ux, Uy and Uz = 0) to simulate contact between the bone and the compression platen. The top surface was constrained in x and y (Ux and Uy = 0) and a uniform pressure P_{uni} = 100 N was applied in the z direction. The model was assigned elastic isotropic properties with a Young's modulus of 150 MPa and a Poisson's ratio of 0.30. Once the simulation was complete, the strain components were exported from the software. The Poisson's ratio was re-obtained by applying the same VFM and constant stress approaches used on the experimentally tested porcine bone. Two further models were analysed using ABAQUS with identical settings to the original model. However, the height of the specimen was varied, heights of 10 and 100 mm were analysed.

Figure 123 and Figure 124 illustrate that the experimental test set up shown in Figure 115 applied a non-uniform load to the specimen which implies the compression platens were non-parallel. This is especially evident in compression step 1 where a heterogeneous strain distribution is induced away from the compression platens. To investigate the combined effect of the application of a non-uniform load and strain concentrations at the contact areas, a non-uniform pressure P_{app} was applied to the top surface using the relationship $P_{app} = P*(Y/L)$ where P = 100 N and L is the specimen height, over a ramp time of 5 s, and the FE analysis was repeated.

5.1.2.1 *Compression Results*

Strain Results

All the load steps were analysed with DVC parameters previously described to give volume maps from which strains were calculated without smoothing. The first, third and final compression steps are reported here. In addition to the displacement vector fields, the correlation maps for the volumes were also exported into VGStudio Max 2.1 to assess the correlation quality. Figure 122 illustrates the correlation maps for a central section of the bone at compression steps one, three and six. The maps clearly show the degradation of correlation adjacent to the compression platen where the bone is being crushed resulting in the loss of the bone's natural internal pattern required for DVC. The correlation map between Scans 1 and 2 after 0.8 mm compression shows that the majority of the specimen shows a satisfactory correlation coefficient above 0.95 (Figure 122). However, adjacent to the bottom platen there was a reduction in coefficient to 0.90. Correlation between the third and fourth scan after 1.9 mm compression showed that the region with a correlation coefficient between 0.75 - 0.85 had increased and there had been the introduction of a poorly correlated region with values ranging from 0.10 – 0.50. This poorly correlated region increased in size after the final compression step with a sharp gradient to the highly correlated region. After the final compression the poorly correlated region was not only contained in the region next to the

bottom platen but also spread along a diagonal stripe to the edge. This stripe was due to a section of bone fracturing away from the main bone volume.

Figure 122 shows the resulting ε_{zz} strain maps for the central section for compression steps one, three and six. The first compression step exhibited strain values ranging from -0.030 to 0.002. The maximum compressive strain was located along the right hand edge whilst the minimum strain was located on the opposite top edge indicating that non-axial compression was applied. These strains were significantly higher than the strain standard deviation values obtained from the stationary and rigid body translation tests and indicate that they were due to material behaviour and not a noise artefact. The amount of displacement was larger between Scans 3 and 4 and this was reflected by the higher compressive strain recorded (-0.050). The elimination of poorly correlated data highlighted the rapid decline in compressive strain next to the crushed zone. Away from the crushed layer, strains varied between -0.007 to -0.009 for the third compression step.

In the final compression step the strain varied from -0.025 to 0.015. The maximum compressive strains were located in concentrated regions adjacent to the crushed zone with the strain in the majority of the remaining area being between -0.009 to -0.005. As the crushed layer was identified as a source of unreliable data, sections were also taken through horizontal sections at the top of the specimen.

Figure 123 shows a central strain map from the load step in the elastic region away from the crushed zone and showed how the loading conditions changed during the test. It has been highlighted that in the first compression step the loading was non-uniform and this is shown in Figure 122. Figure 123 also shows it to be diagonally orientated across the specimen with the maximum compressive strain concentrated in the bottom right hand side indicating corner loading, with it slightly more concentrated along the x-axis. In compression step 3 the load remained non-uniform but the maximum compressive strain was now located along the bottom edge and decreasing to a minimum along the y-axis. In the final compression step the loading became more uniform as the slack in the loading rig had been accommodated.

Figure 122 shows the correlation maps for the first, third and last compression steps at a distance of 8, 6 and 4 mm from the top compression platen and the resulting strain values. Within these sections, the correlation coefficient remained above 0.95 for all compression steps apart from one instance where it reduced to below 0.90 at the front right corner of the specimen in the final compression step. Within this well correlated region for the same section the ε_{zz} strain values ranged between -0.030 and zero after the first load step. The maximum compressive strain was located in the front right corner and decreased to zero in the opposing corner showing the application of a non-uniform load. The third compression step also showed a non-uniform load setup with the maximum compressive strain (-0.015) being located at the back of the specimen. After the final compression step the strain ranged from -0.015 to 0.005 with the maximum compressive strain located next to the section of bone

which had fractured from the main body. The majority of the section was at a strain between -0.005 and -0.010.

Table 16 shows the maximum compressive strain recorded at each compression step. These are the incremental strains documented between two consecutive compression steps, (e.g. 1-2, 2-3, 3-4) and therefore represented the evolution of strain as a function of step number, their addition providing an overall strain value of -0.17 for a total of 6.9 mm compression.

Figure 125 and Table 17 illustrate and quantify the difference in bone morphology between the unloaded and crushed section of bone. The bone volume fraction increased from 14.9 % to 34.4 % as the crushed region formed causing trabecular separation to reduce from 0.56 to 0.37 and the trabecular number per mm to increase from 1.08 to 2.10.

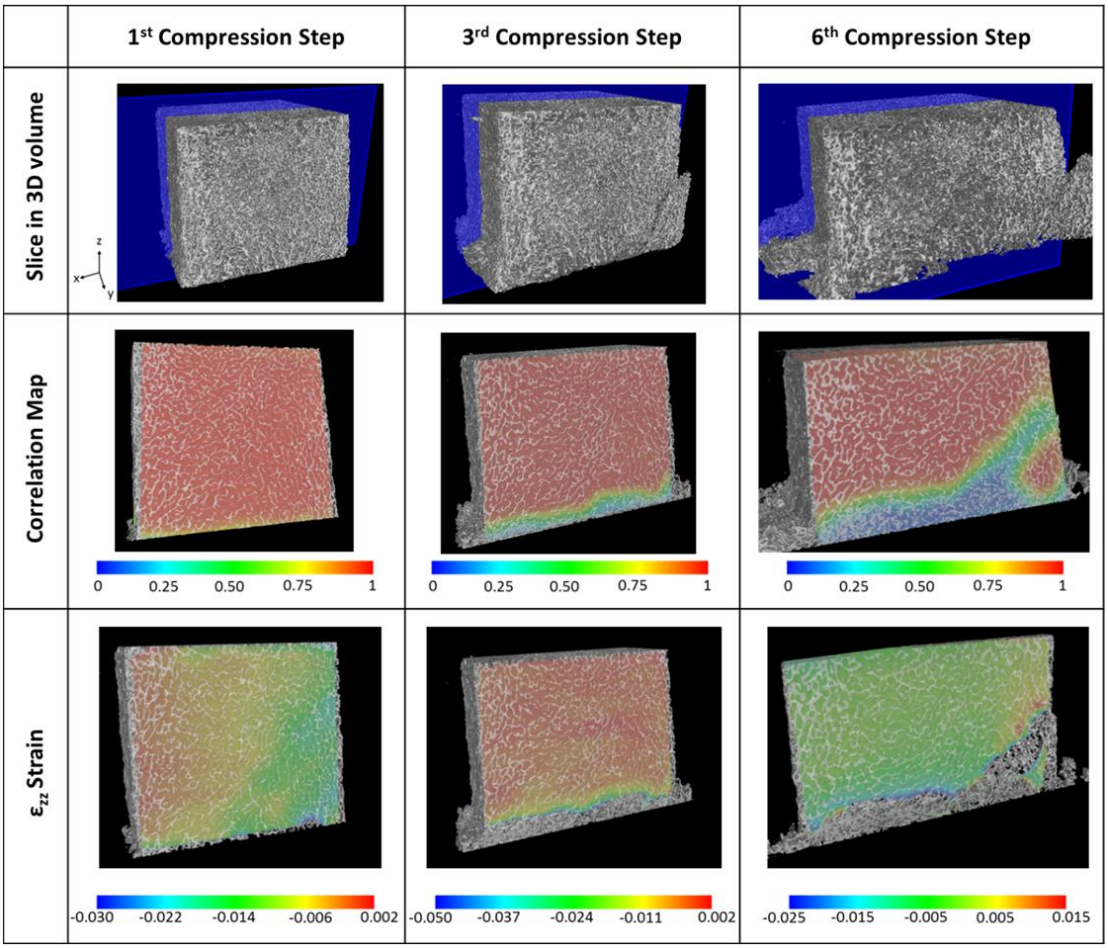

Figure 122: Correlation maps and ε_{zz} strain maps for central slice of the specimens between Scans 1 & 2 (0.8 mm displacement), Scans 3 & 4 (1.9 mm displacement) and Scans 6 & 7 (0.9 mm displacement). Strain values within crushed zone and correlation coefficient below 0.90 removed.

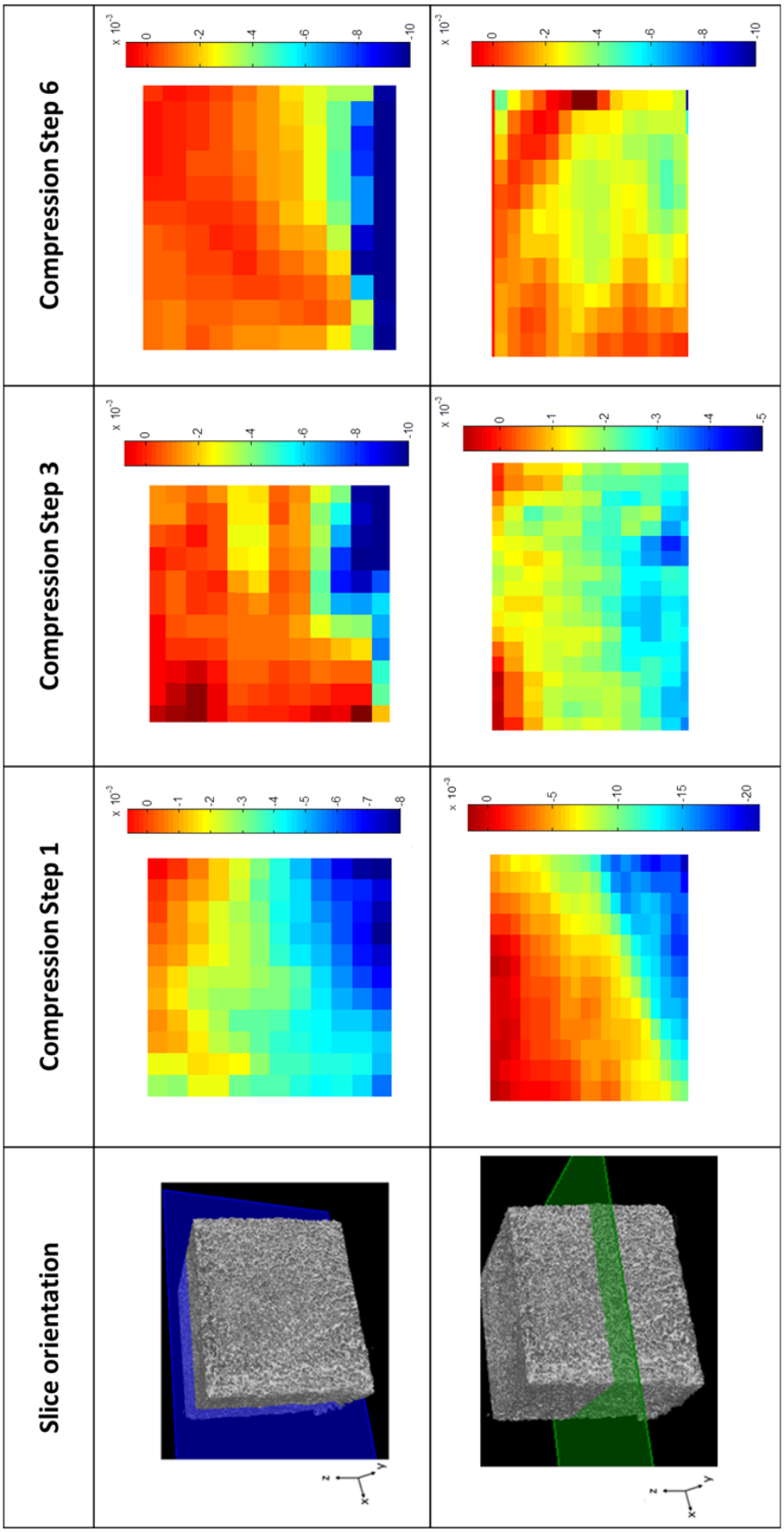

Figure 123: ε_{zz} strain maps of a section of bone away from the crushed zone for the 1st, 3rd and 6th compression steps

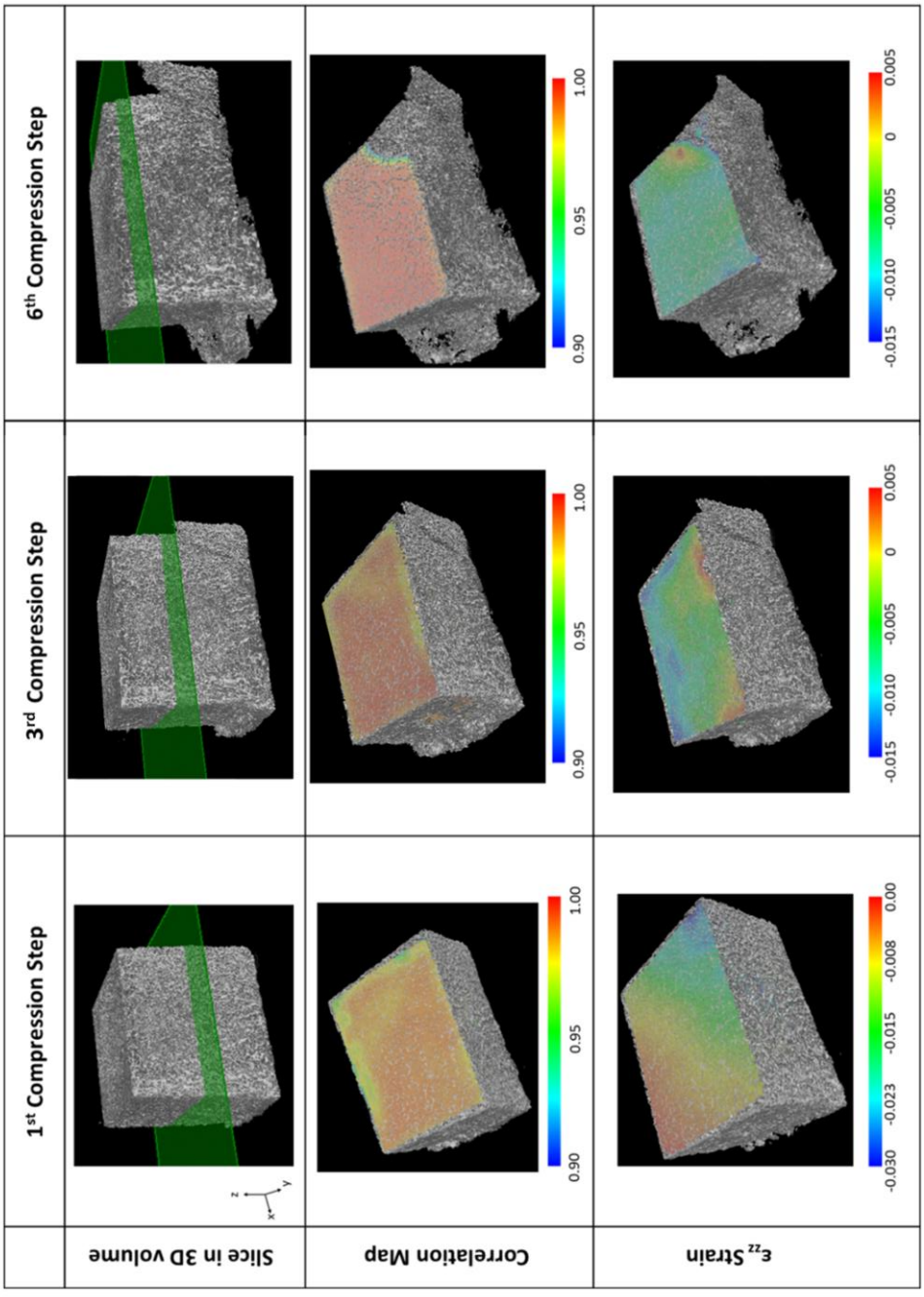

Figure 124: Correlation maps and ε_{zz} strain maps for central slice with good correlation of the specimens between Scans 1 & 2 (0.8 mm displacement) and Scans 6 & 7 (0.9 mm displacement). Strain values within crushed zone and correlation coefficient below 0.90 removed away from the crushed zone for the 1st, 3rd and 6th compression steps

Table 16: Maximum compressive strain recorded at each compression step.

Compression Step	Maximum strain recorded outside of crushed zone
1	-0.030
2	-0.040
3	-0.050
4	-0.010
5	-0.016
6	-0.025
TOTAL	**-0.171**

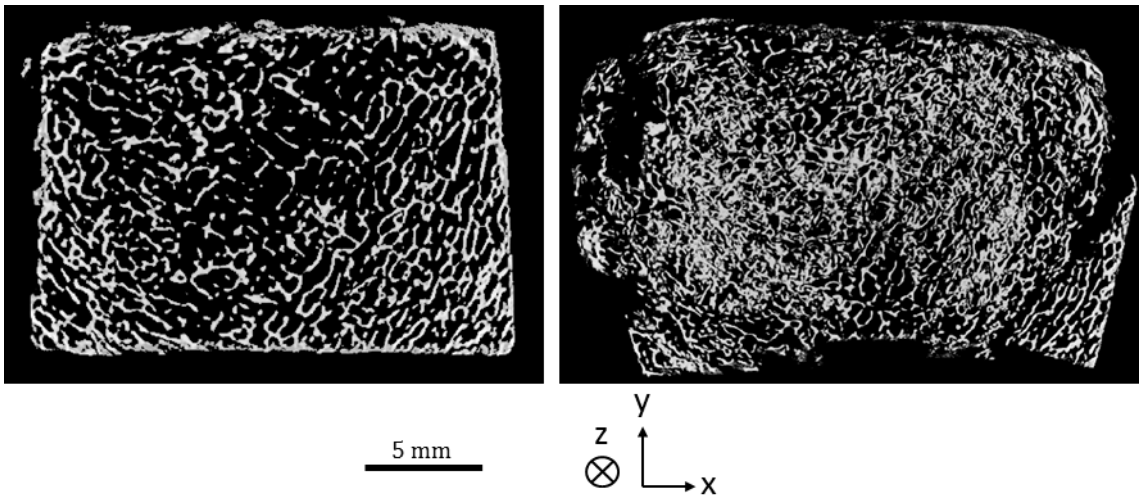

Figure 125: Slice through uncompressed section (left) and compressed section after six displacement steps (right), highlighting the loss of natural trabeculae pattern required for the correlation procedure.

Table 17: Bone morphology at each load step.

	Scan Number						
Parameter	***1***	***2***	***3***	***4***	***5***	***6***	***7***
Bone Volume Fraction (%)	14.9	21.6	28.9	29.6	32.1	31.0	34.4
Trabecular Separation Tb.Sp (mm)	0.56	0.52	0.48	0.42	0.43	0.40	0.37
Trabecular Number Tb.N (mm^{-1})	1.08	1.34	1.52	1.65	1.81	1.93	2.10

Poisson Ratio Results

Table 18 shows the evolution of the Poisson's ratio for a central cube of trabecular bone within the specimen adjacent to the crushed zone with increasing compression. The Poisson's ratio decreased from 0.32 to 0.21 as compression increased. The Poisson's ratio calculated using the uniaxial approach showed a similar trend to the VFM Poisson's ratio

although both components were lower and more erratic in behaviour because of the effect of stress multi-axiality as detailed previously.

Figure 126 and Figure 127 show the strain maps predicted for the FE 3D model under uniform and non-uniform loading. In both cases shear and transverse stresses were produced at the compression platen boundaries. This was due to the transverse strains being close to zero at the top and bottom surfaces but a strain gradient was present for both transverse components away from the constrained surfaces (Figure 126) while in the middle it was nearly uniform.

The virtual field applied to the compressed DVC bone data was applied to the FE strain data that was output from ABAQUS for both models and compared to the constant stress approach also calculated from the FE data. The results for each loading condition are presented in Table 19 as well as the data gathered from the models with varying height geometry. Both loading conditions documented a similar lower and inaccurate result than the VFM analysis. It was also documented that the errors produced between the reference Poisson's ratio value (0.30) and the constant stress value decreased as the height of the specimen increases.

Table 18: Evolution of the Poisson's ratio in a cube of bone with compressive deformation for virtual fields and uniaxial approach. $\nu_{\text{virtual field}}$ is the Poisson's ratio calculated by the virtual field method. ν_{xz} and ν_{yz} are the Poisson's ratio's calculated in the xz and yz directions.

Compression Step	$\nu_{\text{virtual field}}$	ν_{xz}	ν_{yz}
1	0.32	0.28	0.19
2	0.31	0.28	0.22
3	0.27	0.26	0.20
4	0.25	0.22	0.19
5	0.23	0.16	0.11
6	0.21	0.15	0.10

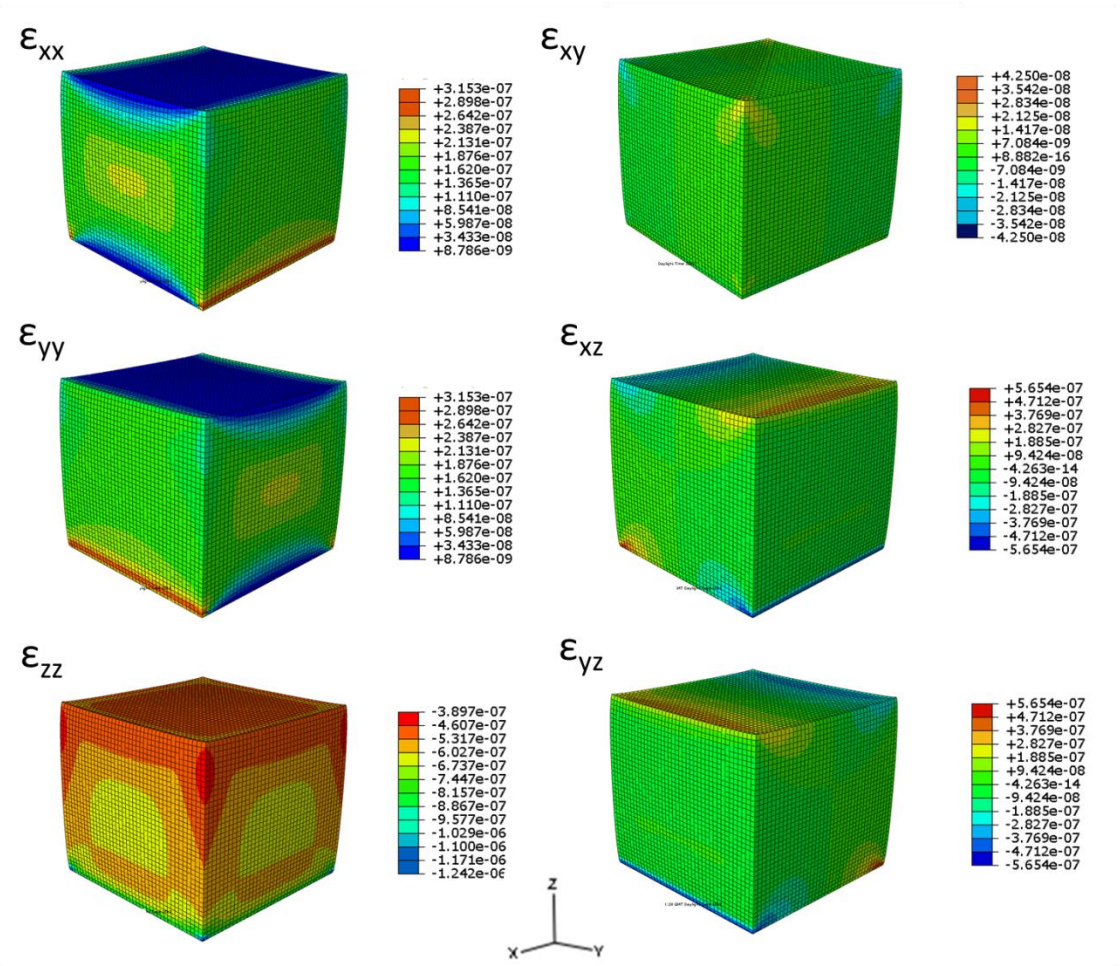

Figure 126: The ε_{xx}, ε_{yy} and ε_{zz} strains predicted by ABAQUS for the 20 x 20 x 20 cube under uniform loading

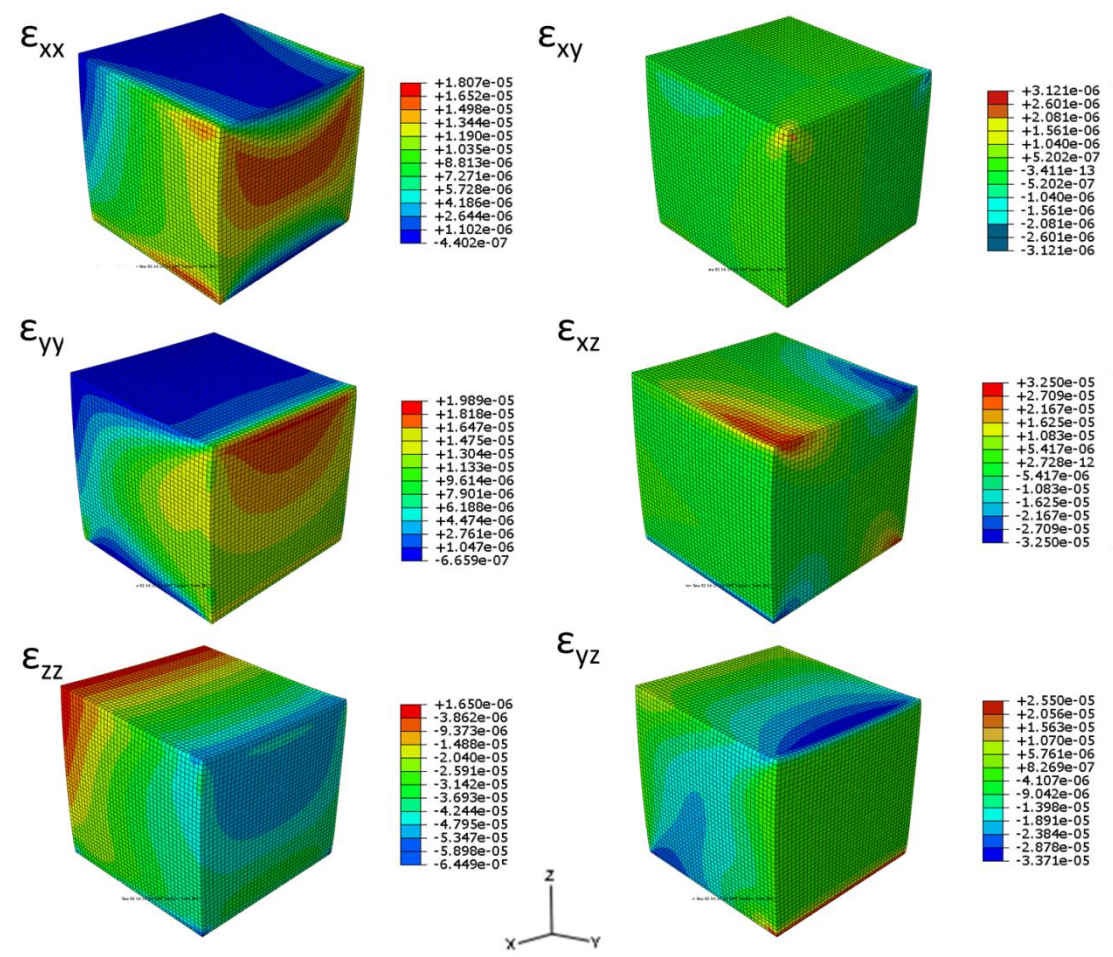

Figure 127: The ε_{xx}, ε_{yy} and ε_{zz} strains predicted by ABAQUS for the 20 x 20 x 20 cube under non-uniform loading.

Table 19: Poisson's Ratio results obtained from the VFM and constant stress approach. Poisson's ratio is equal to 0.30.

	Uniform load			**Non-uniform load**		
	Poisson's Ratio, *ν*			**Poisson's Ratio, *ν***		
Specimen dimension (width x thickness x height)	**20x20x10 mm**	**20x20x20 mm**	**20x20x100 mm**	**20x20x10 mm**	**20x20x20 mm**	**20x20x100 mm**
VFM, $\nu_{virtual\ field}$	0.30	0.30	0.30	0.30	0.30	0.30
Constant Stress, ν_{xz}	0.19	0.25	0.29	0.18	0.24	0.29
Constant Stress, ν_{yz}	0.19	0.25	0.29	0.18	0.24	0.29

5.1.2.2 *Compression Discussion*

Measurement resolution should be considered in the context of the strains that were expected within the analysed specimen (256). It was visually apparent from Figure 120 that there was trabecular bone failure adjacent to the lower platen generating a crushed layer which increased in thickness with compression. However, the remaining volume underwent little deformation and the compressive strain was seen to increase rapidly near the edge of the crushed layer. Previous experimental studies have shown the onset of trabecular bone failure to be between 0.8 – 1.0 % (8×10^{-3} - 1×10^{-2}) strain for human and bovine specimens (240, 337). However, Teo et al. (2006) (338) have reported a significantly higher yield strain of 16 % for a 5 mm^3 porcine vertebral specimen, although the standard deviation was relatively high. The strain values measured in this study are more in-line with the cited data for human and bovine specimens. It is suggested that this was due to differences in donor site, donor age and load orientation axis. It is well known that these factors can influence the mechanical properties of bone with mean values of modulus showing a difference by more than an order of magnitude (339). Aside from these factors, strain is usually measured in this common platen compression test using an extensometer attached to the end platens which introduces end artefacts. These artefacts have been shown to introduce errors in the measurement when damage occurs at the ends of the machined specimens, adjacent to the platen and could also suggest a reason for the differences in failure strain values.

Based on these results and the range of maximum strain values recorded in this study (0.5 – 0.9 %), the measurement resolution in this study (0.02 – 0.08 %) should be low enough for authentic strain to be recorded within the specimen at the onset of trabecular bone failure. The strain values documented represent the evolution of strain as a function of step number (e.g. strain between compression steps). Table 16 illustrates that the addition of the maximum strains between load steps gives an overall strain value of ~0.2 which is significantly higher than the measurement resolution.

The DVC process splits the image volume into sub-volumes and maps the deformation of each sub-volume in the reference (undeformed) and deformed volumes. The process relies on the variation of grayscale values (i.e. the material's natural pattern within each sub-volume) to calculate the displacement. If the material's internal pattern is excessively deformed or the material does not initially exhibit a distinctive pattern, DVC will be impossible. Figure 122 illustrates the correlation coefficient for a central section of the compressed sample between Scans 1 and 2 (0.8 mm compression), 3 and 4 (0.9 mm compression) and 6 and 7 (0.9 mm compression). The figures show the volumes were well correlated in the region with little deformation (coefficient above 0.98). However, within the crushed zone the correlation coefficient was very low and unsatisfactory for DVC calculations (between 0.1 and 0.5). It is clear that this was due to the crushed bone morphology excessively changing to a texture which was unable to be correlated by the DVC algorithm. Consequently, as the programme forced a solution, the strains calculated within

these poorly correlated regions were meaningless, highlighting one of the limitations when using DVC on a specimen which has experienced excessive deformation. To obtain authentic strain results, values within these poorly correlated crushed regions should be ignored. To filter out data calculated from sub-volumes with a poor correlation, data was removed from sub-volumes with a correlation coefficient value below 0.90. This produced strain values which coincided with published strain failure data of trabecular bone (240, 337). This outcome was crucial for the next investigation where the strain generated around the CFRPEEK acetabular component were assessed. After implantation it is likely that a crushed bone layer will form around the component and unreliable strain data will be generated in these sub-volumes adjacent to the component edge. The application of a 0.90 filter should allow reliable data to be extracted from the analysis.

In the first compression step (Figure 122) an irregular strain map was identified due to the application of non-uniaxial compression evidenced by the concentration in strain at the bottom right corner of the specimen. The strain values calculated away from the crushed zone were compressive with the majority of the strain recorded around -6×10^{-3} (0.6 %) which is below the failure strain in published data (240, 337) and above the strain resolution values calculated in the stationary and rigid body translation tests. Figure 123 further illustrates the application of a non-uniform load in the initial stages of compression with it more evident in compression steps 1 and 3 and subsiding to a more uniform loaded setup in compression step 6.

The majority of the ε_{zz} strain generated between Scans 6-7 (0.9 mm compression) were below -5×10^{-3} which was significant as it was above the strain resolution calculated Section 5.1.1. Adjacent to the crush zone was a thin band of material with strain varying between -2.5×10^{-2} and -8×10^{-3}, again consistent with failure strains in previous studies (240, 337). DVC calculations in the region of bone with modest deformation near the top platen exhibited satisfactory correlation and the strains in this area were lower than the strain adjacent to the crushed zone but still significant as they were above the strain resolution value (Figure 123).

A typical stress-strain curve for an open-celled porous structure undergoes initial linear elasticity, plastic yielding and densification (340). Table 17 shows the micro-architectural parameters of the crushed zone at each compression step. The results show densification with the bone volume fraction increasing and trabecular separation decreasing, which consequently increased the number of trabeculae within a certain region. It is likely that the trabecular damage occurred through transverse cracks, shear bands, parallel cracks and complete trabecular fracture as previously observed by Wachtel and Keaveny (1997) (341). However, spatial resolution limitations did not allow failure on the trabecular surface to be identified and a future study could be conducted on a specimen imaged at a higher spatial resolution.

The Poisson's ratio was identified using the virtual field equation [13] and the optimised virtual field from Section 4.3.1. The results are shown in Table 19 and it can be seen that the

Poisson's ratio was positive but decreased with increasing compression. The Poisson's ratio ranged between 0.32 and 0.21 lying within the range given in published data (325-329). It is not uncommon for the Poisson's ratio of a material to vary with the strain level (342). A similar decrease in the Poisson's ratio has been found for standard low density polyurethane foam tested under compression (320). This study also found a similar deformation relationship in which the compression initiated where the load was applied. The mechanism for generating the strain pattern in the foam and the resulting decrease in the Poisson's ratio was concluded to be related to the collapse of whole rows of cells by buckling of the cell walls. It is known that trabecular bone has rod and plate trabeculae which fail at varying levels of strain depending on their orientation to the applied load (343). In compression the trabecular rods orientated parallel to the loading axis buckle and collapse similarly to the cell walls in the foam.

Comparison with the uniaxial average Poisson's ratio approach showed this technique slightly underestimated the Poisson's ratio, with a value of 0.28 and 0.19 for ν_{xz} and ν_{yz} respectively compared to 0.32 calculated by the VFM (Table 19). Discrepancies between these values are suggested to be due to two issues. The first one was due to friction at the platen interface which generated shear and transverse stresses. The second was the application of a non-axial load which generated rotation and which was evident in the first load step in Figure 123. These factors violated the constant uniaxial approach decreasing the accuracy of the obtained Poisson's ratio. The constant stress approach has been used in previous analyses (239, 335) to obtain the Poisson's ratio of trabecular bone and the shortcomings of this approach are highlighted in the FE analysis. Table 19 shows the Poisson's ratio results calculated from the uniformly and non-uniformly loaded FE models and highlighted an underestimation from the reference value 0.30.

The FE strain maps for the uniform and non-uniform loaded models (Figure 126 and Figure 127) showed the generation of the shear and transverse stresses adjacent to the platen boundary especially at the corners of the specimen and these were most evident under uniform loading (Figure 126). Table 19 illustrates the influence of specimen height on the accuracy of the constant stress approach illustrating that the accuracy was improved with increasing specimen height. This was expected as the local strain heterogeneities concentrated at the contact boundaries were diluted into a larger volume of constant strain material (Table 19). In all cases the Poisson's ratio obtained using VFM was exact and showed that the technique was fully insensitive to boundary conditions as the virtual field had been set up to filter out unknown stresses at the boundary. The non-uniaxial compression was evident in Figure 122 and Figure 123 especially in the first compression step and highlighted the progression from initial corner loading to a more uniform load application (compression step 6). The results from the FE model loaded non-uniformly revealed that the constant stress approach underestimated the Poisson's ratio by a similar amount to the uniformly loaded setup. This relationship was also reflected in the experimental results as there was little

difference in the underestimation for compression step 1 which experienced non-uniform loading and compression step 6 which experienced more uniform loading (Figure 123, Table 18). It is suggested that the non-uniform load generated a strain gradient with low and high strain located on either side of the specimen which were cancelled out when calculating the average result.

This study and the results must be interpreted with consideration of their strengths and limitations. The conclusions drawn from the stationary and rigid body translation tests are limited to the material, equipment and parameters used. In addition, the number of specimens analysed in this section also limited the strength of the relationships obtained. Undertaking similar stationary and rigid body translation tests on a variety of materials and equipment would enable a reference of expected strain uncertainties to be available for future analyses with the intention of providing an insight into potential aspects that introduce biases in DVC.

Densification of the porcine specimen generated a poorly correlated crushed region which was a consequence of the material's internal pattern no longer being adequate for the DVC technique. Unfortunately, the crushed zone developed within the first displacement step resulting in data being removed from the initial analysis and therefore strains prior to bone failure were not identified. Although, this study quantified the strains within the specimen, the relationship between failure and the effect on the mechanical properties of bone (e.g. Young's modulus) could not be identified as the imposed compression load was not known. This study has only briefly touched on the possibilities for future analyses that can be performed using the full-field data extracted from a strained specimen using DVC. There is the possibility for future studies to use this information to extract other parameters including the materials Young's modulus and observe how it varies with compression, the effect of boundary conditions on the material behaviour, the influence of bone morphology on the material behaviour and material heterogeneity.

It has already been mentioned that a limitation of this analysis was the inability to record the imposed load. Without the known load the Poisson's ratio could only be determined as it can be calculated from the ratio between Q_{xy} and Q_{xx}; meaning it was not necessary to measure a force to identify it. The use of an electromechanical test rig which is compatible with a μCT scanner such as the Deben CT 5 kN tensile/compression loading rig (Deben UK Ltd, UK) will allow a similar analysis to be conducted but with the imposed load recorded. With this additional data the Poisson's ratio and the Young's modulus can be determined. The test rig would also allow the displacement to be more easily controlled permitting smaller displacements to be applied to the bone. Smaller displacement steps should capture the deformed bone prior to crushing enabling the evolution of mechanical properties to be determined. The tests boundary conditions have also been identified as a factor that should be further investigated due to the controversial issues that can arise. The compression platen test carried out in this analysis is a standard test method adopted by many researchers for

Poisson's ratio and Young's modulus determination (344, 345). Without access to the measurement systems and analysis methods adopted in this thesis, the strain required for modulus obtainment is usually measured using an extensometer attached to the end platens which hold the trabecular specimen. This is a simple method which assumes a frictionless interface at the loading platens, however controversy over this method exists due to this frictionless assumption and the presence of various experimental artefacts namely 'end artefacts' (345). These artefacts can cause the strains to be inaccurately calculated in the undamaged bone due to the strains being calculated from the relative displacement between the platens (346). The experimental artefacts have caused published values of trabecular tissue's elastic properties to vary considerably with documented ranges between 381 and 2380 MPa (239, 240) for bovine proximal tibia and 1.4 to 552 MPa (240-242) for human proximal tibia. Although these ranges could be reduced by applying the attainment of full-field deformation measurement generated through DVC, little is known how changes in boundary conditions i.e. frictionless or bonded surfaces affect internal strains. The effect of boundary conditions was briefly investigated in this section although by chance, as there was the application of a non-uniform load in the first load step which became more uniform as the test proceeded. Nevertheless, lack of control over the boundaries and the use of a single specimen did not allow for a conclusive outcome on the effect of boundary conditions. The compression discussion section briefly highlighted that the decrease in Poisson's ratio was attributed to the collapse of trabecular cells by buckling of the individual trabeculae and that the morphology of the trabecular network may influence its failure behaviour. The spatial resolution and lack of volume data prior to bone crushing did not allow this aspect to be investigated further and it is suggested that a future investigation is performed on the same compression setup but scans are performed with improved imaging resolution i.e. below 10 μm and deformations are captured between smaller displacement steps. The final area of investigation involves assessing heterogeneities of the strain fields whereby the VFM is set up to allow the Young's modulus to spatially vary throughout the material. In this analysis the calculation presented followed the assumption that the constitutive material was homogeneous. The VFM can be applied to heterogeneous materials, where the specimen is split into subregions over which the material is assumed to be homogeneous within these regions but have different stiffness components. Therefore, the parameters can be sought out of the integrals calculated over each of these subregions (312). If the investigated solid is assumed to be comprised of two different materials i.e. two different values of modulus are possible, then the number of virtual fields required is four as there are four sought parameters. As the number of assumed moduli increases, the number of sought parameters increases and the VFM analysis becomes more complex as more virtual fields are required for calculation. Heterogeneous materials have been explored in 2D with through thickness assumptions and the reader is directed to Pierron and Grédiac (2012) for these analyses (258).

5.1.3 **Conclusions**

This study has presented a repeatable set of tests for assessing the strain resolution when digital volume correlation is applied to μCT volume images of trabecular bone in order to measure compressive strains.

The results demonstrated that the strain resolution was low enough to measure strains generated from bone deformation when the specimen was compressed and similar scan settings should be used in future analyses.

The first important outcome was the detection of a crushed bone layer adjacent to the compression platen which confounded the DVC process and produced unrealistic strain values. It was found that a filter which removed data from sub-volumes possessing a correlation coefficient lower than 0.90 ensured realistic values were obtained. This was important for the next implantation investigations as it has been predicted that a crushed bone layer forms around the implanted component. The second finding was the successful coupling of DVC and the VFM and the prospect for future analyses.

6 Study 6: Implantation of Components and Assessment of Deformation of Animal and Analogue Bone Models.

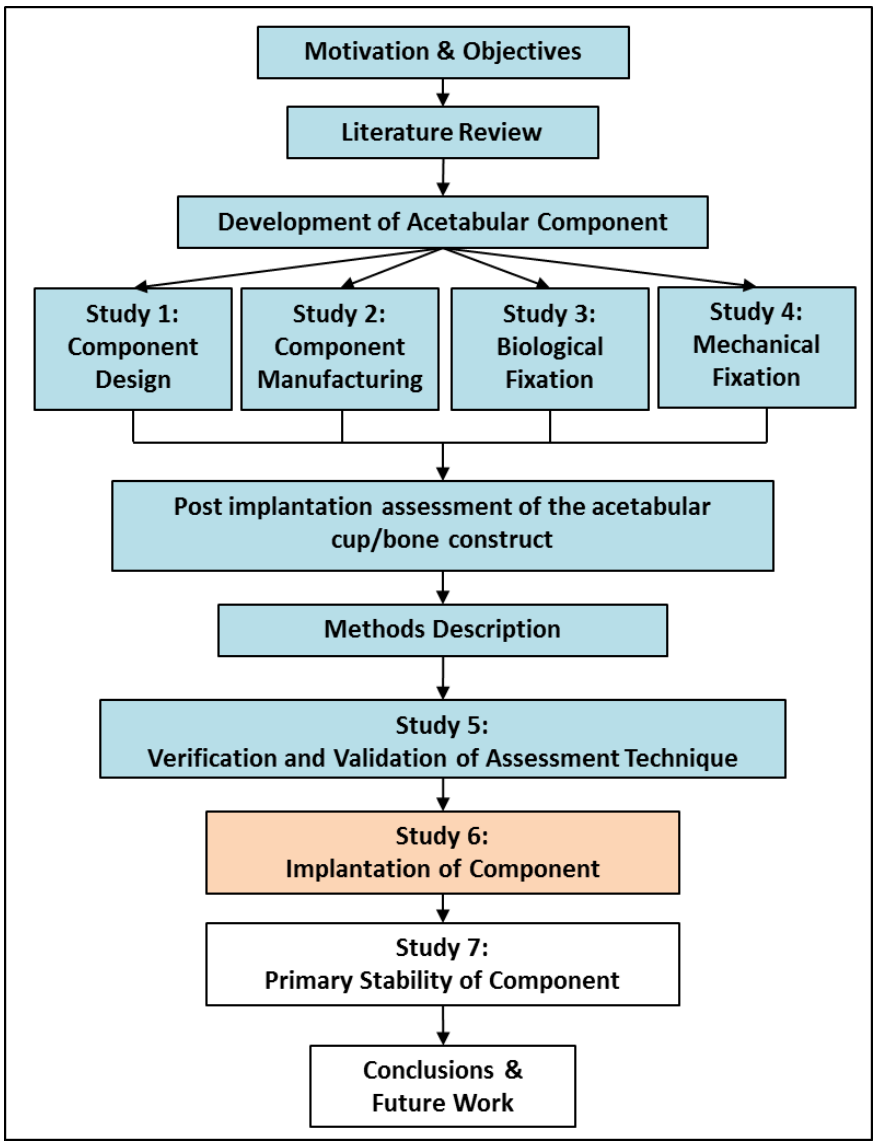

6.1 Investigation 1: Assessment of analogue bone deformation surrounding acetabular components of different stiffness.

The main aim of this thesis was to develop a more biomechanically compliant acetabular component comprising of a new material, new fixation method and proposing an overall new design. The polymer composite CFRPEEK was chosen as a potential material alternative to current materials used in traditional large diameter bearing acetabular components.

Section 2.7 established that the change in pre- and post-operative peri-prosthetic strains can give an indication of the bone adaption stimulus resulting from implantation of a component (66). DVC is a technique that can calculate full-field strain data and was successfully used in Section 5 to calculate strains in trabecular bone during a simple compression study. It was proposed that the method could be extended to record the strains generated around an

acetabular component with the potential of investigating the relationship between the stiffness of a component and the alteration of strain in the surrounding peri-prosthetic bone after implantation. This aspect was of particular interest to Aurora Medical Ltd as one of their key goals was to develop a more biomechanically compliant component from CFRPEEK with a more natural load path into the acetabulum.

Using the outcomes from Section 5.1, this section investigated the feasibility of applying DVC to assess the strain generation around two acetabular components implanted into an undersized cavity in an analogue bone model. The acetabular components were a low modulus CFRPEEK component coated with TiHA and a contemporary stiff metal backed, ceramic lined component.

Analogue bone models are a popular substitute for natural bone in biomechanical tests as they are readily available, cost-effective and attempt to replicate the stiffness of bone. Studies (347, 348) have concluded that analogue models can offer an alternative to human bone for a range of static and dynamic mechanical tests especially as they do not degrade, reduce inter-specimen variation and are generally low in cost in comparison to natural bone. Nevertheless, the morphology can differ (347) to natural bone as it has thicker and more widely spaced elements in comparison to trabeculae in human cancellous bone. This has been shown to have implications on the mechanical behaviour of the foam, which differs from that of natural bone specimens (347). In addition, the foam has been found to be more brittle than human bone (349). These aspects are potential limiting factors for its use as a bone substitute material in a strain analysis study of this kind. A difference in morphology may result in the foam deforming and failing differently to natural bone which will reduce the validity of using it as a substitute bone model. In the early stages of compression, elastic-brittle foam shows a linear-elastic regime up until a critical stress. Above this critical stress cells collapse by brittle fracture which is non-recoverable. This non-recoverable process may limit the foam's ability to replicate the visco-elastic properties of bone.

This section will identify the strain generated in analogue foam surrounding an implanted acetabular component. The accuracy and precision of the DVC procedure will be investigated using the protocol described in Section 5.1.1. A novel aspect of this DVC study is the inclusion of a component in the second scan to generate deformation in the analysed material (foam in this case); as previous studies have only analysed one material (256, 292, 299) usually with the same set up as described in Section 5.1.1.

Bone has been described as an ideal material candidate for DVC due to its porous nature. Section 5.1.1 showed that an adequate strain resolution was determined when the analysed volumes are obtained using μCT allowing small strains to be recorded in deformed specimens. The introduction of a second material with a higher attenuation coefficient in the deformed volume is likely to introduce artefacts such as beam hardening and scatter as described in Section 4.1.3 which will degrade the quality of the volumes, degrading the strain

resolution and making it more difficult to identify significant strains in the surrounding foam.

This study's main aim was to investigate the feasibility of using DVC to assess foam deformation when an acetabular component was implanted into an under-reamed cavity. Within the scope of this investigation, the possible affect that artefacts may have on the DVC procedure was also assessed.

Materials & Methods

One 180 x 130 x 40 mm block of SAWBONE open celled polyurethane rigid foam (Sawbone AB, Sweden) with density 0.12 g/cc was reamed to enable implantation of a 54 mm outer diameter (OD), 44 mm inner diameter (ID) DeltaMotion acetabular cup (DePuy, Warsaw Indiana) with approximately 0.5 mm diametric press-fit (Figure 128). The DeltaMotion component (DePuy, Warsaw Indiana) is the first large diameter pre-assembled fourth generation CoC bearing consisting of a BIOLOX DELTA ceramic liner assembled within a titanium alloy shell. The component also has a rough outer surface with a TiHA coating.

A second block of similar size and density was reamed for a 54 mm outer diameter (OD), 48 mm inner diameter (ID) prototype CFRPEEK TiHA coated cup without the secondary fixation features described in Section 3.4 (Figure 129) with approximately 0.5 mm diametric press-fit. 0.12 g/cc density foam was chosen as it is used to model very low density bone (349). This bone type was selected as it is highly porous and made of interconnected struts which represent osteoporotic cancellous bone suggested to be a worst-case scenario due to the brittle nature of this bone type.

The arrowhead backing features were not present as it was determined that the large pore size of the foam (~3.20 mm (347)) and the brittle nature of the material would not result in arrowhead encapsulation.

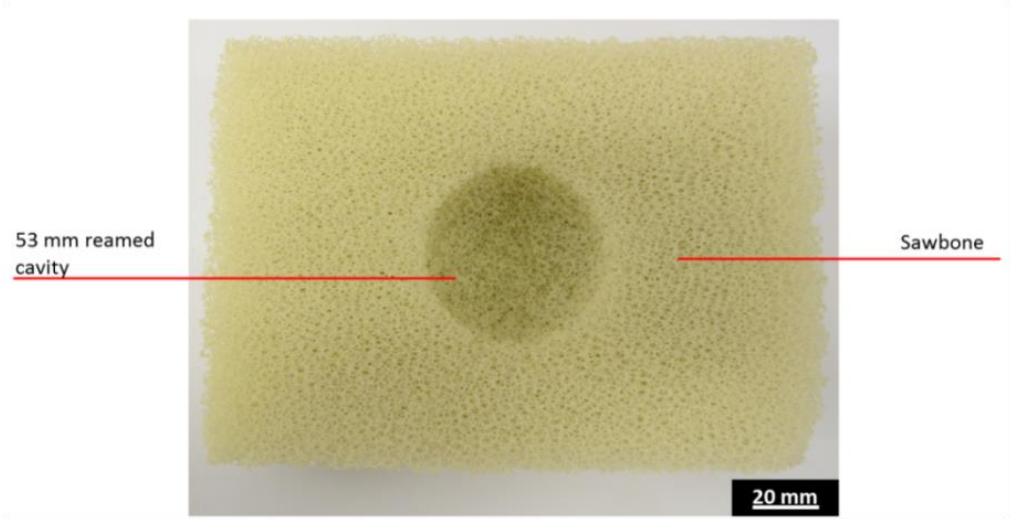

Figure 128: Open celled polyurethane rigid foam (SAWBONES) with a 53 mm diameter cavity.

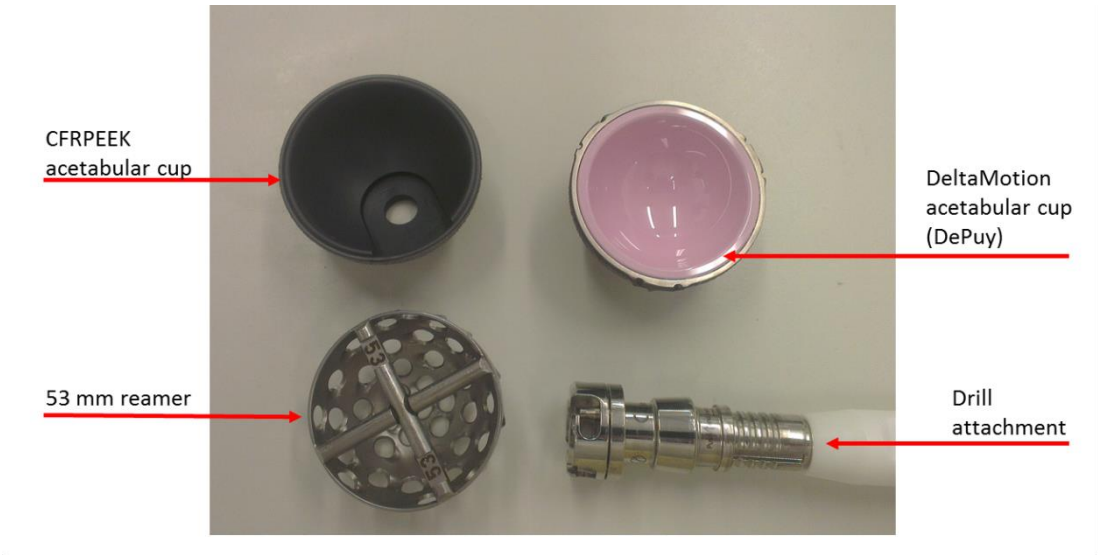

Figure 129: CFRPEEK and DeltaMotion acetabular components with the 53 mm reamer used to ream the cavity in each block.

Micro-focus X-ray computed tomography measurements were carried out using a customised 450 keV Nikon/Metris HUTCH scanner (Nikon Metrology NV). An X-ray tube potential of 380 keV with a tungsten reflection target was found to satisfactorily penetrate both the samples, with a reasonable contrast-to-noise ratio being achieved between the air, foam and components. To reduce the effects of beam hardening a 1 mm copper filter was applied to 'pre-harden' the beam. A voxel resolution of 126.3 μm was selected which yielded a dataset encompassing the entire specimen. The projection data for each scan consisted of 3142 projections taken over a 3 hour period. Projections were reconstructed into 3D volumes using CT-Pro via filtered-back projection (simple Ram-Lak filter). After reconstruction each image voxel was converted to 8-bit which allows for faster processing times without loss in fidelity.

Digital volume correlation was performed on the reconstructed volumes using DaVis 8.1.3 software (LaVision, Göettingen, Germany). The sub-volumes located within the component were not required for analysis as the region of importance was the foam meaning sub-volumes present within the acetabular cup were masked out using a MATLAB code (Appendix 2).

6.1.1 Evaluation of Measurement Resolution

To investigate the metrological performance of the DVC procedure in this study the same measurement resolution protocol was followed as in the trabecular compression study in Section 5.1.1. The stationary, translation and sub-volume tests were performed on identical scans with the implant resting within the cavity. In the implantation analysis the reference scan was performed without the component present to prevent any strains developing within the foam under the weight of the component. The addition of the component in the implanted scan was likely to generate artefacts that did not exist in the first reference scan. Beam hardening, scatter and streaking are all likely to be generated from the components

especially the highly attenuating and dense DeltaMotion component. Section 4.1.3 discussed the influence of artefacts and shows how their presence can obscure features in the surrounding material. To assess the influence of these artefacts on the strain resolution, an implant presence test was conducted. Each foam block was scanned without the component present in the cavity using identical scan settings as the stationary and translation tests. Strain resolution was determined by performing DVC between this scan and Scan A in Table 20. For the stationary, translation and implant presence tests a 64 sub-volume was applied with a 50 % overlap. The optimum sub-volume size was determined by evaluating the strain resolution using five different sub-volume sizes (128, 96, 64, 48 and 32). Figure 130 illustrates the typical structural content within different sub-volume sizes.

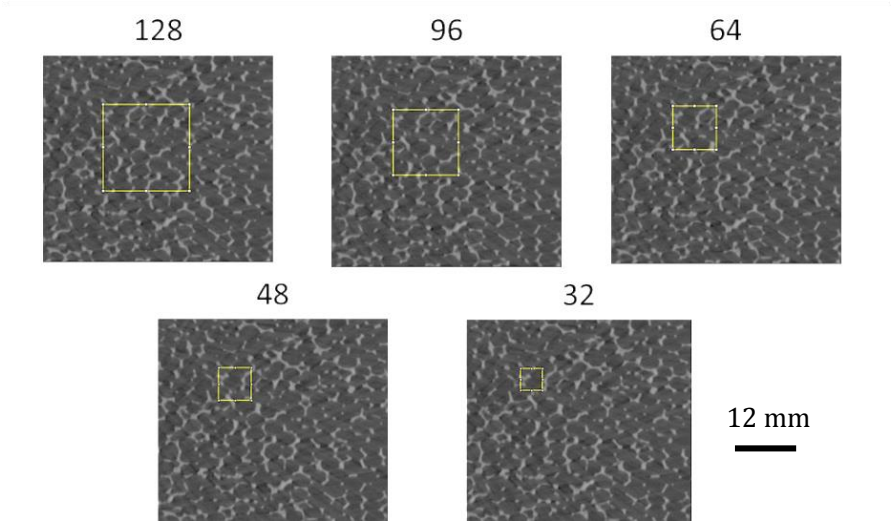

Figure 130: CT slices with sub-volume of different sizes in relation to features of the foam.

Table 20 provides a summary of the μCT measurements completed in the noise study.

Table 20: Summary of Scans A-D undertaken in noise study.

Scan Number	Scan Details
Warm up	Unloaded foam with implant present
A	Unloaded stationary scan of foam with implant present
B	Unloaded stationary scan of foam with implant present
C	Vertical rigid body translation of 125 μm introduced in the z-direction with implant present in foam
D	Unloaded foam scan without implant present

6.1.1.1 *Measurement Resolution Results*

Each of the scans were analysed with DVC and the resulting strain maps were used to produce the mean strain and standard deviation results throughout the foam for the CFRPEEK component and the DeltaMotion component.

Figure 131 shows the DeltaMotion strain map through a central horizontal section of the component and confirmed the presence of non-authentic strain calculations from the sub-volumes located within and along the component and its boundary. The stationary test correlation map for the DeltaMotion component ranged between 0.98 and 1. A correlation of 1 was seen for the sub-volumes located within the component and two sub-volumes away from the component edge. Unlike the trabecular study the variation in the mean strain resolution did not vary between positive and negative values indicating that a bias was formed due to the extreme positive and negative patterns seen in the strain maps (Figure **132**). The standard deviation increased from ~0.4 x 10^{-3} to 1.7 x 10^{-3} between slice 10 and 30 where the component was located and non-authentic strains were calculated. This showed the importance of applying a mask to remove the poorly calculated data from within the sub-volumes located in the component.

Masking reduced the mean strain which varied between +/- 1.5 x 10^{-3} (Figure 131) compared to the unmasked data which varied between +/- 5 x 10^{-3}. The mean strain varied between +/- 5 x 10^{-5} and the standard deviation was below 4 x 10^{-4} for the DeltaMotion specimen with masking applied (Figure 131).

The coefficient was between 0.98 - 1 in the stationary test, 0.97 - 1 in the translation test and 0.96 - 1 in the implant presence test for the DeltaMotion component (Figure 132). The coefficient was between 0.99 - 1 in the stationary test, 0.98 - 1 in the translation test and 0.98 - 1 in the implant presence test for the CFRPEEK component. Section 5.1 showed that high correlation coefficients were essential as sub-volumes with coefficients below 0.90 produce unreliable strain results. Based on this outcome the high coefficients obtained in this analysis should produce reliable results.

Masking was conducted on the CFRPEEK component and Figure 134 showed that the mean strain resolution varied between +/-4 x 10^{-5} and the standard deviation was below 3 x 10^{-4}. The mean strains calculated in the translation test were +/- 1.5 x 10^{-4} and +/- 4 x 10^{-5} for the DeltaMotion and CFRPEEK foams respectively (Figure 134 and Figure 135). Although an end effect present in the CFRPEEK component increased the mean value to +/- 12 x 10^{-5}.

The second noise investigation aimed to assess the influence of the presence of the implant between scans under zero strain. The mean strain resolution was recorded as +/- 4 x 10^{-4} and +/- 3.5 x 10^{-4} for the DeltaMotion and CFRPEEK components respectively. These values were higher than the stationary and translation tests conducted on each component. The standard deviations were also higher and recorded as 11 x 10^{-4} and 10 x 10^{-4} for the DeltaMotion and CFRPEEK components respectively.

Figure 136 illustrates the variation of the strain standard deviations calculated using sub-volumes sizes of 128, 96, 64, 48, and 32 voxels with a 50 % overlap for the entire volume. A similar decreasing trend for both specimen types was highlighted while the standard deviation increased considerably when a sub-volume smaller than 48 voxels was chosen (Figure 136). The implication of choosing a too large or small sub-volume was explained in Section 5.1.

Figure 137 shows a slice taken through the reconstructed volumes of each component and clearly shows the scatter produced by the DeltaMotion component which caused the increased strain standard deviation.

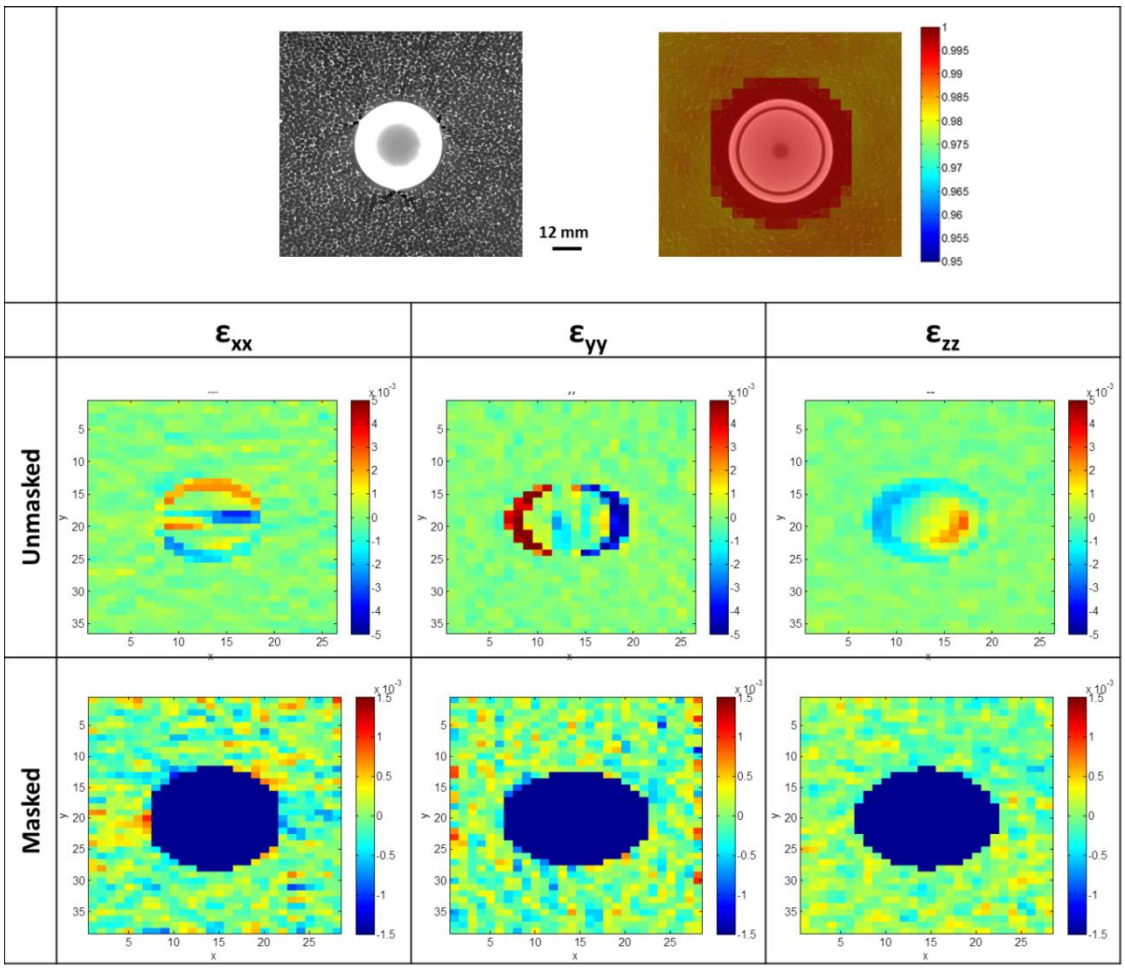

Figure 131: Unmasked and masked strain maps take from a central horizontal cross-section through the DeltaMotion component and surrounding foam. The top right image is the correlation taken from the unmasked data.

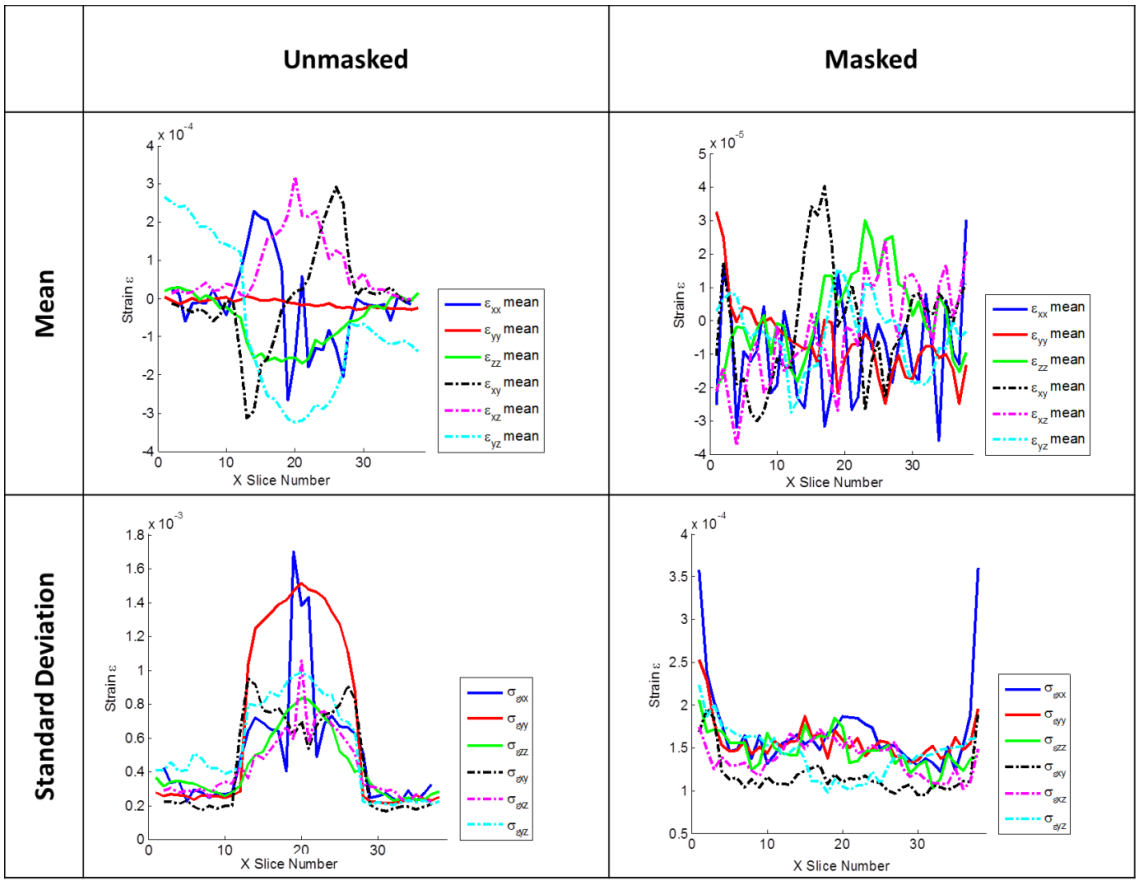

Figure 132: a) Mean strain resolution and standard deviation between the first two repeat stationary scans (A and B) of the DeltaMotion foam with and without masking applied (A 64 voxel size with a 50 % overlap was used in the DVC calculation).

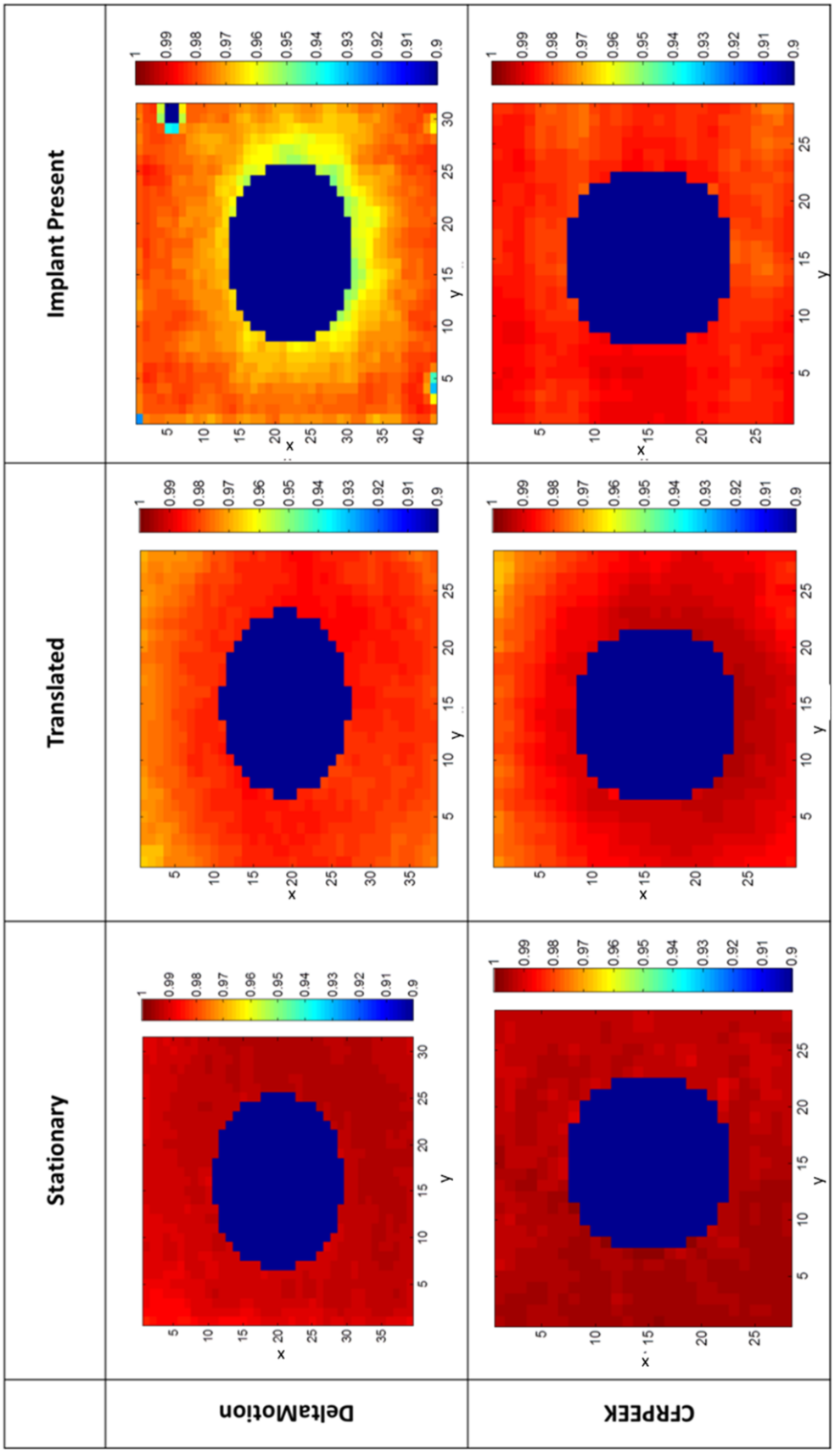

Figure 133: Correlation coefficient for a central cross-section taken through the stationary, translation and implant presence study for both the CFRPEEK and DetlaMotion foams.

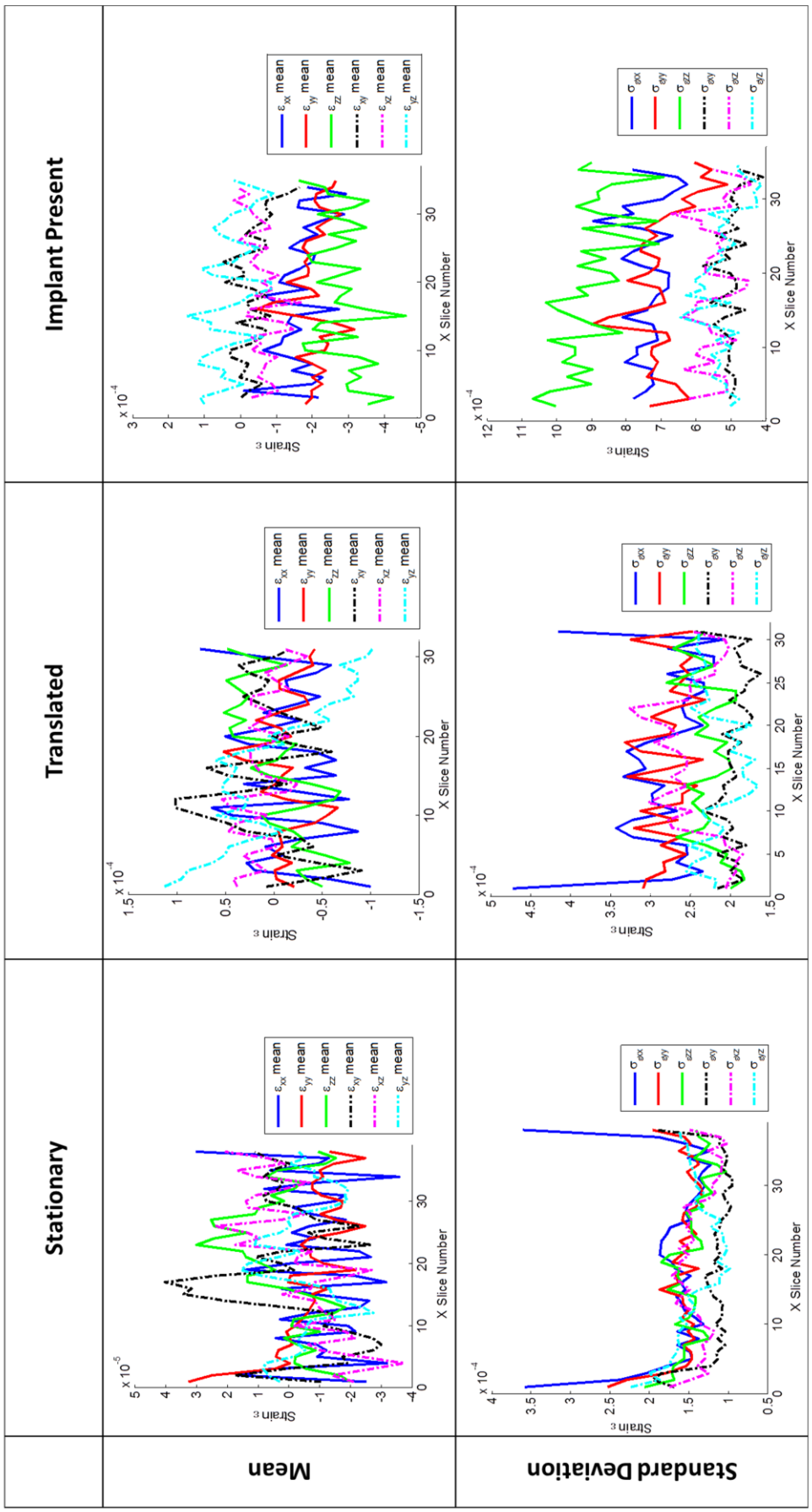

Figure 134: a) Mean strain resolution and standard deviation between the stationary (A and B), translation (B & C) and and implant presence (Scan C & D) scans of the CFRPEEK foam with masking applied. (A 64 voxel size with a 50 % overlap was used in the DVC calculation).

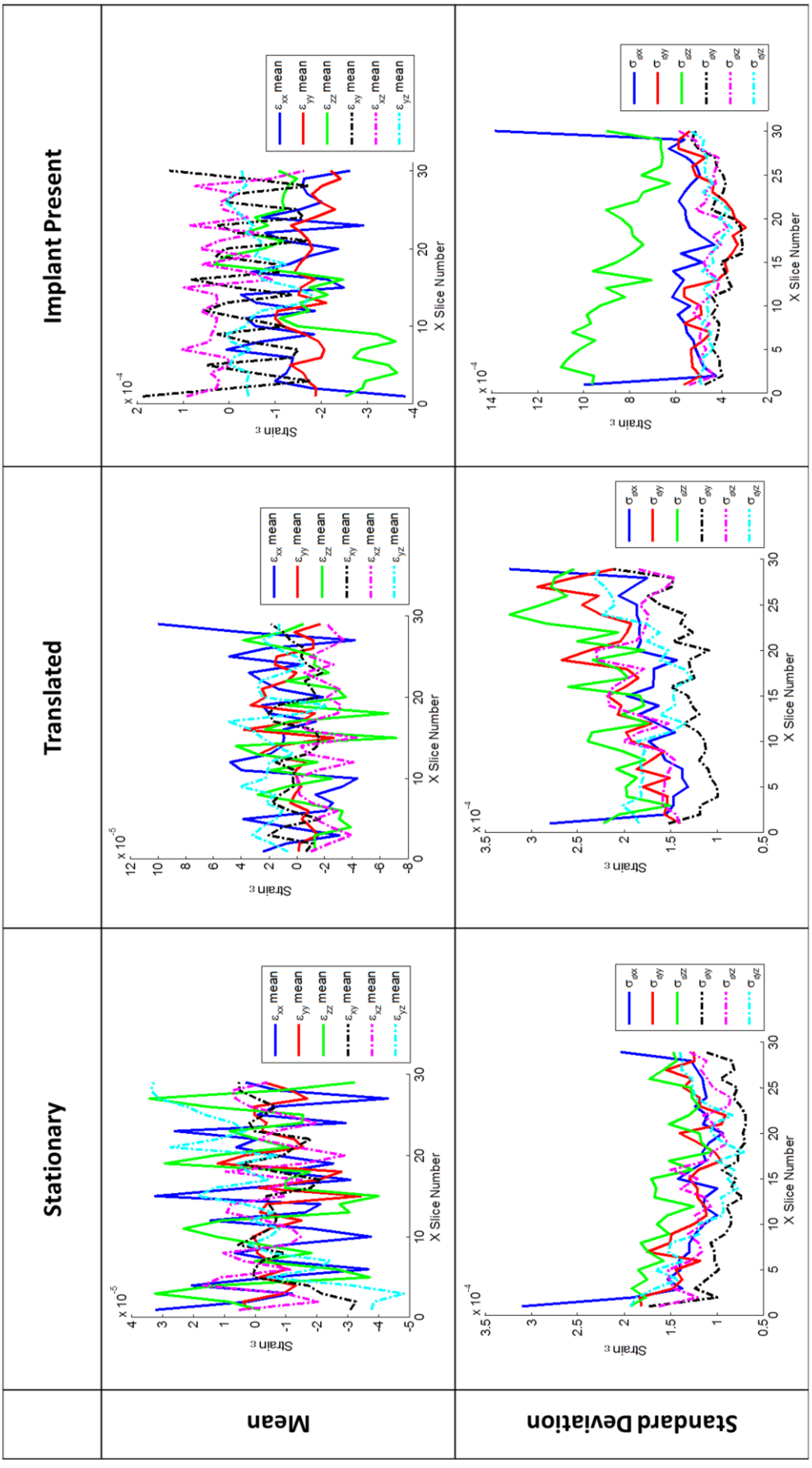

Figure 135: a) Mean strain resolution and standard deviation between the stationary (A and B), translation (B & C) and implant presence (Scan C & D) scans of the DeltaMotion foam with masking applied. (A 64 voxel size with a 50 % overlap was used in the DVC calculation).

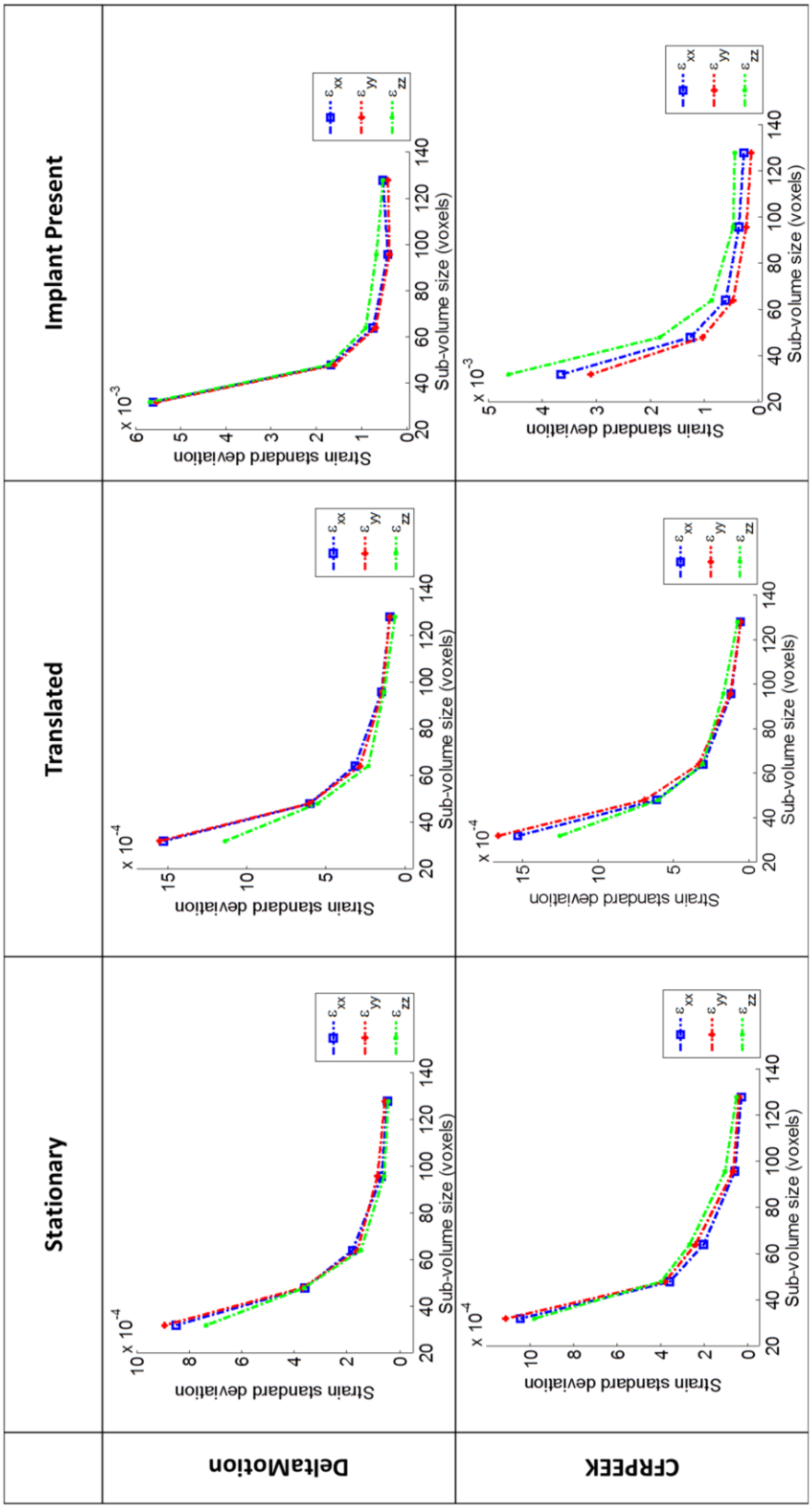

Figure 136: a) Strain resolution for stationary test (Scans A & B), translation test (Scans B & C) and the implant presence test (Scan C & D) for different sub-volume sizes for the CFRPEEK and DeltaMotion implanted foams.

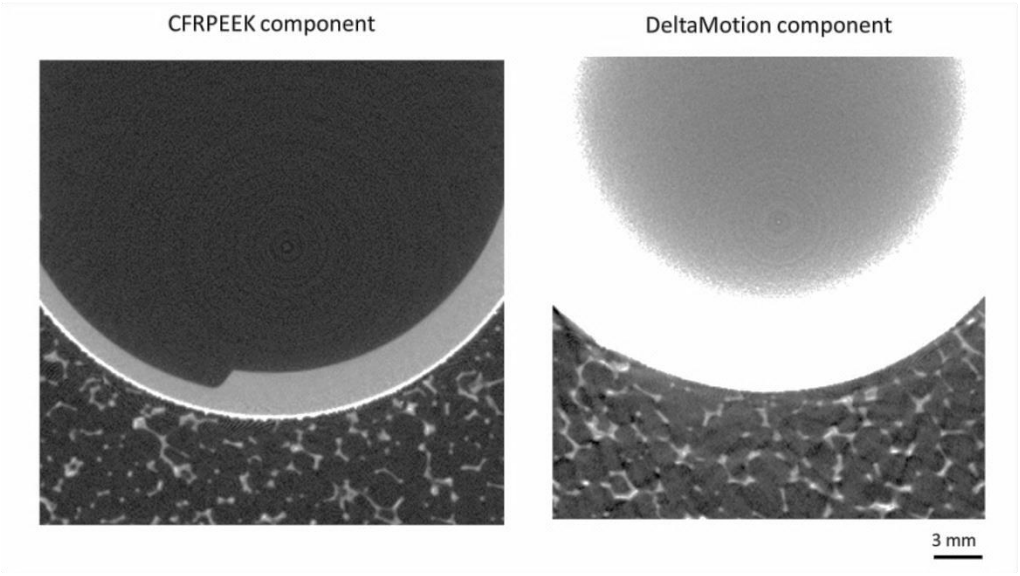

Figure 137: Slice through top of both acetabular components showing the increase in noise artefacts produced by the DeltaMotion component.

6.1.1.2 *Measurement Resolution Discussion*

Figure 131 shows that the sub-volumes located within the component and along its edge possessed significantly higher/lower strain values than in the bulk of the material. The ε_{yy} strain map showed positive and negative strains on the left and right side of the component, whilst the ε_{xx} strain map showed positive and negative strains at the top and bottom edges of the component respectively. The reason behind this pattern is unclear but the presence of these artefacts negatively influenced the strain resolution. The volumes analysed in the stationary and translation tests should be nearly identical as the material was under zero strain. Therefore the strain values should be close to zero and the correlation coefficient close to one indicating a perfect match between sub-volumes in the paired scans. The correlation map for a central cross-section taken parallel to the rim of the DeltaMotion component (Figure 131) showed a coefficient between 0.98 - 1. The coefficient within the component was close to one however the strains calculated from the sub-volumes within this region were unrealistically high/low and this was suggested to be due to the component not containing a distinctive random internal pattern. The consequence was that when the software forced a solution for these sub-volumes, it was assessing the change in random noise patterns within the material meaning the displacement data for the sub-volumes had a number of solutions as shown in Figure 138, each with varying degrees of error.

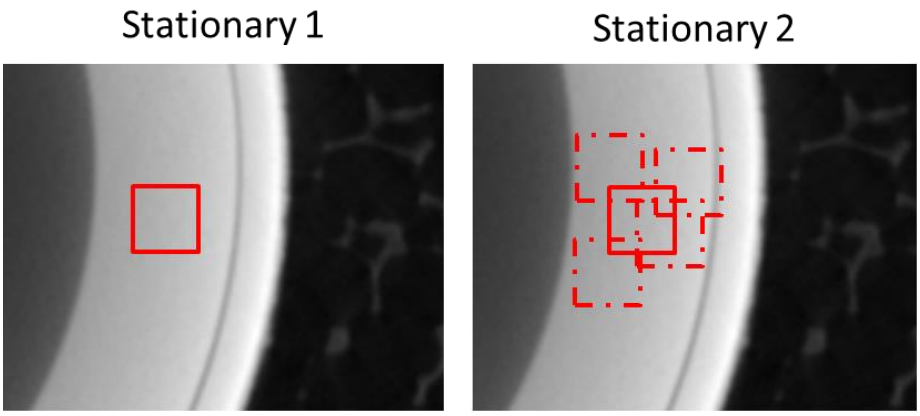

Figure 138: Left image shows the assignment of a sub-volume within the component on the first scan and the right image indicates possible locations where the sub-volume could have been displaced due to the lack of internal pattern within the component.

The influence of the poorly calculated regions is shown in Figure 131 where the standard deviation was low ~0.4 x 10^{-3} between slice 1-10 and 30-35 and increased to 1.7 x 10^{-3} between slices 10-30. The location of this increase (between slice 10-30) was consistent with the location of the component within the foam cavity showing that it was essential that masking was applied to the data to determine an authentic strain resolution. However, as the correlation coefficient was an unreliable parameter, a geometric mask was developed in MATLAB which used the sphere equation to mask out the data within the region of the component prior to strain calculation. As well as the sub-volumes within the component being affected, a radius of two sub-volumes around the components edge was also shown to be affected. This adverse effect was due to the pronounced edge between the implant and the foam where the grayscale levels were largely different (Figure 137) and due to the overlap present between the sub-volumes. The DeltaMotion component possessed a grayscale value of around 180 - 200 whilst the foam and air have values between 29 - 40 and 10 - 16 respectively. One would expect the cross-correlation algorithm to rely on the presence of pronounced edges between black and white, however as shown in DIC analyses, the algorithm prefers softer edges as it is easier to fit gradients to the data (350). Therefore the introduction of a high gradient between the grayscale levels increased the erroneous contribution of the correlation result and introduced higher interpolation errors. In addition, the software allowed for an overlap to be set between sub-volumes with the intention of increasing the accuracy of the correlation procedure, but sub-volumes producing an unrealistic strain result influenced neighbouring sub-volumes. In this analysis it was found that a 50 % overlap resulted in two sub-volumes from the edge being affected by the edge effect. From this finding the mask's radius was enlarged to include these sub-volumes.

The implementation of the correlation procedure on the two specimen types allowed the calculation of strain standard deviation values between 3.0 x 10^{-4} and 3.5 x 10^{-4} for the CFRPEEK component and between 4 x 10^{-4} and 5 x 10^{-4} for the DeltaMotion component using a sub-volume size of 64 voxels with a 50 % overlap (Figure 134 and Figure 135). As expected

both values were higher than the results documented in Section 5.1 for the trabecular specimen. This was due to artefacts generated by the implants which can be clearly seen in Figure 137. These artefacts were generated from beam hardening and scattering and affected the quality of the image. A clear difference was seen in image quality between the trabecular bone in Section 5.1 (Figure 120) and the foam (Figure 137). The strain resolution was higher for the translation than the stationary test in both implantation types which agreed with the trabecular study. This was expected as the translational test suffered from the same noise and discrepancy sources as the stationary test but it also suffered from interpolation biases because of the specimen movement.

Aside from the standard noise tests an additional noise investigation was conducted between two scans each under zero strain but with the component only present in the second scan. This test was investigated as it represented the scan setup in the implantation analysis as the component would not be present in the reference (unloaded) scan. It was suggested that by conducting a similar investigation on two unloaded scans the noise produced by the implant itself could be quantified. A lower correlation coefficient was shown for the implant presence test and a higher standard deviation was recorded for both components compared to their respective stationary and translation results (Figure 133). Figure 139 shows the obscured appearance of the surrounding foam when the dense DeltaMotion component was present.

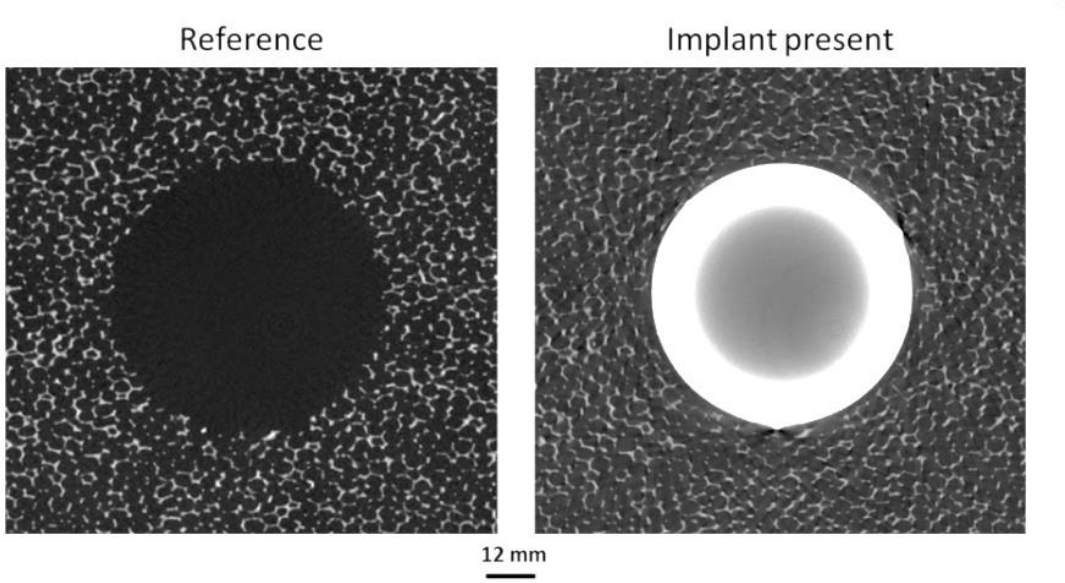

Figure 139: A reference scan of the foam without (left) and with (right) the component present. The right image shows increased scatter in the surrounding foam.

The evaluation of sub-volume size on the correlation precision indicated that for both the stationary and rigid body translation evaluations a 64 voxel sub-volume with a 50 % overlap was an adequate compromise between strain resolution and spatial resolution. Figure 130 shows the typical proportion of foam structure within sub-volume of different sizes. The influence of sub-volume size has been discussed previously in Section 5.1.1.

The neighbouring sub-volumes that are affected by the incorrectly calculated sub-volumes at the component/foam boundary are located within the foam and this was an important aspect to consider when assessing the compressive behaviour of the brittle foam around an implanted component. It was assumed that the compressive strain would be greatest in the region immediately adjacent to the implanted component due to the cavity being 1 mm smaller in diameter than the component. The strain was then expected to decrease to zero at a radius away from the boundary. If the affected material was restricted to within two sub-volumes from the implant edge, reliable strain data from this region was unlikely to be obtained as the signal-to-noise ratio was low. This was a potential problem associated with the use of analogue foam models as the material was brittle and has limited elasticity (349) meaning the foam within the sub-volumes near the implant edge may collapse and fracture relieving any potential deformation and strain in the foam further from the implant edge and away from edge effects. This aspect was investigated in the implantation study in the next section.

Aside from these aspects measurement resolution should be considered in the context of the strains that were expected within the analysed specimen and previous analyses have documented that the yield strain of the foam used in this analysis was ~0.05 (347). Based on these results, the largest measurement resolution found in this study was 0.0011 and 0.0010 for the DeltaMotion and CFRPEEK components respectively. These values were found in the implant presence study and although they were higher than the stationary and translation scans these would be low enough for authentic strains to be recorded within the foam after component implantation providing the extent of material deformation extended to beyond two sub-volumes from the component boundary and the foam did not fracture.

6.1.2 Implantation Test Methodology

For the implantation study, reference and deformed μCT volume images were obtained. Micro-focus X-ray computed tomography measurements were carried out on the reference foam blocks with the acetabular components removed from the reamed cavities. The scan parameters were identical to that of the noise study scans. Micro-focus X-ray computed tomography measurements were also carried out on the deformed blocks with the acetabular components implanted into the ream cavities. A trained orthopaedic surgeon implanted both components into the separate blocks.

The DeltaMotion component was implanted in accordance with the surgical guidelines set out in the operational technique (OPTEC) document. The component was provided attached to the impaction cap and was implanted using standard surgical implantation equipment (Figure 140) provided by Aurora Medical Ltd. As the CFRPEEK component was still in the development stage, no standard implantation equipment was available and a prototype impaction cap was specifically designed. The cap contained a horseshoe raised section with a plug which orientated and coupled the component to the DeltaMotion introducer. The implantation process for the DeltaMotion and CFRPEEK components are shown in Figure 140 and Figure 141.

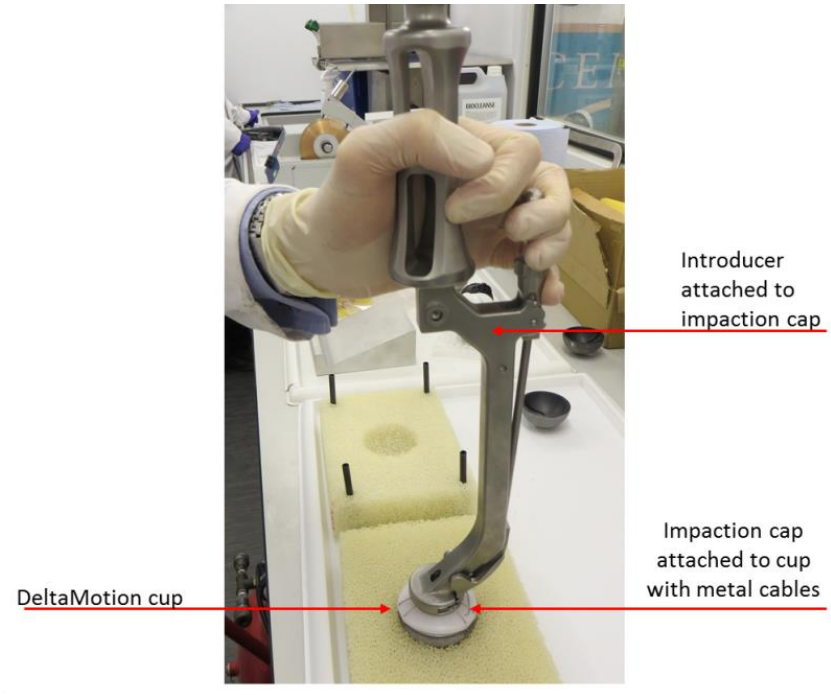

Figure 140: Implantation of DeltaMotion acetabular component.

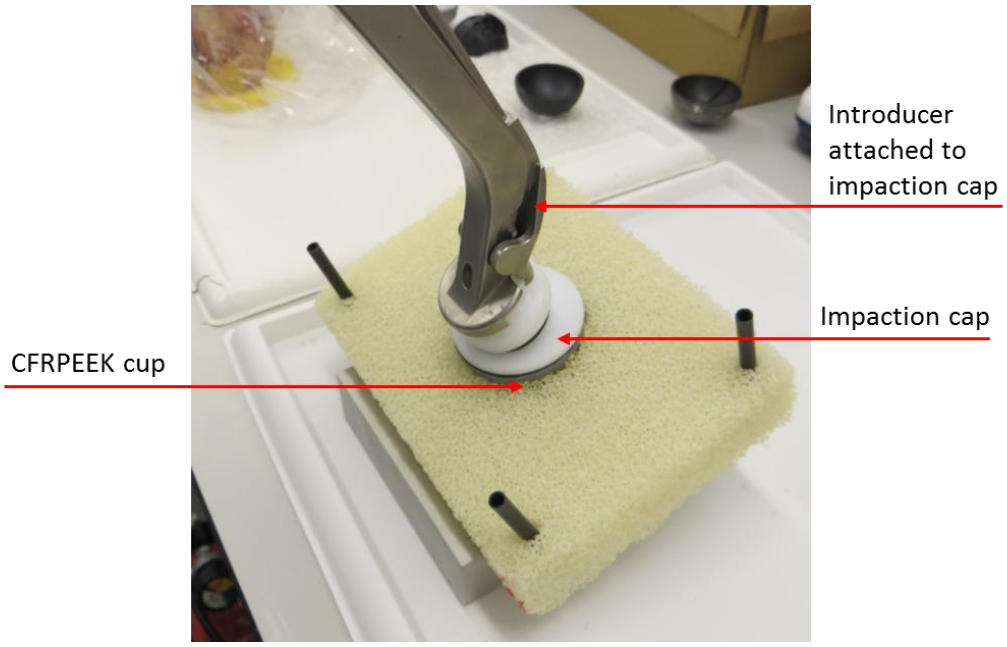

Figure 141: Implantation of CFRPEEK acetabular component.

DVC was carried out on both acetabular components between the un-implanted and implanted blocks using a sub-volume of 64 voxels with a 50 % overlap. The same spherical mask was applied to each volume to remove the grayscale values within the acetabular components as applied in the previous section. Strain was calculated using MATLAB's gradient function described in Section 5.1. Data from sub-volumes exhibiting a correlation coefficient below 0.90 were removed from the analysis in order to provide authentic strain results as described in Section 5.1. For visualisation the strain vector fields were exported into Avizo Fire 7 software (VSG Inc., Burlington, MA, USA). No smoothing was applied to the imported data. Figure 142 and Figure 143 show the analysed cross sections taken through the implanted DeltaMotion and CFRPEEK components.

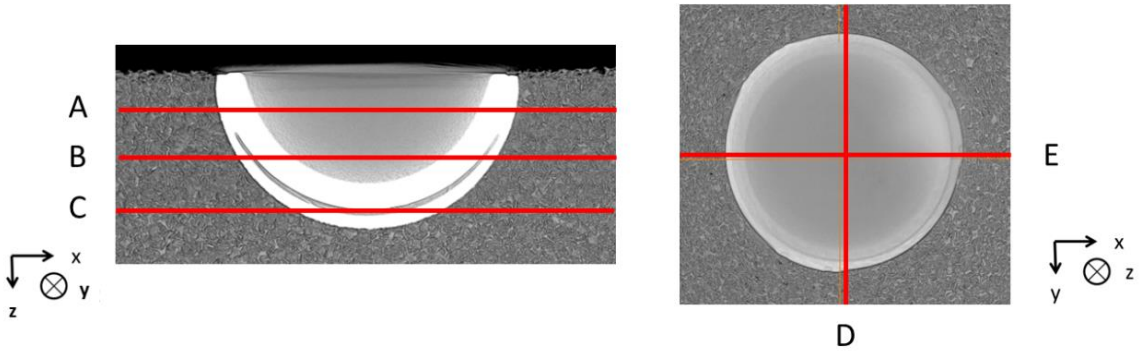

Figure 142: Cross-sections of the implanted DeltaMotion component visualised in Avizo.

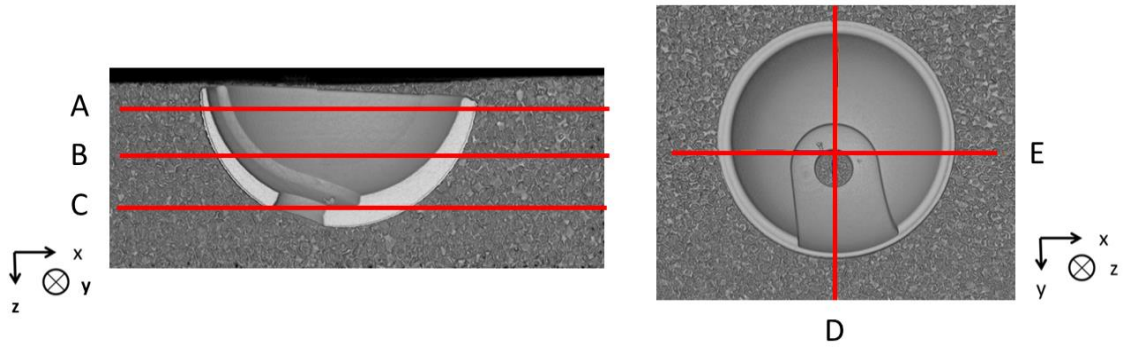

Figure 143: Cross-sections of the implanted CFRPEEK component visualised in Avizo.

6.1.2.1 *Implantation Test Results*

Both implantations were analysed with DVC parameters previously described to give volume maps from which the strain was calculated without smoothing. Five cross-sections were taken through each component and the strain maps are presented in Figure 144 to Figure 147. Masking was applied prior to strain calculation to remove sub-volumes located within the component and from around the boundary where unreliable strain calculations had been identified in the measurement precision tests.

Figure 144 shows the strain maps for sections A to C for the CFRPEEK component; the maximum compressive strain recorded was -0.007 located at the base of the material. All the strain components for section A were between +/- 0.0025 (Figure 144**)**. All the strain components for section B ranged between +/- 0.003, while Section C showed a larger range between -0.007 and 0.003. The strain maps showed a strain pattern which was similar to the stationary test strain maps suggesting that these strains were due to noise artefacts and not material behaviour.

The strain maps were similar to the stationary test, suggesting that these strains were due to a noise artefact (Figure 131). This pattern was especially evident in the ε_{xx} and ε_{yy} strain maps of Section C and ε_{zz} strain map through Section D. As the maximum and minimum strains in the ε_{zz} strain map were located randomly within the bulk of the material they were assumed to be due to a noise artefact.

The maximum compression strain was -0.009 for section E taken through the CFRPEEK component which was located near the foam/component boundary (Figure 146). This was considered significant as it was above the strain resolution.

The strains ranged between -0.005 and 0.0035 for each of the vertical sections taken through the DeltaMotion component, close to the strain resolution (Figure 145 and Figure 147).

Figure 148 is a cross section (Section B) taken through the foam before and after the implantation of the CFRPEEK component and shows evidence of foam strut fracture near the edge of the component and also struts which have plastically deformed. However, in the majority of the specimen the struts appeared to be undeformed. A similar trend was shown for the DeltaMotion foam (Figure 149).

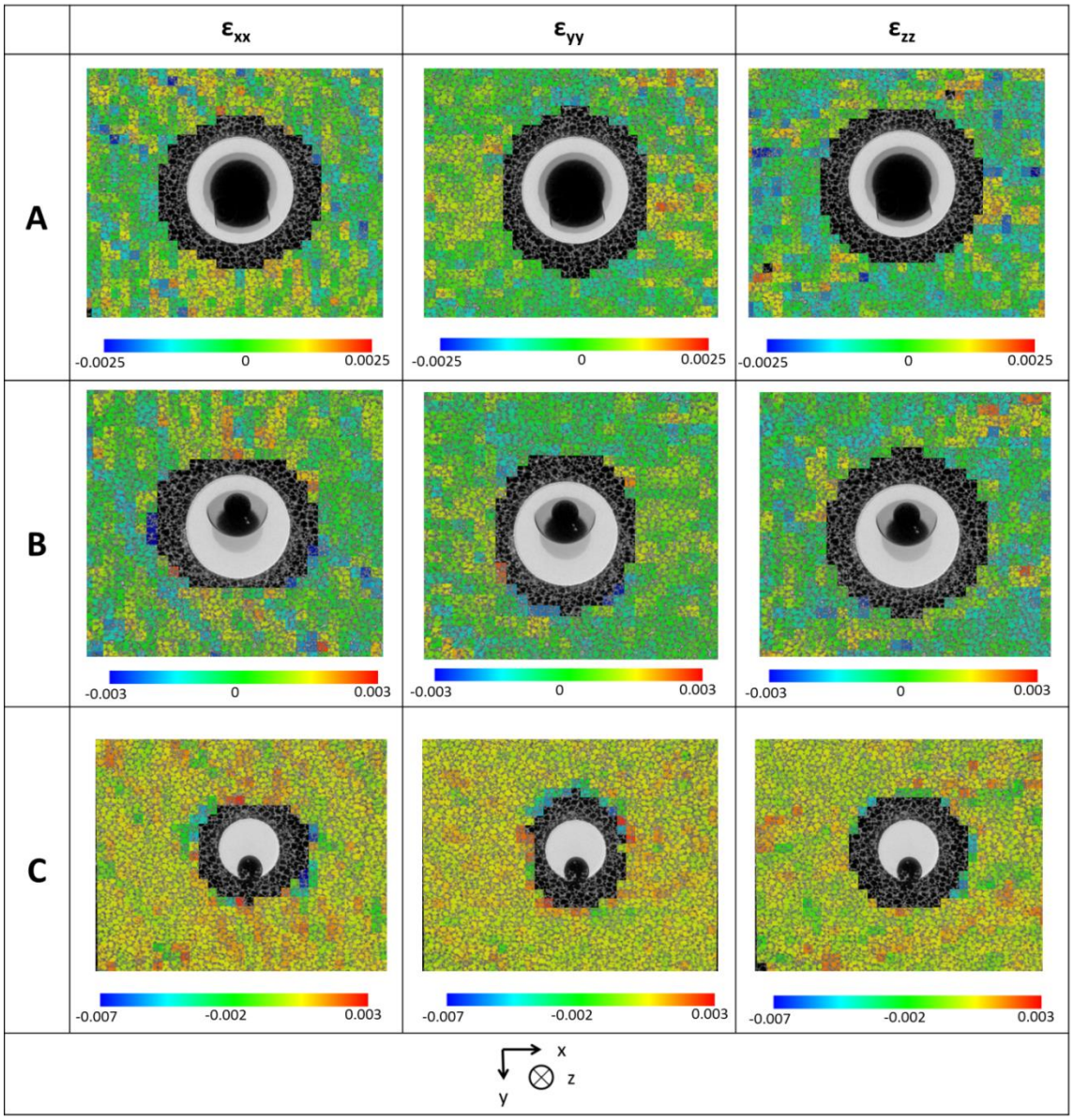

Figure 144: Strain results in surrounding open celled foam after implantation of CFRPEEK component for cross-sections A-C.

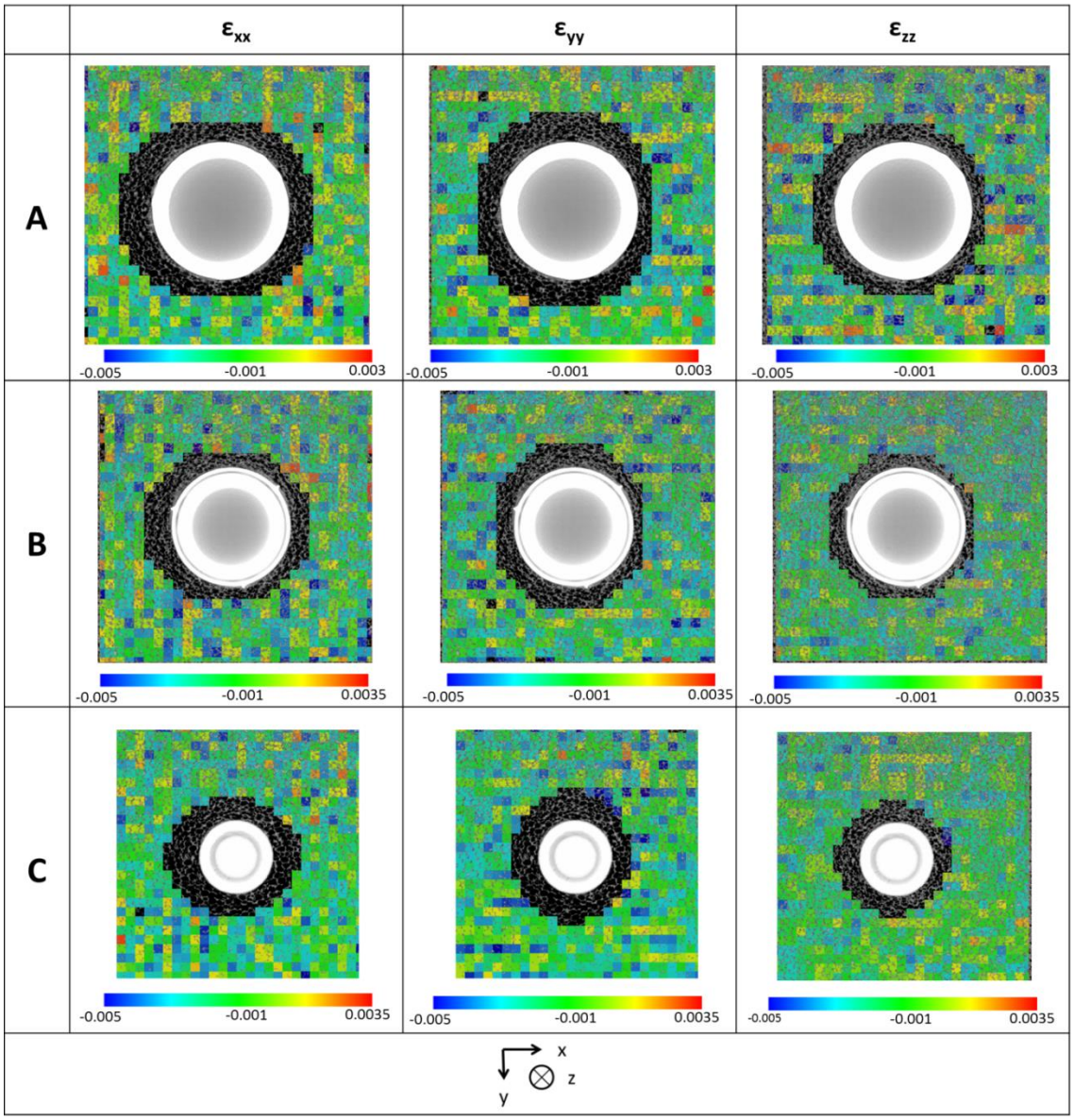

Figure 145: Strain results in surrounding open celled foam after implantation of DeltaMotion component for cross-sections A-C.

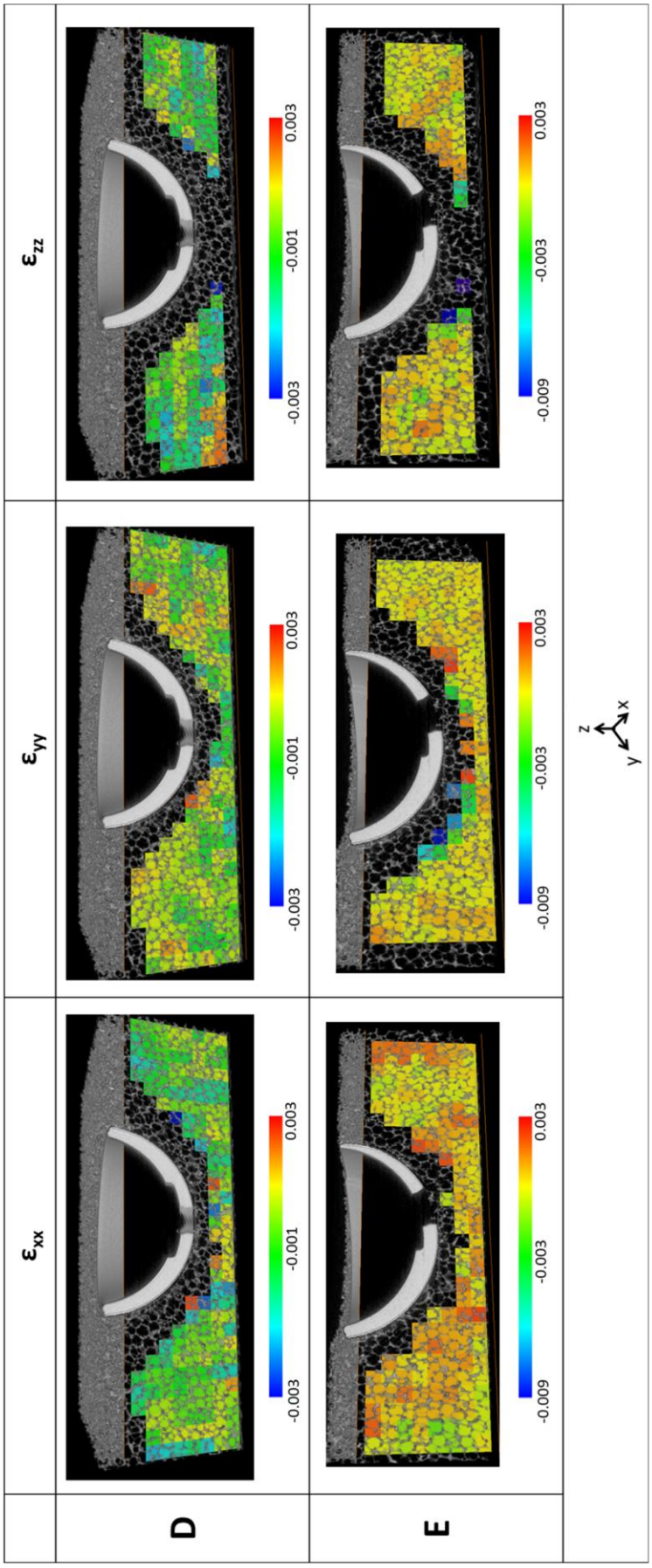

Figure 146: Strain results in surrounding open celled foam after implantation of CFRPEEK component for cross-sections D-E.

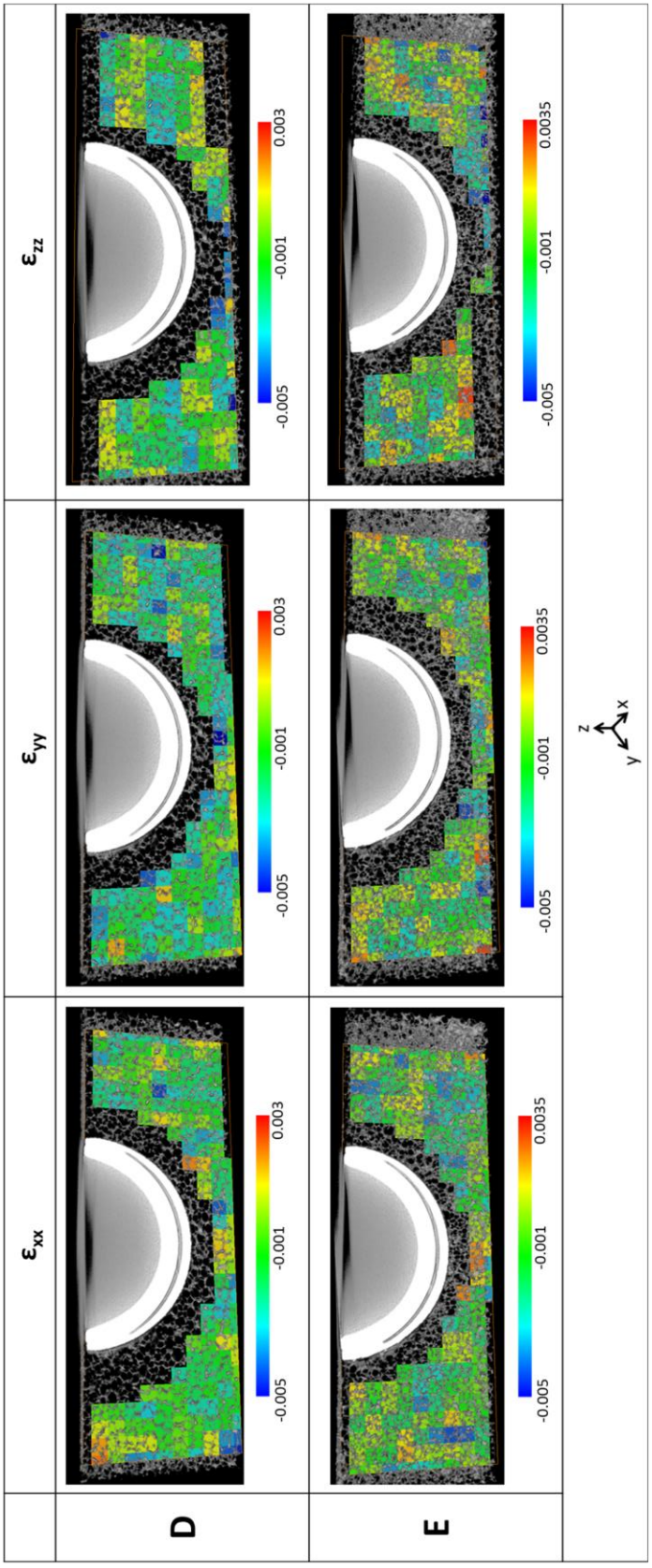

Figure 147: Strain results in surrounding open celled foam after implantation of DeltaMotion component for cross-sections D-E.

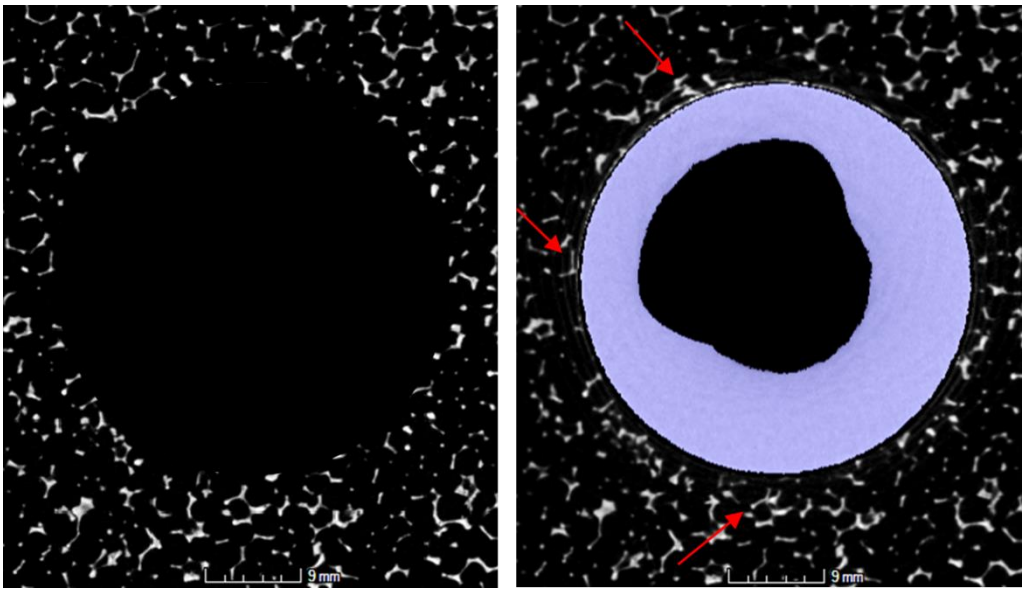

Figure 148: A cross-section taken through the foam before and after implantation of the CFRPEEK component. The red arrow highlights an area of fracture and deformation.

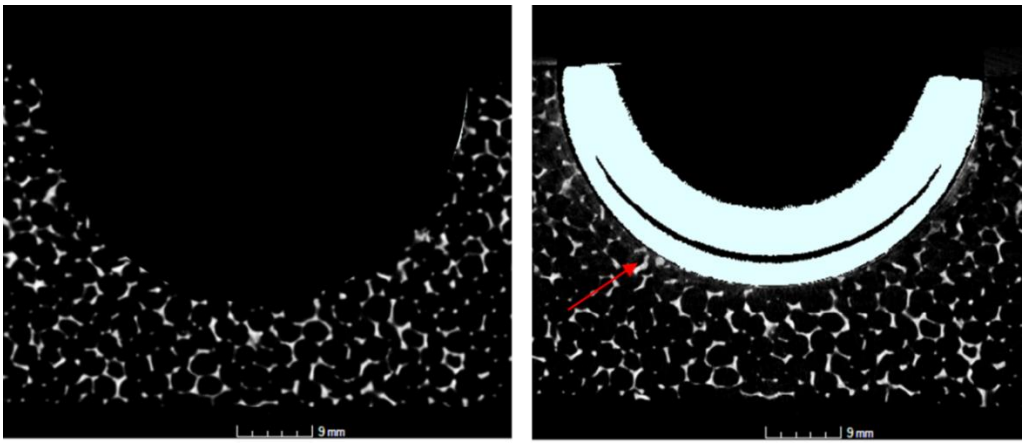

Figure 149: A cross-section taken through the foam before and after implantation of the DeltaMotion component. The red arrow highlights an area of crushing.

6.1.2.2 *Implantation Test Discussion*

The measurement resolution and strains recorded between the unimplanted and implanted foam models were similar and made it difficult to distinguish between strains generated by material behaviour and strains generated by noise artefacts. There were three main problems associated with applying DVC to assess the strain distribution around components when implanted into brittle foam.

The first problem was the noise associated with the components themselves which made it difficult to calculate significant strains. This was especially significant for the DeltaMotion component. The inclusion of the components in the second scan generated artefacts which increased the strain resolution as the quality of the images decreased. As the DeltaMotion component was highly attenuating, artefacts were produced as the average energy of the X- ray beam increased; this raised the strain values required to extract significant data from

the deformed foam. It was predicted that the maximum compressive strains would be located adjacent to the component/foam boundary, decreasing as the distance from the boundary increased. Based on this assumption, it was concluded that the strain data extracted from the DeltaMotion implantation were not significant. The strain maps shown in Figure 145 and Figure 147 display a strain range between -0.005 and 0.0035 which was above the standard deviation of the strain resolution recorded (0.001ε) but the pattern of the strain map did not reflect the predicted relationship. The maximum compressive strain was located in random sub-volume in the bulk of the material away from the implant/foam boundary and the maps exhibited a strain pattern which was similar to the maps shown in the stationary, translation and implant presence tests (Figure 132).

The CFRPEEK component produced less scatter and this was reflected in the higher strain resolution obtained in the noise analysis. The higher strain resolution allowed significant strains to be obtained from the CFRPEEK analysis and this was especially evident in Section C in Figure 144. It can be seen that the maximum compressive strain was located in the sub-volumes close to the implant/foam boundary with the strains in the remainder of the foam showing a strain pattern similar to the noise study strain maps.

The concentration of foam deformation close to the implant/foam boundary introduced two further problems. These two problems were interlinked and involve the failure mechanism of the brittle foam and the requirement for masking out the data within sub-volumes adjacent to the foam/implant boundary. The method of press-fitting for primary fixation has been discussed in Section 2.7. The fixation method relies on the insertion of an 'oversized' cup into an 'under reamed' cavity. The implantation of the oversized component into the 1 mm undersized foam cavity was likely to have resulted in a stress which exceeded the critical stress for brittle failure of the foam. The high impaction force experienced by the introducer during implantation was likely to have resulted in the thin foam struts collapsing at the implant/foam boundary resulting in brittle crushing of the foam. The broken fragments could either remain adjacent to the contact area or drop through the interstices of the foam and away from the contact area (351). It was likely that both occurred in this study as only a few of the failed fragments could be seen adjacent to the component after implantation is shown in Figure 148 and Figure 149.

A previous analysis has documented the foam's yield strain to be ~ 0.05 ε (347) and based on this value, significant strains should have been observed as the strain resolution for both the CFRPEEK and DeltaMotion components was a magnitude lower. However, strut fracture implied that during implantation, the yield strain was achieved and surpassed. The figures also highlighted that apart from the struts adjacent to the component, minimal deformation was experienced by the rest of the foam. This localised deformation and failure of the struts adjacent to the component coupled with the fact that the implant was not loaded when the implanted scan was taken implied that the surrounding foam was only minimally strained and not to the extent which allowed significant strains to be recorded.

The localised deformation introduced the third problem associated with the use of brittle foam for assessing deformation about implanted components. The component/foam boundary produced errors similar to edge effects seen in DIC and it was concluded in the noise study that data from sub-volumes located within the component must be ignored due to non-authentic strain being calculated. In addition, it was highlighted that the implant/foam boundary acted in a similar way to an edge and introduced errors that degraded the strain resolution. Due to the overlap set in the correlation procedure, strains calculated from sub-volumes located at the boundary of the implant/foam and also from their neighbouring sub-volumes must be masked out to ensure authentic strains were calculated. It was found that the spherical mask should have a radius which was equal to the component's radius plus two sub-volumes in order to effectively mask out the poorly calculated data. In this investigation, any deformation in the foam within ~ 8 mm from the component's edge could not be accurately calculated and if the deformation was restricted to within this area the strains around the component could not be obtained. This was suggested to be one of the main reasons why significant strains could not be extracted from the data and it could be proposed that bone is a more suitable material for this study. Firstly, the visco-elastic mechanical behaviour of bone prior to crushing should result in additional deformation prior to failure. In addition, the bone marrow present between the trabeculae means fractured individual trabeculae cannot move away from the contact region meaning broken fragments should form a crushed zone as seen in Section 5.1.

This study has concluded that polyurethane foam was not a suitable material for assessing strain generation around implanted component using DVC as the brittle nature does not allow for adequate deformation to be recorded prior to failure.

6.2 Investigation 2: Assessment of animal bone deformation surrounding acetabular components of different stiffness.

Investigation 1 (Section 6.1) concluded that the use of foam as an analogue bone model was not an appropriate bone substitute to assess strain generation around implanted acetabular cups due to its brittle nature. This section assessed the use of bovine bone as the implantation medium and performed a DVC feasibility study to assess bone deformation around coated CFRPEEK and DeltaMotion components. The three components used are shown in Figure 150.

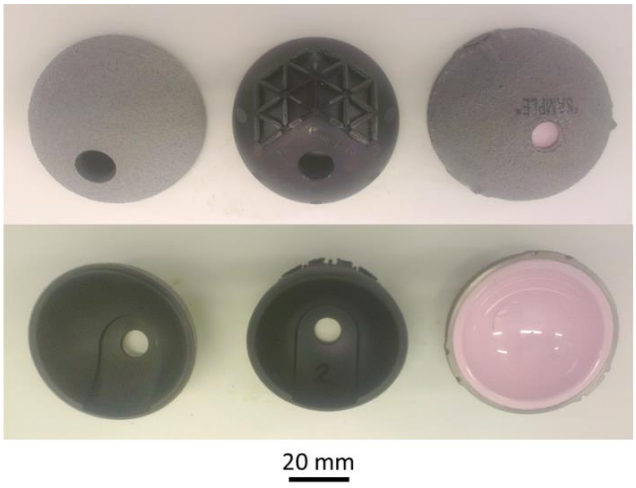

Figure 150: Machined CFRPEEK component with TiHA coating (left), injection moulded CFRPEEK component with backing features (middle) and the DeltaMotion component (right).

Materials and Methods

Two femurs from ~24 month old steers were obtained from a local butcher. A section was cut from the popliteal surface on the posterior medial side of the femur and a flat surface was prepared for implantation. A cavity was reamed in each femur to enable implantation of the 54 mm outer diameter (OD), DeltaMotion acetabular cup (DePuy, Warsaw Indiana) and machine CFRPEEK component with approximately 0.5 mm diametric press-fit using standard surgical reaming equipment.

Figure 151: Site of reamed cavity on bovine femur (left) and reamed cavity in section of femur prepared for CFRPEEK implantation.

6.2.1 **Evaluation of Measurement Resolution**

A series of metrological performance tests were performed on the femurs prior to the implantation study in order to quantify the strain resolution. The reamed specimens were left for 8 hours prior to scanning to minimise specimen movement.

Micro X-ray computed tomography measurements were carried out using a custom 450 keV Nikon/Metris HUTCH scanner (Nikon Metrology NV). An X-ray tube potential of 380 keV with a tungsten reflection target was found to satisfactorily penetrate both the samples, with a reasonable contrast-to-noise ratio being achieved between the air, bone and components. To reduce the effects of beam hardening a 1 mm copper filter was applied to 'pre-harden' the beam. A voxel resolution of 62 μm was achieved which encompassed the entire specimen in one scan. The projection data for each scan consisted of 3142 projections taken over approximately 3 hours. Projections were reconstructed into 3D volumes using CTPro via filtered-back projection (simple Ram-Lak filter).

After reconstruction each image voxel was converted to 8-bit which allowed for faster processing times without loss in fidelity. Digital volume correlation was performed on the reconstructed volumes using DaVis 8.1.3 software.

To investigate the metrological performance of the DVC procedure in this study the same measurement resolution protocol was followed as in Section 5.1. The stationary, translation and sub-volume tests were performed on identical scans with the implant resting within the cavity in the femur. An implant presence study was also conducted between a stationary scan containing the component and a scan without the component. The rationale behind these scans was explained in Section 6.1.1. For the stationary, translation and implant presence tests a 64 sub-volume was applied with a 50 % overlap meaning measurements were taken at a spacing half the voxel size. The optimum sub-volume size was determined by evaluating the strain resolution using five different sub-volume sizes (128, 96, 64, 48 and 32). Table 20 provides an outline of the scans undertaken in the foam study, identical to those performed in this study.

In the previous two DVC analyses, calculations in the air outside of the specimen were masked out using MATLAB. However, due to the complex shape of the femurs this was not applicable in this study. Therefore, the bone specimen was segmented from the surrounding air using the commercial package VGStudio Max 2.1 (Volume Graphics, Heidelberg, Germany). Using a similar approach to Section 3.4.2.2 the region growing tool was used to outline the bone specimen. As the tool thresholds out data based on grayscale values, air pockets within the bone were not automatically selected due to their grayscale value being similar to the surrounding bone. The erosion and dilation techniques were used to select voxels within these air pockets allowing the grayscale values in the surrounding air to be set to zero. Figure 152 shows one of the femurs before and after segmentation from the surrounding air. The method of segmentation was explained in more detail in the void analysis in Section 3.4.2.2.

Sub-volumes located within the component in Section 5.1.1 calculated an unrealistic strain result which compromised the validity of the strain resolution. The displacement data from these sub-volumes were masked out in MATLAB prior to strain calculation and the same approach was adopted in this study.

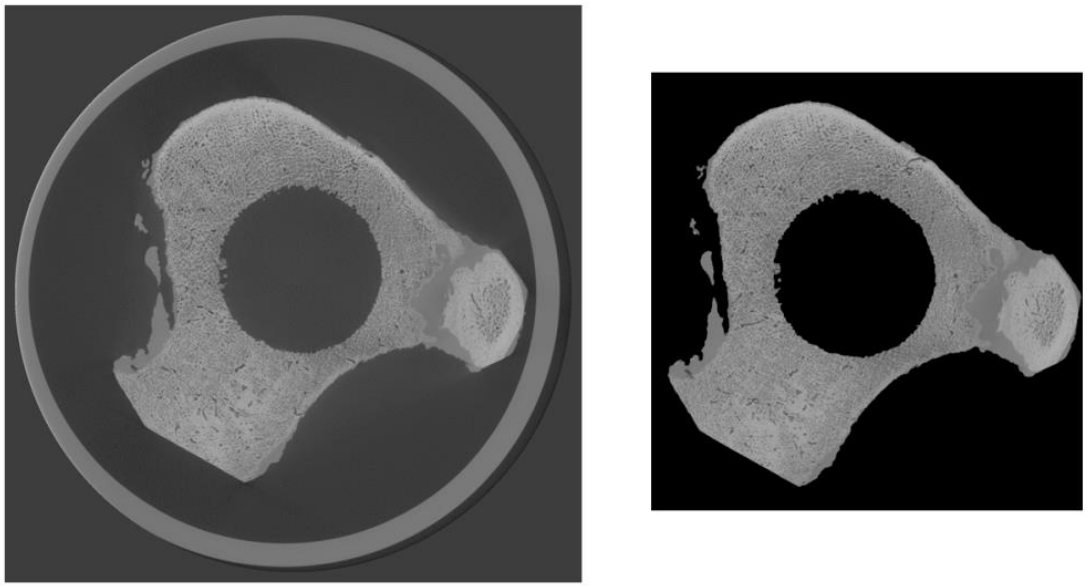

Figure 152: Original reconstructed volume of the bone (left), segmented volume with voxels outside of bone set to zero to prevent the correlation procedure occurring in this region (right).

6.2.1.1 *Measurement Resolution Results*

Each of the scans were analysed with DVC and the resulting strain maps were used to calculate the mean strain and standard deviation throughout the bone for the CFRPEEK and DeltaMotion components.

Non-authentic strains were calculated in the sub-volumes located within the component, along its boundary and in the cortical bone layer when masking was not applied (Figure 153). The standard deviation showed a similar decreasing trend as the foam study (Figure 132) with it decreasing from 0.02 to 16 x 10^{-4} when masking was applied (Figure 154). The maximum standard deviation in the unmasked data was recorded between slices 10-20 which was consistent with the position of the DeltaMotion component.

Figure 155 illustrates the correlation coefficient for a masked cross-section taken through each specimen parallel to the rim of the component. The coefficient was between 0.90-1 in the stationary and translation tests but decreased to between 0.70-1 in the implant presence test for the DeltaMotion component. The CFRPEEK component showed a similar trend although the application of a 0.90 threshold removed a lower number of sub-volumes from the volume.

The stationary mean strain resolution varied between +/- 4 x 10^{-6} and the standard deviation was below 2 x 10^{-4} for the CFRPEEK component (Figure 156). The mean strain calculated in

the translation test was +/- 4 x 10^{-5} and the standard deviation was below 4 x 10^{-4}. The implant presence test produced a mean strain resolution of +/- 1 x 10^{-4} and a standard deviation of 3 x 10^{-4}.

For the DeltaMotion component the stationary mean strain resolution varied between +/- 4 x 10^{-4} and the standard deviation was below 10 x 10^{-4} (Figure 157). The mean strain calculated in the translation test was +/- 6 x 10^{-4} and the standard deviation was below 2 x 10^{-3}. The implant presence test produced a mean strain resolution of +/- 1 x 10^{-3} and a standard deviation of 4 x 10^{-3}.

Figure 158 illustrates the variation of strain standard deviations calculated using five different sub-volume sizes ranging from 32 to 128 voxels cubed each with a 50 % overlap applied. A similar decreasing trend to the previous noise analyses (Section 5.1.1) can be seen and the standard deviation increased considerably when a sub-volume smaller than 64 voxels was chosen.

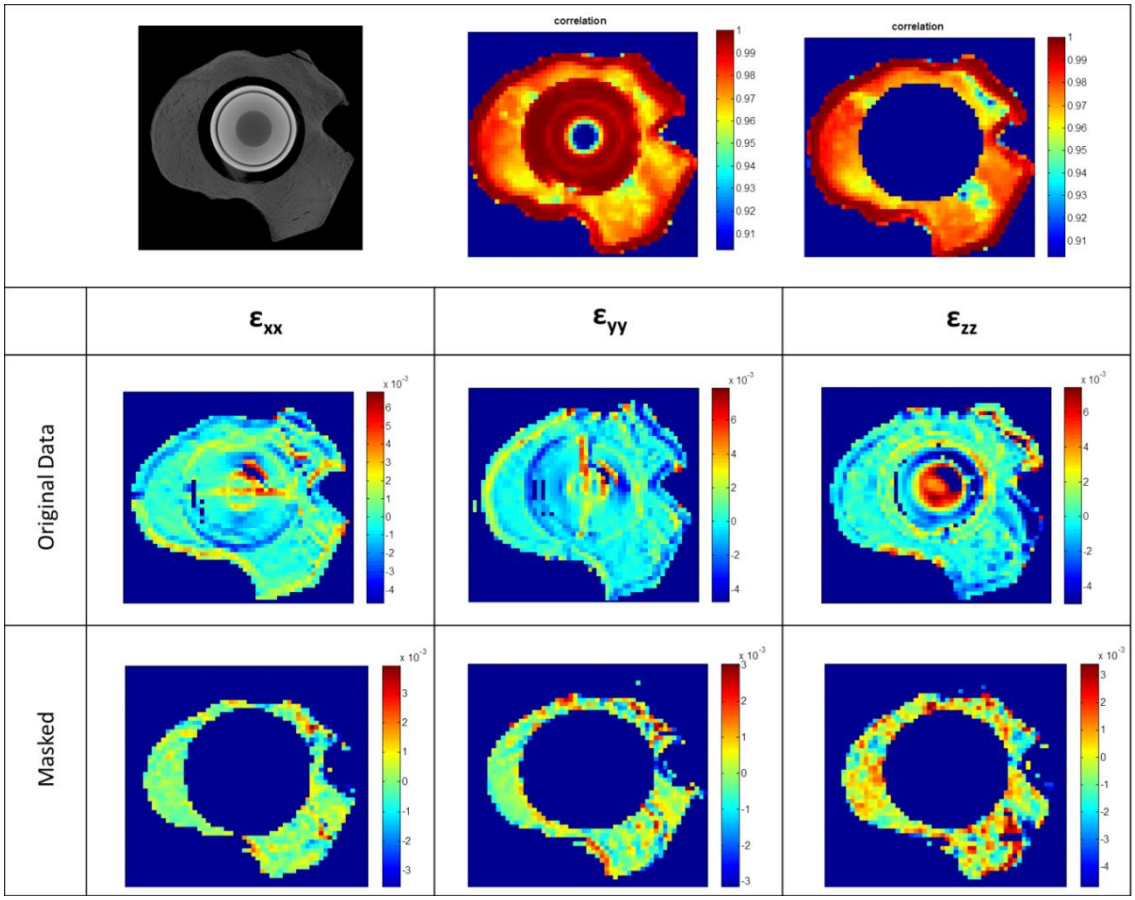

Figure 153: Removal of sub-volume from within the component to produce authentic strain results.

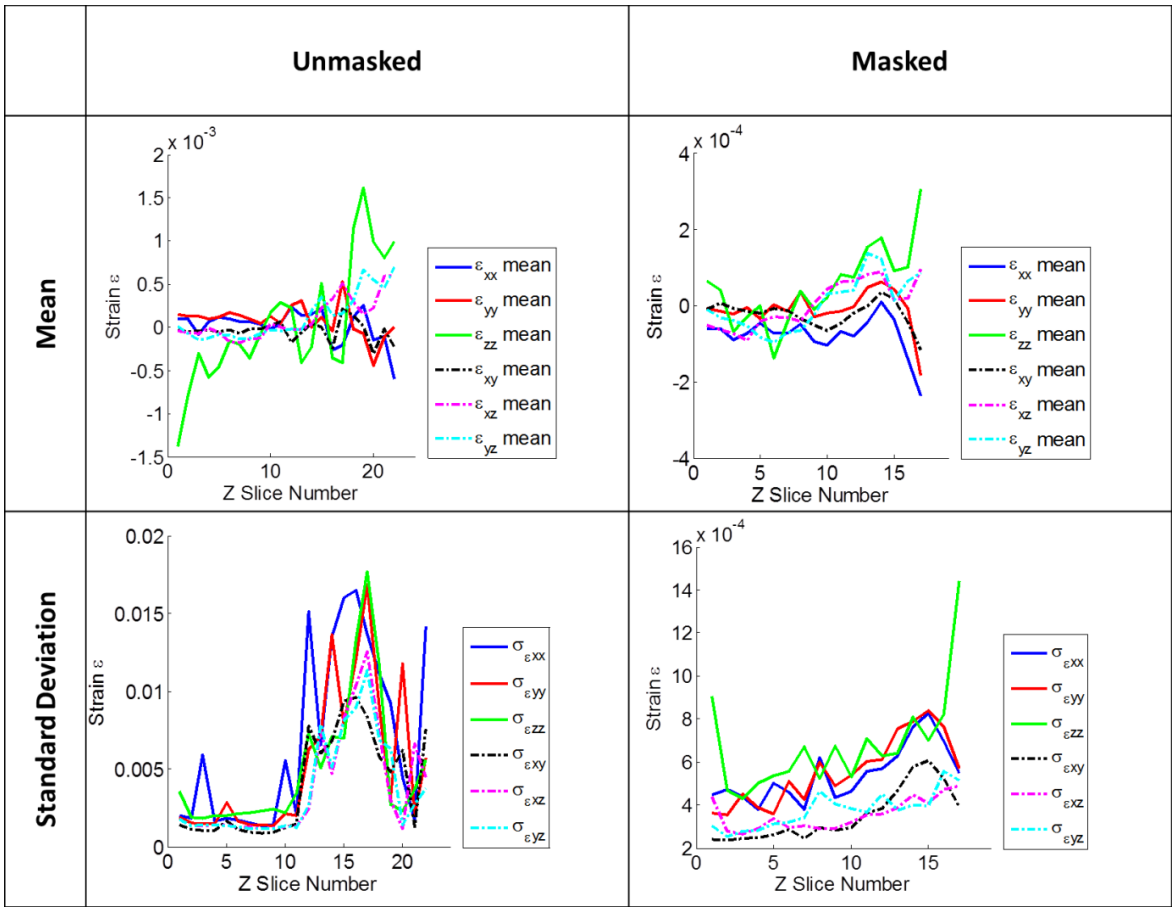

Figure 154: a) Mean strain resolution and standard deviation between the first two repeat stationary scans (A and B) of the DeltaMotion bone specimen with and without masking applied (A 64 voxel size with a 50 % overlap was used in the DVC calculation).

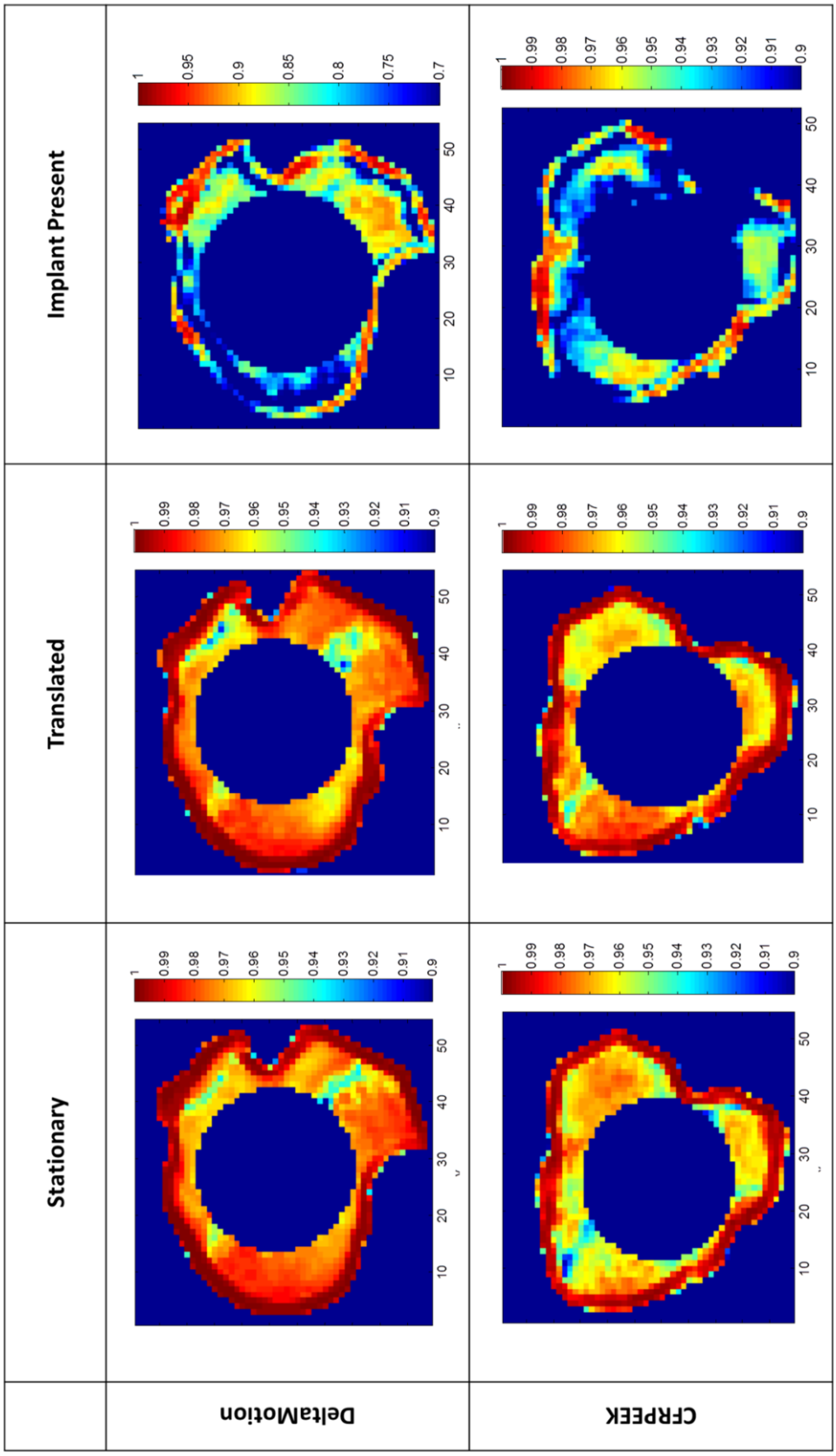

Figure 155: Correlation coefficient for a central cross-section taken through the stationary, translation and implant presence study for both the CFRPEEK and DetlaMotion bone specimens

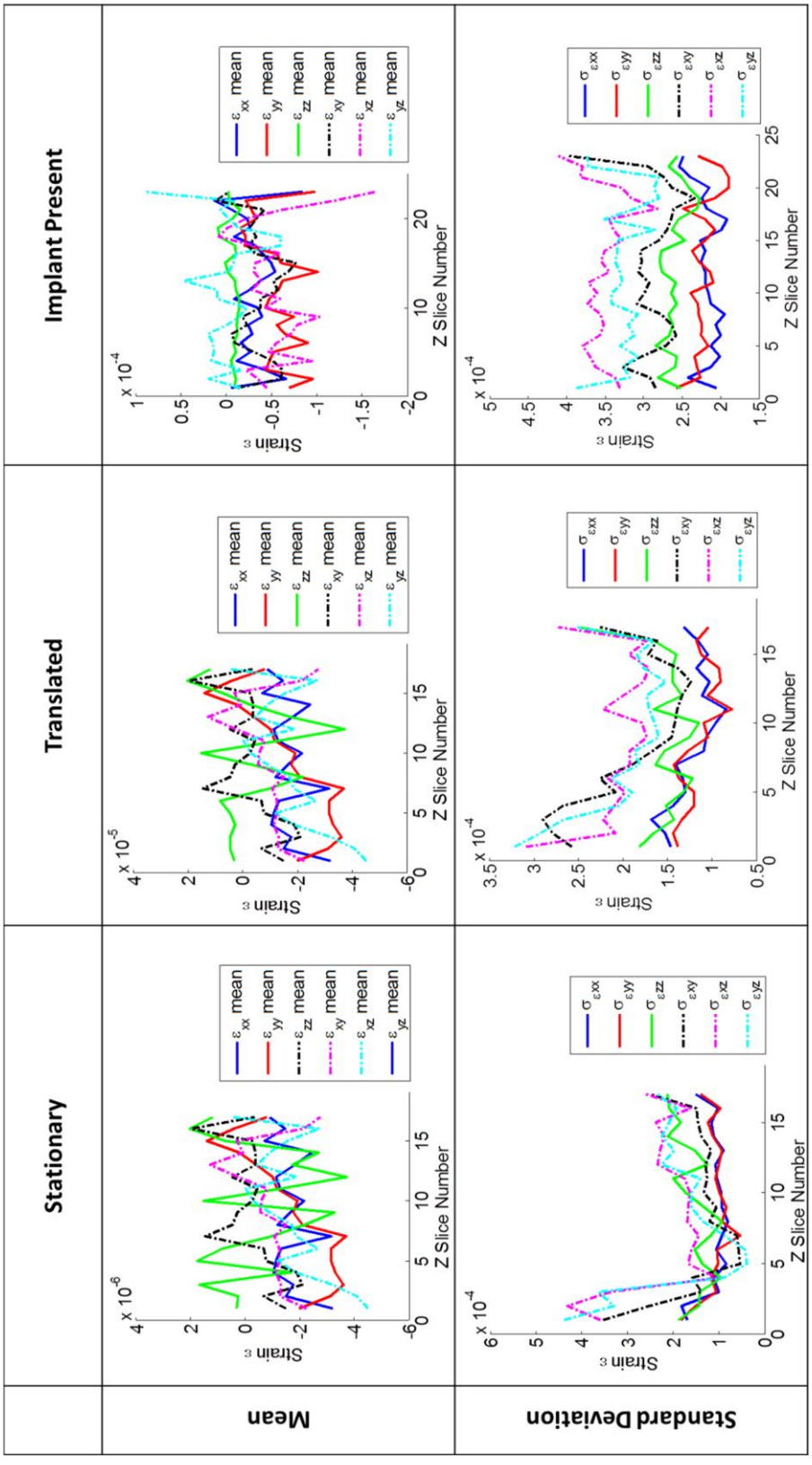

Figure 156: a) Mean strain resolution and standard deviation between the stationary (A and B), translation (B & C) and the implant presence scans of the CFRPEEK bone with masking applied. (A 64 voxel size with a 50 % overlap was used in the DVC calculation).

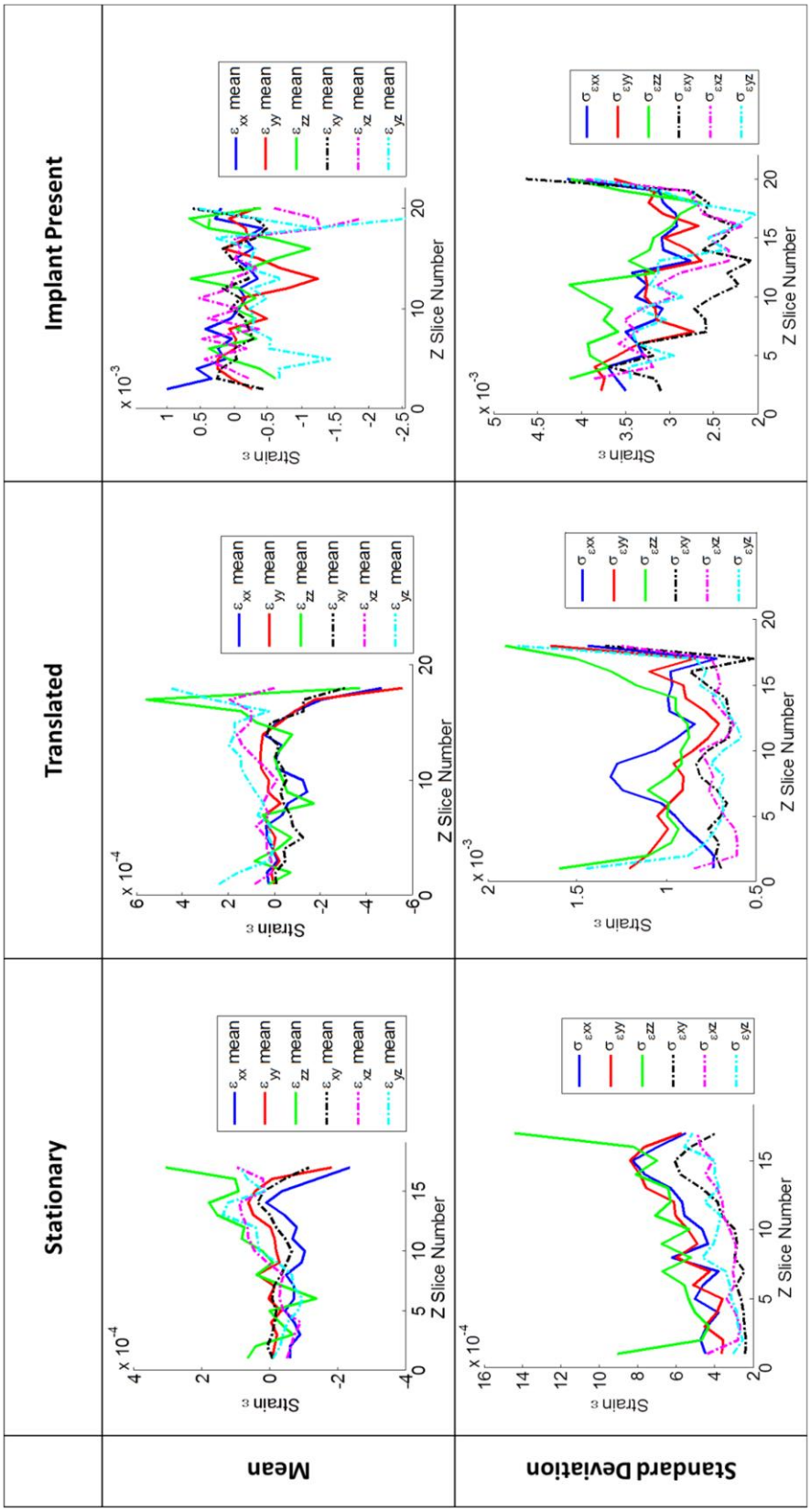

Figure 157: a) Mean strain resolution and standard deviation between the stationary (A and B), translation (B & C) and implant presence (Scan C & D) scans of the DeltaMotion bone with masking applied. (A 64 voxel size with a 50 % overlap was used in the DVC calculation).

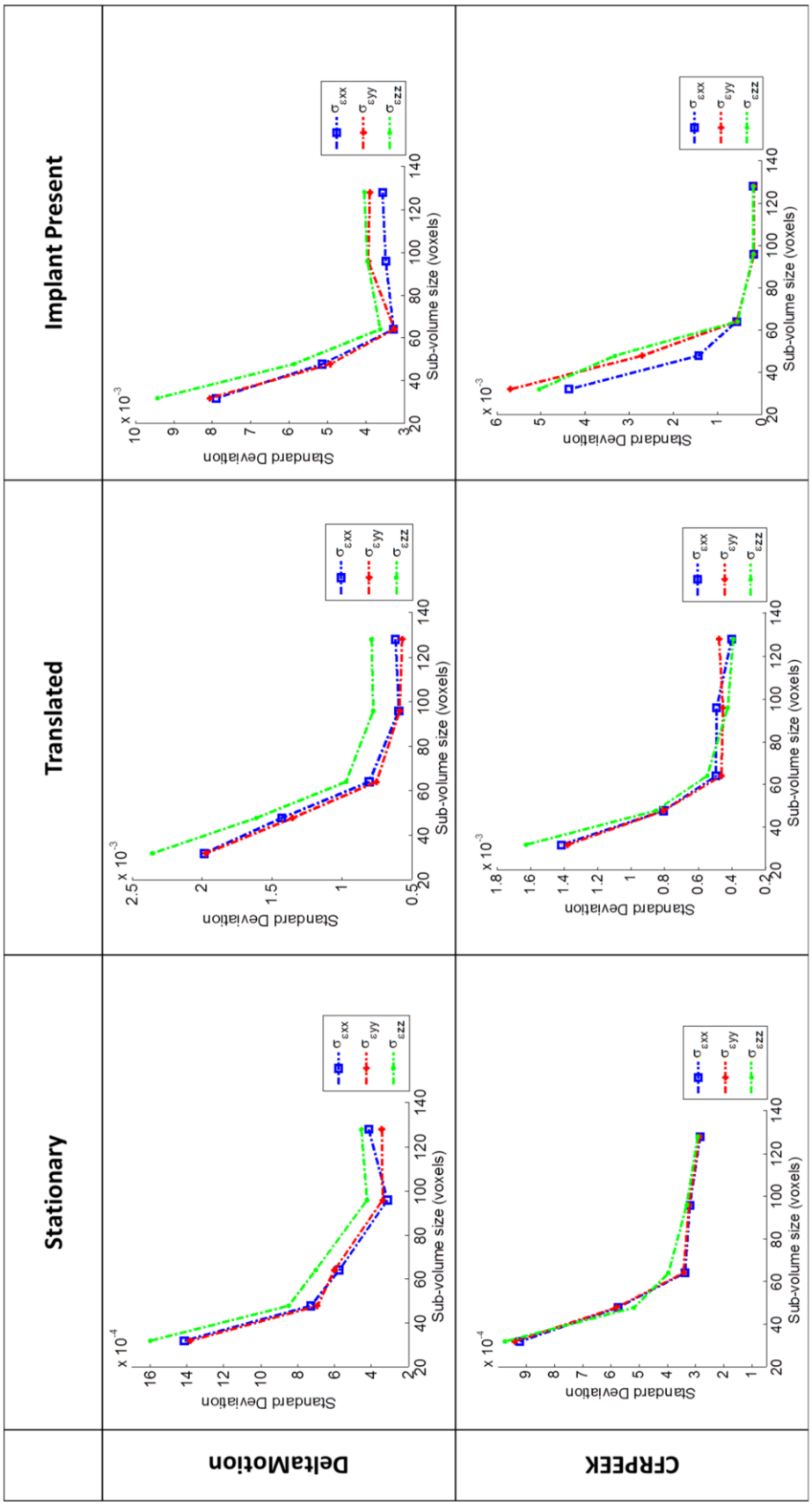

Figure 158: a) Strain resolution for stationary test (Scans A & B), translation test (Scans B & C) and the implant presence test (Scan C & D) for different sub-volume sizes for the CFRPEEK and DeltaMotion implanted bone specimens

6.2.1.2 *Measurement Resolution Discussion*

A similar trend to the foam implantation analysis was found in which the sub-volumes located within the component and along the edge of the implant possessed significantly higher/lower strain values than in the bulk of the material (Figure 153). Strains calculated in these regions were unrealistic for a study between scans where no strain was introduced. It was concluded this was due to the correlation procedure forcing a solution in a region where no distinctive internal pattern existed. In addition to this issue, Figure 153 showed that there was a distinctive outline to each of the specimens where the sub-volumes exhibited a higher coefficient value than in the bulk of the material. In this region excessively high/low strain values were also calculated (Figure 153) and their location was consistent with the location of the cortical bone layer surrounding the trabecular bone. It is suggested that the dense nature of cortical bone meant it also did not contain a distinct enough pattern for the correlation procedure to track, resulting in unrealistic results being obtained here as well as within the component. In addition to a lack of traceable pattern, the location of the cortical bone on the outer surface of the femur caused edge effects. Sub-volumes located on the edge have fewer neighbouring sub-volumes for estimation of the strain tensor, which introduced errors.

The influence of the poorly calculated regions is shown in Figure 154 where the standard deviation increased from ~5 x 10^{-3} to 0.02 between slice 10 and 20 where the DeltaMotion component was located. Masking reduced the standard deviation by ~25 times and it was essential that areas possessing a non-distinct pattern were removed from the analysis in order to provide a plausible strain resolution. In agreement with the foam analysis, sub-volume data from within the component region were removed using a spherical mask with a radius that was equal to the radius of the component plus the length of two sub-volumes. The radius was enlarged from the component radius to ensure sub-volumes affected by the boundary effects (discussed in Section 6.1) were also removed.

The poorly calculated data from sub-volumes located in the cortical bone and along the edge of the femur were also removed through additional masking. A restriction of the correlation procedure was that it calculated a high correlation coefficient for sub-volumes in regions which did not possess a distinct pattern for successful correlation. The correlation was very high and nearly equal to 1 in two regions within the volume (Figure 153 and Figure 155). The first was where the component was located and the second was along the specimen boundary where the cortical bone was present. It was found that by applying a mask which filtered sub-volumes possessing a coefficient greater than 0.998, data from along the cortical boundary was removed.

The implementation of the masking procedure allowed the calculation of reliable strain resolution values. The strain standard deviation produced by the CFRPEEK component was half that of the DeltaMotion component. The standard deviations recorded for the translation tests were both higher than the stationary results for each specimen type. The CFRPEEK

component standard deviation was below 4×10^{-4} whereas the DeltaMotion result was nearly a magnitude larger (2×10^{-3}). The higher standard deviation experienced in the translation test has been explained previously and is due to the value incorporating the combined errors of the stationary test as well as the interpolation errors introduced during the rigid body correction step. The artefacts produced by the DeltaMotion component produced a poorer strain resolution which was due to the high attenuation coefficient and thickness of the component. Beam hardening and scatter were the main artefacts evident. Their presence has been shown to obscure features (262) and can make it difficult to determine the quality of bone stock surrounding the implant (352).

Degradation in the correlation coefficient existed when the correlation procedure was performed between two stationary scans where the implant was present in only one of the scans (Figure 155). This had a negative influence on the strain resolution with both components exhibiting a higher standard deviation for the implant presence study. For the implant presence study, the CFRPEEK component exhibited a standard deviation strain resolution of 5×10^{-4}. In the trabecular compression study a strain of around 8×10^{-3} initiated bone crushing which implied the strain resolution value for the CFRPEEK component should be low enough to record significant strains. The DeltaMotion component recorded a value of 4×10^{-3} which made extraction of significant strains difficult as there was little difference between the strain resolution and bone failure strains. The scatter and its effect on the correlation procedure were considered further in the implantation analysis.

The evaluation of sub-volume size on the correlation precision indicated that for both the stationary and rigid body correction evaluations a 64 voxel sub-volume with a 50 % overlap was an adequate compromise between strain resolution and spatial resolution (Figure 158).

6.2.2 Implantation Test Methodology

Following the stationary and rigid body translation tests, microfocus X-ray computed tomography measurements were carried out on the two femurs used in the metrological study with the acetabular components removed from the reamed cavities. The scan parameters were detailed in Section 6.2.1. These volumes provided the reference scans for the DVC analysis.

An additional femur was obtained and prepared using the same protocol as described in Section 6.2.1. An injection moulded CFRPEEK MOTIS acetabular cup (Figure 98) was provided by Ensinger Ltd. This was heated in an air circulating oven (BINDER FED 53) for 3 hours at 150 °C in line with the annealing conditions set out in Invibio Biomedical Solutions processing guide. The reforming part and the reforming conditions outlined in Section 3.4.2.2 were used to reform the upstanding beams on the outer surface of the cup. The acetabular cup was left uncoated.

A TiHA coated CFRPEEK component and DeltaMotion component were implanted into each of the femurs used in the measurement resolution study. For the implantation process to remain consistent between the three specimens (outlined in Figure 150) the bovine bone was mounted onto a 20 ° inclined block and the cup was placed into the reamed cavity. To complete the setup a second 20 ° inclined block with a raised circular feature was placed on top of the cup. Figure 159 shows the implantation setup. This setup ensured arrowheads present on the injection moulded component were orientated vertically with the rim of the cup parallel to the bone's surface. To control and record the implantation load of the CFRPEEK component a servo-hydraulic axial testing machine (Dartec 9601, Dartec Ltd, Stourbridge, UK) was used. The cup was implanted under a displacement of 0.5 mm/min until the rim of the cup was flush with the bone's surface. The compressive load was recorded during implantation. The implanted specimens were left for 8 hours to allow any movement caused by visco-elastic effects to cease prior to scanning.

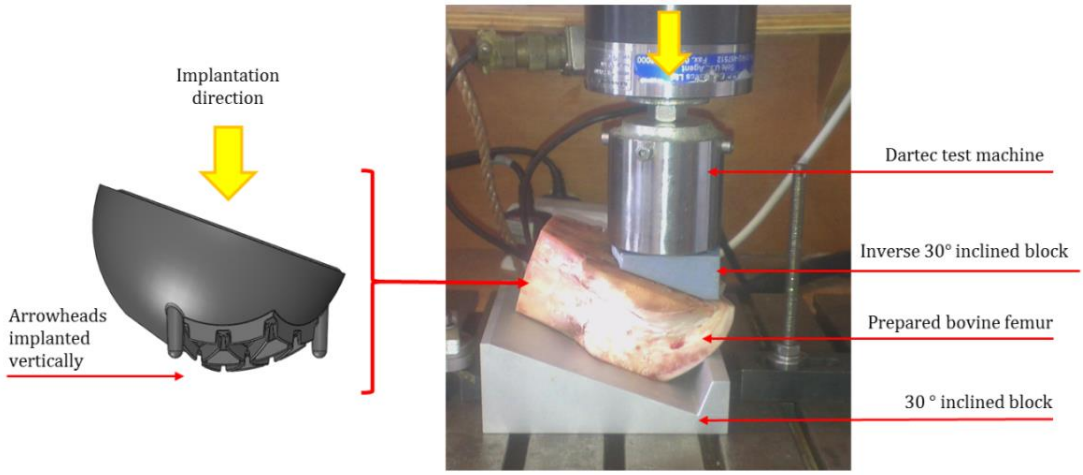

Figure 159: Implantation of the CFRPEEK component into bovine bone showing that the arrowheads were implanted in-line with the vertical axis.

The implanted femurs were scanned to generate the deformed image volumes for the DVC procedure. DVC was carried out on the machined CFRPEEK component with no backing structures and the DeltaMotion component using the un-implanted and implanted scan data. Section 6.2.1 describes the scanning protocol followed in this section. For visualisation the strain vector fields were exported into Avizo Fire 7 software (VSG Inc., Burlington, MA, USA) and no smoothing was applied to the imported data. DVC was not performed on the injection moulded component with the backing features as it was thought that the extent of masking required would not allow the strains produced around the arrowheads to be recorded.

It was found in Section 6.2.1 that the scatter produced by the implant obscured the trabecular structure in the surrounding bone consequently degrading the calculated strain resolution. There was also a decrease in the correlation coefficient in this region as the procedure struggled to calculate a meaningful solution from the now poorly defined internal pattern. Even without the presence of a component, the grayscale values of the pixels in the reconstructed volume will alter slightly between subsequent scans due to noise produced by the scanner. The normalised cross correlation algorithm used in the LaVision software can accommodate for minimal changes through intensity normalisation (353) but it can be very challenging to normalise the intensities for complex changes such as the scatter generated from dense components.

6.2.2.1 *Implantation Results*

Figure 160 highlights that bone crushing extended ~3 mm from the CFRPEEK component's surface. A 15 mm deep contact region from the rim of CFRPEEK component and the surrounding bone was evident (Figure 161). In addition a 1 mm gap between the pole of the component and the reamed cavity was seen.

It can be seen in Figure 162 that the trabecular structure was obscured by scatter produced by the DeltaMotion component. A larger surface area of the DeltaMotion component was in contact with the bone (Figure 163) compared to the CFRPEEK component with only a small (<0.5 mm) polar gap present.

A polar gap of ~3 mm existed between the CFRPEEK component with backing features and the bone (Figure 165). The gap increased in size towards the pole of the component (Figure 164). None of the features failed during implantation but the features further from the pole of the cup were increasingly encapsulated by the bone (Figure 165b and c, Figure 166b and c) due to the reduced gap between the implant and the reamed bone. Arrowheads near the pole showed no signs of encapsulation and were located within the gap space (Figure 166d).

6.2.2.2 *DVC Results*

Figure 167 illustrates the correlation coefficient possessed by the sub-volumes for a slice parallel to the rim of the CFRPEEK component. The correlation was above 0.90 for the

majority of specimen apart from two linear sections either side of the femur. A correlation above 0.95 was seen in the lower side sections of the bone below the growth plate.

The sub-volume coefficients range between 0.90 and 0.97 around the edge of the DeltaMotion component, with a large central region possessing a correlation below 0.90 (Figure 168).

The maximum compressive strain recorded for each strain component was above the strain resolution recorded for a parallel section taken through the CFRPEEK component (Figure **169**). In comparison a reduced number of sub-volumes were available for the DeltaMotion analysis due to the poor correlation coefficient. The values of the x, y and z-strains were close to the strain resolution value of +/- 0.004 (Figure 170).

Figure 171 illustrates a vertical cross section taken through the centre of the CFRPEEK component. The maximum compressive x-strain was located on the right side of the component. The y-component strain ranged between -0.008 and 0.006 which was larger than the other components and above the strain resolution.

Figure 172 illustrates a vertical cross section through the centre of DeltaMotion component. The correlation coefficient in the top half of the component was below 0.90 and these sub-volumes have been masked out. The maximum compressive x and y strains were located in the centre of the section and at the edges of the section respectively. The maximum compressive z-strain was -0.005 and located beneath the pole of the component. All of the strain values documented were close to the strain resolution making it difficult to conclude whether they were due to material behaviour or a noise artefact. The introduction of the component resulted in very little difference in bone definition for the CFRPEEK component compared to the DeltaMotion component (Figure 173).

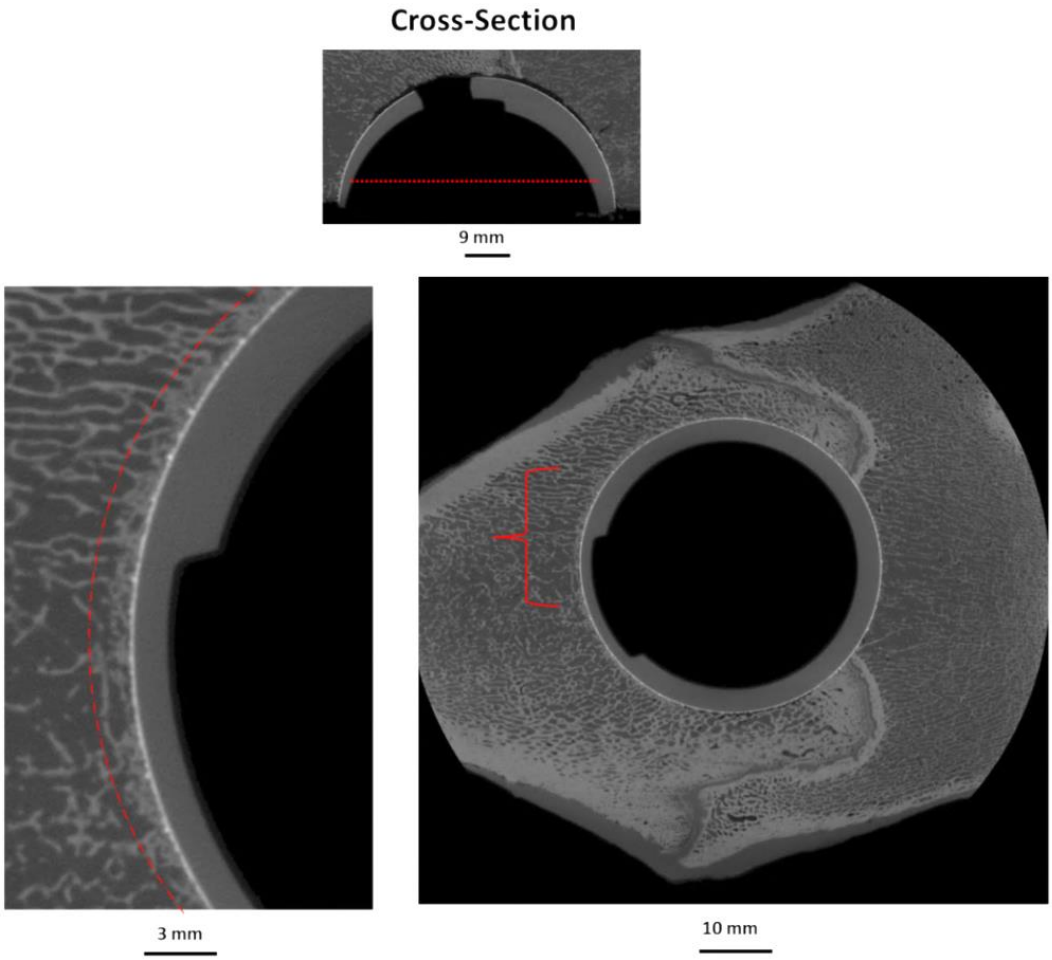

Figure 160: Cross-section taken parallel to the rim of the CFRPEEK component showing bone deformation and crushing around the implanted component. The red dotted line indicates the extent of crushing which extends to around 2 mm from the components edge.

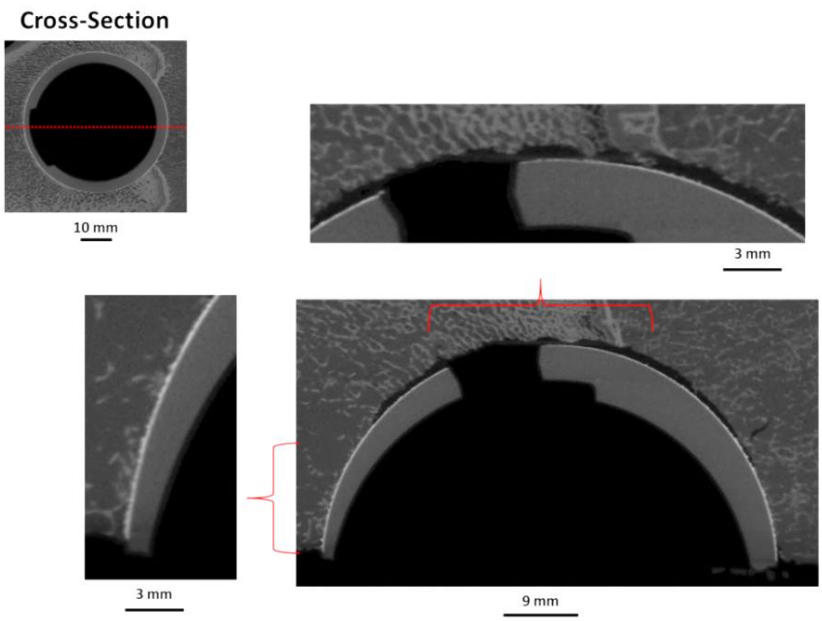

Figure 161: Cross-section taken perpendicular to the rim of the CFRPEEK component highlight the extent of the contact region between the component and the bone. Bone contact extends to around 15 mm from the rim of the component. A polar gap of around 1 mm is present between the bone and the component.

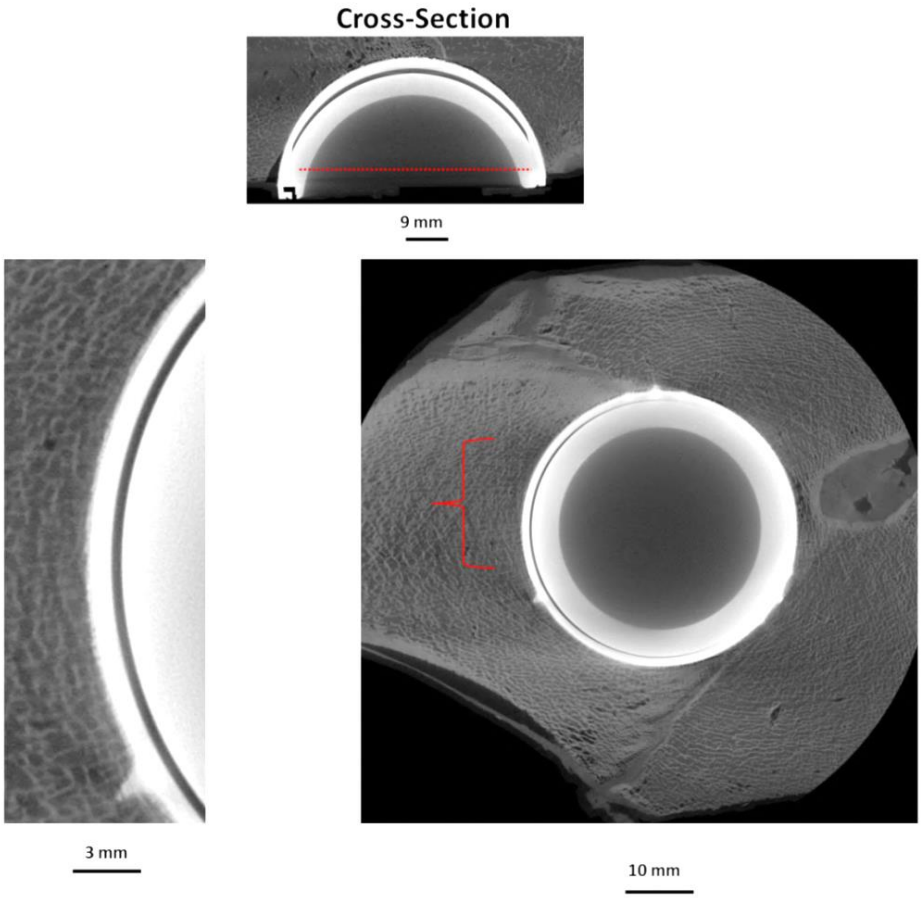

Figure 162: Cross-section taken parallel to the rim of the DeltaMotion component. The artefacts produced by the component make it difficult to observe the bone deformation.

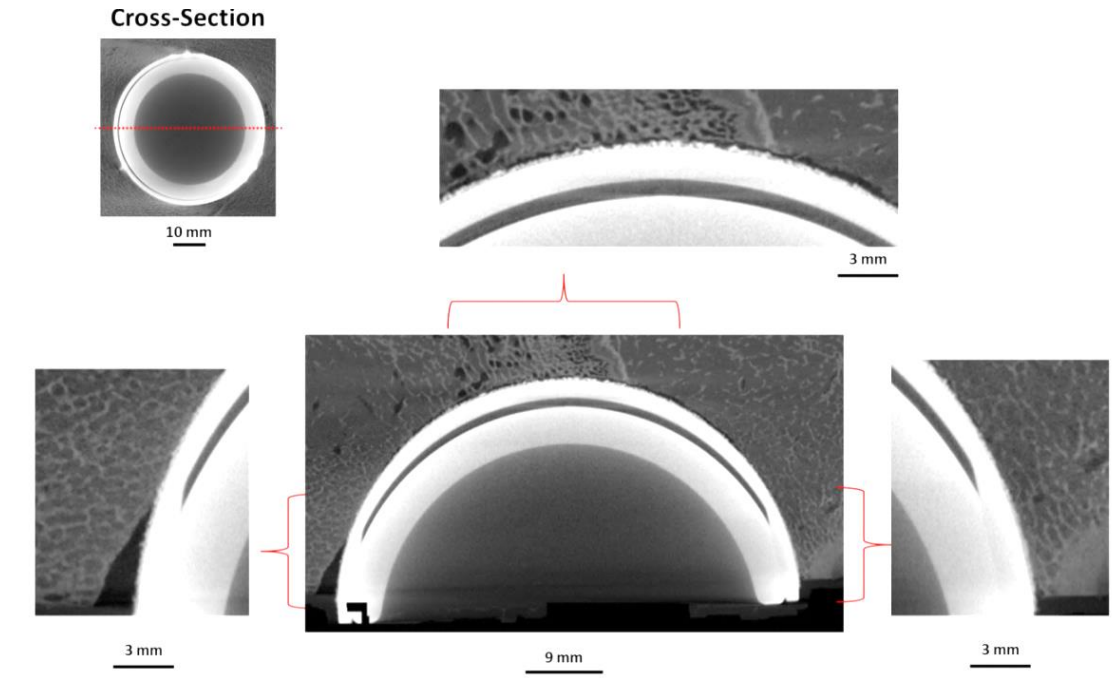

Figure 163: Cross-section taken perpendicular to the rim of the DeltaMotion component shows that there is good contact between the component and the bone and there is small polar gap <0.5 mm present. A reaming error is present on the left side of the component.

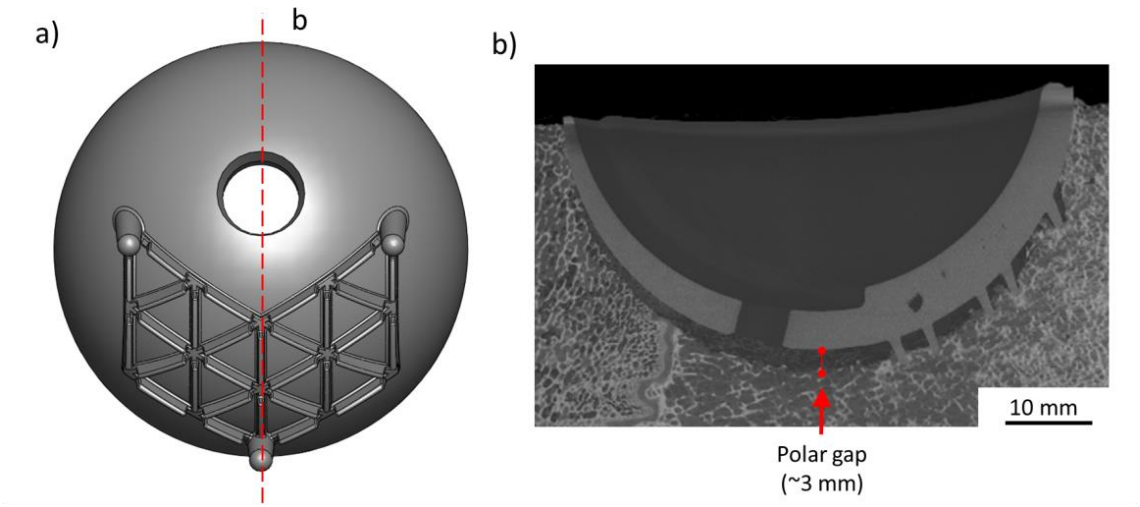

Figure 164: a) Model of injection moulded CFRPEEK component with backing features, b) cross section taken through the centre of the implanted component showing the polar gap.

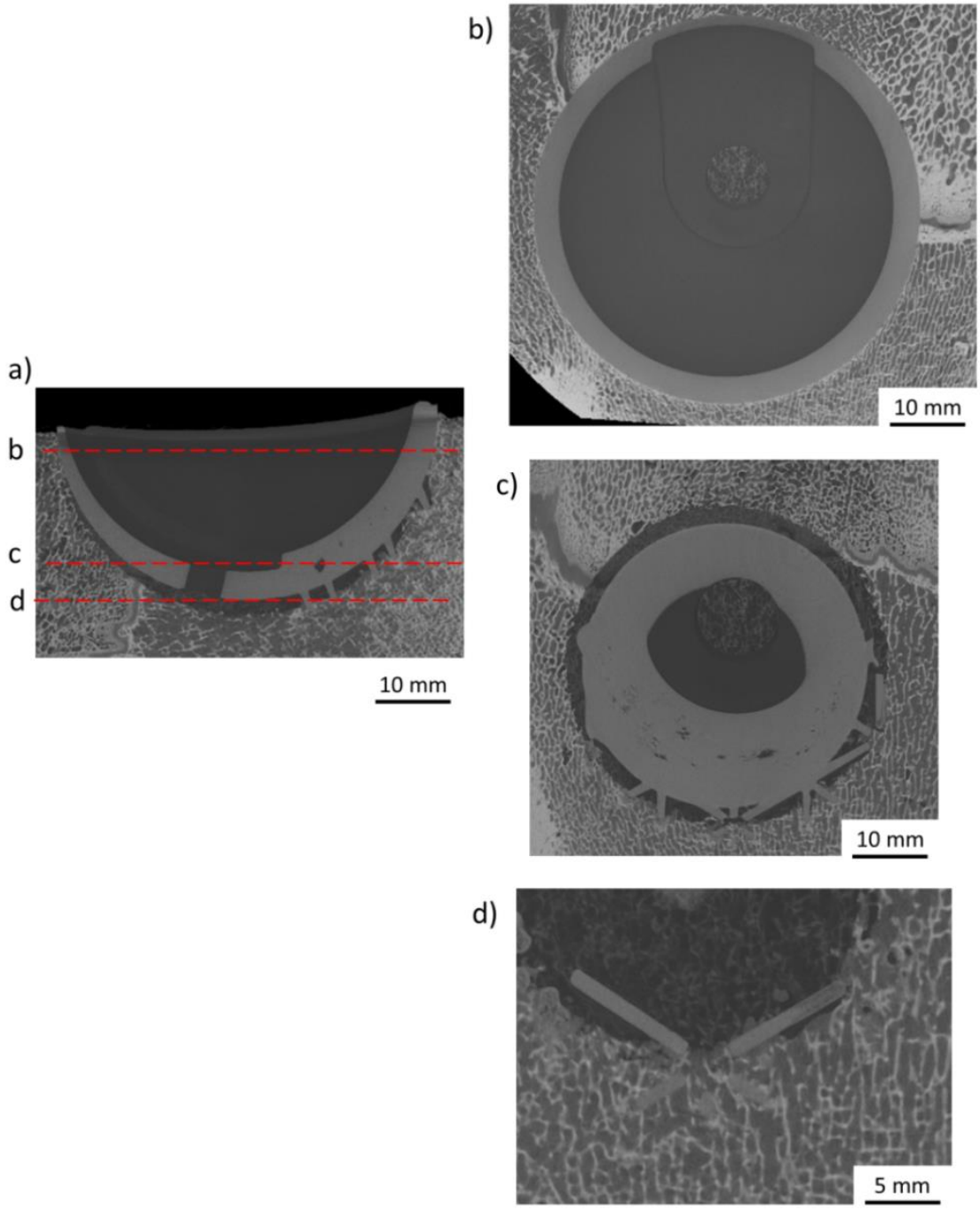

Figure 165: a) Cross section taken through the centre of the injection moulded CFRPEEK cup. b), c) & d) are horizontal sections taken through the cup as indicated in a).

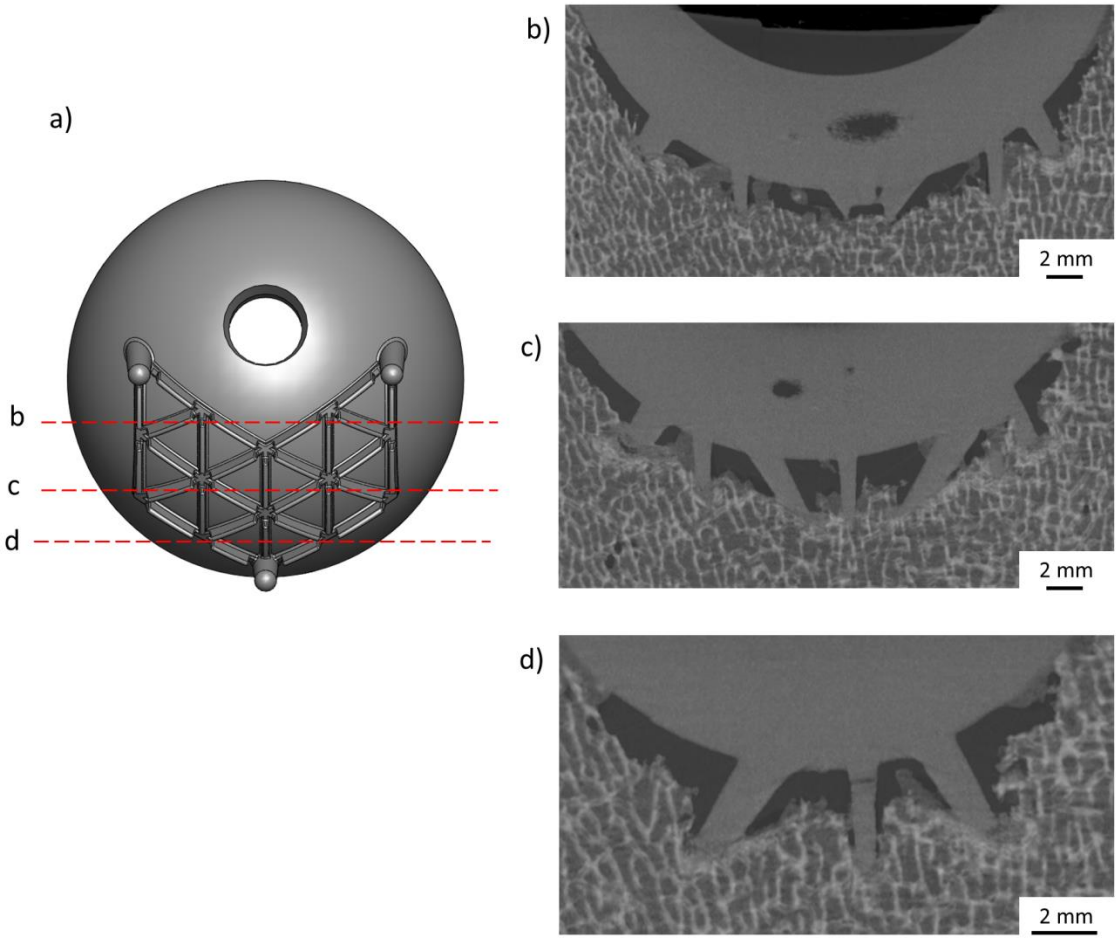

Figure 166: a) Model of injection moulded CFRPEEK acetabular cup. b), c) & d) Cross section taken through the implanted CFRPEEK cup. The red lines in a) indicate the site of the cross sections.

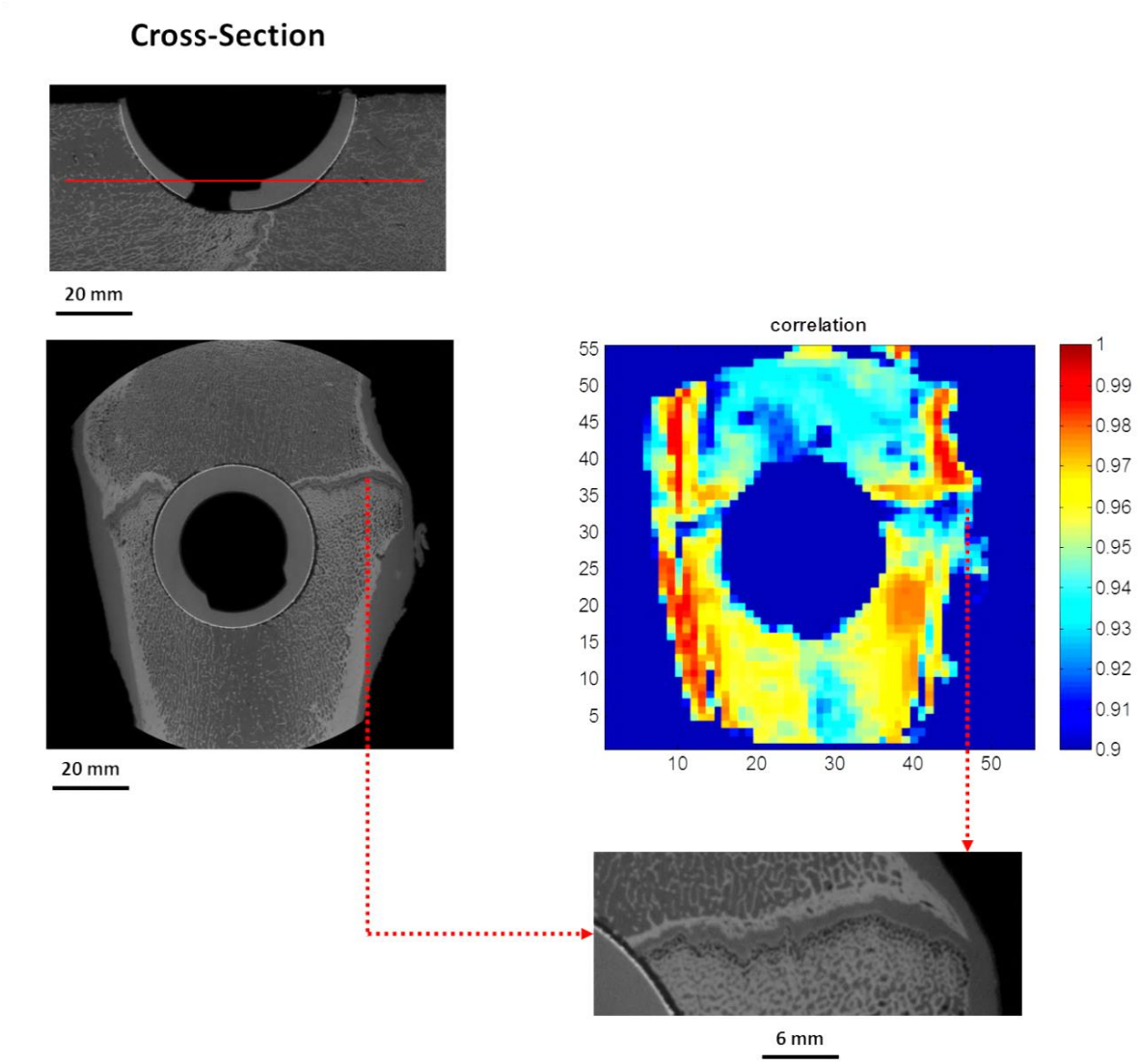

Figure 167: Correlation coefficient for a slice taken parallel to the rim of the CFRPEEK component. Reasonable correlation is seen throughout the specimen but poor correlation is seen along the growth plate where an indistinct pattern is seen.

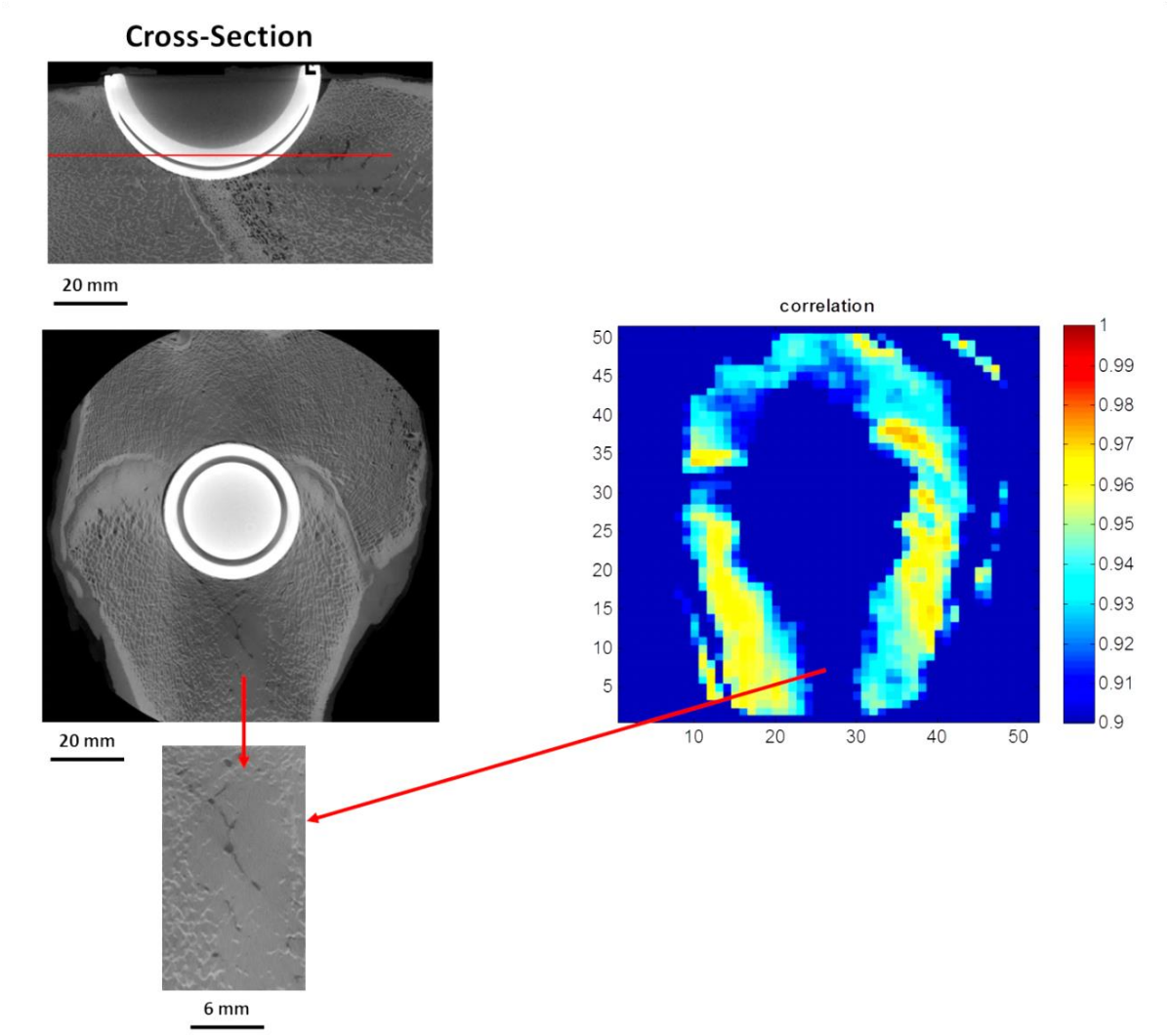

Figure 168: Correlation coefficient for a slice taken parallel to the rim of the DeltaMotion component. The correlation is generally poor (equal to or below 0.94) around the implanted component. It is especially poor in the region where bone marrow is introduced (red arrow).

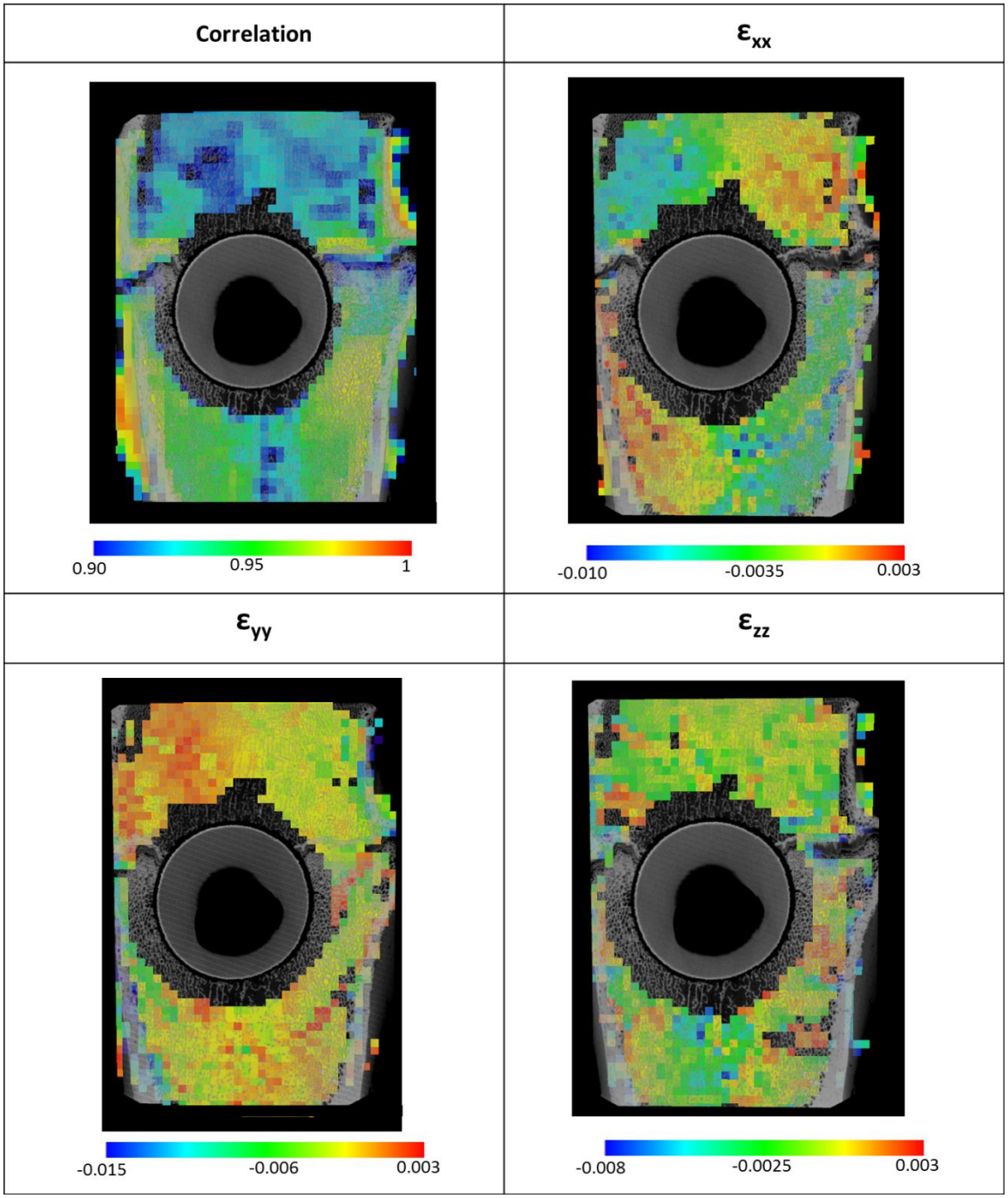

Figure 169: Strain results in the surrounding bone around the CFRPEEK component.

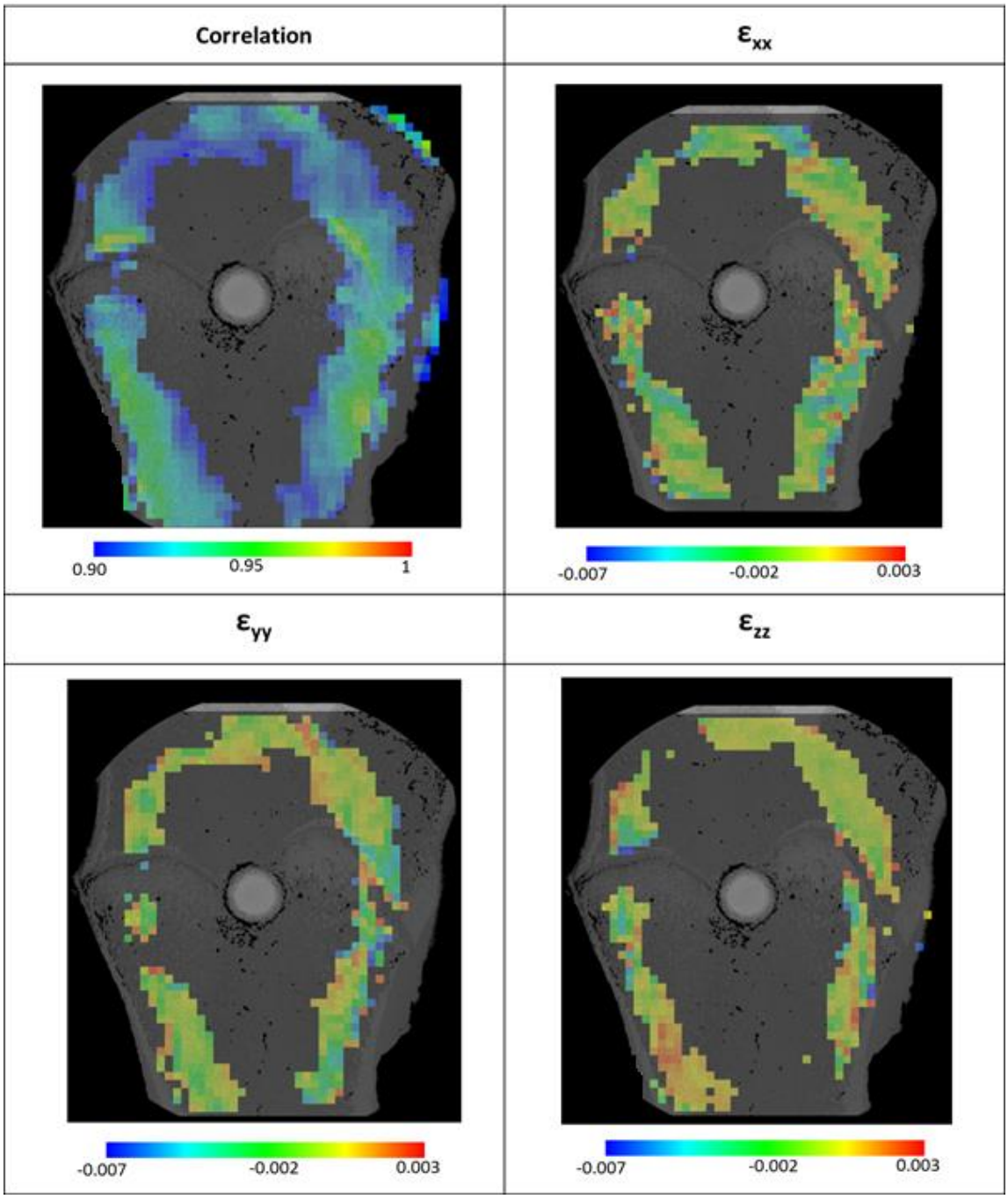

Figure 170: Strain results in the surrounding bone around the DeltaMotion component.

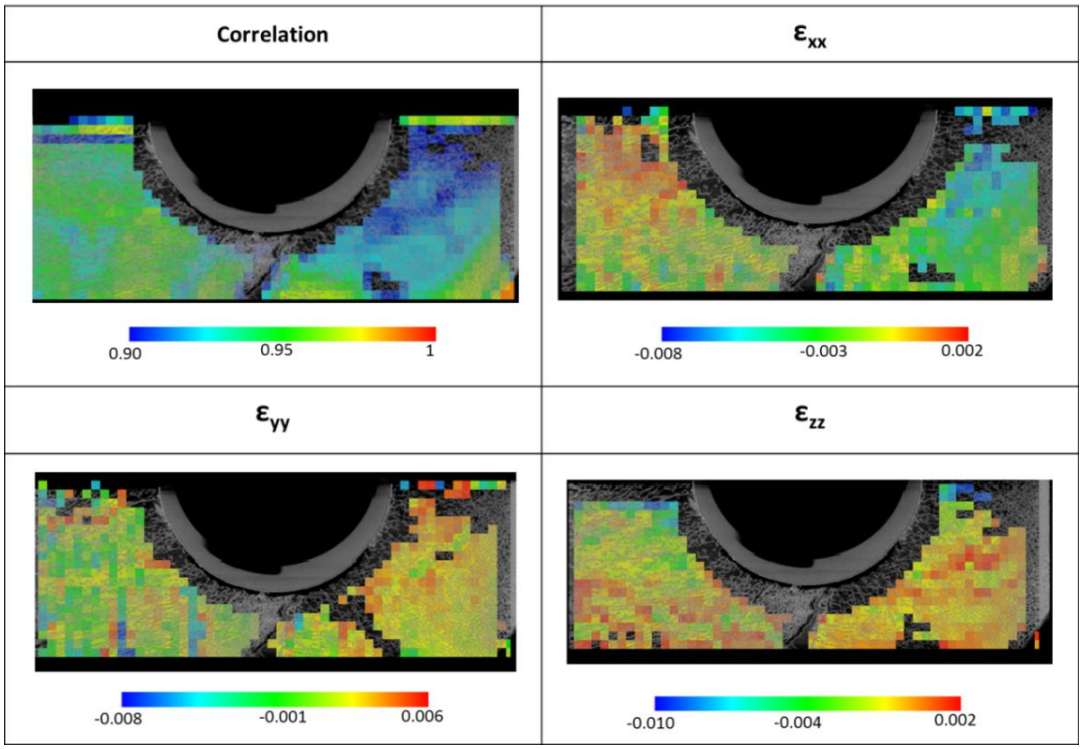

Figure 171: Strain results in the surrounding bone around the CFRPEEK component from a perpendicular to the rim section taken from the centre of the component.

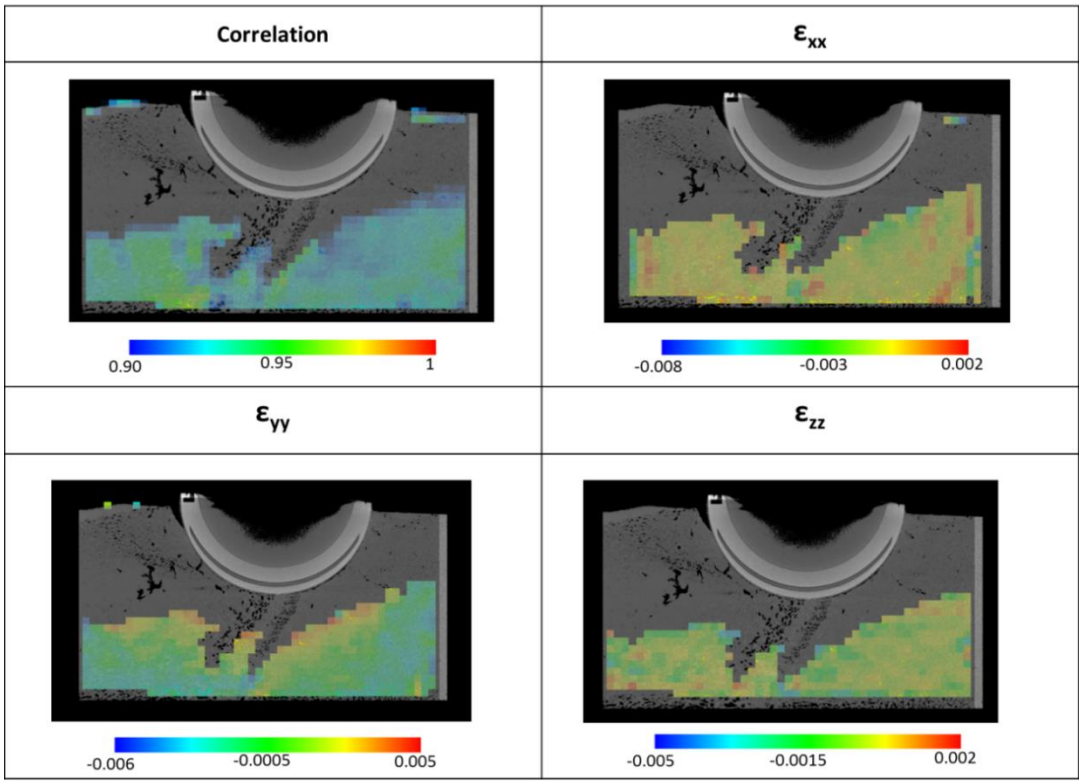

Figure 172: Strain results in the surrounding bone around the DeltaMotion component from a perpendicular to the rim section taken from the centre of the component.

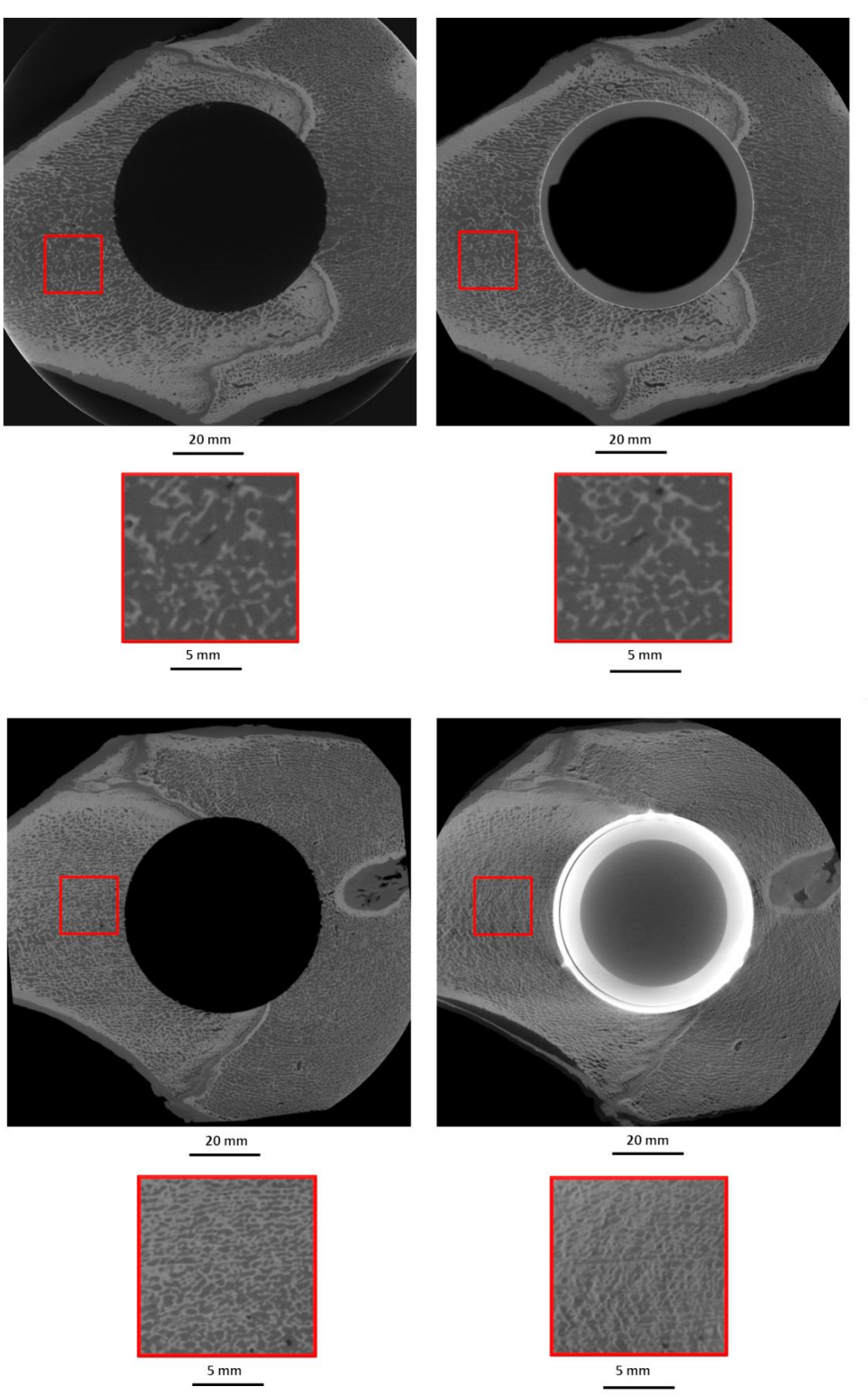

Figure 173: Slice through central part of the CFRPEEK and DeltaMotion bone specimens with and without the component present. It can be seen that the DeltaMotion specimen produces scatter which compromises the definition of the trabecular structure.

6.2.2.3 *Implantation Discussion*

This study aimed to assess the response of different stiffness components to implantation with particular interest in assessing the response of the arrowheads.

The cross section scans (Figure 160 to Figure 166) taken through each of the components showed that the DeltaMotion component was better seated in the cavity than the two CFRPEEK components, meaning it had a larger contact area with the bone and a smaller polar gap was present. This can be attributed to both of the CFRPEEK components' rims not being flush with the surface of the bone which indicated inadequate seating of the component. Peripheral contact was seen between the rim of the cup and the surrounding bone with gap formation between the cavity floor and the cup (Figure 161 and Figure 164). The formation of the polar gap limited the extent of arrowhead engagement. There were regions of positive contact where the bone did behave elastically encapsulating the arrowheads (Figure 166) but there were also regions with no contact after implantation (Figure 165d). The regions in contact did not show signs of failure proving that the design alterations made in Section 3.4.1 strengthened the individual arrowhead features.

Initial dome gaps are frequently seen with the press-fit technique and have been reported to occur in 16 % and 39 % of titanium and CoCr modular cups fixed using a 1 to 3 mm press-fit technique (153, 354, 355). In addition a maximum allowable bone ingrowth has being reported (354, 355). Sandborn et al. (1988) (355) reported that new bone could grow within the porous structure of an acetabular implant with gaps up to 2 mm; above this, bone ingrowth was limited and a new 'effective joint space' would form in which debris could accumulate (109). Nakasone et al. (2012) (354) found that in 11.5 % of small gaps (ranging between 1.0 - 1.9 mm) gap filling was present at 3 months with this percentage rising to 100 % at 2 years. The studies also showed a reduced growth rate for large gaps (ranging between 2.1 - 4.3 mm) with 9.5 % of all cases showing gap filling at 3 months but this did increase to 100 % at 2 years. Based on these studies, it is suggested that bone ingrowth could eventually occur in the gap between the CFRPEEK component and the surrounding bone. However, it is unlikely that the primary fixation generated by the arrowheads in the current state would generate stable enough conditions for bone growth to occur.

The extent of the polar gap depends on a number of factors including the amount of press-fit, component stiffness and bone quality. A press-fit of 1 mm was chosen for this investigation to coincide with the press-fit conditions of the ADEPT component (MatOrtho Ltd) whose geometry was used as the basis for the CFRPEEK component design. Bovine bone was chosen due to ease of access and to generate a worst case implantation scenario due to its high stiffness (381 – 2380 MPa (239, 240, 356)) compared to human bone (1.4 - 552 MPa (240-242)); it is proposed that the resultant polar gap was an extreme value and that implantation into human bone would yield a lower result. Nevertheless, it was important that the worst case scenario was investigated as bone stiffness will vary between patients, depending on a range of factors including age, gender and general health. One of

the reasons for investigating CFRPEEK as a substitute material was due to it possessing a lower stiffness than a traditional metal component that was closer to bone. During implantation the CFRPEEK component will deform more than a traditional metal component (167) which should result in lower bone damage and lower strain generation around the implant (66). Although the latter aspect is positive, increased deformation could lead to rim contact between the cup and the cavity and less area available for osseointegration, as seen in this study. In addition, it has been suggested that excessive deformation could increase wear due to induced changes in component sphericity, degradation of fluid-film lubrication, or induced equatorial contact (157, 158), all of which can be related to the press-fit and bone quality. Bone quality is a factor which was outside the control of the operator, unlike the press-fit. Reducing the press fit will decrease component deformation allowing an increase in peripheral contact; this should decrease the polar gap and increase the number of arrowheads encapsulated by the bone.

The implantation method did not mimic the surgical environment but the controlled technique employed was repeatable and the load could be recorded easily. Furthermore it avoided the influences of surgeon variability and complex physiological boundary conditions. To produce more realistic implantation procedures a future analysis could be conducted where the component is implanted by a surgeon. This study ensured the arrowheads were implanted vertically, minimising shear forces a factor which made the arrowheads in Section 3.4.1 susceptible to failure. It is unlikely that this would be replicated by a surgeon and a means of ensuring alignment in the implantation instrumentation will be required. In addition, a future analysis should be conducted whereby the arrowheads are not implanted vertically which will assess the features resistance to shear forces during implantation.

6.2.2.4 *DVC Discussion*

The DVC foam study in Section 4.5.1 concluded that the brittle nature of the bone analogue foam model made it unsuitable for assessing strain generation around acetabular components. It is hypothesised that bone would be a more suitable candidate for this type of analysis due to its visco-elastic nature and highly contrasted internal pattern.

The CFRPEEK cross sections revealed that the trabecular structure was still distinctively present in the implantation scan and a ~3 mm thick crushed layer was evident around the edge of the component. This indicated that although the CFRPEEK was increasingly deformed bone failure still occurred. The trabecular pattern was more difficult to distinguish around the DeltaMotion component (Figure 173) due the presence of the artefacts produced by the component. The sources of these artefacts were discussed in Section 4.1.3 and they were largely due to the high attenuation coefficient of the DeltaMotion component. These artefacts negatively affected the correlation coefficient of the sub-volumes in the trabecular bone (Figure 167 and Figure 168). The removal of data from within sub-volumes possessing a correlation coefficient below 0.90 was applied as this data was considered unreliable

(Section 4.4.1). In the trabecular study, filtering removed data from the sub-volumes within the crushed region where the internal trackable material pattern was lost. In this study it removed data from regions where the internal pattern was not lost through crushing but due to it being obscured by the scatter produced by the component. The surrounding bone was only marginally affected by the CFRPEEK components presence with the sub-volumes possessing a coefficient between 0.90 - 0.95 in the majority of the specimen. A lower coefficient was documented in the CFRPEEK component but only in regions where the internal pattern was not distinct enough to track. These regions were along the growth plate and in the bone marrow section (Figure 167). It was important that the data within these regions was removed to avoid unrealistic strain calculations. However, in the DeltaMotion specimen the correlation coefficient in the sub-volumes surrounding the component below 0.90 constituted the majority of the specimen leaving a small number of sub-volumes for analysis which limited the conclusions.

The strain data gathered from the CFRPEEK implantation study was considered to be due to trabecular bone deformation and not a noise artefact as the strain values recorded for the x, y and z-components were larger than the strain resolution recorded in the noise analysis. The strain map showed that below the growth plate the strain varied from positive on the left side to negative on the right hand side. An opposite relationship was shown above the growth plate. In both cases the compressive strain was greater than the tensile strain but this relationship suggested than the component had rotated within the cavity and deformed the surrounding bone. As the trabecular bone was attached to the stiff outer cortical bone, the compression of trabecular bone along the left hand edge in the region above the growth plate caused minimal tension in the trabecular structure on the opposite side. The position of the growth plate within the bone stopped the compressed region of trabecular bone on the top left side from compressing the bone beneath the growth plate. This boundary meant the trabecular region remained in tension but the trabecular bone on the opposite side of the growth plate was in compression. The maximum compression strain recorded was -0.01 which from the trabecular study should initiate bone failure. However, this was not observed and could be attributed to a change in bone quality associated with donor site, donor age and load orientation axis.

The recorded bone deformations are believed to be authentic and not due to noise artefacts for a number of reasons. Firstly, the strains recorded were a magnitude larger than the strain resolution (4×10^{-4}). Secondly, the strains were calculated from sub-volumes possessing a correlation above 0.90 meaning unreliable strains were excluded from indistinct patterned areas such as cortical bone and/or obscured trabecular regions. Unreliable strains were identified in the measurement resolution study as extremely high or low strain values. The x-strain component showed that these outliers were positive on the bottom outline and negative along the top outline with a near-zero value located along the horizontal mid-line section through the component. This relationship was not seen for the x-strain component in

the CFRPEEK implantation study meaning unreliable strains were effectively masked out. Based on these findings it can be assumed that the strain behaviour in the x-direction was due to material behaviour and not a noise artefact. The y-strain map possessed a less distinct pattern although the maximum compressive strains existed at opposite sides of the specimen at the cortical/trabecular bone boundary suggesting component rotation had occurred. The majority of the specimen was in compression which was consistent with the implantation direction. There were a few sub-volumes possessing a positive strain value and the source of this relationship is unknown but it may be due to parts of the trabecular bone being restrained more than others. The maximum compressive z-strain was found near the rim of the component which was consistent with rim contact shown in Figure 171.

The bone lost its natural pattern due to crushing and authentic strain data could not be extracted in the region 3 mm adjacent to the implant. Whilst this region clearly experiences the greatest strain, the map only showed the effect away from the implant where the values remained relatively constant.

It has already been suggested that the scatter produced by the DeltaMotion component compromised the ability to track trabecular deformation reliably as the natural trabecular pattern was obscured. The number of sub-volumes available for analysis after masking was minimal due to the poor correlation possessed by the majority of the sub-volumes (Figure **170** and Figure 172). Scatter is difficult to remove entirely especially when scanning highly attenuating material such as ceramic and titanium. Due to the large area covered by the flat panel, the deflected scatter is recorded, reducing image contrast. To reduce scatter effects and improve image quality a line array detector could be used in a future analysis. In this case, the single line of pixels on the detector would only detect photons which are directed in the line of sight between the source and the detector. However, this would require considerably longer scan times.

The number and form of the bone specimens used in this study limits the strength of the relationships. The femurs were taken from steers of around a similar age, but there is great variation in the properties of bone between each individual case, meaning that the stiffness of bone supporting the cup would' vary from case to case (238). There may also be variation in the fit of the cavity due to reaming errors which may alter the effective sizing and the symmetry of the cavity (238). Clearly, further analyses would need to be carried out to ascertain the reproducibility of these results.

The use of bovine femurs revealed the presence of a growth plate within the cavity. While this section (the posterior side) of the femur is suitable due to its large size (which allowed a 53/54 mm cavity to be reamed, the growth plate influenced the strain results obtained as it restricted the deformation of the trabecular bone. It would be advisable to use cadaver pelvises for this type of study, but cadaver samples were unavailable for this project due to the acquisition costs involved.

6.3 Conclusion of implantation studies

DVC was used to compare the strain generated around a CFRPEEK component against a contemporary large diameter bearing acetabular component. An analogue bone model was analysed to assess its suitability as a bone substitute in this type of study.

In both studies a poorer strain resolution was recorded than in the trabecular compression analysis in Section 4.4.1. This made it difficult to distinguish between strains generated by material behaviour and strains generated by noise artefacts. Due to the concentration of foam deformation close to the implant/foam boundary, brittle failure of the foam itself, and the presence of edge effects, significant strains could not be extracted from either data set. The study concluded polyurethane foam was not a suitable material for assessing strain generation around an implanted component using DVC. The study was repeated in bovine bone and it was concluded that while a dense ceramic component was unsuitable for DVC analysis, strains could be measured around implanted polymeric and composite cups.

7 Study 7: Assessment of Acetabular Component Primary Stability

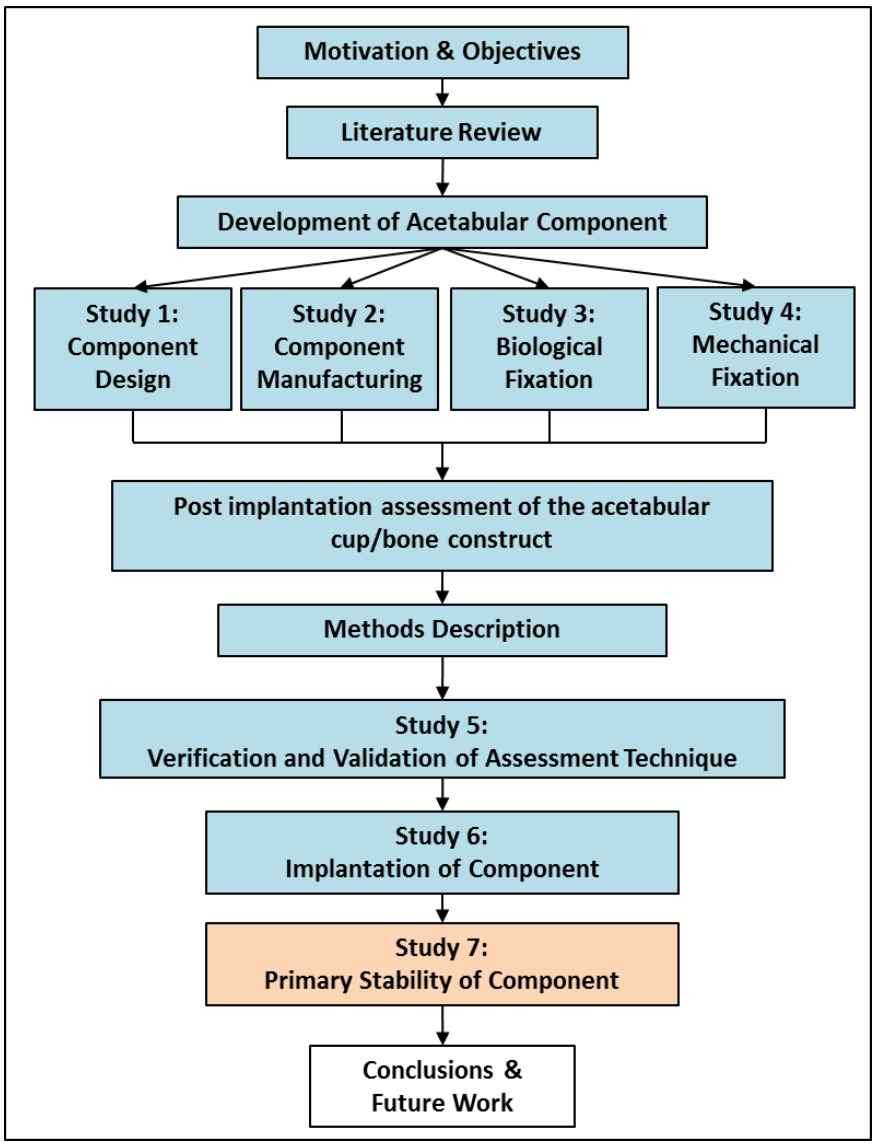

As a measure of the potential longer term loosening of a component, primary stability tests are commonly conducted. In this final verification study, the efficacy of the arrowhead fixation features is determined using torque-out testing in which the load required to unseat the implant is ascertained. Similar tests were also conducted on traditional implant designs.

Materials & Methods

Five femurs from ~24 month old steers were obtained from a local butcher. A flat section was prepared using the technique discussed in Section 6.2.1. Due to the inability to seat the injection moulded CFRPEEK component with the backing features in Section 3.4, the implantation cavity was increased to investigate whether this encouraged implant seating. In one of the femurs a 54 mm diameter cavity was reamed using standard surgical reaming equipment to generate a size-for-size fit for a 54 mm outer diameter acetabular component. An injection moulded CFRPEEK acetabular cup with the arrowheads present was prepared

using the protocol set out in Section 3.4.2.2 and implanted into the cavity using the protocol described in Section 6.2.1.

The four remaining femurs were reamed to a 0.5 mm diametric press-fit (53 mm diameter cavity) in line with the two femurs that were prepared in Section 6.2.1. Using the same implantation technique, machined TiHA coated CFRPEEK MOTIS acetabular components without the backing features present were implanted into two of the femurs and DeltaMotion (DePuy Ltd, UK) acetabular components were implanted into the remaining two femurs. Each implanted specimen was left for 8 hours before initial stability was assessed.

Primary stability was assessed for the components previously described and the three femurs in the previous DVC analysis. This was assessed by applying a point load to the rim of the component whilst the bone specimen was clamped to the base a test machine. A compressive load was applied at a rate of 1 mm/min and the maximum compressive load applied before the cup commenced to rotate within the cavity was measured. This test follows Aurora Medical Ltd test protocol FD206 and evaluates the anterior-posterior stability as shown in Figure 174. The resistance value provides an indication of the components primary stability and resistance to torque due to bearing friction. In order to correctly mimic the *in-vivo* loading conditions the rim load was applied to the outer edge of the CFRPEEK component with the backing features as shown in Figure 175.

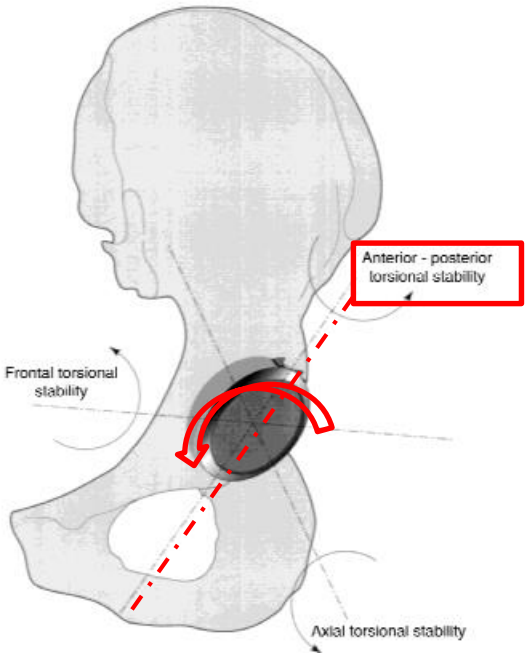

Figure 174: The illustration shows the anterior-posterior torsional stability highlighted in red investigated in this experiment (357).

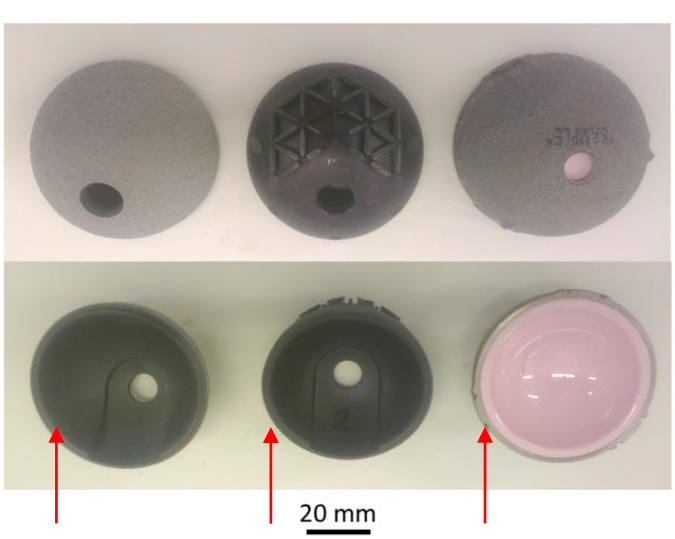

Figure 175: Edge loading was applied on the anterior side of the component to mimic *in-vivo* conditions.

Figure 176: Test setup of edge loading experiment on the implanted components to investigate their primary stability.

Primary Stability Results

Table 21 shows the load applied to the edge of the component to initiate rotation within the cavity. The DeltaMotion component sustained the largest load (-5.68 kN). The lowest value was recorded for the injection moulded CFRPEEK component with backing structures implanted into a 53 mm cavity. Figure 177 shows the condition of the bone and the backing structures of the injection moulded CFRPEEK components after testing. Two of the arrowheads failed on the component implanted into a 53 mm cavity. At least seven arrowheads were either completely sheared off from the main body of the component or failed at the root of the arrowhead through shearing when implanted into the 54 mm cavity.

Table 21: Compressive load required to implant and initiate component rotation within cavity.

Sample Type	Cavity Diameter (mm)	Implantation Load (N)	Load required to initiate rotation (N)
Machined CFRPEEK component with TiHA coating	53	-5.66 +/- 0.46	-5.20 +/- 0.78
DeltaMotion	53	-7.93 +/- 0.36	-5.68 +/-0.97
Injection moulded CFRPEEK with backing structures (from study in Section 3.4)	53	-7.00	-1.81
Injection moulded CFRPEEK with backing structures (from study in Section 3.4)	54	-7.50	-2.68

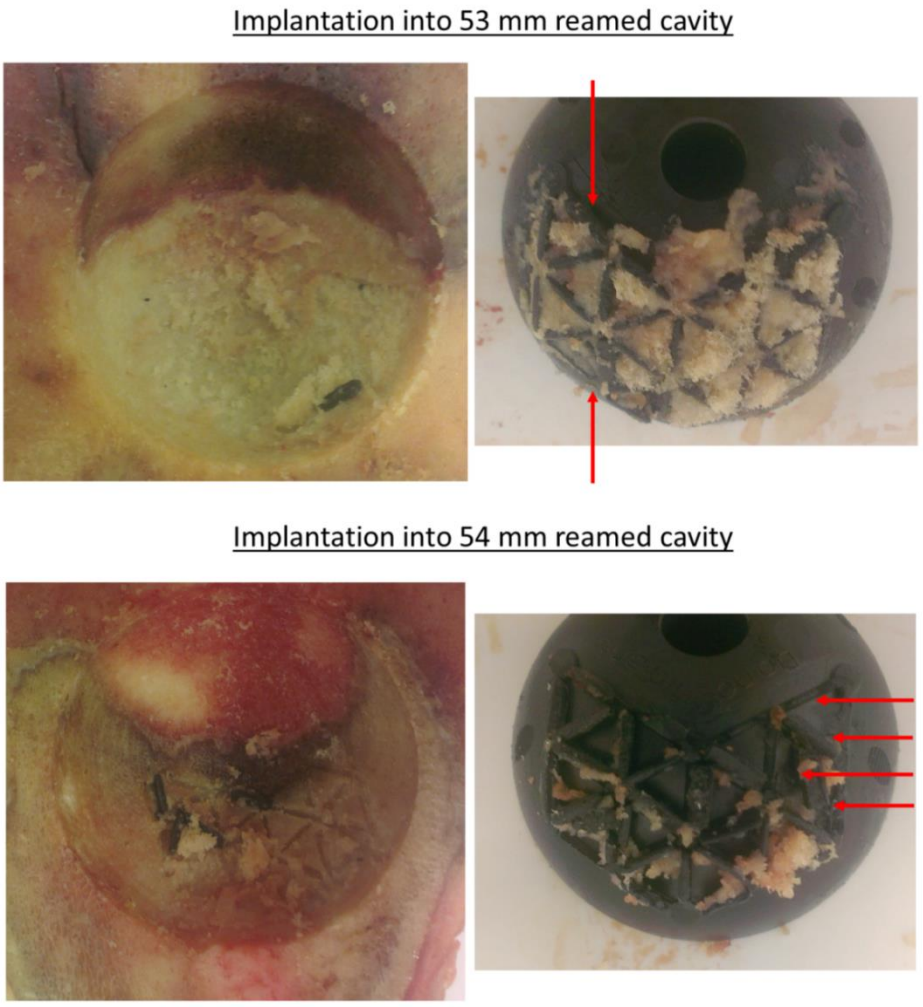

Figure 177: The condition of the implanted bone and injection moulded component after extraction of each component from the 53 and 54 mm cavities.

Discussion

The results of the 53 mm cavity implantation study showed that the DeltaMotion component exhibited the greatest cup stability. This was followed by the machined CFRPEEK component and finally the injection moulded CFRPEEK component. The difference between the DeltaMotion and machined CFRPEEK components was not statistically significant ($p>0.05$).

The difference between the results was attributed to the initial implantation state i.e. how well the component was seated and the outer surface roughness. Better cup/bone contact was observed with the DeltaMotion and machined CFRPEEK components (Figure 161 and Figure 163) than the poorly seated injection moulded CFRPEEK component in Figure 166. The increased contact region, together with the rough coatings on both samples increase pre-compression and friction at the peripheral interface of the acetabulum (122) subsequently increasing the resistance to movement.

Note the injection moulded component was left uncoated to allow the primary stability provided by the arrowheads alone to be assessed. The final injection moulded component would be coated which should improve primary stability.

In the case of the size-for-size fit (54 mm cavity), primary stability was solely due to the arrowheads. There was improved primary stability compared to the 53 mm implanted component. However, the 53 mm implanted component was not fully seated and a repeat study should be conducted which ensures that the components are seated correctly. A concern is that the arrowhead did not achieve the same resistance as the coated CFRPEEK which could be due to poor seating and lack of correct instrumentation. The component may not have been seated properly for a number of reasons (358). Firstly, variation in the fit of the cavity due to reaming errors may have altered the effective sizing and the asymmetry of the reamed cavity (358). Secondly, contact between the bone and the component occurred at the rim. The ideal implantation technique would allow for a tight press-fit at the rim while achieving complete seating of the component to maximise host bone contact for bony ingrowth. Clinically the implantation setup would be different with the cup firmly attached to a stiff impaction cap. Usually during impaction, the impaction cap supports the cup and energy is transferred into the surrounding bone, which allows the cup to be inserted more easily (359). Once the component is fully inserted the impaction cap is removed which allows the cup to deform. Implantation of the CFRPEEK component into the 53 mm cavity was completed with a prototype impaction cap which was not securely fixed to the component. During implantation it was likely that the cup did not maintain its shape as it was not supported by the impaction cap resulting in improper seating.

Figure 177 shows that some of the arrowhead features failed during the test. The imprints of the arrowhead features are more evident in the 54 mm implanted cavity suggesting that this component was better seated than the 53 mm equivalent.

The lack of repetitions means further analyses would need to be carried out to ascertain the reproducibility of these results. Further testing is required to assess reproducibility; these could be complemented by μCT measurements to assess degree of seating and arrowhead penetration. Other factors affecting the test results such as the use of animal bone and the variation in the reamed cavity have been discussed previously.

This investigation analysed the initial stability of the component under simulated flexion-extension frictional torque levels induced *in-vivo*. The load required to initiate rotation was not significantly different for coated CFRPEEK and DeltaMotion components. While an arrowhead component in an under reamed cavity had poor primary stability, in a size-for-size cavity greater primary stability was observed; this should be a consideration for the operative technique protocol development for this component.

8 Conclusions & Future Work

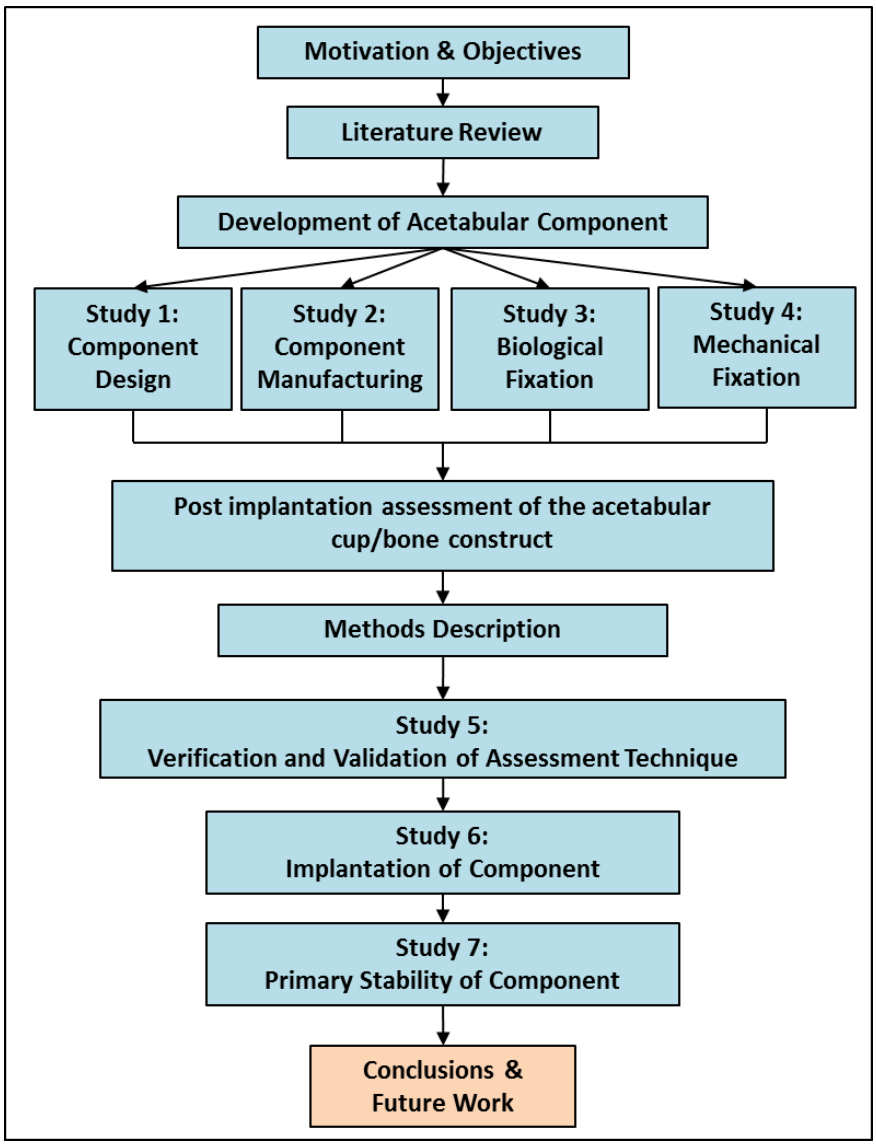

8.1 Conclusions

The following is a synopsis of the key research conclusions.

Component Design

- Patient data from 24 human dry full- and hemi-pelvis specimens were used to determine the geometry of the acetabulum and the acetabular notch. This knowledge was important for the design of the CFRPEEK component which aimed to be more biomechanically compliant by incorporating a raised bearing surface which replicated the natural horseshoe cartilage geometry and load path into the acetabulum.
- It was found that the acetabulum was non-spherical, which suggested that the kinematics of the hip joint is more complex than purely rotational motion, and that a move away from the traditional ball-and-socket replacement design may be appropriate.

- The acetabular notch edges were observed to be curved, with males exhibiting deeper, wider and shorter notches than females, although the difference was not statistically significant (mean: $p = 0.30$) and supports the use of non-gender-specific models in anatomical studies.
- Based on the outcomes, the bearing geometry outline was updated from a circular shape to an extended section with two parallel sides joined with a semi-circular feature.

Component Manufacturing

- Injection moulding was pre-defined by Aurora Medical Ltd as the acetabular component's manufacturing method. The effect of the processing parameters on fibre orientation and defect population was assessed with the intention of informing the manufacturer of aspects which could improve the processing technique. Fibre orientation was related to the material injection location and a good fibre distribution was found.
- The outcomes suggested the current injection moulding processing conditions adopted by the material supplier should be altered for successful moulding of standard (dog-bone) and complex components (acetabular component) to ensure void-free parts with a homogeneous fibre distribution and optimum fibre orientation.
- The voids identified in the dog-bone specimens were suggested to be due to insufficient material in the mould because of inadequate holding pressure and/or holding time.

Component Fixation

- Plasma spraying had no deleterious effect on the static tensile or tensile-tensile fatigue properties of CFRPEEK.
- A dual layer TiHA coating possessed higher tensile and shear adhesion strength compared with the HA coating alone.
- It was found that standard procedures for testing plasma sprayed coatings are not suitable for non-metallic substrates such as CFRPEEK as non-uniform stress distributions exist across the coating surface on the substrate due to stiffness mismatch.
- A novel primary fixation method was developed which used arrowheads on the backing surface of the component. The arrowheads were formed from upstanding beams via induction heating at 343 °C using a specially designed moulding tool. Bone elastically deformed around the arrowheads, resulting in an increased extraction load.
- The outcomes of the investigations showed that the secondary processing technique requires refinements to avoid voids forming within the reformed material.

Bone response to implantation

- In this project, a novel method of evaluating the response of bone to implantation was applied. This method, digital volume correlation (DVC), first required rigorous evaluation on μCT images of a cubic bone sample, to quantify any noise effects and to determine the strain resolution.

- The response of bone under compression was assessed and good agreement with published strain results for bone failures was observed. During compression a crushed layer formed adjacent to the boundary plate which increased in thickness as the specimen was further deformed. The structure of the crushed layer was altered to such an extent that it confounded the correlation method. It was found that for reliable strain calculations a correlation coefficient of 0.90 or above was required between the sub-volumes in the reference and the deformed volumes.
- The recently developed 'virtual fields method' (VFM) was applied to the full-field DVC data to extract the Poisson's ratio. Several areas were identified as having potential for future research, in particular using the full-field data with the VFM to calculate the Young's modulus of the material and investigate how it varies with compression, the effect of boundary conditions on the material behaviour, the influence of bone morphology on the material behaviour and material heterogeneity.
- Analogue models such as polyurethane foam are a popular substitute for human bone, however, the mechanical response (brittle failure) of polyurethane foam during compression resulted in it not being a suitable material for assessing strain generation around implanted components using DVC; Animal bone was a more appropriate medium due to its visco-elastic nature and highly contrasted internal pattern.
- A noise study was conducted to calculate the measurement resolution of the DVC procedure when assessing strain in a trabecular bone specimen and the peri-prosthetic bone surrounding CFRPEEK and ceramic-titanium acetabular components. The strain resolution was poorest in the peri-prosthetic bone surrounding the ceramic-titanium component due to the scatter introduced by the component.
- For the implantation studies compressive strains were recorded which were above the measurement resolution (5×10^{-4}) for the CFRPEEK component which was attributed to the mechanical behaviour of the peri-prosthetic bone and not a noise artefact. However, the recorded strains and the strain resolution (4×10^{-3}) were similar in the case of the DeltaMotion component, rendering the strain data unreliable.
- DVC was found to be suitable for assessing strain generation around polymeric and composite implants but unsuitable for highly attenuating components such as the ceramic/titanium DeltaMotion component.

8.2 Future Work

The research detailed in this thesis focussed on four main areas: component design, component manufacture, implant fixation, and bone response to implantation. A discussion of future work was presented at the end of each study and these are summarised below:

Component Design

- It was found that the acetabulum more closely fitted an ellipsoid; however, this conclusion was based on a limited number of samples. To improve the statistical power of the acetabulum geometry characterisation, further studies are required. The additional data could be exploited in cartilage regeneration research, statistical shape modelling (SSM) and principal component analysis (PCA). Definitive geometry characterisation could be achieved using the developed methodology with large numbers of cadaver acetabulums with intact cartilage.

Component Manufacturing

- Research into the effects of moulding temperature, pressure and material flow is needed to identify which parameters are most likely to influence void formation.
- The fibre characterisation method should be applied to the full injection moulded acetabular component to investigate fibre orientation in a complex mould design where the material flow will be less predictable.

Component Fixation

- Deconsolidation was identified as a likely explanation for void formation. Research into the effects of reforming pressure, temperature, moisture uptake and the design of the reforming part is needed to identify which parameter is most influential to deconsolidation.
- Annealing prior to material reforming reduced void formation but research is required into the possible crystallinity changes which could have occurred due to prolonged heat exposure. Changes could be identified by performing a differential scanning calorimetry (DSC) experiment on annealed and un-annealed CFRPEEK specimens.
- A TiHA rough coating was identified as possessing the most favourable characteristics for enhancing the acetabular component's fixation, exhibiting the highest adhesion strength with minimal effect on the fatigue and tensile properties of the material. Further research is required into the suggestion that the titanium interlayer reduced the residual stresses in the HA layer as the mismatch in coefficient of thermal expansion between the HA and CFRPEEK was minimised, consequently improving crack resistance and preventing coating debonding. The difference in failure mechanisms of the two coating types due to this factor should be investigated in a four point bend test using acoustic emissions to detect damage and sections taken from interrupted-test specimens to visually identify cracks and observe their progress.

Bone response to implantation

- Coupling full-field strain measurements from DVC with VFM has the potential for a number of future studies including further characterisation of the mechanical behaviour of bone (i.e. extraction of Young's modulus) and the exploration of anisotropic and heterogeneous bone behaviour.
- To improve the scan quality of the implanted DeltaMotion component, further analyses should be conducted with a line detector to obtain a more authentic characterisation of bone response. In addition, analogue cups to represent the DeltaMotion component out of less highly attenuating material (e.g. aluminium) could be used.
- DVC was used as a tool in this thesis with consistent parameter settings in each analysis. The application of DVC to bone would benefit from a sensitivity analysis on variation in overlap, number of iterations and correlation coefficient threshold changes in order to investigate the algorithms influence on noise and interpolation bias.
- The cup with arrowhead primary fixation structures possessed poor stability compared to the plain coated CFRPEEK component which was attributed to incomplete seating. Further development is required on the instrumentation to identify and achieve optimum seating before further studies examining primary stability are conducted.

The work presented in this thesis forms part of the preliminary design stage of the product development process and is an important element of the design history file that is submitted for regulatory approval. This process must be completed to bring a new component to market and involves a series of stages. The preliminary design stage is the largest part of the project and alongside this work, additional supporting investigations into sterilisation, biocompatibility and wear of the component as well as instrument design and the completion of cadaver and pre-clinical trials need to be undertaken. These areas were investigated by other members of a consortium as part of the EU 7th Framework Research Programme entitled 'Enhanced Durability Resurfacing Endoprosthesis' (Ref 232151). Completion of the programme in 2013 has provided the necessary material for the project to progress to the EU board review which achieved a highly commendable grading.

The orthopedic companies in the consortium will use the design history file generated which incorporated all the thesis research work to progress the project to a clinical trial prior to the introduction of the new innovative implant system.

List of References

1. McMinn D, Daniel J. History and modern concepts in surface replacement. *Proc Inst Mech Eng H*. 2006;220(2):239-51.
2. *National Joint Registry for England and Wales 10th Annual Report*. Hemel Hempstead: 2013.
3. *Australian Orthopaedic Association National Joint Replacement Registry, Annual Report 2012*. Adelaide AOA: University of Adelaide, 2012.
4. *National Joint Registry for England and Wales 9th Annual Report*. Hemel Hempstead: 2012.
5. Huiskes R, Weinans H, Vanrietbergen B. The Relationship between Stress Shielding and Bone-Resorption around Total Hip Stems and the Effects of Flexible Materials. *Clin Orthop Relat Res*. 1992(274):124-34.
6. Kishida Y, Sugano N, Nishii T, Miki H, Yamaguchi K, Yoshikawa H. Preservation of the bone mineral density of the femur after surface replacement of the hip. *J Bone Joint Surg Br*. 2004;86(2):185-9.
7. Cobb AG, Schmalzreid TP. The clinical significance of metal ion release from cobalt-chromium metal-on-metal hip joint arthroplasty. *Proc Inst Mech Eng H*. 2006;220(H2):385-98.
8. Manley MT, Sutton K. Bearings of the Future for Total Hip Arthroplasty. *J Arthroplasty*. 2008;23(S7):47-50.e1.
9. Kurtz SM. *PEEK Biomaterials Handbook*. Oxford: Elsevier Science Ltd; 2012.
10. Cailliet R. *The illustrated guide to functional anatomy of the musculoskeletal system*. USA: AMA Press; 2004.
11. Gray H. *Anatomy of the Human Body*. 20th Online ed. Philadelphia: Lea & Febiger; 2000.
12. Gu DY, Chen YZ, Dai KR, Zhang S, Yuan JB. The shape of the acetabular cartilage surface: A geometric morphometric study using three-dimensional scanning. *Med Eng Phys*. 2008;30(8):1024-31.
13. Bergmann G, Graichen F, Rohlmann A. Hip joint contact forces during stumbling. *Langenbeck Arch Surg*. 2004;389(1):53-9.
14. *The Swedish National Hip Arthroplasty Register Annual Report 2012*. Gothenburg, Sweden: Sahlgren Hospital, 2012.
15. Goldberg B, Trivieri, L., Andersin, J.W. *Alternative medicine: the definitive guide*. 2nd ed. USA: Celestial Arts Berkeley; 2002.
16. Bachiller FGC, Caballer AP, Portal LF. Avascular necrosis of the femoral head after femoral neck fracture. *Clin Orthop Relat Res*. 2002(399):87-109.
17. Alexander M, Fawcett J, Runciman P. *Nursing practice: Hospital and Home: The Adult*. illustrated ed. Philadelphia: Churchill Livingstone; 2006.
18. McKee GK, Watson-Farrar J. Replacement of arthritic hips by the McKee-Farrar prosthesis. *J Bone Joint Surg Br*. 1966;48-B(2):245-59.
19. Delaunay C. The Charnley Total Hip Replacement: The gold standard of primary hip replacement, 36 years on. Available from: http://www.maitrise-orthop.com/corpusmaitri/orthopaedic/mo83_delaunay/delaunay_us.shtml.
20. *The Swedish National Hip Arthroplasty Register Annual Report 2008*. Gothenburg, Sweden: Sahlgren Hospital, 2008.
21. Jameson SS, Langton DJ, Natu S, Nargol TVF. The influence of age and sex on early clinical results after hip resurfacing. *J Arthroplasty*. 2008;23(6):50-5.
22. De Haan R, Pattyn C, Gill HS, Murray DW, Campbell PA, De Smet K. Correlation between inclination of the acetabular component and metal ion levels in metal-on-metal hip resurfacing replacement. *J Bone Joint Surg Br*. 2008;90-B(10):1291-7.
23. Vendittoli PA, Mottard S, Roy AG, Dupont C, Lavigne M. Chromium and cobalt ion release following the Durom high carbon content, forged metal-on-metal surface replacement of the hip. *J Bone Joint Surg Br*. 2007;89B(4):441-8.
24. Grigoris P, Roberts P, Panousis K, Jin Z. Hip resurfacing arthroplasty: the evolution of contemporary designs. *Proc Inst Mech Eng H*. 2006;220(2):95-105.
25. Head WC. Wagner Surface Replacement Arthroplasty of the Hip - Analysis of 14 Failures in 41 Hips. *J Bone Joint Surg Am*. 1981;63(3):420-7.
26. Frankel A, Balderston RA, Booth RE, Jr., Rothman RH. Radiographic demarcation of the acetabular bone-cement interface. The effect of femoral head size. *J Arthroplasty*. 1990;5 Suppl:S1-3.
27. Heaton-Adegbile P, Russery B, Taylor L, Tong J. Failure of an uncemented acetabular prosthesis – a case study. 2006;13(1):163-9.
28. August A, Aldam C, Pynsent P. The McKee-Farrar hip arthroplasty. A long-term study. *J Bone Joint Surg Br*. 1986;68-B(4):520-7.

29. Dumbleton JH, Manley MT. Metal-on-Metal total hip replacement: what does the literature say? *J Arthroplasty*. 2005;20(2):174-88.
30. Berry DJ, Von Knoch M, Schleck CD, Harmsen WS. Effect of femoral head diameter and operative approach on risk of dislocation after primary total hip arthroplasty. *J Bone Joint Surg Am*. 2005;87A(11):2456-63.
31. Goldsmith A, Dowson D, Isaac G, Lancaster J. A comparative joint simulator study of the wear of metal-on-metal and alternative material combinations in hip replacements. *Proc Inst Mech Eng H*. 2000;214(1):39-47.
32. Dowson D, Hardaker C, Flett M, Isaac GH. A hip joint simulator study of the performance of metal-on-metal joints: Part I: the role of materials. *J Arthroplasty*. 2004;19(8 Suppl 3):118-23.
33. Cawley J, Metcalf JEP, Jones AH, Band TJ, Skupien DS. A tribological study of cobalt chromium molybdenum alloys used in metal-on-metal resurfacing hip arthroplasty. *Wear*.255(7-12):999-1006.
34. Wang K, Wang A, Gustavson L. *Cobalt-based Alloys for Bio-medical Applications*. West Conshohocken: ASTM International; 1999.
35. Helsen JA, Breme HJ. *Metals as biomaterials*. Storrington: Wiley; 1998.
36. Sedel L. Evolution of alumina-on-alumina implants - A review. *Clin Orthop Relat Res*. 2000(379):48-54.
37. Willmann G. Ceramic femoral head retrieval data. *Clin Orthop*. 2000;379:6.
38. Firkins PJ, Tipper JL, Ingham E, Stone MH, Farrar R, Fisher J. A novel low wearing differential hardness, ceramic-on-metal hip joint prosthesis. *J Biomech*. 2001;34(10):1291-8.
39. Germain MA, Hatton A, Williams S, et al. Comparison of the cytotoxicity of clinically relevant cobalt-chromium and alumina ceramic wear particles in vitro. *Biomaterials*. 2003;24(3):469-79.
40. Morlock MM, Bishop N, Zustin J, Hahn M, Ruther W, Amling M. Modes of implant failure after hip resurfacing: morphological and wear analysis of 267 retrieval specimens. *J Bone Joint Surg Am*. 2008;90 Suppl 3:89-95.
41. Walter WL, Insley GM, Walter WK, Tuke MA. Edge loading in third generation alumina ceramic-on-ceramic bearings: stripe wear. *J Arthroplasty*. 2004;19(4):402-13.
42. Adelani MA, Keeney JA, Palisch A, Fowler SA, Clohisy JC. Has total hip arthroplasty in patients 30 years or younger improved? A systematic review. *Clin Orthop Relat Res*. 2013;471(8):2595-601.
43. Smith AJ, Dieppe P, Vernon K, Porter M, Blom AW. Failure rates of stemmed metal-on-metal hip replacements: analysis of data from the National Joint Registry of England and Wales. *Lancet*. 2012;379(9822):1199-204.
44. Riviere C, Lavigne M, Alghamdi A, Vendittoli P-A. Early Failure of Metal-on-Metal Large-Diameter Head Total Hip Arthroplasty Revised with a Dual-Mobility Bearing A Case Report. *J Bone Joint Surg*. 2013;3(95):1-6.
45. Willert HG, Buchhorn GH, Fayyazi A, et al. Metal-on-metal bearings and hypersensitivity in patients with artificial hip joints. A clinical and histomorphological study. *J Bone Joint Surg Am*. 2005;87(1):28-36.
46. Amstutz HC, Le Duff MJ. Eleven years of experience with metal-on-metal hybrid hip resurfacing: a review of 1000 conserve plus. *J Arthroplasty*. 2008;23(6 S1):36-43.
47. Treacy RBC, McBryde CW, Pynsent PB. Birmingham hip resurfacing arthroplasty - A minimum follow-up of five years. *J Bone Joint Surg Br*. 2005;87B(2):167-70.
48. *National Joint Registry for England and Wales 7th Annual Report*. Hemel Hempstead: 2009.
49. Langton DJ, Jameson SS, Joyce TJ, Hallab NJ, Natu S, Nargol AVF. Early failure of metal-on-metal bearings in hip resurfacing and large-diameter total hip replacement: A consequence of excess wear. *J Bone Joint Surg Br*. 2010;92-B(1):38-46.
50. Langton DJ, Joyce TJ, Jameson SS, et al. Adverse reaction to metal debris following hip resurfacing: The influence of component type, orientation and volumetric wear. *J Bone Joint Surg Br*. 2011;93-B(2):164-71.
51. Jolley M, Salvati E, Brown G. Early results and complications of surface replacement of the hip. *J Bone Joint Surg Am*. 1982;64A:10.
52. Morlock MM, Bishop N, Ruether W, Delling G, Hanh M. Biomechanical, morphological, and histological analysis of early failures in hip resurfacing arthroplasty. *Proc Inst Mech Eng H*. 2006;220(H2):333-44.
53. Griffith MJ, Seidenstein MK, Williams D, Charnley J. Socket wear in Charnley low friction arthroplasty of the hip. *Clin Orthop Relat Res*. 1978(137):37-47.
54. Scott J. MacInnes, Gordon A, Wilkinson JM. *Risk Factors for Aseptic Loosening Following Total Hip Arthroplasty, .* In: Fokter DS, editor. Recent Advances in Arthroplasty: InTech; 2012.

55. Semlitsch M, Willert H. Clinical wear behaviour of ultra-high molecular weight polyethylene cups paired with metal and ceramic ball heads in comparison to metal-on-metal pairings of hip joint replacements. *Proc Inst Mech Eng H*. 1997;211(1):73-88.
56. Wolff JA. *Das Gestetz der Transformation der Knochen*. Berlin: A Hirschwald; 1982.
57. Andersen PJ, Jacobs CH, Crowninshield RD, Parr JE. Comment on Fatigue Properties of Carbon-Coated and Porous-Coated Ti-6al-4v Alloy. *J Biomed Mater Res*. 1985;19(5):607-8.
58. Christel P, Meunier A, Leclercq S, Bouquet P, Buttazzoni B. Development of a Carbon-Carbon Hip-Prosthesis. *J Biomed Mater Res-A*. 1987;21(A2):191-218.
59. Gallo J, Konttinen Y, Goodman S, et al. *Aseptic Loosening of Total Hip Arthroplasty as a Result of Local Failure of Tissue Homeostasis*. In: Fokter DS, editor. Recent Advances in Arthroplasty 2012.
60. Kubo T, Inoue S, Maeda T. Cementless Lord total hip arthroplasty: cup loosening common after minimum 10-year follow-up of 103 hips. . *Acta Orthop Scand*. 2001;72.
61. Bobyn JD, Mortimer ES, Glassman AH, Engh CA, Miller JE, Brooks CE. Producing and Avoiding Stress Shielding - Laboratory and Clinical Observations of Noncemented Total Hip-Arthroplasty. *Clin Orthop Relat Res*. 1992(274):79-96.
62. Pitto RP, Bhargava A, Pandit S, Munro JT. Retroacetabular stress-shielding in THA. *Clin Orthop Relat Res*. 2008;466(2):353-8.
63. Wright JM, Pellicci PM, Salvati EA, Ghelman B, Roberts MM, Koh JL. Bone density adjacent to press-fit acetabular components. A prospective analysis with quantitative computed tomography. *J Bone Joint Surg Am*. 2001;83A(4):529-36.
64. Manley MT, Ong KL, Kurtz SM. The potential for bone loss in acetabular structures following THA. *Clin Orthop Relat Res*. 2006(453):246-53.
65. Thompson MS, Northmore-Ball MD, Tanner KE. Effects of acetabular resurfacing component material and fixation on the strain distribution in the pelvis. *Proc Inst Mech Eng H*. 2002;216(H4):237-45.
66. Dickinson AS, Taylor AC, Browne M. The influence of acetabular cup material on pelvis cortex surface strains, measured using digital image correlation. *J Biomech*. 2012;45(4):719-23.
67. Field RE, D Cronin M, Singh PJ, Burtenshaw C, Rushton N. Bone remodeling around the Cambridge cup - A DEXA study of 50 hips over 2 years. *Acta Orthop*. 2006;77(5):726-32.
68. Latif AMH, Mehats A, Elcocks M, Rushton N, Field RE, Jones E. Pre-clinical studies to validate the MITCH PCR (TM) Cup: a flexible and anatomically shaped acetabular component with novel bearing characteristics. *J Mater Sci-Mater M*. 2008;19(4):1729-36.
69. Kurtz SM. *The UHMWPE handbook: ultra-high molecular weight polythylene in total joint replacement*. Oxford: Academic Press; 2004.
70. Bradford L, Baker DA, Graham J, Chawan A, Ries MD, Pruitt LA. Wear and Surface Cracking in Early Retrieved Highly Cross-linked Polyethylene Acetabular Liners. *J Bone Joint Surg Am*. 2004;86(6):1271-82.
71. Tower SS, Currier JH, Currier BH, Lyford KA, Van Citters DW, Mayor MB. Rim Cracking of the Cross-Linked Longevity Polyethylene Acetabular Liner After Total Hip Arthroplasty. *J Bone Joint Surg Am*. 2007;89(10):2212-7.
72. Learmonth ID, Cunningham JL. Factors contributing to the wear of polyethylene in clinical practice. *Proc Inst Mech Eng H*. 1997;211(1):49-57.
73. Green S. *Chapter 3 - Compounds and Composite Materials*. PEEK Biomaterials Handbook. Oxford: William Andrew Publishing; 2012. p. 23-48.
74. Granoc Chopped and Milled Fibers [database on the Internet]. Nippon Graphite Fiber Corporation. 2013. Available from: http://www31.ocn.ne.jp/~ngf/english/product/p4.htm.
75. Agarwal BD, Broutman LJ, Chandrashekhara K. *Analysis and performance of fiber composites*. USA: John Wiley & Sons; 2006.
76. Harris B. *Engineering composite materials*. London: IOM Communications; 1999.
77. Campbell FC. *Structural Composite Materials*. Materials Park, OH, USA: ASM International; 2010.
78. Anon. Basic Explantation and Schematic View - Injection moulding process. Toolcraft Plastics; 2013 [cited 2013 06/09]; Available from: http://www.toolcraft.co.uk/help-injection-moulding-process.htm.
79. Invibio Ltd. MOTIS Polymer Processing Guide. 2009.
80. Henninger F, Ye L, Friedrich K. Deconsolidation behaviour of glass fibre-polyamide 12 composite sheet material during post-processing. *Plast Rub Compos Pro*. 1998;27(6):287-92.
81. Ye L, Lu M, Mai YW. Thermal de-consolidation of thermoplastic matrix composites - I. Growth of voids. *Compos Sci Technol*. 2002;62(16):2121-30.
82. Saint-Martin G, Schmidt F, Devos P, Levaillant C. Voids in short fibre-reinforced injection-moulded parts: density control vs. mass control. *Poly Test*. 2003;22(8):947-53.

83. Malloy RA. *Plastic Part Design for Injection Molding: An Introduction*. USA: Hanser Publishers; 1994.
84. Agassant JF, Kamal MR, Isayev AI. *Injection Molding: Technology and Fundamentals*. USA: Hanser; 2009.
85. De S, White JR. *Short Fibre-Polymer Composites*. Cambridge: Taylor & Francis; 1996.
86. Hegler RP, Mennig G. Phase separation effects in processing of glass-bead- and glass-fiber-filled thermoplastics by injection molding. *Polym Eng Sci*. 1985;25(7):395-405.
87. Kubát J, Szalánczi A. Polymer-glass separation in the spiral mold test. *Polym Eng Sci*. 1974;14(12):873-7.
88. Fu SY, Lauke B. Effects of fiber length and fiber orientation distributions on the tensile strength of short-fiber-reinforced polymers. *Compos Sci Technol*. 1996;56(10):1179-90.
89. Rasheva Z, Zhang G, Burkhart T. A correlation between the tribological and mechanical properties of short carbon fibers reinforced PEEK materials with different fiber orientations. *Tribol Int*. 2010;43(8):1430-7.
90. Scholes SC, de Jong S, Unsworth A. Effect of carbon fibre orientation on the wear of CFR-PEEK/CFR-PEEK bearing couples. *J Bone Joint Surg Br*. 2010;92-B(S1):131-2.
91. Wang A, Lin R, Stark C, Dumbleton JH. Suitability and limitations of carbon fiber reinforced PEEK composites as bearing surfaces for total joint replacements. *Wear*. 1999;225:724-7.
92. Scholes SC, Unsworth A. The wear performance of PEEK-OPTIMA based self-mating couples. *Wear*. 2010;268(3-4):380-7.
93. Scholes SC, Unsworth A. The wear properties of CFR-PEEK-OPTIMA articulating against ceramic assessed on a multidirectional pin-on-plate machine. *Proc Inst Mech Eng H*. 2007;221(3):281-9.
94. Flanagan S, Jones E, Birkinshaw C. In vitro friction and lubrication of large bearing hip prostheses. *Proc Inst Mech Eng H*. 2010;224(H7):853-64.
95. Scholes SC, Inman IA, Unsworth A, Jones E. Tribological assessment of a flexible carbon-fibre-reinforced poly(ether–ether–ketone) acetabular cup articulating against an alumina femoral head. *Proc Inst Mech Eng H*. 2008;222(3):273-83.
96. Polineni VK, Wang AG, Essner A, et al. Characterization of carbon fiber-reinforced PEEK composite for use as a bearing material in total hip replacements. *Am Soc Test Mater*. 1998;1346:266-73.
97. Wang QQ, Wu JJ, Unsworth A, et al. Biotribological study of large diameter ceramic-on-CFR-PEEK hip joint including fluid uptake, wear and frictional heating. *J Mater Sci-Mater M*. 2012;23(6):1533-42.
98. Brockett CL, John G, Williams S, Jin ZM, Isaac GH, Fisher J. Wear of ceramic-on-carbon fiber-reinforced poly-ether ether ketone hip replacements. *J Biomed Mater Res B*. 2012;100B(6):1459-65.
99. Smith SR, Paul IL, Rose RM, Radin EL. 'Stiction-friction' of total hip prostheses and its relationship to loosening. *J Bone Joint Surg Am*. 1975;57(2):4.
100. Pace N, Marineeli M, Spurio SM, R. Primary total hip arthroplasty with carbon fibre reinforced poly-ether-ether-ketone composite acetabular cup component 36 months results. Trans Int Soc Technol Arthroplasty (ISTA)2005. p. 13.
101. Pace N, Marinelli M, Spurio S. Technical and Histologic Analysis of a Retrieved Carbon Fiber-Reinforced Poly-Ether-Ether-Ketone Composite Alumina-Bearing Liner 28 Months After Implantation. *J Arthroplasty*. 2008;23(1):151-5.
102. Field RE, Rushton N. Five-year clinical, radiological and postmortem results of the Cambridge Cup in patients with displaced fractures of the neck of the femur. *J Bone Joint Surg Br*. 2005;87-B(10):1344-51.
103. Dumbleton JH, Manley MT. Current concepts review - Hydroxyapatite-coated prostheses in total hip and knee arthroplasty. *J Bone Joint Surg Am*. 2004;86A(11):2526-40.
104. Field RE, Rajakulendran K, Eswaramoorthy VK, Rushton N. Three-year prospective clinical and radiological results of a new flexible horseshoe acetabular cup. *Hip Int*. 2012;22(6):598-606.
105. Andersson GB, Freeman MA, Swanson SA. Loosening of the cemented acetabular cup in total hip replacement. *J Bone Joint Surg Br*. 1972;54(4):590-9.
106. Kavanagh BF, Dewitz MA, Ilstrup DM, Stauffer RN, Coventry MB. Charnley Total Hip-Arthroplasty with Cement - 15-Year Results. *J Bone Joint Surg Am*. 1989;71A(10):1496-503.
107. Hedia HS, Abdel-Shafi AAA, Fouda N. Shape optimization of metal backing for cemented acetabular cup. *Biomed Mater Eng*. 2000;10(2):73-82.
108. Kim YH, Kook HK, Kim JS. Total hip replacement with a cementless acetabular component and a cemented femoral component in patients younger than fifty years of age. *J Bone Joint Surg Am*. 2002:770-4.
109. Callaghan JJ, Rosenberg AG, Rubash HE. *The Adult Hip* Philadelphia: Lippincott Williams & Wilkins; 2007.

110. Kwong LM, O'Connor DO, Sedlacek RC, Krushell RJ, Maloney WJ, Harris WH. A quantitative in vitro assessment of fit and screw fixation on the stability of a cementless hemispherical acetabular component. *J Arthroplasty*. 1994;9(2):163-70.
111. Wasielewski RC, Cooperstein LA, Kruger MP, Rubash HE. Acetabular anatomy and the transacetabular fixation of screws in total hip arthroplasty. *J Bone Joint Surg Am*. 1990;72(4):501-8.
112. Won CH, Hearn TC, Tile M. Micromotion of cementless hemispherical acetabular components. Does press-fit need adjunctive screw fixation? *J Bone Joint Surg Br*. 1995;77B(3):484-9.
113. Geeraerts T, Chhor V, Cheisson G, et al. Clinical review: initial management of blunt pelvic trauma patients with haemodynamic instability. *Crit Care*. 2007;11(1):204.
114. Feugier P, Fessy MH, Bejui J, Bouchet A. Acetabular anatomy and the relationship with pelvic vascular structures. Implications in hip surgery. *Surg Radiol Anat*. 1997;19(2):85-90.
115. Goosen JHM, Castelein RM, Verheyen CCPM. Silent osteolysis associated with an uncemented acetabular component: A monitoring and treatment algorithm. *Curr Orthopaed*. 2005;19(4):288-93.
116. Clohisy JC, Harris WH. The Harris-Galante Porous-Coated Acetabular Component with Screw Fixation. An Average Ten-Year Follow-up Study. *J Bone Joint Surg Am*. 1999;81(1):66-73.
117. Parvizi J, Sullivan T, Duffy G, Cabanela ME. Fifteen-year clinical survivorship of Harris-Galante total hip arthroplasty. *J Arthroplasty*. 2004;19(6):672-7.
118. Curry HG, Lynskey TG, Frampton CM. Harris-Galante II acetabular cup: a survivial anaylsis. *J Orthop Surg*. 2008;16(2):4.
119. Adler E, Stuchin SA, Kummer FJ. Stability of press-fit acetabular cups. *J Arthroplasty*. 1992;7(3):295-301.
120. Dorr LD, Wan ZN, Cohen J. Hemispheric titanium porous coated acetabular component without screw fixation. *Clin Orthop Relat Res*. 1998(351):158-68.
121. Morscher E, Masar Z. Development and 1st Experience with an Uncemented Press-Fit Cup. *Clin Orthop Relat Res*. 1988(232):96-103.
122. Schmalzried TP, Wessinger SJ, Hill GE, Harris WH. The Harris-Galante porous acetabular component press-fit without screw fixation. Five-year radiographic analysis of primary cases. *The Journal of arthroplasty*. 1994;9(3):235-42.
123. Jasty M, Bragdon C, Burke D, O'Connor DO, J L, Harris WH. In Vivo Skeletal Responses to Porous-Surfaced Implants Subjected to Small Induced Motions. *J Bone Joint Surg Am*. 1997;79(5):707-14.
124. Pupparo F, Engh CA. Comparison of Porous-Threaded and Smooth-Threaded Acetabular Components of Identical Design - 2-Year to 4-Year Results. *Clin Orthop Relat Res*. 1991(271):201-6.
125. Manley MT, Capello WN, D'Antonio JA, Edidin AA, Geesink RGT. Fixation of acetabular cups without cement in total hip arthroplasty - A comparison of three different implant surfaces at a minimum duration of follow-up of five years. *J Bone Joint Surg Am*. 1998;80A(8):1175-85.
126. Ihle M, Mai S, Pfluger D, Siebert W. The results of the titanium-coated RM acetabular component at 20 years: A long-term follow-up of an uncemented primary total hip replacement. *J Bone Joint Surg Br*. 2008;90-B(10):1284-90.
127. Markel DC, Hora N, Grimm M. Press-fit stability of uncemented hemispheric acetabular components: a comparison of three porous coating systems. *Int Orthop*. 2002;26(2):72-5.
128. Della Valle CJ, Berger RA, Shott S, et al. Primary total hip arthroplasty with a porous-coated acetabular component - A concise follow-up of a previous report. *J Bone Joint Surg Am*. 2004;86A(6):1217-22.
129. Petersen MB, Poulsen IH, Thomsen J, Solgaard S. The hemispherical Harris-Galante acetabular cup, inserted without cement - The results of an eight to eleven-year follow-up of one hundred and sixty-eight hips. *J Bone Joint Surg Am*. 1999;81A(2):219-24.
130. Long PH. Medical Devices in Orthopedic Applications. *Exp Toxicol Pathol*. 2008;36(1):85-91.
131. Furlong RJ, Osborn JF. Fixation of Hip Prostheses by Hydroxyapatite Ceramic Coatings. *J Bone Joint Surg Br*. 1991;73(5):741-5.
132. Hardy DCR, Frayssinet P, Bonel G, Authom T, Lenaelou SA, Delince PE. 2-Year Outcome of Hydroxyapatite-Coated Prostheses - 2 Femoral Prostheses Retrieved at Autopsy. *Acta Orthop Scand*. 1994;65(3):253-7.
133. Buma P, Gardeniers JW. Tissue reactions around a hydroxyapatite-coated hip prosthesis. Case report of a retrieved specimen. *J Arthroplasty*. 1995;10(3):389-95.
134. Stiehl JB, MacMillan E, Skrade DA. Mechanical stability of porous-coated acetabular components in total hip arthroplasty. *J Arthroplasty*. 1991;6(4):295-300.
135. Jeffers JRT, Roques A, Taylor A, Tuke MA. The problem with large diameter metal-on-metal acetabular cup inclination. *Bull NYU Hosp Jt Dis*. 2009;67(2):4.

136. Greenwald AS, Oconnor JJ. Transmission of Forces through Human Hip-Joint. *Phys Med Biol*. 1971;16(2):339.
137. Clarke IC, Amstrutz HC. *Human hip joint geometry and hemiarthroplasty selection*. The Hip. USA: C. V. Mosby Company; 1975. p. 63-89.
138. Noble PC, Alexander JW, Lindahl LJ, Yew DT, Granberry WM, Tullos HS. The Anatomic Basis of Femoral Component Design. *Clin Orthop Relat Res*. 1988(235):148-65.
139. Rubin P, Leyvraz P, Aubaniac J, Argenson J, Esteve P, de Roguin B. The morphology of the proximal femur. A three-dimensional radiographic analysis. *J Bone Joint Surg Br*. 1992;74-B(1):28-32.
140. Thompson MS, Dawson T, Kuiper JH, Northmore-Ball MD, Tanner KE. Acetabular morphology and resurfacing design. *J Biomech*. 2000;33(12):1645-53.
141. Menschik F. The hip joint as a conchoid shape. *J Biomech*. 1997;30(9):971-3.
142. Kohnlein W, Ganz R, Impellizzeri FM, Leunig M. Acetabular Morphology: Implications for Joint-preserving Surgery. *Clin Orthop Relat Res*. 2009;467(3):682-91.
143. Rasquinha BJ, Sayani J, Rudan JF, Wood GCA, Ellis RE. Articular surface remodeling of the hip after periacetabular osteotomy. *Int J Comput Ass Rad*. 2012;7(2):241-8.
144. Pienkowski D, Resig J, Talwalkar V, Tylkowski C. Novel Three-Dimensional MRI Technique for Study of Cartilaginous Hip Surfaces in Legg-Calve-Perthes Disease. *J Orthopaed Res*. 2009;27(8):981-8.
145. Amstutz HC, Le Duff MJ. Background of metal-on-metal resurfacing. *Proc Inst Mech Eng H*. 2006;220(2):85-94.
146. Arokoski JPA, Jurvelin JS, Vaatainen U, Helminen HJ. Normal and pathological adaptations of articular cartilage to joint loading. *Scand J Med Sci Spor*. 2000;10(4):186-98.
147. Guilak F, Ratcliffe A, Mow VC. Chondrocyte deformation and local tissue strain in articular cartilage: A confocal microscopy study. *J Orthopaed Res*. 1995;13(3):410-21.
148. Daniel M, Iglic A, Kralj-Iglic V. The shape of acetabular cartilage optimizes hip contact stress distribution. *J Anat*. 2005;207(1):85-91.
149. Jin ZM, Meakins S, Morlock MM, et al. Deformation of press-fitted metallic resurfacing cups. Part 1: experimental simulation. *Proc Inst Mech Eng H*. 2006;220(H2):299-309.
150. Ong KL, Manley MT, Kurtz SM. Have contemporary hip resurfacing designs reached maturity? A review. *J Bone Joint Surg Am*. 2008;90A:81-8.
151. Ries MD, Harbaugh M, Shea J, Lambert R. Effect of cementless acetabular cup geometry on strain distribution and press-fit stability. *J Arthroplasty*. 1997;12(2):207-12.
152. Engh CA, Hopper RH, Engh CA. Long-term porous-coated cup survivorship using spikes, screws, and press-fitting for initial fixation. *J Arthroplasty*. 2004;19(7):54-60.
153. Udomkiat P, Dorr LD, Wan Z. Cementless hemispheric porous-coated sockets implanted with press-fit technique without screws: average ten-year follow-up. *J Bone Joint Surg Am*. 2002;84-A(7):1195-200.
154. Kim YS, Callaghan JJ, Ahn PB, Brown TD. Fracture of the Acetabulum during Insertion of an Oversized Hemispherical Component. *J Bone Joint Surg Am*. 1995;77A(1):111-7.
155. Sharkey PF, Hozack WJ, Callaghan JJ, et al. Acetabular fracture associated with cementless acetabular component insertion - A report of 13 cases. *J Arthroplasty*. 1999;14(4):426-31.
156. Wirth AJ, Müller R, Harry van Lenthe G. The discrete nature of trabecular bone microarchitecture affects implant stability. *J Biomech*. 2012;45(6):1060-7.
157. Ong KL, Rundell S, Liepins I, Laurent R, Markel D, Kurtz SM. Biomechanical modeling of acetabular component polyethylene stresses, fracture risk, and wear rate following press-fit implantation. *J Orthopaed Res*. 2009;27(11):1467-72.
158. Schmidig G, Patel A, Liepins I, Thakore M, Markel DC. The Effects of Acetabular Shell Deformation and Liner Thickness on Frictional Torque in Ultrahigh-Molecular-Weight Polyethylene Acetabular Bearings. *J Arthroplasty*. 2010;25(4):644-53.
159. Liu F, Chen ZF, Gu YQ, Wang Q, Cui WD, Fan WM. Deformation of the Durom Acetabular Component and Its Impact on Tribology in a Cadaveric Model-A Simulator Study. *Plos One*. 2012;7(10).
160. Huiskes R. Finite-Element Analysis of Acetabular Reconstruction - Noncemented Threaded Cups. *Acta Orthop Scand*. 1987;58(6):620-5.
161. Levenston ME, Beaupre GS, Schurman DJ, Carter DR. Computer simulations of stress-related bone remodeling around noncemented acetabular components. *J Arthroplasty*. 1993;8(6):595-605.
162. Hothi HS, Busfield JJC, Shelton JC. Deformation of uncemented metal acetabular cups following impaction: experimental and finite element study. *Comput Methods Biomech Biomed Engin*. 2012:1-14.
163. Kroeber M, Ries MD, Suzuki Y, Renowitzky G, Ashford F, Lotz J. Impact biomechanics and pelvic deformation during insertion of press-fit acetabular cups. *J Arthroplasty*. 2002;17(3):349-54.

164. Fritsche A, Bader R, Kolp W, Mittelmeier W, Tokar I. Experimental investigations of the primary stability of press-fit cups in THA in dependence of insertion force and bone quality. *J Bone Joint Surg Br*. 2010;92-B(S5):515.
165. Fritsche A, Bialek K, Mittelmeier W, et al. Experimental investigations of the insertion and deformation behavior of press-fit and threaded acetabular cups for total hip replacement. *J Orthop Sci*. 2008;13(3):240-7.
166. Fritsche A, Zietz C, Teufel S, et al. A851. In-virto and in-vivo investigations of the impaction and pull-out behavior of metal-backed acetabular cups. *J Bone Joint Surg Br*. 2011;93-B(SUPP IV):406.
167. Everitt H, Evans SL, Holt CA, Bigsby R, Khan I. Acetabular Component Deformation under Rim Loading using Digital Image Correlation and Finite Element Methods. *Ad Exp Mech VII*. 2010;24-25:275-80.
168. Meneghini RM, Ford KS, McCollough CH, Hanssen AD, Lewallen DG. Bone Remodeling Around Porous Metal Cementless Acetabular Components. *J Arthroplasty*. 2010;25(5):741-7.
169. Sztefek P, Vanleene M, Olsson R, Collinson R, Pitsillides AA, Shefelbine S. Using digital image correlation to determine bone surface strains during loading and after adaptation of the mouse tibia. 2010;43(4):599-605.
170. Cordey J, Gautier E. Strain gauges used in the mechanical testing of bones Part I: Theoretical and technical aspects. *Injury*. 1999;30, Supplement 1:SA7-SA13.
171. Cerveri P, Manzotti A, Baroni G. Patient-specific acetabular shape modelling: comparison among sphere, ellipsoid and conchoid parameterisations. *Comput Methods Biomech Biomed Engin*. 2012:1-8.
172. Shimmin AJ, Bare J, Back DL. Complications associated with hip resurfacing arthroplasty. *Orthop Clin North Am*. 2005;36(2):187-93.
173. Gu DY, Dai KR, Hu F, Chen YZ. The Shape of the Acetabular Cartilage Surface and its Role in Hip Joint Contact Stress. *IEEE Eng Med Bio*. 2010:3934-7.
174. Manley M, Ong K, Kurtz S, Rushton N, Field R. Biomechanical assessment of a novel deformable acetabular cup design. *J Bone Joint Surg Br*. 2008;90-B(S2):304.
175. Rushton N. An orthopaedic surgeon's perspective on implant design. BioTiNet - 3rd Workshop Training Material: Surface Science & Engineering; 10th January; Cambridge2013.
176. Krogman WM. *The human skeleton in forensic medicine*. Illinois: C.C. Thomas; 1962.
177. Rushfeldt PD, Mann RW, Harris WH. Improved techniques for measuring in vitro the geometry and pressure distribution in the human acetabulum--I. Ultrasonic measurement of acetabular surfaces, sphericity and cartilage thickness. *J Biomech*. 1981;14(4):253-60.
178. Petrov Y. ellipsoid fit. 2012; Available from: http://www.mathworks.co.uk/matlabcentral/fileexchange/24693-ellipsoid-fit.
179. Oberlander W, Kurrat HJ, Breul R. Examination of Extension of Osseous Facies Lunata - Functional Study. *Z Orthop Grenzgeb*. 1978;116(5):675-82.
180. Murtha PE, Hafez MA, Jaramaz B, DiGioia AM, 3rd. Variations in acetabular anatomy with reference to total hip replacement. *J Bone Joint Surg Br*. 2008;90(3):308-13.
181. Gubener Plastinate GmbH. Body Donation. 2012 [cited 2012 28th August]; Available from: <http://www.plastinarium.de/en/plastinarium_e/body_donation.html>
182. Nelson DA, Pettifor JM, Barondess DA, Cody DD, Uusi-Rasi K, Beck TJ. Comparison of cross-sectional geometry of the proximal femur in white and black women from Detroit and Johannesburg. *J Bone Miner Res*. 2004;19(4):560-5.
183. Rawal BR, Ribeiro R, Malhotra R, Bhatnagar N. Anthropometric measurements to design best-fit femoral stem for the Indian population. *Indian J Orthop*. 2012;46(1):46-53.
184. Theobald TM, Cauley JA, Gluer CC, et al. Black-white differences in hip geometry. *Osteoporosis Int*. 1998;8(1):61-7.
185. Bryan R, Mohan PS, Hopkins A, Galloway F, Taylor M, Nair PB. Statistical modelling of the whole human femur incorporating geometric and material properties. *Med Eng Phys*. 2010;32(1):57-65.
186. Heimann T, Meinzer HP. Statistical shape models for 3D medical image segmentation: A review. *Med Image Anal*. 2009;13(4):543-63.
187. Rajamani KT, Styner MA, Talib H, Zheng GY, Nolte LP, Ballester MAG. Statistical deformable bone models for robust 3D surface extrapolation from sparse data. *Med Image Anal*. 2007;11(2):99-109.
188. Stevens DR, Flores-Mir C, Nebbe B, Raboud DW, Heo G, Major PW. Validity, reliability, and reproducibility of plaster vs digital study models: Comparison of peer assessment rating and Bolton analysis and their constituent measurements. *Am J Orthod Dentofacial Orthop*. 2006;129(6):794-803.
189. Todd TW. The Effect of Maceration and Drying upon the Linear Dimensions of the Green Skull. *J Anat*. 1923;57(Pt 4):336-56.

190. Trotter M, Gleser GC. Estimation of Stature from Long Limb Bones of American Whites and Negroes - Reply. *Am J Phys Anthropol*. 1977;47(2):355-6.
191. Athawale MC. Estimation of Height from Lengths of Forearm Bones. A Study of One Hundred Maharashtrian Male Adults of Ages between Twenty-Five and Thirty Years. *Am J Phys Anthropol*. 1963;21:105-12.
192. Han EH, Bae WC, Hsieh-Bonassera ND, et al. Shaped, stratified, scaffold-free grafts for articular cartilage defects. *Clin Orthop Relat Res*. 2008;466(8):1912-20.
193. Koh JL, Wirsing K, Lautenschlager E, Zhang LO. The effect of graft height mismatch on contact pressure following osteochondral grafting - A biomechanical study. *Am J Sport Med*. 2004;32(2):317-20.
194. Fu SY, Lauke B. The elastic modulus of misaligned short-fiber-reinforced polymers. *Compos Sci Technol*. 1998;58(3–4):389-400.
195. Karger-Kocsis J. *Applications of Fracture Mechanics to Composite Materials- Microstructure and fracture mechanical performance of short-fibre reinforced thermoplastics*. Amsterdam: Elsevier Science; 1989. 189-247 p.
196. Norman DA, Robertson RE. The effect of fiber orientation on the toughening of short fiber-reinforced polymers. *J Appl Polym Sci*. 2003;90(10):2740-51.
197. Zak G, Park CB, Benhabib B. Estimation of three-dimensional fibre-orientation distribution in short-fibre composites by a two-section method. *J Compos Mater*. 2001;35(4):316-39.
198. Zhu YT, Blumenthal WR, Lowe TC. Determination of non-symmetric 3-D fiber-orientation distribution and average fiber length in short-fiber composites. *J Compos Mater*. 1997;31(13):1287-301.
199. Papathanasiou TD, Guell DC. *Flow-induced alignment in composite materials*: Woodhead; 1997.
200. Clarke AR, Eberhardt CN. *Microscopy techniques for materials science*. Cambridge: CRC Press; 2002.
201. Davidson NC, Clarke AR, Archenhold G. Large-area, high-resolution image analysis of composite materials. *J Microsc*. 1997;185:233-42.
202. Yurgartis SW. Measurement of Small-Angle Fiber Misalignments in Continuous Fiber Composites. *Compos Sci Technol*. 1987;30(4):279-93.
203. Hine PJ, Duckett RA, Davidson N, Clarke AR. Modeling of the Elastic Properties of Fiber Reinforced Composites - Orientation Measurement. *Compos Sci Technol*. 1993;47(1):65-73.
204. Diebel J. *Representing Attitude: Euler Angles, Unit Quaternions, and Rotation Vectors*. California: Stanford University, 2006.
205. Stobie RS. The Cosmos Image Analyzer. *Pattern Recogn Lett*. 1986;4(5):317-24.
206. Eberhardt C, Clarke A, Vincent M, Giroud T, Flouret S. Fibre-orientation measurements in short-glass-fibre composites—II: a quantitative error estimate of the 2D image analysis technique. *Compos Sci Technol*. 2001;61(13):1961-74.
207. Liu KC, Ghoshal A. Validity of random microstructures simulation in fiber-reinforced composite materials. *Compos Part b-Eng*. 2014;57(0):56-70.
208. Zangenberg J, Brøndsted P. Determination of the minimum size of a statistical representative volume element from a fibre-reinforced composite based on point pattern statistics. *Acta Mater*. 2013;68(7):503-5.
209. Zappini G, Robotti P, editors. Metal and HA Coating Technologies for PEEK Implants. MD&M; 2010; Minneapolis: Eurocoating.
210. Beauvais S, Decaux O. Plasma Sprayed Biocompatible Coatings on PEEK Implants. International Thermal Spray Conference and Exposition; Beijing 2007.
211. Vedova S, Robotti P, Fabbri A, Zeni D, D.Amato M, Monelli B. Effects of plasma spray HA coating process onto mechanical properties of PEEK and carbon fiber reinforced PEEK. 8th World Biomaterials Congress; May 28- June 1; Amsterdam, The Netherlands2008.
212. Laonapakul T, Otsuka Y, Nimkerdphol AR, Mutoh Y. Acoustic emission and fatigue damage induced in plasma-sprayed hydroxyapatite coating layers. *J Mech Behav Biomed*. 2012;8(0):123-33.
213. Laonapakul T, Rakngarm Nimkerdphol A, Otsuka Y, Mutoh Y. Failure behavior of plasma-sprayed HAp coating on commercially pure titanium substrate in simulated body fluid (SBF) under bending load. *J Mech Behav Biomed*. 2012;15(0):153-66.
214. Rakngarm A, Mutoh Y. Characterization and fatigue damage of plasma sprayed HAp top coat with Ti and HAp/Ti bond coat layers on commercially pure titanium substrate. *J Mech Behav Biomed*. 2009;2(5):444-53.
215. Xue WC, Liu XY, Zheng XB, Ding CX. Plasma-sprayed diopside coatings for biomedical applications. *Surf Coat Tech*. 2004;185(2-3):340-5.
216. Ha SW, Gisep A, Mayer J, Wintermantel E, Gruner H, Wieland M. Topographical characterization and microstructural interface analysis of vacuum-plasma-sprayed titanium and hydroxyapatite coatings on carbon fibre-reinforced poly(etheretherketone). *J Mater Sci-Mater M*. 1997;8(12):891-6.

217. Ha SW, Mayer J, Koch B, Wintermantel E. Plasma-Sprayed Hydroxylapatite Coating on Carbon-Fiber-Reinforced Thermoplastic Composite-Materials. *J Mater Sci-Mater M*. 1994;5(6-7):481-4.
218. Sim G-D, Lee Y-S, Lee S-B, Vlassak JJ. Effects of stretching and cycling on the fatigue behavior of polymer-supported Ag thin films. 2013;575(0):86-93.
219. Kim B-J, Shin H-AS, Jung S-Y, et al. Crack nucleation during mechanical fatigue in thin metal films on flexible substrates. 2013;61(9):3473-81.
220. Geesink RG, de Groot K, Klein CP. Bonding of bone to apatite-coated implants. *J Bone Joint Surg Br*. 1988;70(1):17-22.
221. Finch CA. Adhesion and adhesives technology—an introduction, 2nd edn. AV Pocius. Carl Hanser Gardener Verlag, Munchen, 2002. *Poly Int*. 2004;53(9):1394-.
222. Adams R, Peppiatt N. Stress analysis of adhesive-bonded lap joints. *J Strain Anal Eng Des*. 1974;9(3):185-96.
223. CGTec. PEEK Surface Modification of PEEK Polymer 2009 19/10/2010. Available from: http://www.cgtec.eu/category/fiche-matieres/peek-fiche-matieres/victrex-peek-fiche-matieres-fiche-matieres.
224. Bonk RB, Osterndorf, J.F., Pettenger, B.L. Methods for evaluation adhesive systems and adhesion. Technical Report ARAED-TR-95025. *US Army Armament Research, Development and Engineering Center* [Internet]. 1996.
225. Zeiler T. Oberflächenmodifizierung von thermoplastischen Polymerwerkstoffen in Hinblick auf die Verbesserung ihrer Verklebbarkeit, : Universität Erlangen- Nürnberg; 1997.
226. Heijink A, Zobitz ME, Nuyts R, Morrey BF, An KN. Prosthesis design and stress profile after hip resurfacing: a finite element analysis. *J Orthop Surg*. 2008;16(3):326-32.
227. Brockmann W, Geiss P, Klingen J, Schröder K, Mikhail B. *Adhesive Bonding: Materials, Applications and Technology*: Wiley-VCH Verlag GmbH; 2009.
228. Mencik J. *Mechanics of components with treated or coated surfaces.* London: Kluwer Academic Publishers; 1995.
229. Evans AG, Crumley GB, Demaray RE. On the mechanical behavior of brittle coatings and layers. *Oxidat Met*. 1983;20:10.
230. Dickinson A, Taylor A, Roques A, Browne M. Measuring the Adhesion of Ti/HA Coatings to Non-Metallic Implant Materials. 2013;95-B(SUPP 34):286.
231. Tsui YC, Doyle C, Clyne TW. Plasma sprayed hydroxyapatite coatings on titanium substrates Part 1: Mechanical properties and residual stress levels. *Biomaterials*. 1998;19(22):2015-29.
232. Dickinson AS, Roques AC, Browne M, Taylor AC. Measuring the adhesion of Ti/HA coatings to non-metallic implant materials. ISTA - 26th Annual Congress; 16-19 October 2013; Palm Beach, Florida 2013.
233. Roman SR. Comparing Kirschner wire fixation to a new device used for proximal interphalangeal fusion. http://www.podiatryinstitute.com/textbooks.htm#update2012 [cited 2013 6th October]; Available from: http://www.podiatryinstitute.com/pdfs/Update_2011/2011_30.pdf.
234. Bergmann G, Graichen F, Rohlmann A, et al. Realistic loads for testing hip implants. *Biomed Mater Eng*. 2010;20(2):65-75.
235. Eschweiler J, Fieten L, Schmidt F, et al. Comparison of the orientation of the resultant force of different biomechanical models. *J Bone Joint Surg Br*. 2012;94-B:54.
236. Pedersen DR, Brand RA, Davy DT. Pelvic muscle and acetabular contact forces during gait. *J Biomech*. 1997;30(9):959-65.
237. Roman SR, inventor; *Intramedullary fixation device and methods for bone fixation and stabilization*2011 20 Oct 2011.
238. Macdonald W, Carlsson LV, Charnley GJ, Jacobsson CM. Press-fit acetabular cup fixation: principles and testing. *Proc Inst Mech Eng H*. 1999;213(H1):33-9.
239. Kelly N, McGarry JP. Experimental and numerical characterisation of the elasto-plastic properties of bovine trabecular bone and a trabecular bone analogue. *J Mech Behav Biomed*. 2012;9(0):184-97.
240. Kopperdahl DL, Keaveny TM. Yield strain behavior of trabecular bone. 1998;31(7):601-8.
241. Goldstein SA. The mechanical properties of trabecular bone: dependence on anatomic location and function. *J Biomech*. 1987;20(11-12):1055-61.
242. Rohl L, Larsen E, Linde F, Odgaard A, Jorgensen J. Tensile and compressive properties of cancellous bone. *J Biomech*. 1991;24(12):1143-9.
243. Beahm B, Ward J. New Catheter Tipping Process Aids Tubing's Accuracy and Throughput. 2005 [cited 2013 7th October]; Available from: http://www.mdtmag.com/product-releases/2005/06/new-catheter-tipping-process-aids-tubing%E2%80%99s-accuracy-and-throughput#.UnoDJvnQCYR.

244. Tsai CJ. A study of thermal degradation of poly(aryl-ether-ether-ketone) using stepwise pyrolysis/gas chromatography/mass spectrometry. *Rapid Commun Mass Spectrom*. 1997;11:8.
245. Yeh GSY, Hosemann R, Lobodacackovic J, Cackovic H. Annealing Effects of Polymers and Their Underlying Molecular Mechanisms. *Polymer*. 1976;17(4):309-18.
246. Lambert J, Chambers AR, Sinclair I, Spearing SM. 3D damage characterisation and the role of voids in the fatigue of wind turbine blade materials. *Compos Sci Technol*. 2012;72(2):337-43.
247. Plataniotis KN, Venetsanopoulos AN. *Color Image Processing and Applications*: Springer; 2000.
248. Scott AE, Mavrogordato M, Wright P, Sinclair I, Spearing SM. In situ fibre fracture measurement in carbon–epoxy laminates using high resolution computed tomography. *Compos Sci Technol*. 2011;71(12):1471-7.
249. Nixon M, Aguado AS. *Feature Extraction & Image Processing*: Elsevier Science; 2008.
250. Greenwood GW, Johnson RH. The Deformation of Metals Under Small Stresses During Phase Transformations. *Proceedings of the Royal Society of London Series A Mathematical and Physical Sciences*. 1965;283(1394):403-22.
251. Lee YC, Porter RS. Double-Melting Behavior of Poly(Ether Ether Ketone). *Macromolecules*. 1987;20(6):1336-41.
252. Fougnies C, Damman P, Dosière M, Koch MHJ. Time-Resolved SAXS, WAXS, and DSC Study of Melting of Poly(aryl ether ether ketone) (PEEK) Annealed from the Amorphous State. *Macromolecules*. 1997;30(5):1392-9.
253. Wei C-L, Chen M, Yu F-E. Temperature modulated DSC and DSC studies on the origin of double melting peaks in poly(ether ether ketone). *Polymer*. 2003;44(26):8185-93.
254. Hall SA, Bornert M, Desrues J, et al. Discrete and continuum analysis of localised deformation in sand using X-ray mu CT and volumetric digital image correlation. *Geotechnique*. 2010;60(5):315-22.
255. Sjödahl M, Siviour CR, Forsberg F. Digital Volume Correlation Applied to Compaction of Granular Materials. *Procedia IUTAM*. 2012;4(0):179-95.
256. Bay BK, Smith TS, Fyhrie DP, Saad M. Digital volume correlation: Three-dimensional strain mapping using X-ray tomography. *Exp Mech*. 1999;39(3):217-26.
257. De Man B, Nuyts J, Dupont P, Marchal G, Suetens P. Reduction of metal streak artifacts in x-ray computed tomography using a transmission maximum a posteriori algorithm. *IEEE T Nucl Sci*. 2000;47(3):977-81.
258. Stock SR. *MicroComputed Tomography: Methodology and Applications*. USA: CRC Press Taylor & Francis Group; 2008.
259. Feldkamp LA, Davis LC, Kress JW. Practical Cone-Beam Algorithm. *J Opt Soc Am A*. 1984;1(6):612-9.
260. Lim KS, Barigou M. X-ray micro-computed tomography of cellular food products. *Food Res Int*. 2004;37(10):1001-12.
261. Landis EN, Keane DT. X-ray microtomography. *Materials Characterization*. 2010;61(12):1305-16.
262. Ketcham RA, Carlson WD. Acquisition, optimization and interpretation of X-ray computed tomographic imagery: applications to the geosciences. *Comput Geosci-Uk*. 2001;27(4):381-400.
263. Hsieh J. *Computed Tomography: Principles, Design, Artifacts, and Recent Advances*. Washington: SPIE Press; 2003.
264. Christoph R, Neumann HJ. *X-ray Tomography in Industrial Metrology: Precise, Economical and Universal*. Germany: Verlag Moderne Industrie; 2011.
265. Buzug TM. *Computed Tomography: From Photon Statistics to Modern Cone-Beam CT*. Germany: Springer; 2008.
266. Moulart R, Pierron F, Hallett SR, Wisnom MR. Full-Field Strain Measurement and Identification of Composites Moduli at High Strain Rate with the Virtual Fields Method. *Exp Mech*. 2011;51(4):509-36.
267. Reprinted with permission, from ASTM Standard E 1441-00, 'Standard Guide for Computed Tomography (CT) Imaging'. copyright ASTM International, 100 Barr Harbor Drive, West Conshohocken, PA 19428. A copy of the complete standard may be obtained from ASTM International, www.astm.org2000.
268. Limodin N, Rethore J, Adrien J, Buffiere JY, Hild F, Roux S. Analysis and Artifact Correction for Volume Correlation Measurements Using Tomographic Images from a Laboratory X-ray Source. *Exp Mech*. 2011;51(6):959-70.
269. Prell D, Kyriakou Y, Kalender WA. Comparison of ring artifact correction methods for flat-detector CT. *Phys Med Biol*. 2009;54(12):3881-95.
270. Boas FE, Fleischmann D. CT artifacts: causes and reduction techniques. *Imaging in Medicine*. 2012;4(2):229-40.
271. Barrett JF, Keat N. Artifacts in CT: Recognition and Avoidance. *RadioGraphics*. 2004;24(6):1679-91.

272. Cordey J, Gautier E. Strain gauges used in the mechanical testing of bones Part II: "In vitro" and "in vivo" technique. *Injury*. 1999;30, Supplement 1:SA14-SA20.
273. Hoc T, Henry L, Verdier M, Aubry D, Sedel L, Meunier A. Effect of microstructure on the mechanical properties of Haversian cortical bone. *Bone*. 2006;38(4):466-74.
274. Horta J, Brostow W, Martinez G, Castano VM. Characterization of bones by speckle interferometry. *J Med Eng Technol*. 2003;27(2):49-53.
275. Moreno V, Vázquez-Vázquez C, Gallas M, Crespo J. Speckle shearing pattern interferometry to assess mechanical strain in the human mandible jaw bone under physiological stress. 2011:800131-.
276. Su M, Samala PR, Jiang HH, Liu S, Yang L, Yokota H. Measurement of Bone Strain Using Electronic Speckle Pattern Interferometry. *J Holography Speckle*. 2005;2(1):34-9.
277. Kohles SS, Vanderby Jr R. Thermographic strain analysis of the proximal canine femur. *Med Eng Phys*. 1997;19(3):262-6.
278. Vanderby R, Jr., Kohles SS. Thermographic stress analysis in cortical bone. *J Biomech Eng*. 1991;113(4):418-22.
279. Krawitz AD. Neutron strain measurement. *Mater Sci Tech*. 2011;27(3):589-603.
280. Wentzell S, Nesbitt RS, Macione J, Knapp R, Kotha SR. Bone Strain Measurement Using 3D Digital Image Correlation of Second Harmonic Generation Images. 2011.
281. Christen D, Levchuk A, Schori S, Schneider P, Boyd SK, Müller R. Deformable image registration and 3D strain mapping for the quantitative assessment of cortical bone microdamage. 2012;8(0):184-93.
282. Thompson MS, Schell H, Lienau J, Duda GN. Digital image correlation: A technique for determining local mechanical conditions within early bone callus. 2007;29(7):820-3.
283. Hollister SJ, Brennan JM, Kikuchi N. A Homogenization Sampling Procedure for Calculating Trabecular Bone Effective Stiffness and Tissue-Level Stress. *J Biomech*. 1994;27(4):433-44.
284. Niebur GL, Feldstein MJ, Yuen JC, Chen TJ, Keaveny TM. High-resolution finite element models with tissue strength asymmetry accurately predict failure of trabecular bone. *J Biomech*. 2000;33(12):1575-83.
285. Van Rietbergen B, Müller R, Ulrich D, Rüegsegger P, Huiskes R. Tissue stresses and strain in trabeculae of a canine proximal femur can be quantified from computer reconstructions. *J Biomech*. 1999;32(2):165-73.
286. Van Rietbergen B, Weinans H, Huiskes R, Odgaard A. A new method to determine trabecular bone elastic properties and loading using micromechanical finite-element models. *J Biomech*. 1995;28(1):69-81.
287. Verhulp E, van Rietbergen B, Huiskes R. A three-dimensional digital image correlation technique for strain measurements in microstructures. *J Biomech*. 2004;37(9):1313-20.
288. Ruffoni D, Kohler T, Voide R, et al. High-throughput quantification of the mechanical competence of murine femora — A highly automated approach for large-scale genetic studies. *Bone*. 2013;55(1):216-21.
289. Verhulp E, van Rietbergen B, Müller R, Huiskes R. Indirect determination of trabecular bone effective tissue failure properties using micro-finite element simulations. *J Biomech*. 2008;41(7):1479-85.
290. Durand EP, Ruegsegger P. High-Contrast Resolution of CT Images for Bone-Structure Analysis. *Med Phys*. 1992;19(3):569-73.
291. Elke RPE, Cheal EJ, Simmons C, Poss R. 3-Dimensional Anatomy of the Cancellous Structures within the Proximal Femur from Computed-Tomography Data. *J Orthopaed Res*. 1995;13(4):513-23.
292. Bay BK. Methods and applications of digital volume correlation. *J Strain Anal Eng*. 2008;43(8):745-60.
293. Gates M, Lambros J, Heath MT. Towards High Performance Digital Volume Correlation. *Exp Mech*. 2011;51(4):491-507.
294. Smith TS, Bay BK, Rashid MM. Digital volume correlation including rotational degrees of freedom during minimization. *Exp Mech*. 2002;42(3):272-8.
295. Smith TS, Bay BK. Experimental measurement of strains using digital volume correlation. *Am Soc Test Mater*. 2001;1323:117-26.
296. Pierron F, McDonald SA, Hollis D, Withers PJ, Alderson A. Assessment of the deformation of low density polymeric auxetic foams by X-ray tomography and digital volume correlation. *Ad Exp Mech VIII*. 2011;70:93-8.
297. Roux S, Hild F, Viot P, Bernard D. Three-dimensional image correlation from X-ray computed tomography of solid foam. *Compos Part a-Appl S*. 2008;39(8):1253-65.
298. Forsberg F, Sjodahl M, Mooser R, Hack E, Wyss P. Full Three-Dimensional Strain Measurements on Wood Exposed to Three-Point Bending: Analysis by Use of Digital Volume Correlation Applied to Synchrotron Radiation Micro-Computed Tomography Image Data. *Strain*. 2010;46(1):47-60.
299. Liu L, Morgan EF. Accuracy and precision of digital volume correlation in quantifying displacements and strains in trabecular bone. *J Biomech*. 2007;40(15):3516-20.

300. Madi K, Tozzi G, Zhang QH, et al. Computation of full-field displacements in a scaffold implant using digital volume correlation and finite element analysis. *Med Eng Phys*. 2013;35(9):1298-312.
301. Scarano F. Tomographic PIV: principles and practice. *Meas Sci Technol*. 2013;24(1):012001.
302. Da Fonseca JQ, Mummery PM, Withers PJ. Full-field strain mapping by optical correlation of micrographs acquired during deformation. *J Microsc*. 2005;218:9-21.
303. Germaneau A, Doumalin P, Dupre JC. 3D strain field measurement by correlation of volume images using scattered light: Recording of images and choice of marks. *Strain*. 2007;43(3):207-18.
304. Bruck HA, Mcneill SR, Sutton MA, Peters WH. Digital Image Correlation Using Newton-Raphson Method of Partial-Differential Correction. *Exp Mech*. 1989;29(3):261-7.
305. Zauel R, Yeni YN, Bay BK, Dong XN, Fyhrie DP. Comparison of the linear finite element prediction of deformation and strain of human cancellous bone to 3D digital volume correlation measurements. *J Biomech Eng*. 2006;128(1):1-6.
306. Lenoir N, Bornert M, Desrues J, Besuelle P, Viggiani G. Volumetric digital image correlation applied to X-ray microtomography images from triaxial compression tests on argillaceous rock. *Strain*. 2007;43(3):193-205.
307. Bremand F, Germaneau A, Doumalin P, Dupre JC, editors. Study of mechanical behaviour of cancellous bone by Digital Volume Correlation and X-ray Micro-Computed Tomography. Proceedings of the XIth International Congress and Exposition; 2008 June 2-5; Orlando, Florida: Society for Experimental Mechanics Inc.
308. Forsberg F, Siviour CR. 3D deformation and strain analysis in compacted sugar using x-ray microtomography and digital volume correlation. *Meas Sci Technol*. 2009;20(9):095703.
309. Hussein AI, Barbone PE, Morgan EF. Digital Volume Correlation for Study of the Mechanics of Whole Bones. *Procedia IUTAM*. 2012;4(0):116-25.
310. Franck C, Hong S, Maskarinec S, Tirrell D, Ravichandran G. Three-dimensional Full-field Measurements of Large Deformations in Soft Materials Using Confocal Microscopy and Digital Volume Correlation. 2007;47(3):427-38.
311. Fu J, Haghighi-Abayneh M, Pierron F, Ruiz PD. *Assessment of Corneal Deformation Using Optical Coherence Tomography and Digital Volume Correlation*. In: Prorok BC, Barthelat F, Korach CS, Grande-Allen KJ, Lipke E, Lykofatitits G, et al., editors. Mechanics of Biological Systems and Materials, Volume 5: Springer New York; 2013. p. 155-60.
312. Pierron F, Grédiac M. *The Virtual Fields Method: Extracting Constitutive Mechanical Parameters from Full-field Deformation Measurements*. New York: Springer; 2012.
313. Hoc T, Rey C, Viaris de Lesengo P. Mesostructure of the localization in prestrained mild steel. 2000;42(8):749-54.
314. Grediac M, Pierron F, Avril S, Toussaint E. The virtual fields method for extracting constitutive parameters from full-field measurements: A review. *Strain*. 2006;42(4):233-53.
315. Hendricks MAN. Identification of the mechanical properties of solid materials. [Doctoral Dissertation]. The Netherlands Eindhoven; 1991.
316. Claire D, Hild F, Roux S. Identification of damage fields using kinematic measurements. *Cr Mecanique*. 2002;330(11):729-34.
317. Geymonat G, Hild F, Pagano S. Identification of elastic parameters by displacement field measurement. *Cr Mecanique*. 2002;330(6):403-8.
318. Ikehata M. Inversion Formulas for the Linearized Problem for an Inverse Boundary-Value Problem in Elastic Prospection. *Siam J Appl Math*. 1990;50(6):1635-44.
319. Dym CL, Shames IH. *Solid mechanics: a variational approach*. USA: McGraw-Hill; 1973.
320. Pierron F. Identification of Poisson's ratios of standard and auxetic low-density polymeric foams from full-field measurements. *J Strain Anal Eng*. 2010;45(4):233-53.
321. Dally JW, Riley WF. *Experimental stress analysis*. New York: McGraw-Hill Higher Education; 1978.
322. Kim JH, Pierron F, Wisnom MR, Syed-Muhamad K. Identification of the local stiffness reduction of a damaged composite plate using the virtual fields method. *Compos Part a-Appl S*. 2007;38(9):2065-75.
323. Tattoli F, Pierron F, Rotinat R, Casavola C, Pappalettere C. Full-Field Strain Measurement On Titanium Welds And Local Elasto-Plastic Identification With The Virtual Fields Method. *AIP Conf Proc*. 2010;1315:860-5.
324. Avril S, Pierron F, Sutton MA, Yan JH. Identification of elasto-visco-plastic parameters and characterization of Luders behavior using digital image correlation and the virtual fields method. *Mech Mater*. 2008;40(9):729-42.
325. Dalstra M, Huiskes R, Odgaard A, van Erning L. Mechanical and textural properties of pelvic trabecular bone. *J Biomech*. 1993;26(4–5):523-35.

326. Rincon-Kohli L, Zysset PK. Multi-axial mechanical properties of human trabecular bone. *Biomech Model Mechan*. 2009;8(3):195-208.
327. Jorgensen CS, Kundu T. Measurement of material elastic constants of trabecular bone: a micromechanical analytic study using a 1 GHz acoustic microscope. *J Orthopaed Res*. 2002;20(1):151-8.
328. Zysset PK, Edward Guo X, Edward Hoffler C, Moore KE, Goldstein SA. Elastic modulus and hardness of cortical and trabecular bone lamellae measured by nanoindentation in the human femur. *J Biomech*. 1999;32(10):1005-12.
329. Burr DR. The mechanical adaptations of bones. By John Currey. Princeton, New Jersey: Princeton University Press. 1984. *Am J Phys Anthropol*. 1985;68(1):141-2.
330. Kahn-Jetter Z, Chu T. Three-dimensional displacement measurements using digital image correlation and photogrammic analysis. *Exp Mech*. 1990;30(1):10-6.
331. Peters WH, Ranson WF. Digital Imaging Techniques in Experimental Stress-Analysis. *Opt Eng*. 1982;21(3):427-31.
332. Sutton MA, Cheng MQ, Peters WH, Chao YJ, Mcneill SR. Application of an Optimized Digital Correlation Method to Planar Deformation Analysis. *Image Vision Comput*. 1986;4(3):143-50.
333. Pierron F, McDonald SA, Hollis D, Withers PJ, Alderson A. Comparative investigation of the mechanical behaviour of standard and auxetic low density polyurethane foams by X-ray tomography and Digital Volume Correlation. *Strain*. 2013;in press.
334. Yaofeng S, Pang JHL. Study of optimal subset size in digital image correlation of speckle pattern images. *Opt Laser Eng*. 2007;45(9):967-74.
335. Lim TH, Hong JH. Poroelastic properties of bovine vertebral trabecular bone. *J Orthopaed Res*. 2000;18(4):671-7.
336. Dassault Systemes Simulia Corp P, RI, USA. *ABAQUS Theory Manual (version 6.9)*. 2009.
337. Keaveny TM, Wachtel EF, Ford CM, Hayes WC. Differences between the tensile and compressive strengths of bovine tibial trabecular bone depend on modulus. *J Biomech*. 1994;27(9):1137-46.
338. Teo JCM, Si-Hoe KM, Keh JEL, Teoh SH. Relationship between CT intensity, micro-architecture and mechanical properties of porcine vertebral cancellous bone. *Clin Biomech*. 2006;21(3):235-44.
339. Keaveny TM, Morgan EF, Niebur GL, Yeh OC. Biomechanics of trabecular bone. *Annu Rev Biomed Eng*. 2001;3:307-33.
340. Gibson LJ. Biomechanics of cellular solids. *J Biomech*. 2005;38(3):377-99.
341. Wachtel EF, Keaveny TM. Dependence of trabecular damage on mechanical strain. *J Orthopaed Res*. 1997;15(5):781-7.
342. Smith CW, Wootton RJ, Evans KE. Interpretation of experimental data for Poisson's ratio of highly nonlinear materials. *Exp Mech*. 1999;39(4):356-62.
343. Liu XS, Bevill G, Keaveny TM, Sajda P, Guo XE. Micromechanical analyses of vertebral trabecular bone based on individual trabeculae segmentation of plates and rods. *J Biomech*. 2009;42(3):249-56.
344. Bayraktar HH, Morgan EF, Niebur GL, Morris GE, Wong EK, Keaveny TM. Comparison of the elastic and yield properties of human femoral trabecular and cortical bone tissue. *J Biomech*. 2004;37(1):27-35.
345. Keaveny TM, Pinilla TP, Crawford RP, Kopperdahl DL, Lou A. Systematic and random errors in compression testing of trabecular bone. *J Orthopaed Res*. 1997;15(1):101-10.
346. Bevill GR, University of California B. *Micromechanical Modeling of Failure in Trabecular Bone*: University of California, Berkeley; 2008.
347. Johnson AE, Keller TS. Mechanical properties of open-cell foam synthetic thoracic vertebrae. *J Mater Sci-Mater M*. 2008;19(3):1317-23.
348. Patel PSD, Shepherd DET, Hulkins DWL. Mechanical properties of polyurethane foam compared with values for normal and osteoporotic human cancellous bone. *Proceeding of the ASME Summer Bioengineering Conference*. 2007:837-8.
349. Patel PSD, Shepherd DET, Hukins DWL. Compressive properties of commercially available polyurethane foams as mechanical models for osteoporotic human cancellous bone. *BMC Musculoskelet Disord*. 2008;9(137).
350. Schreier HW, Braasch JR, Sutton MA. Systematic errors in digital image correlation caused by intensity interpolation. *Opt Eng*. 2000;39(11):2915-21.
351. Gibson LJ, Ashby MF. *Cellular Solids: Structure and Properties*. Cambridge: Cambridge University Press; 1999.
352. Robertson DD, Weiss PJ, Fishman EK, Magid D, Walker PS. Evaluation of CT Techniques for Reducing Artifacts in the Presence of Metallic Orthopedic Implants. *J Comput Assist Tomo*. 1988;12(2):236-41.

353. Heo YS, Lee KM, Lee SU. Illumination and camera invariant stereo matching. *Proc Cvpr IEEE*. 2008:2767-74.
354. Nakasone S, Takao M, Nishii T, Sakai T, Sugano N. Incidence and natural course of initial polar gaps in Birmingham Hip Resurfacing cups. *J Arthroplasty*. 2012;27(9):1676-82.
355. Sandborn PM, Cook SD, Spires WP, Kester MA. Tissue response to porous-coated implants lacking initial bone apposition. *J Arthroplasty*. 1988;3(4):337-46.
356. Fyhrie DP, Carter DR. A unifying principle relating stress to trabecular bone morphology. *J Orthopaed Res*. 1986;4(3):304-17.
357. Baleani M, Fognani R, Toni A. Initial stability of a cementless acetabular cup design: Experimental investigation on the effect of adding fins to the rim of the cup. *Artif Organs*. 2001;25(8):664-9.
358. Kim YS, Brown TD, Pedersen DR, Callaghan JJ. Reamed surface topography and component seating in press-fit cementless acetabular fixation. *J Arthroplasty*. 1995;10(21):S14-21.
359. Hothi HS, Busfield JJC, Shelton JC. Explicit Finite Element Modelling of the Impaction of Metal Press-Fit Acetabular Components. *Proc Inst Mech Eng H*. 2011;225(3):303-14.

Appendix 1: Ellipsoid Fit used in Section 3.1.1 to determine whether the acetabulum fits a sphere or ellipsoid more closely.

Ellipse Fit

```
S = dlmread('S12_notch.XYZ'); x = S(:,1); y = S(:,2); z = S(:,3)*-1;
% * center    -  ellispoid center coordinates [xc; yc; zc]
% * ax        -  ellipsoid radii [a; b; c]
% * evecs     -  ellipsoid radii directions as columns of the 3x3 matrix
% * v         -  the 9 parameters describing the ellipsoid algebraically:
%               Ax^2 + By^2 + Cz^2 + 2Dxy + 2Exz + 2Fyz + 2Gx + 2Hy + 2Iz = 1
% fit ellipsoid in the form Ax^2 + By^2 + Cz^2 + 2Gx + 2Hy + 2Iz = 1
D = [ x .* x,  y .* y, z .* z, 2 * x, 2 * y, 2 * z ];
% solve the normal system of equations
v = ( D' * D ) \ ( D' * ones( size( x, 1 ), 1 ) );
 % form the algebraic form of the ellipsoid
 v = [ v(1) v(2) v(3) 0 0 0 v(4) v(5) v(6) ];
  center = ( -v( 7:9 ) ./ v( 1:3 ) )';    gam = 1 + ( v(7)^2 / v(1) + v(8)^2 / v(2) + v(9)^2 / v(3) );
    radii = ( sqrt( gam ./ v( 1:3 ) ) )';     evecs = eye( 3 );
```

Determination of Distances and Angles between points

```
Complete = dlmread('S1_notch_x_all.txt');
%centre of ellipsoid
x0 = center(1,1); y0 = center(2,1); z0 = center(3,1);
Centre_vector_length = (x0*x0) + (y0*y0) + (z0*z0);
Centre_vector_length = sqrt(Centre_vector_length);
% radius of ellipsoid
Radii_x = radii(1,1); Radii_y = radii(2,1); Radii_z = radii(3,1);

Cc = Complete;
%equation of sphere
%Error of points from ellipsoid using equation (x-xo)^2/a^2 + (y-yo)^2/b^2
%+ (z-zo)^2/c^2 = 1 % a,b,c radius
q1 = Cc(:,1)-x0; q2 = Cc(:,2)-y0; q3 = Cc(:,3)-z0;
q1_squared = q1.*q1; q2_squared = q2.*q2; q3_squared = q3.*q3;
Rx = Radii_x*Radii_x; Ry = Radii_y*Radii_y; Rz = Radii_z*Radii_z;
% error
Errorx = q1_squared./Rx; Errory = q2_squared./Ry; Errorz = q3_squared./Rz;
%sum of error
Error_total = Errorx + Errory + Errorz;
%matrix of x,y,z coordinates and error
Data = [Cc(:,1), Cc(:,2), Cc(:,3),Error];
Vector_length = Errorx.*Errorx + Errory.*Errory + Errorz.*Errorz;
Vector_length1 = sqrt(Vector_length); Error_vector = 1 - Vector_length1;
% remove data that exhibits an error of +/-0.05 from ideal ellipsoid
[p,n] = size (Data); % ellipse
for i = 1:p
   row=p+1-i;
   if (Data(row,4) >= 0.05  );%
      Data(row,:) = [];
   end
end
[p,n] = size (Data); % ellipse
for i = 1:p
   row=p+1-i;
   if (Data(row,4) <= -0.05  );
      Data(row,:) = [];
```

Appendix 2: DVC strain calculation and masking code used in Section 5 and 6.

MATLAB calculation

```
clear;
Resolution = 126.28; %in microns
Overlap = 0.50;
Voxel_size = 64*(1-Overlap);
%read data from text file – text file has 6 columns x, y and z co-ordinates and x, y and z displacements
M = dlmread('PEEK_64_50%_stat.txt');
L = dlmread('Delta_stat_correlation.txt', '\t');
M(M==0)=NaN;
% find length of matrix e.g. length of each side of volume
nx = length(unique(M(:,1))); ny = length(unique(M(:,2))); nz = length(unique(M(:,3)));
% get each vector component and reshape on to a 3-dimensional grid, that matches the dimensions above
uxx_orig = reshape(M(:,4), nx, ny, nz); %x displacements in 3D grid
uyy_orig = reshape(M(:,5), nx, ny, nz); % y displacements in 3D grid
uzz_orig = reshape(M(:,6), nx, ny, nz); % z displacements in 3D grid
% set spacing between the centre of each sub-volume,
Spacing = Voxel_size*Resolution*0.001;
Spacingx = Spacing; Spacingy = Spacingx; Spacingz = Spacingy;
% if correlation mask is required it is applied here
% if spherical mask is required it is applied here
% use MATLAB gradient command to calculate strain. Gradient function estimates the first derivative of a
function supplied as the displacement points. At the edge points it uses the first order finite difference
approximation e.g. da/dx = (the change in y)/(the change in x). For the central points it uses a second order
central difference (y(3) - y(1)) / (2*deltax)
[uxy,epsxx,uxz]=gradient(uxx_orig,Spacingx,Spacingy,Spacingz);
uxy=-uxy;
[epsyy,uyx,uyz]=gradient(uyy_orig,Spacingx,Spacingy,Spacingz);
epsyy=-epsyy;
[uzy,uzx,epszz]=gradient(uzz_orig,Spacingx,Spacingy,Spacingz);
uzy=-uzy;
epsxy=0.5*(uxy+uyx);epsxz=0.5*(uxz+uzx);epsyz=0.5*(uyz+uzy);

% geometrically mask the air/edge effects out of the matrix by defining the matrix boundaries.
x1=8; x2=43;y1=10; y2=35;z1=1; z2=16;
 % reduce size of strain and correlation matrices
epsxx=epsxx(x1:x2,y1:y2,z1:z2);epsyy=epsyy(x1:x2,y1:y2,z1:z2);epszz=epszz(x1:x2,y1:y2,z1:z2);
epsxy=epsxy(x1:x2,y1:y2,z1:z2);epsxz=epsxz(x1:x2,y1:y2,z1:z2);epsyz=epsyz(x1:x2,y1:y2,z1:z2);
correlation=correlation(x1:x2,y1:y2,z1:z2);
```

Spherical Mask – this is applied prior to strain calculation so the displacement data is masked.

```
% define matrix of ones which is the same size as the displacement matrix
[x,y,z] = ndgrid(1:nx,1:ny,1:nz);
%define radius of sphere
radius =10.75;
% define centre locations of the sphere
xo = 15;yo = 15;zo = 21.25;
%equation of the sphere
sphere = ((x-xo).^2+(y-yo).^2+(z-zo).^2 < radius^2);
% make values within the sphere not a number.
sphere = (sphere -1).*-1;
sphere(sphere==0)=NaN;
```

Virtual Field Method

```
%specify the region of interest in MATLAB
 x1=16;   x2=22; y1=12;  y2=18; z1=2;  z2=9;
% Construct the matrices of coordinates
Xa=z2-z1+1-0.5;  Ya=x2-x1+1-0.5; Za=y2-y1+1-0.5;
X=[0.5:1:Xa]; Y=[Ya:-1:0.5]; Z=[0.5:1:Za];
[X,Y,Z]=meshgrid(Z,Y,X);
Xa=y2-y1; Ya=x2-x1; Za=z2-z1;
% Virtual strains
epszzv=(2*Z-Za).*X.*(X-Xa).*Y.*(Y-Ya);
epsxzv=0.5*(2*X-Xa).*Y.*(Y-Ya).*Z.*(Z-Za);
epsyzv=0.5*(2*Y-Ya).*Z.*(Z-Za).*X.*(X-Xa);
% top of equation
a1=mean(mean2(epszz.*epszzv))+2*mean(mean2(epsyz.*epsyzv))+2*mean(mean2(epsxz.*epsxzv));
%bottom of equation
b1=mean(mean2(epszzv.*(epsxx+epsyy+epszz)));
K1=-a1/b1;
Nu1_orig=K1/(1+2*K1);
%constant stress approach
Vxz = mean_x/mean_z; Vyz = mean_y/mean_z
```